



TECHNISCHE UNIVERSITÄT MÜNCHEN

Fakultät für Physik

**The Search for  $0\nu\beta\beta$  Decay with LEGEND: Signal the Background and Back the Signal**

Felix Johann Fischer

Vollständiger Abdruck der von der Fakultät für Physik der Technischen Universität München zur Erlangung des akademischen Grades eines

Doktors der Naturwissenschaften

genehmigten Dissertation.

Vorsitzender: Prof. Dr. Björn Garbrecht

Prüfer der Dissertation: 1. Priv.-Doz. Dr. Béla Majorovits  
2. Prof. Dr. Susanne Mertens

Die Dissertation wurde am 13.04.2022 bei der Technischen Universität München eingereicht und durch die Fakultät für Physik am 03.05.2022 angenommen.



# Declaration of Authorship

I, Felix FISCHER, declare that this thesis titled, “The Search for  $0\nu\beta\beta$  Decay with LEGEND: Signal the Background and Back the Signal” and the work presented in it are my own. I confirm that:

- This work was done wholly or mainly while in candidature for a research degree at this University.
- Where any part of this thesis has previously been submitted for a degree or any other qualification at this University or any other institution, this has been clearly stated.
- Where I have consulted the published work of others, this is always clearly attributed.
- Where I have quoted from the work of others, the source is always given. With the exception of such quotations, this thesis is entirely my own work.
- I have acknowledged all main sources of help.
- Where the thesis is based on work done by myself jointly with others, I have made clear exactly what was done by others and what I have contributed myself.

Signed:

---

Date:

---



*“There is a theory which states that if ever anyone discovers exactly what the Universe is for and why it is here, it will instantly disappear and be replaced by something even more bizarre and inexplicable.*

*There is another theory mentioned, which states that this has already happened.”*

Douglas Adams



## Abstract

The search for neutrinoless double beta ( $0\nu\beta\beta$ ) decay plays a major role in answering important fundamental questions about neutrinos. A still unanswered question that can be assessed by observing  $0\nu\beta\beta$  decay is, whether the neutrino is a Majorana particle, in other words, whether it is identical to its own antiparticle. This property is connected to the origin of neutrino mass. In fact, many extensions of the Standard Model of particle physics naturally predict Majorana neutrinos. In addition, the Majorana nature of neutrinos is also represented in leading theories that explain the baryon asymmetry of the universe (BAU). Since detection of the lepton-number violating  $0\nu\beta\beta$ -decay would prove that neutrinos have a Majorana mass term, its experimental search has been underway for decades with various isotopes. The theoretical half-life of the  $0\nu\beta\beta$ -decay is inversely proportional to the neutrino mass which leads to very high experimental requirements in terms of background reduction and isotope mass.

The LEGEND experiment is based on  $^{76}\text{Ge}$ -enriched *high-purity germanium* (HPGe) detectors and will use the infrastructure of the *GERmanium Detector Array* (GERDA) experiment. In its first phase, which is also referred to as LEGEND-200, a total of 200 kg of HPGe detectors will be deployed. In the tonne-scale phase, LEGEND-1000, a sensitivity on  $0\nu\beta\beta$ -decay half-life of  $> 10^{28}$  yr with 10 t·yr of exposure is targeted. In order to reach the sensitivity goal of LEGEND-1000, the background level in the region of interest has to be reduced by a factor of 50 compared to its predecessor GERDA.

In this work, two aspects of background suppression are elaborated for LEGEND. In the first, the background identification was improved by introducing *poly(ethylene 2,6-naphthalate)* (PEN) as new optically transparent and scintillating structural material. This commercially-available plastic can be moulded to almost arbitrarily-shaped scintillating structures with high intrinsic radiopurity, good mechanical strength and wavelength-shifting properties. In order to use PEN in LEGEND-200, a production process including a dedicated cleaning procedure was developed. Through radiopurity measurements and optical characterisation of the custom-made PEN scintillators, it was shown that all requirements for the use in the ultra-low background environment are fulfilled and that they are compatible for the use in close

vicinity of HPGe detectors. As result, all HPGe detectors in LEGEND-200 will be mounted on the newly developed PEN holding structures.

In the second aspect, a simulation-based analysis chain to determine  $0\nu\beta\beta$ -decay detection efficiency for individual germanium detectors was developed. The detection efficiency of rare-event search experiments is a crucial parameter which in case of LEGEND has to be determined for all detectors individually. Former analyses were completely data-driven by using a so-called *signal proxy* with similar characteristics as expected for  $0\nu\beta\beta$  decay. However, this entails uncertainties as the spatial distributions and Bremsstrahlung effect of the different energy deposition processes are not comparable. With the presented analysis, these effects are taken into account by pulse-shape simulations. Each step of the analysis chain was validated using GERDA data of broad-energy germanium (BEGe) detectors. Here, a good agreement between data and simulation was achieved resulting in an overall  $0\nu\beta\beta$ -decay detection efficiency of  $(85.9 \pm 1.8)\%$  with a significantly reduced total uncertainty compared to data-driven analyses.

## Zusammenfassung

Die Suche nach dem neutrinolosen Doppelbetazerfall ( $0\nu\beta\beta$ ) spielt eine entscheidende Rolle bei der Beantwortung wichtiger grundlegender Fragen über die Natur der Neutrinos. Eine dieser Fragen kann durch die Messung des  $0\nu\beta\beta$  Zerfalls untersucht werden. Dabei handelt es sich um die Frage, ob das Neutrino ein Majorana Teilchen ist, also ob es identisch zu seinem eigenen Antiteilchen ist. Diese Eigenschaft steht in Verbindung mit dem Ursprung der Neutrinomasse. In der Tat, Majorana Neutrinos werden von vielen Erweiterungen des Standard Modells der Teilchenphysik auf natürliche Weise vorhergesagt. Zusätzlich ist die Majorana Eigenschaft der Neutrinos ein wichtiger Bestandteil in vielen führenden Theorien, die die Baryonenasymmetrie des Universums (BAU) erklären. Da die Messung des leptonzahlverletzenden  $0\nu\beta\beta$  Zerfalls zeigen würde, dass Neutrinos eine Majorana-Masse besitzen, ist dessen experimentelle Suche bereits seit Jahrzehnten mit verschiedenen Isotopen im Gange. Die theoretische Halbwertszeit des  $0\nu\beta\beta$  Zerfalls ist umgekehrt proportional zur effektiven Majorana-Neutrinomasse, wodurch die experimentellen Anforderungen an den radioaktiven Untergrund und die Masse des Isotops sehr hoch sind.

Das LEGEND Experiment basiert auf *high-purity germanium* (HPGe) Detektoren angereichert mit dem Isotop  $^{76}\text{Ge}$  und wird zu Beginn die Infrastruktur des *GERmanium Detector Array* (GERDA) Experiments nutzen. In der ersten Phase, welche auch als LEGEND-200 bezeichnet wird, werden gesamt ungefähr 200 kg an HPGe Detektoren betrieben. In der Tonnenmaßstabsphase, LEGEND-1000, wird eine Sensitivität auf die  $0\nu\beta\beta$  Zerfallshalbwertszeit von  $> 10^{28}$  a mit 10 t-a Exposition angestrebt. Um das Ziel der Sensitivität von LEGEND-1000 zu erreichen, muss der Strahlungshintergrund im Vergleich zu seinem Vorgänger GERDA um den Faktor 50 verringert werden.

In dieser Arbeit wurden zwei Aspekte zur Unterdrückung von Strahlungshintergründen für LEGEND ausgearbeitet. Im ersten wurde die Erkennung des Strahlungshintergrundes durch die Einführung von *Polyethylen-naphthalat* (PEN) als neues optisch transparentes und szintillierendes Strukturmaterial verbessert. Dieses kommerziell erhältliche Plastik lässt sich nahezu zu jeder beliebigen szintillierenden Form gießen und das mit einer niedrigen intrinsischen Konzentration an radioaktiven Unreinheiten, mit guter

mechanischer Stabilität und wellenlängenverschiebenden Eigenschaften. Um PEN in LEGEND-200 verwenden zu können, wurde ein Herstellungsverfahren mit einem speziellem Reinigungsprozess entwickelt. Durch anschließende Messung der radioaktiven Unreinheiten und einer Charakterisierung der optischen Eigenschaften der PEN Szintillatoren wurde gezeigt, dass PEN alle Anforderungen an die Nutzung in einer Umgebung mit extrem niedrigem Strahlungshintergrund erfüllt und dass es in der näheren Umgebung von HPGe Detektoren verwendet werden kann. Als Ergebnis werden in LEGEND-200 alle HPGe Detektoren auf den neu entwickelten PEN Halterungen montiert.

Im zweiten Aspekt wurde eine simulationsbasierte Analyseketten zur Bestimmung der Detektionseffizienz des  $0\nu\beta\beta$  Zerfalls für einzelne Detektoren entwickelt. Die Detektionseffizienz eines Experiments zur Suche nach seltenen Zerfällen ist ein entscheidender Parameter und muss im Falle von LEGEND für jeden Detektor individuell bestimmt werden. Die bisherigen Analysen wurden komplett datengestützt ausgeführt und verwendeten ein sogenanntes *Signalproxy* mit ähnlichen Eigenschaften wie sie von  $0\nu\beta\beta$  Zerfällen erwartet werden. Allerdings zieht das Unsicherheiten mit sich, da die räumliche Verteilungen der Ereignisse und die Effekte der Bremsstrahlung durch verschiedene Energiedepositionsverfahren nicht vergleichbar sind. Mit der präsentierten Analyse werden diese Effekte durch Pulsformsimulationen berücksichtigt. Jeder Schritt der Analyseketten wurde anhand von GERDA-Daten für *broad-energy germanium* (BEGe) Detektoren validiert. Hier wurde eine gute Übereinstimmung zwischen Daten und Simulation erzielt, was zu einer Detektionseffizienz des  $0\nu\beta\beta$  Zerfalls von  $(85.9 \pm 1.8)\%$  führte. Im Vergleich zu datengestützten Analysen konnten auch die Unsicherheiten signifikant verringert werden.

## *Acknowledgements*

I would first like to thank my thesis advisors PD Dr. Béla Majorovits, Dr. Anna Zsigmond and Dr. Luis Manzanillas as well as Dr. Iris Abt of the Max Planck Institute for Physics in Munich, Germany. The doors to their offices were always open whenever I ran into a trouble spot or had a question about my research or writing. They consistently allowed this thesis to be my own work, but steered me in the right direction whenever I needed it.

I would also like to acknowledge Prof. Dr. Susanne Mertens as the second reader of this thesis, and I am gratefully indebted for her very valuable comments on this thesis.

Finally, I must express my very profound gratitude to my family and beloved partner Bianca Paulus for providing me with unfailing support and continuous encouragement throughout my years of study and through the process of researching and writing this thesis. This accomplishment would not have been possible without them. Thank you!



# Contents

<b>Declaration of Authorship</b>	<b>iii</b>
<b>Abstract</b>	<b>vii</b>
<b>Zusammenfassung</b>	<b>ix</b>
<b>Acknowledgements</b>	<b>xi</b>
<b>1 Introduction</b>	<b>1</b>
<b>2 Neutrinoless Double Beta Decay</b>	<b>5</b>
2.1 Neutrino Masses . . . . .	5
2.2 Double Beta Decay . . . . .	8
2.3 Experimental Search for $0\nu\beta\beta$ Decay . . . . .	12
<b>3 Germanium-Based <math>0\nu\beta\beta</math>-Decay Search Experiments</b>	<b>15</b>
3.1 GERDA . . . . .	16
3.2 MAJORANA DEMONSTRATOR . . . . .	18
3.3 The Next Generation $0\nu\beta\beta$ -Decay Search Experiment LEGEND	19
3.4 LEGEND-200 Design & Status . . . . .	20
3.5 LEGEND-1000 Design Plans . . . . .	22
<b>4 Radiation Detection using Germanium Detectors</b>	<b>25</b>
4.1 Working Principle of Germanium Detectors . . . . .	25
4.2 Signal Generation . . . . .	27
4.3 Pulse-Shape Simulation using <i>SolidStateDetectors.jl</i> . . . . .	28
<b>5 Background Sources and their Identification in GERDA</b>	<b>31</b>
5.1 Internal Background Sources . . . . .	31
5.2 External Background Sources . . . . .	32
5.3 Background Event Identification in GERDA . . . . .	33
5.4 Background Considerations in LEGEND . . . . .	38

<b>6</b>	<b>Polyethylene Naphthalate as Optically Active Structural Material</b>	<b>41</b>
6.1	Optical Properties . . . . .	42
6.2	Requirements for PEN in LEGEND-200 . . . . .	46
<b>7</b>	<b>PEN as Optically Active Structural Material in LEGEND-200</b>	<b>49</b>
7.1	From PEN Granulate to Optically Active Ultra-Low Background Components . . . . .	50
7.2	PEN Integration Tests . . . . .	56
7.3	Setups for Optical Characterisation . . . . .	64
7.4	Optical Characterisation of the LEGEND-200 PEN Scintillator . . . . .	76
7.5	Summary . . . . .	90
<b>8</b>	<b><math>0\nu\beta\beta</math>-Decay Detection Efficiency for GERDA Phase II</b>	<b>93</b>
8.1	Data Sets & Event Selection . . . . .	94
8.2	Detector Simulation . . . . .	96
8.3	Energy Calibration . . . . .	101
8.4	$A/E$ Calibration . . . . .	106
8.5	$A/E$ Cut Survival Fractions for Different Energy Regions . . . . .	115
8.6	$0\nu\beta\beta$ -Decay Detection Efficiency . . . . .	120
8.7	Uncertainty Evaluation . . . . .	124
8.8	Summary . . . . .	129
<b>9</b>	<b>Conclusions &amp; Outlook</b>	<b>131</b>
<b>A</b>	<b>Appendix - Part I</b>	<b>135</b>
A.1	PMT Setup . . . . .	135
A.2	Detection Efficiency & Energy Threshold of the Small and Medium Type Holder . . . . .	141
<b>B</b>	<b>Appendix - Part II</b>	<b>145</b>
B.1	Julia Implementation of the Electronics Response Function . . . . .	145
B.2	Detector Parameters for Simulation and Electronics Model . . . . .	147
B.3	Achieved Energy Resolution Compared to GERDA . . . . .	148
B.4	FWHM Comparison of Data and Simulation . . . . .	149
B.5	Energy Ranges for $A/E$ Energy Dependence Determination . . . . .	151
B.6	$A/E$ Cut Survival Fractions . . . . .	157
	<b>Bibliography</b>	<b>161</b>

# List of Figures

2.1	Nucleon energy illustration for beta and double beta decay . . .	9
2.2	Double beta decay energy spectrum . . . . .	10
2.3	Feynman diagrams of $2\nu\beta\beta$ and $0\nu\beta\beta$ decays . . . . .	11
2.4	Probability density of the effective Majorana neutrino mass . . .	12
3.1	Schematic structure of GERDA . . . . .	16
3.2	GERDA Phase II detector arrangement . . . . .	17
3.3	Modular design of MAJORANA DEMONSTRATOR . . . . .	18
3.4	$0\nu\beta\beta$ -decay half-life $T_{1/2}^{0\nu}$ sensitivity as function of exposure .	20
3.5	Germanium detector geometries used in LEGEND-200 . . . . .	21
3.6	Schematic structure of LEGEND-200 . . . . .	21
3.7	Baseline design of the LEGEND-1000 cryostat . . . . .	23
4.1	Electric potential for a GERDA germanium detector . . . . .	29
4.2	3D illustration of energy deposits in a germanium detector . .	30
4.3	Simulated charge signals . . . . .	30
5.1	GERDA background identification methods . . . . .	34
5.2	Weighting potential for different germanium detector types .	36
5.3	Charge pulses with different pulse-shape characteristics . . . .	37
5.4	GERDA Phase II energy spectrum before and after analysis cuts	38
5.5	Expected background contributions of LEGEND-200 . . . . .	39
6.1	Emission spectra of PEN and BC-408 scintillator samples . . .	42
6.2	Comparison of the light output of PEN and PS . . . . .	43
6.3	Comparison of WLS properties of PEN and TPB . . . . .	44
6.4	Illustration of reflection types and micro facets . . . . .	46
7.1	Clean bench and vacuum tank used for PEN cleaning . . . . .	51
7.2	Moulding and CNC milling machine used for PEN disc pro- duction . . . . .	53
7.3	Final LEGEND-200 PEN holder designs . . . . .	54
7.4	Experimental setup in the underground laboratory of TUM . .	57

7.5	Results of the baseline measurement taken at TUM . . . . .	58
7.6	Arrangement of the four detector strings during PGT-phase . . . . .	59
7.7	Germanium detector mounted on a PEN holder during the PGT . . . . .	60
7.8	Calibration spectrum of an ICPC detector mounted on PEN during PGT . . . . .	61
7.9	Mean baseline over time during the PGT for nine detectors . . . . .	62
7.10	Change of mean baseline over time for two detectors . . . . .	63
7.11	Example height map of the surface of a PEN holder . . . . .	66
7.12	Photograph of the PMT setup . . . . .	68
7.13	Simulated beam spot and its effect on the resolution . . . . .	70
7.14	Beam spot hit distribution and hit probability for large PEN holder . . . . .	71
7.15	Energy spectra in the scintillator sample . . . . .	71
7.16	Example for typical SPE waveforms . . . . .	73
7.17	Example for a typical SPE distribution . . . . .	74
7.18	Dark count measurement in the PMT setup . . . . .	75
7.19	Emission spectrum of a LEGEND-200 PEN sample . . . . .	77
7.20	3D surface scans of a PEN holder . . . . .	77
7.21	Height and angular distributions of 3D surface scans of PEN . . . . .	78
7.22	Attenuation length measurement results . . . . .	80
7.23	Light loss in large PEN holder due to attenuation . . . . .	81
7.24	Light output of PEN, PS32 and EJ-200 . . . . .	82
7.25	Detection efficiency of the large PEN holder . . . . .	84
7.26	930 keV peak fit and linear dependency . . . . .	86
7.27	Energy threshold of the large PEN holder . . . . .	86
8.1	Cross section of BEGe detector showing the state of depletion . . . . .	97
8.2	Configuration of a charge-sensitive preamplifier . . . . .	98
8.3	DEP charge superpulses for data and simulation . . . . .	99
8.4	Mean baseline RMS for GERDA BEGe detectors . . . . .	100
8.5	Fit of the DEP and the FEP of $^{208}\text{Tl}$ . . . . .	103
8.6	Energy spectrum for $^{228}\text{Th}$ calibration data . . . . .	104
8.7	FWHM at DEP and $Q_{\beta\beta}$ for GERDA BEGe detectors . . . . .	105
8.8	FWHM as function of energy for GD35B . . . . .	105
8.9	$A/E$ as function of energy for GD35B . . . . .	106
8.10	$A/E$ peak position $\mu_{A/E}(E)$ and width $\sigma_{A/E}(E)$ for GD35B . . . . .	107
8.11	$A/E$ distribution of DEP events for GD35B . . . . .	108
8.12	$A/E$ classifier $\zeta$ of GD35B . . . . .	108
8.13	DEP of GD35B and corresponding $A/E$ classifier distribution . . . . .	110

8.14	DEP survival fraction as function of the cut value for data and simulation . . . . .	111
8.15	DEP fit before and after $A/E$ low cut . . . . .	112
8.16	$A/E$ peak position $\mu_{A/E}(E)$ and width $\sigma_{A/E}(E)$ comparison for data and simulation . . . . .	113
8.17	$A/E$ peak position $\mu_{DEP}$ and resolution $\sigma_{DEP}$ of the DEP for data and simulation . . . . .	114
8.18	$A/E$ low cut values for all BEGe detectors of data and simulation	115
8.19	Energy spectrum of GD35B of the $^{208}\text{Tl}$ DEP and $^{212}\text{Bi}$ FEP before and after applying $A/E$ cuts . . . . .	116
8.20	Comparison of the $A/E$ cut survival fractions for the DEP, SEP and FEP of $^{208}\text{Tl}$ and the FEP of $^{212}\text{Bi}$ for data and simulation .	118
8.21	Comparison of the survival fractions for two Compton continua and $2\nu\beta\beta$ -decay . . . . .	119
8.22	$A/E$ cut efficiencies for $0\nu\beta\beta$ decay . . . . .	120
8.23	$A/E$ survival fraction as function of energy for $2\nu\beta\beta$ decays .	121
8.24	Spatial distribution of all DEP events of the simulation of GD35B	123
8.25	Spatial distribution of all $0\nu\beta\beta$ events of the simulation of GD35B	123
8.26	Distribution of the determined amplitudes $A$ and energy estimators $E_{\text{uncal.}}$ for simulated DEP pulses of GD35B . . . . .	125
8.27	Distribution of $A/E$ classifier uncertainties for the events in the region of the DEP of GD35B . . . . .	127
A.1	$^{207}\text{Bi}$ decay scheme . . . . .	135
A.2	Calibration spectrum of one PMT . . . . .	137
A.3	Stability of the SPE calibration of the PMTs . . . . .	138
A.4	Quantum efficiency of used PMTs . . . . .	139
A.5	Simulated energy deposition spectrum in trigger scintillator .	140
A.6	Detection efficiency of the small and medium PEN holders . .	141
A.7	Energy threshold of the small and medium PEN holders . . .	142
A.8	Emission spectra of PEN and TPB compared to the absorption spectrum of the WLS fibres . . . . .	143
B.1	Electronics model applied to a simulated charge pulse . . . . .	146
B.2	Energy resolution in this work compared to results of GERDA	148
B.3	FWHM as function of energy for data and simulation . . . . .	149
B.4	$A/E$ scatter plot with highlighted ranges for $A/E$ calibration .	151
B.5	$A/E$ peak position $\mu_{A/E}(E)$ and width $\sigma_{A/E}(E)$ . . . . .	152
B.6	DEP survival fraction as function of the $A/E$ cut value . . . . .	155



# List of Tables

2.1	List of double beta decaying isotopes . . . . .	10
6.1	Young's modulus and yield strength of PEN . . . . .	47
7.1	HPGe screening results of PEN . . . . .	56
7.2	Energy resolution at $Q_{\beta\beta}$ and at the 2.6 MeV peak for nine well-performing HPGe detectors during PGT . . . . .	62
8.1	Main signal libraries of the $^{228}\text{Th}$ calibration spectrum . . . . .	94
8.2	Signal libraries for $A/E$ cut survival fractions analysis . . . . .	116
8.3	Exposure, $2\nu\beta\beta$ and $0\nu\beta\beta$ detection efficiency for all BEGe detectors . . . . .	122
A.1	$^{207}\text{Bi}$ main conversion electrons . . . . .	136
B.1	Impurity levels and HV used for detector simulation . . . . .	147
B.2	$A/E$ cut survival fractions for the DEP of $^{208}\text{Tl}$ and FEP of $^{212}\text{Bi}$ . . . . .	157
B.3	$A/E$ cut survival fractions for the SEP and FEP of $^{208}\text{Tl}$ . . . . .	158
B.4	$A/E$ cut survival fractions for two Compton continua . . . . .	159
B.5	$A/E$ low cut values and uncertainties . . . . .	160



# List of Abbreviations

$0\nu\beta\beta$	Neutrinoless double beta
$2\nu\beta\beta$	Neutrino accompanied double beta
<b>ADC</b>	Analogue to Digital Converter
<b>aGe</b>	Amorphous Germanium
<b>BAU</b>	Baryon Asymmetry of the Universe
<b>BEGe</b>	Broad-Energy Germanium
<b>CCD</b>	Charge-Coupled Device
<b>C.L.</b>	Confidence Level
<b>CMOS</b>	Complementary Metaloxide-Semiconductor
<b>CNC</b>	Computerised Numerical Control
<b>CP</b>	Charge Parity/Charge Conjugation Parity
<b>DEP</b>	Double-Escape Peak
<b>DI</b>	Deionised
<b>FEP</b>	Full-Energy Peak
<b>FWHM</b>	Full-Width Half-Maximum
<b>GBP</b>	Gain-Bandwidth Product
<b>GERDA</b>	Germanium Detector Array
<b>HPGe</b>	High-Purity Germanium
<b>HV</b>	High Voltage
<b>ICPC</b>	Inverted Coaxial Point Contact
<b>ICP-MS</b>	Inductively Coupled Plasma Mass Spectrometry
<b>IO</b>	Inverted Ordering
<b>LAr</b>	Liquid Argon
<b>LC</b>	Leakage Current
<b>LED</b>	Light Emitting Diode
<b>LEGEND</b>	Large Enriched Germanium Experiment for Neutrinoless $\beta\beta$ Decay
<b>LKT</b>	Lehrstuhl für Kunststofftechnik
<b>LMFE</b>	Low-Mass Front-End
<b>LNGS</b>	Laboratori Nazionali del Gran Sasso
<b>LSM</b>	le Laboratoire Souterrain de Modane (Modane underground laboratory)
<b>MSE</b>	Multi-Site Event
<b>MWA</b>	Moving Window Average

<b>NME</b>	Nuclear Matrix Element
<b>NO</b>	Normal Ordering
<b>ORNL</b>	Oak Ridge National Laboratory
<b>PE</b>	Photo electron
<b>PEN</b>	Poly(ethylene 2,6-naphthalate)
<b>PET</b>	Polyethylene Terephthalate
<b>PGT</b>	Post-GERDA Test
<b>PMMA</b>	Poly(methyl methacrylate) (acrylic glass)
<b>PMNS</b>	Pontecorvo-Maki-Nakagawa-Sakata
<b>PMT</b>	Photomultiplier Tube
<b>PNNL</b>	Pacific Northwest National Laboratory
<b>PPC</b>	p-type Point Contact
<b>PS</b>	Polystyrene
<b>PSD</b>	Pulse-Shape Discrimination
<b>PTFE</b>	Polytetrafluoroethylene (Teflon)
<b>RMS</b>	Root Mean Square
<b>ROI</b>	Region of Interest
<b>SEP</b>	Single-Escape Peak
<b>Si</b>	Silicon
<b>SiPM</b>	Silicon Photomultiplier
<b>SM</b>	Standard Model
<b>SPE</b>	Single Photo-Electron
<b>SSD</b>	SolidStateDetectors.jl
<b>SSE</b>	Single-Site Event
<b>TPB</b>	Tetraphenyl Butadienne
<b>TUM</b>	Technische Universität München
<b>UGLAr</b>	Underground-sourced LAr
<b>UV</b>	Ultra Violet
<b>VUV</b>	Vacuum Ultra-Violet
<b>WLS</b>	Wavelength Shifting

# Chapter 1

## Introduction

There are still countless open questions in the universe and since „42“ does not seem to be the right answer to all of them [1], other ways and means must be found. Since their first postulation by Wolfgang Pauli in 1930, neutrinos have repeatedly been confronting the physics community with new puzzles. As neutrinos were introduced to the Standard Model of particle physics, they were assumed to be massless Dirac particles with zero Yukawa couplings to the Higgs field. That this assumption was at least partly wrong, was already confirmed by providing experimental proofs for neutrino oscillations [2, 3, 4]. These are only possible if there is a mass difference between the neutrinos and, thus, if at least two of three have a mass. This raises the question of how their mass is generated.

Although the family of neutrinos is the second most abundant type of known particles in the universe, it was unfortunately not possible to simply weigh them, yet. Currently, three approaches are being pursued to find an answer. In approach number one, cosmological observables are used to indirectly determine the sum of the neutrino masses. In the second, the mass is measured directly via electron capture or beta decay. And in the third, neutrinoless double beta ( $0\nu\beta\beta$ ) decay is searched for, which can also answer questions about the nature of neutrinos. The search for  $0\nu\beta\beta$  decay is one of the most promising ways to search for physics beyond the standard model. Observing this hypothetical lepton-number violating decay would demonstrate that neutrinos are their own antiparticles, or in other words: that they are *Majorana particles* [5]. This observation could have a major impact on the understanding of the matter-antimatter asymmetry in the universe and can provide information on the absolute neutrino mass scale.

The *GERmanium Detector Array* (GERDA) collaboration was searching for  $0\nu\beta\beta$  decay in  $^{76}\text{Ge}$  by using high-purity germanium (HPGe) detectors enriched in the isotope  $^{76}\text{Ge}$ . The use of HPGe detectors is one of the most

promising technologies in  $0\nu\beta\beta$ -decay search as it combines source and detector with an excellent energy resolution. Until GERDA stopped taking data in November 2019, a total exposure of 127.2 kg·yr was accumulated. No positive signal was found, hence a limit on the  $0\nu\beta\beta$ -decay half-life was set to  $T_{1/2}^{0\nu} > 1.8 \cdot 10^{26}$  yr [6]. But the search does not end here. After the merging of the GERDA and MAJORANA collaborations, the next generation of  $0\nu\beta\beta$ -decay search experiments using  $^{76}\text{Ge}$  is just about to take on operation: the *Large Enriched Germanium Experiment for Neutrinoless  $\beta\beta$  Decay*, LEGEND.

LEGEND will start its first phase with about 200 kg of  $^{76}\text{Ge}$ -enriched HPGe detectors, referred to as LEGEND-200. Due to the extremely long expected half-life of  $0\nu\beta\beta$  decay, the background of the experiment must be completely under control, i.e. background free in the region of interest. In order to reach the aimed half-life sensitivity of  $T_{1/2}^{0\nu} > 10^{28}$  yr in the final tonne-scale phase of the experiment, LEGEND-1000, the background level must be reduced by a factor of 50 compared to its predecessor GERDA. [7, 8]

One way to lower the background level of the LEGEND experiment is to replace optically passive and opaque materials in the direct detector surrounding with optically active ones. This means, for example, that support structures themselves are turned into active veto systems in order to improve detection of background events close to the HPGe detectors. In LEGEND-200, *poly(ethylene 2,6-naphthalate)* (PEN) will be used to replace the detector holders which were made of silicon in GERDA. PEN is a commercially available transparent plastic which provides scintillation and wavelength-shifting (WLS) properties to contribute to the background identification system of the experiment [9, 10]. Almost arbitrary structures can be produced of PEN by injection moulding with a very high intrinsic radiopurity. In this thesis, the complete path from raw PEN granulate to the ultra-low background scintillator-grade structural components needed in LEGEND-200 is reported. The results of the optical characterisation and radiopurity measurements are also presented confirming the feasibility.

Another commonly used method to improve the background identification is *pulse-shape discrimination* (PSD) [11, 12]. Here, the pulse-shapes time-structure of individual events recorded using HPGe detectors are analysed to distinguish background from signal. It is important to understand the effect of the analysis cuts on hypothetical  $0\nu\beta\beta$  decay signals. Up to now, signals from events with similar event topology that were classified as comparable to  $0\nu\beta\beta$ -decay signals were used to quantify the PSD efficiency [12]. In this

---

purely data-driven analysis, uncertainties like a not comparable spatial distribution of the energy depositions in HPGe detectors are dominating. In order to improve the determination of the  $0\nu\beta\beta$ -decay detection efficiency and reduce its uncertainty, a new approach is presented in this thesis combining data and simulation-based approaches. Using this method, the  $0\nu\beta\beta$ -decay detection efficiency was determined for GERDA broad-energy germanium (BEGe) detectors verifying the previous results and decreasing the systematic uncertainty on  $0\nu\beta\beta$ -decay detection efficiency. This method is presented in addition to a detailed description and validation of the analysis chain.



## Chapter 2

# Neutrinoless Double Beta Decay

*I have done a terrible thing: I have postulated a particle that cannot be measured.*

- Wolfgang Pauli, 1930

More than 90 years ago, a very light, electrically neutral and weakly interacting particle with spin  $\frac{1}{2}$  was postulated by Wolfgang Pauli to explain the continuous energy spectrum of beta decay. For a long time, he was certain that such a particle could never be measured. But in 1956, Cowan and Reines observed neutrinos experimentally. [13]

The nature of neutrinos was further explored, which led to new findings. However, it also raised important questions: do neutrinos really have no mass? Are they their own antiparticles? If they have mass, which neutrino flavour is the heaviest? How were they involved in the emergence of matter-antimatter asymmetry? The first of these questions could have been answered already by the observation of neutrino oscillations. No clear answer has been found for all the others, yet.

Searching for neutrinoless double beta ( $0\nu\beta\beta$ ) decay is a very good way to find answers on the above questions. The existence of this decay would not only confirm that the neutrino is its own antiparticle. In addition, it would be proof of lepton number violation and could help determining the absolute neutrino mass scale.

This chapter is intended to provide an overview of the current state of knowledge about neutrinos. In addition, an introduction to  $0\nu\beta\beta$  decay and the concept of its experimental search is given.

## 2.1 Neutrino Masses

Neutrinos were introduced in the Standard Model (SM) of particle physics as left-handed massless particles with spin  $\frac{1}{2}$ . Therefore, they only interact

weakly. Neutrinos come in three flavors:  $\nu_e, \nu_\mu$  and  $\nu_\tau$  just as the charged leptons  $l \in [e, \mu, \tau]$  to which they couple. There is a corresponding right-handed anti-neutrino  $\bar{\nu}_l$  for every left-handed neutrino  $\nu_l$ . Each neutrino carries the conserved lepton number  $L(\nu_l) = 1$  and each anti-neutrino  $L(\bar{\nu}_l) = -1$ . [14, 15]

### 2.1.1 Neutrino Oscillation

The first of the questions mentioned at the beginning of this chapter has already been answered by observations of neutrino oscillation. To date, several experiments have found strong evidence for neutrino oscillations. They were detected in solar [2, 16, 17], atmospheric and reactor [3, 18] as well as accelerator neutrinos [4, 19, 20].

In quantum mechanics, flavour and mass eigenstates do not necessary have to be the same. In the flavour basis, the neutrino is described as a superposition of three mass eigenstates,  $\nu_i \in \{1, 2, 3\}$ ,

$$|\nu_l\rangle = \sum_{i=1}^3 U_{li} |\nu_i\rangle. \quad (2.1)$$

Here,  $U_{li}$  are the elements of the *Pontecorvo-Maki-Nakagawa-Sakata* (PMNS) matrix [15]. This matrix describes the lepton mixing and is defined as

$$U = \begin{bmatrix} c_{12}c_{13} & s_{12}c_{13} & s_{13}e^{-i\delta} \\ -s_{12}c_{23} - c_{12}s_{23}s_{13}e^{i\delta} & c_{12}c_{23} - s_{12}s_{23}s_{13}e^{i\delta} & s_{23}c_{13} \\ s_{12}s_{23} - c_{12}c_{23}s_{13}e^{i\delta} & -c_{12}s_{23} - s_{12}c_{23}s_{13}e^{i\delta} & c_{23}c_{13} \end{bmatrix} \quad (2.2)$$

$$\times \begin{bmatrix} 1 & 0 & 0 \\ 0 & e^{i\frac{\alpha_{21}}{2}} & 0 \\ 0 & 0 & e^{i\frac{\alpha_{31}}{2}} \end{bmatrix}$$

where  $c_{ij}$  and  $s_{ij}$  are used as abbreviations for  $\cos \theta_{ij}$  and  $\sin \theta_{ij}$ , respectively, with mixing angles  $\theta_{ij}$ . The Dirac phase  $\delta$  denotes the charge conjugation parity (CP) violation phase, while  $\alpha_{21}$  and  $\alpha_{31}$  describe the two Majorana CP violating phases. The latter only exist when neutrinos are their own antiparticles. In this case, they are called *Majorana particles*.

The probability  $P$  that a neutrino oscillates between its flavor eigenstates depends on several factors: Energy  $E$  of the neutrino, distance between source and detector  $D$  and elements of the PMNS matrix. For the transition of

flavour  $l$  to  $l'$  the probability is given by

$$\begin{aligned}
 P_{l \rightarrow l'} = & \delta_{ll'} - 4 \sum_{i < j}^n \operatorname{Re}(U_{li} U_{l'i}^* U_{lj}^* U_{l'j}) \sin^2 X_{ij} \\
 & + 2 \sum_{i < j}^n \operatorname{Im}(U_{li} U_{l'i}^* U_{lj}^* U_{l'j}) \sin 2X_{ij}
 \end{aligned} \tag{2.3}$$

where

$$X_{ij} = \frac{\Delta m_{ij}^2 D}{4E}. \tag{2.4}$$

In particular, according to Equation 2.4 if the squared mass difference  $\Delta m_{ij}^2$  between the mass eigenstates  $i$  and  $j$  is zero, this implies that the probability of flavor oscillations is zero [15]. As flavor oscillations were observed, this means that  $\Delta m_{ij}^2 \neq 0$ , implying that at least some neutrinos must have a mass.

### 2.1.2 Neutrino Mass Ordering

By measuring neutrino oscillations, only the squares of the mass differences  $\Delta m_{ij}^2$  can be measured. However, no conclusions can be drawn on the absolute neutrino mass scale. Also, it is not yet known which is the lightest mass state. Based on the assumption that the individual states have different masses and  $\Delta m_{21}^2 \ll \Delta m_{31}^2$  known from experiments [21], there are two possibilities: [22]

- Normal ordering (NO):  $m_1 \ll m_2 < m_3$
- Inverted ordering (IO):  $m_3 \ll m_1 < m_2$

### 2.1.3 Dirac and Majorana Neutrino Mass

Almost 100 years ago Paul Dirac developed the *Dirac equation* to describe the properties and behaviour of fermions with spin  $\frac{1}{2}$  [14, 23, 24]. Using this, the Dirac mass term of the Lagrangian

$$\mathcal{L}_D = -m_D \nu \bar{\nu} = -m_D (\bar{\nu}_R \nu_L + \bar{\nu}_L \nu_R). \tag{2.5}$$

can be derived for the neutrino field  $\nu$ . Here,  $m_D$  is the Dirac mass for the neutrino field and  $\nu_L$  ( $\nu_R$ ) are the left (right)-handed neutrino fields. There has not yet been an experimental observation of the right-handed neutrino

field  $\nu_R$ . According to Equation 2.5, this could be explained by the Dirac mass  $m_D$  being zero.

**Majorana neutrino mass:** Ettore Majorana tried to find another solution for Equation 2.5. He left it with the already discovered left-handed neutrino field  $\nu_L$ . With the assumption that the neutrino is its own antiparticle  $\nu = \nu^C$ , it follows for the neutrino field

$$\nu = \nu_L + \nu_R = \nu_L + \nu_L^C \quad (2.6)$$

which relies on the assumption  $\nu_R = C\bar{\nu}_L^T = \nu_L^C$ . This allows the Dirac equation to be reformulated and to add another mass term to the Lagrangian without using the right-handed neutrino field  $\nu_R$ . This results in

$$\mathcal{L}_M = -\frac{1}{2}m_L(\bar{\nu}_L\nu_L^C + \bar{\nu}_L^C\nu_L) \quad (2.7)$$

for the Majorana mass term. This can of course also be formulated for right-handed neutrino fields. In case that right-handed neutrinos exist, it is possible that neutrinos have both a Dirac and a Majorana mass component.

## 2.2 Double Beta Decay

The most promising way to answer the nature of neutrinos is the neutrinoless double beta decay,  $0\nu\beta\beta$ -decay. This decay, if it exists, represents a special form of the neutrino accompanied double beta decay,  $2\nu\beta\beta$ -decay, which is allowed in the SM of particle physics. In the following, these two forms of double beta decay and the implications of a possible  $0\nu\beta\beta$ -decay observation are described.

### 2.2.1 Neutrino Accompanied Double Beta Decay

In the case of a beta decay, a neutron is converted into a proton. In the process, an electron and an anti-neutrino are released, which means that the lepton number is conserved. For the beta decay of a nucleus, this process is described by

$${}^A_ZX \longrightarrow {}^A_{Z+1}Y + e^- + \bar{\nu}_e, \quad (2.8)$$

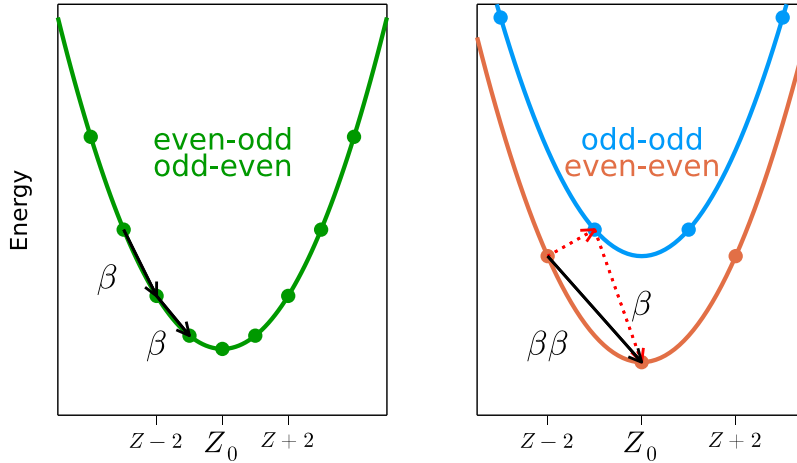
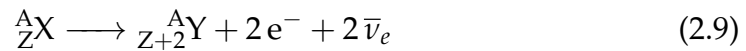


FIGURE 2.1: Illustration of the energy of a nucleon at rest as function of the atomic number  $Z$  for different combinations of odd and even numbers of protons/neutrons for a fixed  $A$ . The black arrows indicate allowed decays while the red dotted indicate an energetically forbidden decay sequence. On the left,  $A$  is odd while it is even on the right. It is assumed, that the

where  $X$ ,  $Y$ ,  $A$  and  $Z$  representing the mother isotope, daughter isotope, mass number and the atomic number, respectively. With the *Bethe-Weizsäcker* formula [25], the binding energy of a nucleus can be calculated. In Figure 2.1 (left) an illustration of the binding energy of an isomer with fixed odd  $A$  is shown as function of  $Z$ . In this example, the number of neutrons and protons are either *odd-even* or *even-odd*. As a result of the beta decay (indicated by black arrows), a lower binding energy level is reached for the daughter nucleus. For the case where  $A$  is even, the number of neutrons and protons are *odd-odd* or *even-even* (Figure 2.1 right) and the beta decay can lead to a state with higher binding energy for the daughter compared to the initial state. This process is energetically forbidden (indicated by red arrow). Instead the double beta decay can occur. This nuclear decay is described by



where two neutrons decay into two protons, two electrons and two anti-neutrinos.

The total energy  $Q_{\beta\beta}$  released in the double beta decay is divided between the final state particles leading to a continuous spectrum for the sum of the energy of the two observable electrons shown in Figure 2.2.

$2\nu\beta\beta$  decay is not forbidden for isotopes that can undergo a single beta decay. However, it will not be observable as this is a second-order process,

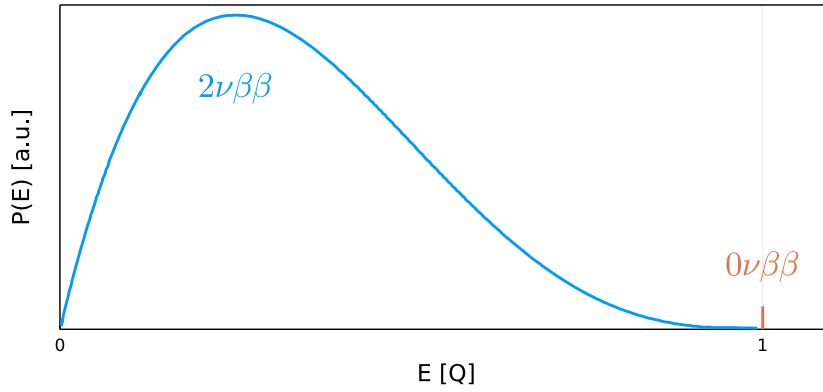


FIGURE 2.2: Energy spectrum of the double beta decay with indicated  $2\nu\beta\beta$  and  $0\nu\beta\beta$  contributions. This illustration is not to scale and assumes perfect energy resolution.

Isotope	$Q_{\beta\beta}$ [keV]	Nat. ab. [%]
$^{48}\text{Ca}$	4273.7	0.187
$^{76}\text{Ge}$	2039.1	7.8
$^{82}\text{Se}$	2995.5	9.2
$^{96}\text{Zr}$	3347.7	2.8
$^{100}\text{Mo}$	3035.0	9.6
$^{110}\text{Pd}$	2004.0	11.8
$^{116}\text{Cd}$	2809.1	7.6
$^{124}\text{Sn}$	2287.7	5.6
$^{130}\text{Te}$	2530.3	34.5
$^{136}\text{Xe}$	2461.9	8.9
$^{150}\text{Nd}$	3367.3	5.6

TABLE 2.1: List of double beta decaying isotopes with corresponding  $Q_{\beta\beta}$  values and natural abundance. Values taken from [27].

the probability is significantly lower than for a simple beta decay. The half-life  $T_{1/2}^{2\nu}$  is different for each isotope but in the range  $10^{18}$  yr to  $10^{24}$  yr [26]. A list of some double beta decaying nuclei, their  $Q_{\beta\beta}$  values and natural abundance is given in Table 2.1.

## 2.2.2 Neutrinoless Double Beta Decay

In the SM, the double beta decay with emission of two neutrinos is predicted as described in Equation 2.9. If  $\nu = \nu^c$  applies, a final state without neutrinos is possible. This decay would then be described by

$$\overset{A}{Z}\text{X} \longrightarrow \overset{A}{Z+2}\text{Y} + 2e^- \quad (2.10)$$

which would lead to a discrete line in the energy spectrum of the two emitted electrons as shown in Figure 2.2 (orange line) since  $Q_{\beta\beta}$  is only divided between the two electrons. Figure 2.3 shows the Feynman diagram for  $2\nu\beta\beta$  decay on the left and for  $0\nu\beta\beta$  decay induced by light Majorana neutrino  $\nu_M$  exchange on the right. Further possibilities of lepton number violating extensions of the SM for the mediator of  $0\nu\beta\beta$  decay are, for example, weak currents or super-symmetric particles. The discovery of this decay would provide direct evidence for the violation of the lepton number conservation ( $\Delta L = 2$ ) and prove that neutrinos must have a Majorana mass component regardless of the mechanism behind the decay. [7, 28, 29]

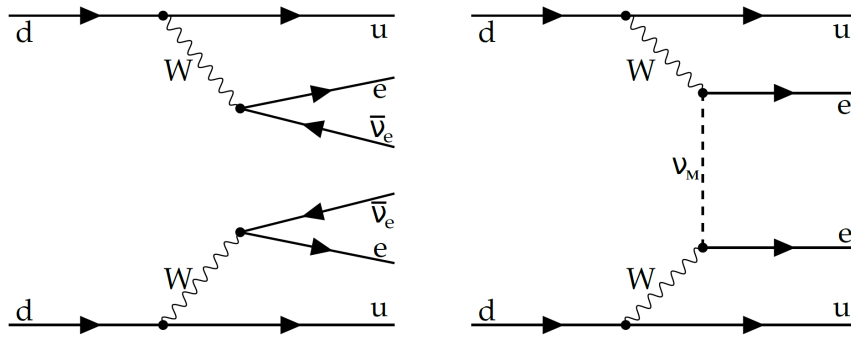


FIGURE 2.3: Feynman diagram for the  $2\nu\beta\beta$ -decay (left) and for the  $0\nu\beta\beta$ -decay (right). The possibility of light Majorana neutrinos  $\nu_M$  as mediator is shown here. [30]

The half-life  $T_{1/2}^{0\nu}$  of the  $0\nu\beta\beta$ -decay can be derived from Fermi's golden rule which was actually derived by Dirac [31, 32]. For the exchange of light Majorana neutrinos  $\nu_M$  it can be expressed as

$$T_{1/2}^{0\nu} = \left( G |\mathcal{M}|^2 \langle m_{\beta\beta} \rangle^2 \right)^{-1} \quad (2.11)$$

where  $G$  and  $\mathcal{M}$  are the phase-space factor and the nuclear matrix element (NME). The last term describes the effective Majorana neutrino mass  $\langle m_{\beta\beta} \rangle$ . It is defined by the sum

$$\langle m_{\beta\beta} \rangle = \left| \sum_{i=1}^3 U_{ei}^2 m_i \right| \quad (2.12)$$

with the matrix elements  $U_{ei}$  of the PMNS matrix from Equation 2.2 and the neutrino mass eigenstates  $m_i$  [15]. The allowed parameter space of  $\langle m_{\beta\beta} \rangle$  is shown in Figure 2.4 as a function of the lightest neutrino mass  $m_l$ . Whereby solid black lines limit the permitted areas for the inverted and the normal ordering of the neutrino masses.

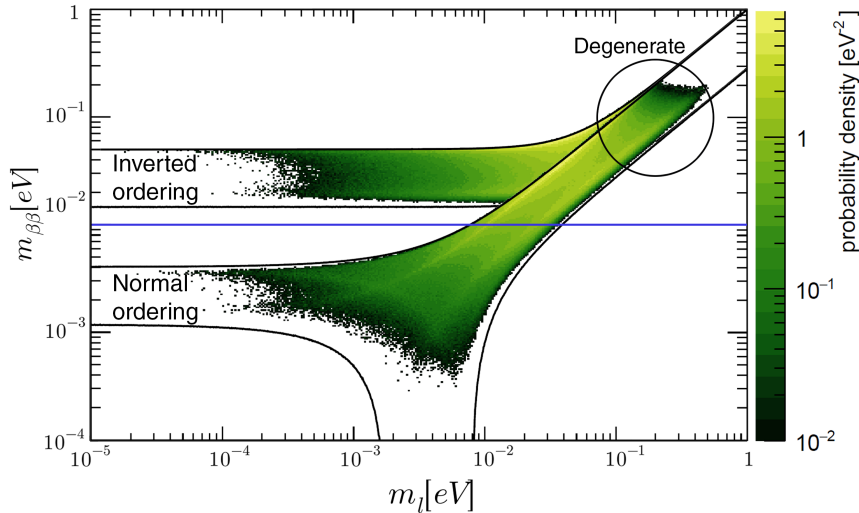


FIGURE 2.4: Probability density of the effective Majorana neutrino mass  $\langle m_{\beta\beta} \rangle$  as function of the lightest neutrino mass  $m_1$ . The solid black lines limit the permitted parameter space for the normal and the inverted ordering. The goal of the next generation is indicated by a blue line. Probability densities taken from [33].

Using Equation 2.11, in case of no observation and a limit set on  $T_{1/2}^{0\nu}$ , also a limit can be set on  $\langle m_{\beta\beta} \rangle$  assuming  $\nu_{\mathcal{M}}$  exchange. The large uncertainties of the NMEs cause large uncertainties in the limits of the effective Majorana neutrino mass. The GERDA collaboration has published a limit of  $\langle m_{\beta\beta} \rangle < 79 - 180$  meV based on  $^{76}\text{Ge}$  [6]. The best limit for  $^{136}\text{Xe}$ -based experiments comes from KamLAND-Zen with  $\langle m_{\beta\beta} \rangle < 61 - 165$  meV [34]. The next generation of  $0\nu\beta\beta$ -decay search experiments aims to achieve a sensitivity of the order of 10 meV for  $\langle m_{\beta\beta} \rangle$  (blue line in Figure 2.4) [7].

The KATRIN collaboration has published the upper limit on the effective electron anti-neutrino mass of  $m_\nu < 0.8$  eV [35, 36] with 90% confidence level (C.L.) using the combined data of their first two measurement campaigns. Further restrictions can be drawn from cosmological observations. The PLANCK collaboration has set several model dependent limits on the sum of the neutrino masses with the simplest being  $\sum m_i < 0.23$  eV [37].

### 2.3 Experimental Search for $0\nu\beta\beta$ Decay

In order to design a  $0\nu\beta\beta$ -decay search experiment, it must first be understood which factors influence the sensitivity. The expected signal is a monoenergetic line at  $Q_{\beta\beta}$  in the energy spectrum of the two electrons.  $Q_{\beta\beta}$  can

usually be measured by independent nuclear experiments with high precision. Thus, the *region of interest* (ROI) can be restricted to a narrow window around  $Q_{\beta\beta}$ , which depends on the energy resolution of the detectors. The number of expected events  $N$  in the ROI in a given measurement time  $t$  for a total source mass  $M$  with an isotopic abundance  $a$  is defined as

$$N = \ln(2) \frac{N_A}{W} \left( \frac{a\epsilon Mt}{T_{1/2}^{0\nu}} \right). \quad (2.13)$$

$N_A$ ,  $W$  and  $\epsilon$  are the Avogadro's number, the molar mass of the source isotope and the detection efficiency of the signal, respectively [38].

The sensitivity  $S_{T_{1/2}^{0\nu}}$  of a  $0\nu\beta\beta$ -decay search experiment can be expressed as:

$$S_{T_{1/2}^{0\nu}} \propto \begin{cases} aM\epsilon t & \text{background free,} \\ a\epsilon \sqrt{\frac{Mt}{B\Delta E}} & \text{with background.} \end{cases} \quad (2.14)$$

In the first case, the ideal case without background contribution in the ROI the sensitivity scales linearly with  $t$ . With background, however,  $S_{T_{1/2}^{0\nu}} \propto \sqrt{t}$  applies and the background index  $B$  and the energy resolution  $\Delta E$  in the ROI play an important role.

According to Equation 2.14, an isotope that can be enriched and/or has a high natural abundance (large  $a$ ), low intrinsic background (low  $B$ ) and the possibility of using it as a detector is considered perfect. Furthermore, this detector needs a very good energy resolution (small  $\Delta E$ ) and can be usable with high quantity (large  $M$ ). Finally, the  $Q_{\beta\beta}$  value is ideally above 2.6 MeV to reduce backgrounds from natural radioactivity. Unfortunately, none of the 35 possible isotopes meet all of these requirements. In fact, less than a third of them can offer a fair balance which makes them candidates for the  $0\nu\beta\beta$ -decay search (see Table 2.1) [38]. In this thesis, one of the most promising candidates is discussed:  $^{76}\text{Ge}$ .



## Chapter 3

# Germanium-Based $0\nu\beta\beta$ -Decay Search Experiments

One of the most suitable isotopes for  $0\nu\beta\beta$ -decay search is  $^{76}\text{Ge}$ . Since it is a semiconductor, it can be used as source and detector at the same time, resulting in a high detection efficiency. At  $Q_{\beta\beta} = 2039.061(7)$  keV [39], an superior resolution of  $\approx 2.0$  keV has already been achieved with germanium detectors. Also, an experiment based on  $^{76}\text{Ge}$ -enriched detectors can be scaled to the tonne-scale without changing the concept [38]. Two other semiconductor technologies are currently being considered for the  $0\nu\beta\beta$ -decay search: CdZnTe based on  $^{116}\text{Cd}$  [40] and a complementary metaloxide-semiconductor (CMOS) pixel array based on  $^{82}\text{Se}$  [41]. However, both are still at a very early stage.

As mentioned in Section 2.3, no isotope is perfect for the  $0\nu\beta\beta$ -decay search. Thus,  $^{76}\text{Ge}$  also has disadvantages. Compared to other isotopes, the  $Q$ -value is relatively low. Primordial radioisotopes from the U and Th chains are unavoidable in the construction of an experiment. In particular for  $^{76}\text{Ge}$ -based experiments, there are three important event types that can lead to background events in the ROI. On the one hand the 2614.5 keV  $\gamma$ -line from  $^{208}\text{Tl}$ , a beta decay energy of up to 3270 keV from  $^{214}\text{Bi}$  (from the  $^{222}\text{Rn}$  chain) and  $^{42}\text{K}$  (short-lived progeny of  $^{42}\text{Ar}$ ) with a  $\beta$ -decay  $Q$  value of 3525 keV. In addition, the natural abundance of  $^{76}\text{Ge}$  is relatively low with only 7.8%. As a result, the detector material must be enriched at high cost in the production process.

Two former experiments based on  $^{76}\text{Ge}$  have proven particularly successful in recent years and have taken the germanium detector design and technology to a new level: the *GERmanium Detector Array* (GERDA) experiment and the MAJORANA DEMONSTRATOR. Both have recently ended their operation and formed the LEGEND collaboration to continue  $0\nu\beta\beta$ -decay search with joint resources.

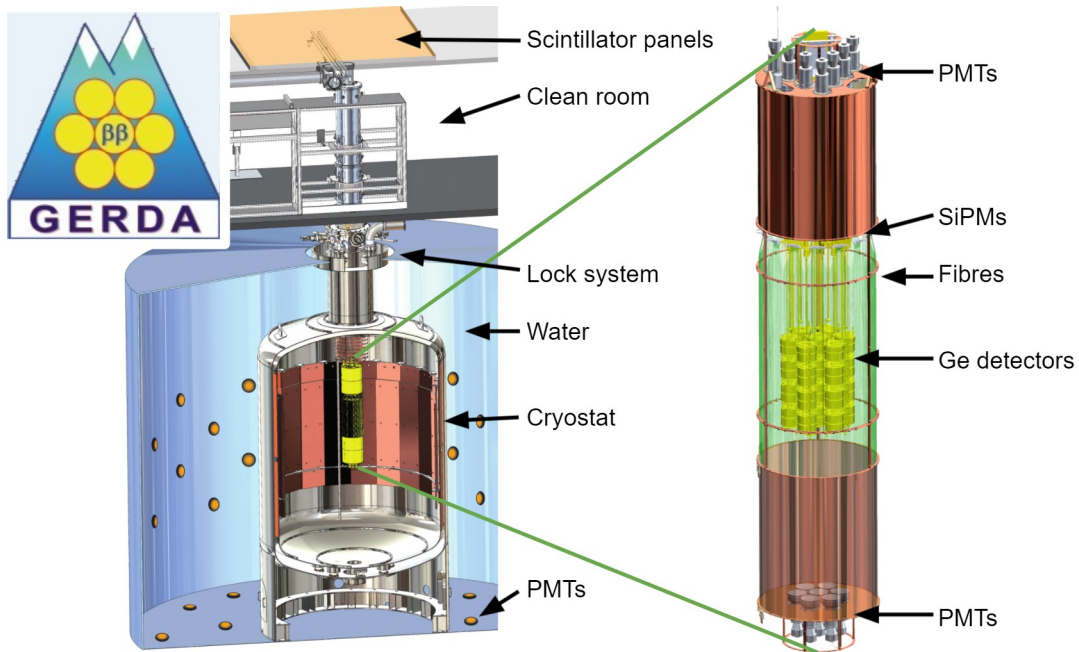


FIGURE 3.1: **Top left:** GERDA collaboration logo. **Left:** Schematic structure of the GERDA experiment with lock system and clean room. **Right:** Schematic close-up of the detector array. The PMTs and the fibre curtain are also clearly visible here. Illustrations adapted from [44, 45].

### 3.1 GERDA

The  $0\nu\beta\beta$ -decay search with the GERDA experiment [6, 42, 43] started in November 2011 and ended in November 2019. The experimental setup was located in Hall A of the underground laboratory *Laboratori Nazionali del Gran Sasso* (LNGS) in Italy at a depth of  $\approx 3500$  m water equivalent. The inevitable flow of cosmic muons can be reduced to  $\approx 1.25 \text{ m}^{-2}\text{h}^{-1}$  through this rock overburden. The experiment was carried out in two phases, with the upgrade to Phase II being carried out in 2013-2015 [44]. Changes in the technology as well as in the number of detectors were made. Only the structure in Phase II is described in this work.

The heart of the experiment were 7 semi-coaxial (15.6 kg) and 30 broad energy (BEGe, 20.0 kg) germanium detectors which were enriched to  $\approx 87\%$  in  $^{76}\text{Ge}$ . These were arranged in seven detector strings to form the detector array. A string consisted of several detectors, each connected vertically with its own holding structure. The arrangement of the strings can be found in the yellow circles in the GERDA collaboration logo (Figure 3.1, top left corner). The position of the detectors in the array is shown in Figure 3.2 for Phase II including one string consisting of three natural (not enriched) germanium detectors on the right. The array deployed during the period from

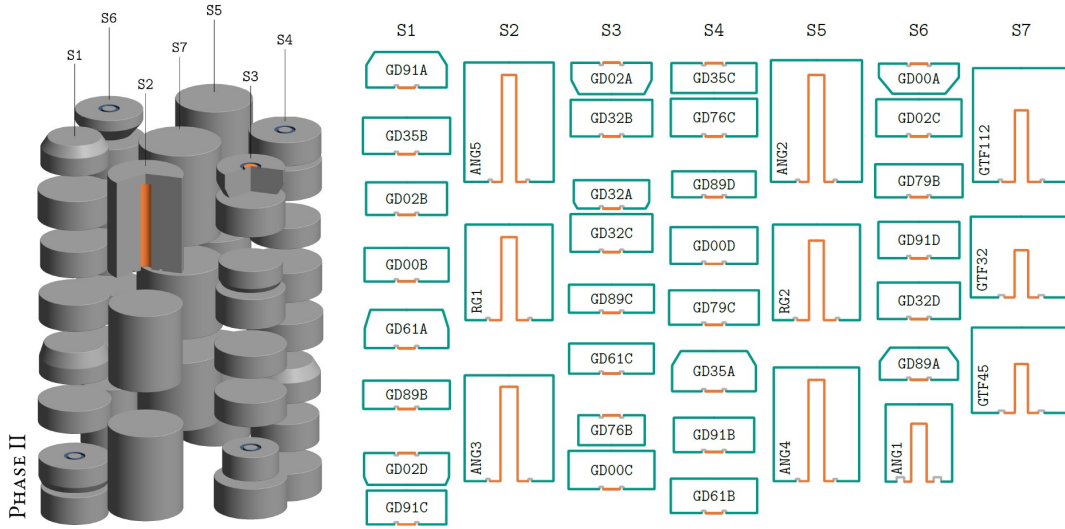


FIGURE 3.2: Arrangement of the germanium detector array during GERDA Phase II (December 2015 - April 2018). The minor changes due to the upgrade in 2018 are not shown. The drawing was created with [46] and adopted from [47].

December 2015 to April 2018 was used for the drawings, later changes due to the upgrade in 2018 are not included.

A schematic representation of the GERDA setup is shown in Figure 3.1. On the right side, a close-up of the detector array with the seven strings in the centre can be seen, surrounded by a curtain of light guiding fibres [48]. The individual strings were enclosed with so-called mini-shrouds made of ultra-pure nylon. These  $125\ \mu\text{m}$  thick films served as barrier for  $^{42}\text{K}$  ions resulting from the decay of  $^{42}\text{Ar}$  [44]. Photomultiplier tubes (PMTs) were mounted above and below the array, as can be seen in Figure 3.1 (right). As shown in Figure 3.1 (left), the detector array was submerged into a cryostat filled with  $64\ \text{m}^3$  of purified liquid argon (LAr). The use of LAr was not only intended to cool the detectors, but also served as a shield against background  $\gamma$ -radiation and as a veto system (see Section 5.3.2). The cryostat was located in a water tank which was filled with up to  $590\ \text{m}^3$  of ultra-pure water. The water served as Cherenkov detector for cosmic muons and as shield against external neutrons. To measure the light generated by the Cherenkov radiation, 66 PMTs were mounted on the walls of the water tank (see Section 5.3.1). A clean room was located above the tank. The array was prepared inside a glove box and then lowered into the cryostat through a dedicated lock system. The lock system contained three weak radioactive sources that could be lowered to the detector array for calibrations. Finally, there were plastic scintillator panels installed above the clean room. They completed the water

Cherenkov veto for vertical muons.

By the end of data collection in November 2019, GERDA achieved an exposure of 127.2 kg·yr in which no candidate for  $0\nu\beta\beta$ -decay was found. With an energy resolution at  $Q_{\beta\beta}$  of 3.3 keV full-width half-maximum (FWHM) and a background index of  $(5.2^{+1.6}_{-1.3}) \times 10^{-4}$  cts/(keV·kg·yr), a new lower limit could be set for  $T_{1/2}^{0\nu}$  in  $^{76}\text{Ge}$  [6]:

$$T_{1/2}^{0\nu} > 1.8 \times 10^{26} \text{ yr.} \quad (3.1)$$

## 3.2 MAJORANA DEMONSTRATOR

While GERDA is an European collaboration, there has been an effort also in the USA to search for  $0\nu\beta\beta$  decay of  $^{76}\text{Ge}$ . The MAJORANA DEMONSTRATOR [49, 50, 51, 52] was located in the *Sanford Underground Laboratory* (in Lead, SD, USA) which provides an 5000 m water equivalent rock overburden. In the experimental setup, the detectors were arranged in modules which are shown in Figure 3.3. The 44.1 kg (29.7 kg enriched to  $\approx 88\%$  in  $^{76}\text{Ge}$ ) of germanium detectors were placed in two vacuum cryostats in arrays similar to the GERDA array. Only ultra-pure materials were used to create an ultra-low background environment and different shields protected the detectors from external radiation. The shield against external radiation around the cryostat was composed of ultra-pure electroformed copper and lead. A borated polyethylene shield was installed as neutron shield and additional plastic scintillators were used to veto muons. Furthermore, the gaps between the shields were filled with ultra-low-radon  $\text{N}_2$  purge gas to expel radon from the detector surrounding.

With the MAJORANA DEMONSTRATOR, data was recorded from 2015 to 2020, and an enriched exposure of 26.0 kg·yr has been achieved. The energy

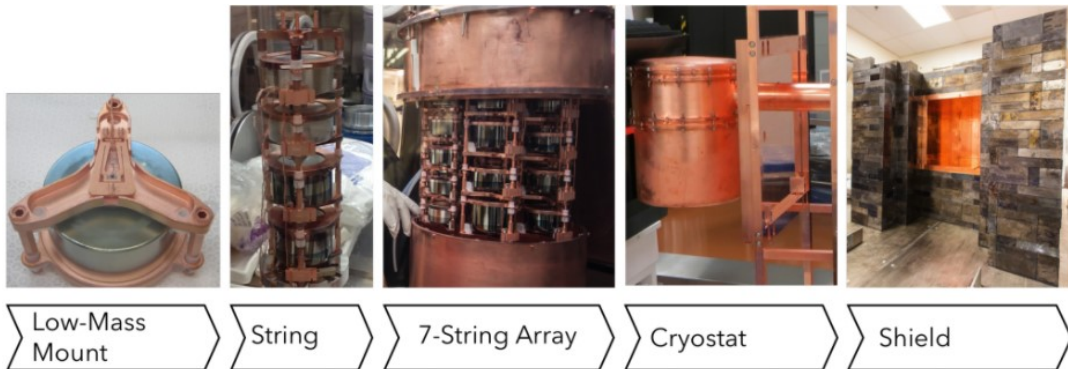


FIGURE 3.3: Modular design of MAJORANA DEMONSTRATOR [52].

resolution achieved at  $Q_{\beta\beta}$  is 2.53 keV (FWHM) is the best in the field thanks to the front-end electronics technology. However, the better resolution was not sufficient to compensate for the higher background compared to GERDA. The background index  $(4.7 \pm 0.8) \times 10^{-3}$  cts/(keV·kg·yr) was reached and the limit for  $T_{1/2}^{0\nu}$  set by the MAJORANA collaboration is [51]:

$$T_{1/2}^{0\nu} > 2.7 \times 10^{25} \text{ yr.} \quad (3.2)$$

### 3.3 The Next Generation $0\nu\beta\beta$ -Decay Search Experiment LEGEND

The declared goal of the next generation of  $0\nu\beta\beta$ -decay search experiments is to reach a sensitivity of  $\approx 10$  meV for the effective Majorana neutrino mass (see blue line in Figure 2.4) and to detect  $0\nu\beta\beta$  decay if it exists. To achieve this goal using germanium technology, the MAJORANA and GERDA collaborations joined forces with other groups in 2017 to form a new international collaboration with more than 250 researchers from about 50 institutions [8]:



The world's largest  $^{76}\text{Ge}$ -based  $0\nu\beta\beta$ -decay search experiment LEGEND is planned to be carried out in two phases: LEGEND-200 followed by LEGEND-1000. The numbers relate to the approximate detector mass to be deployed.

With LEGEND-200 a sensitivity on  $T_{1/2}^{0\nu}$  of  $> 10^{27}$  yr is planned within 5 years of data taking. This corresponds to a limit on the effective Majorana neutrino mass of  $m_{\beta\beta} < (33 - 71)$  meV. For this, the background index must be a factor of 5 lower than that of the predecessors GERDA and MAJORANA.

For LEGEND-1000, the required background index  $< 10^{-5}$  cts/(keV·kg·yr) is much stricter but deemed realistic. With this background level in the range of  $Q_{\beta\beta}$  and an exposure of 10 t·yr, a sensitivity for a limit of  $T_{1/2}^{0\nu} > 10^{28}$  yr with 90% C.L. is planned to be achieved. This would result in  $m_{\beta\beta}(10 - 20)$  meV. The sensitivity on  $T_{1/2}^{0\nu}$  as function of exposure is shown in Figure 3.4. The IO band is highlighted in light blue. The blue solid line represents the background-free and the red the aimed for realistic scenario. The values given for the background index are normalised to an energy resolution of 2.5 keV (FWHM). [7, 8]

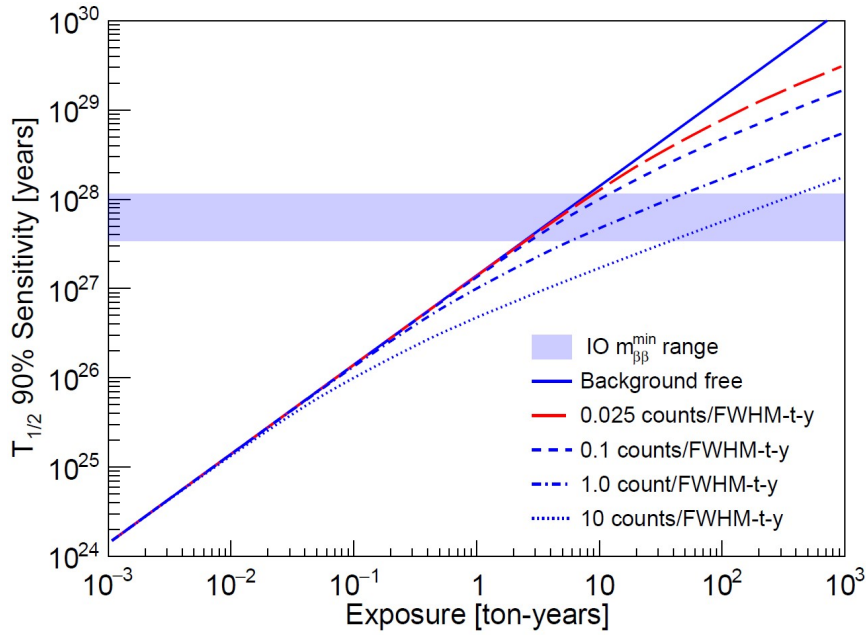


FIGURE 3.4: Sensitivity of the  $0\nu\beta\beta$ -decay half-life  $T_{1/2}^{0\nu}$  for  $^{76}\text{Ge}$  as function of exposure (90% C.L.). Scenarios for different background levels normalised to an energy resolution of 2.5 keV are shown. [7]

### 3.4 LEGEND-200 Design & Status

The first phase of LEGEND started construction in 2020 in the infrastructure of GERDA at the LNGS. Improvements and modifications are made to accommodate the  $\approx 200$  kg of detector mass. The lock system of the cryostat has to be replaced as it does not cope with the high mass of the detector array. The detectors from GERDA and MAJORANA will be shared, additionally more detectors have been produced. Thus, three types of  $^{76}\text{Ge}$ -enriched germanium detectors will be used: BEGe, p-type point contact (PPC) and inverted coaxial point contact (ICPC) detectors. A cross-section of each of the three detector types with their weighting field and example energy depositions<sup>1</sup> can be seen in Figure 3.5. The newly developed ICPC detector (right) has a mass of up to four times larger than that of the others which makes it ideal for the LEGEND experiment.

The design of the modified GERDA cryostat is shown in Figure 3.6 (left). It is planned to accommodate the 200 kg of germanium detectors in 14 strings. To improve the coverage of the fibre curtain, two curtains will be used in LEGEND-200 as can be seen in Figure 3.6 (right). One inside and one surrounding the detector array.

<sup>1</sup>More information about the working principle of germanium detectors can be found in Chapter 4.

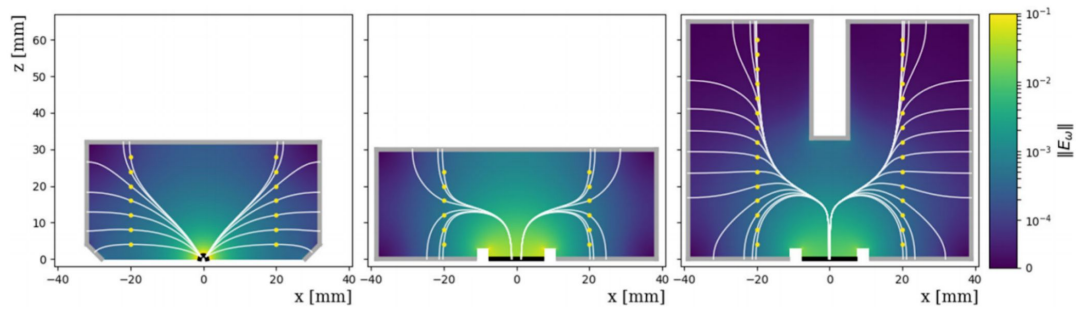


FIGURE 3.5: Geometries of three germanium detector types used in LEGEND-200. The black and grey lines represent the  $p^+$  and  $n^+$  electrodes, respectively. The yellow points are example energy depositions with the drift paths drawn in white. The weighting field is also given. **Left:** p-type point contact (PPC) **Middle:** broad-energy germanium (BEGe) **Right:** inverted coaxial point contact (ICPC). Picture taken from [7].

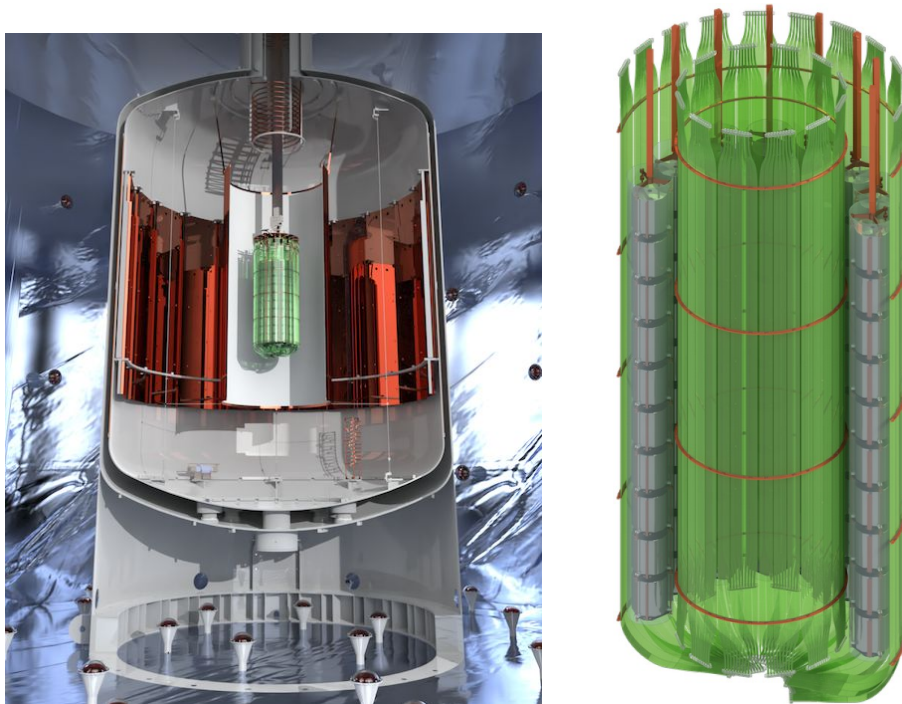


FIGURE 3.6: **Left:** Cross-section of the modified GERDA cryostat for LEGEND-200 including the modified lock system. **Right:** Design of the 14-string array to accommodate 200 kg of germanium detectors. Pictures taken from [7].

The electronics in LEGEND-200 will be based on MAJORANA front-end technology combined with the wire bonding technique of GERDA [8]. This will allow the placement of read-out electronics very close to the detector inside LAr with low noise and low energy threshold.

In GERDA, low-background silicon (Si) was used for the holding plates of the germanium detectors, which will be replaced by poly(ethylene naphthalate) (PEN) [10] in LEGEND-200. In addition to a high degree of radiopurity, this material also has scintillating and wavelength-shifting properties, which are presented in Chapters 6 and 7. In the course of this thesis, these new optically active holding structures were designed, produced, characterised and put into first operation in the GERDA environment as contribution to the LEGEND-200 experiment.

### 3.5 LEGEND-1000 Design Plans

In the next phase of LEGEND, the detector mass is to be increased to about one ton [7]. This will require  $\approx 400$  new ICPC detectors with an average mass of 2.6 kg. With the aim of  $\approx 92\%$  enrichment in  $^{76}\text{Ge}$ , an isotopic mass of  $\approx 910$  kg can be achieved.

The GERDA infrastructure is no longer sufficient for this high number of detectors. A final location has not been determined yet, but the baseline design of the cryostat is already available. As can be seen in Figure 3.7, four detector arrays are planned, each about the size of the LEGEND-200 array with separate access tubes to the cryostat. Research is underway on many of the components of the LEGEND-1000 setup. New holding structures, read-out electronics and veto systems are being developed by groups world wide. Research is also being carried out on LAr, to reduce the  $^{39}\text{Ar}$  and  $^{42}\text{Ar}$  components of the background. Attempts are being made to use Ar depleted in  $^{39/42}\text{Ar}$  from underground sources for this purpose, although the possible level of purification is still unclear. In general, the baseline design can change through experience gained with LEGEND-200. [8]

The work presented in this thesis forms the basis for the use of PEN in LEGEND-1000. Further research is already being conducted on encapsulation for germanium detectors and 3D-printed scintillators. In addition, an analysis chain was formed to determine the  $0\nu\beta\beta$ -decay detection efficiency from simulations for individual germanium detectors.

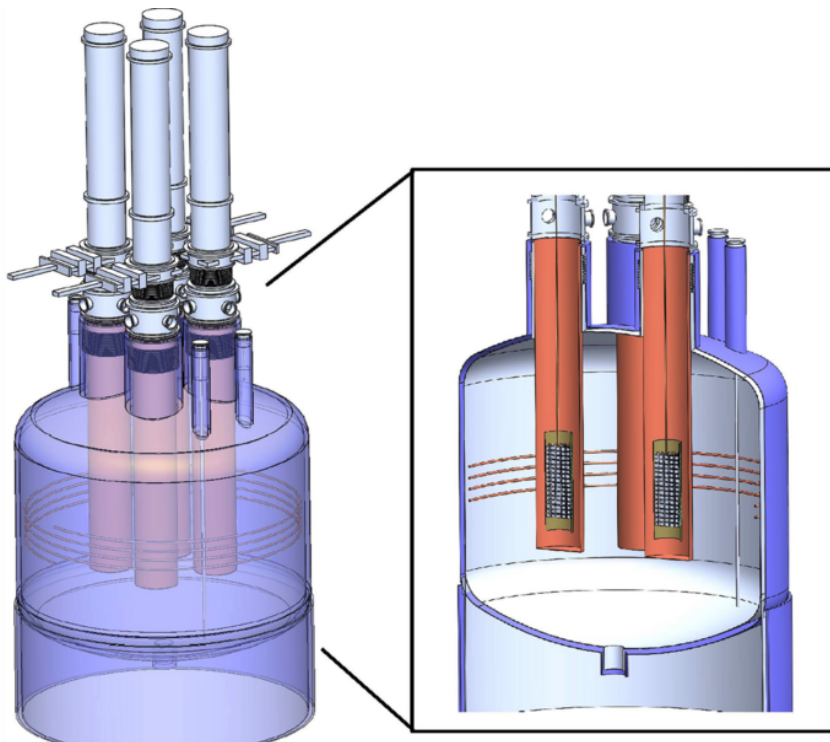


FIGURE 3.7: Baseline design of the LEGEND-1000 cryostat with four separate detector arrays. Picture taken from [8].



## Chapter 4

# Radiation Detection using Germanium Detectors

Germanium semiconductor detectors inevitably play a major role in many radiation detection experiments due to their excellent energy resolution and high dynamic range from keV to  $\approx 10$  MeV. This type of detector also includes the *High-Purity Germanium* (HPGe) detectors used in GERDA and LEGEND (see Chapter 3). In the course of this thesis, an analysis chain is presented that exploits the time structure characteristics of germanium detector signals. For this, it is necessary to have an understanding of how a signal in a germanium detector is created and how it is influenced by the amount and location of the energy deposition. All germanium detectors discussed in this thesis are classified as HPGe detectors.

In this chapter, the working principle of germanium detectors and how signals in a germanium detector are created is described briefly. For more details please refer to [53]. Also, a short introduction to the software package *SolidStateDetectors.jl* [54] is given which was used for detector simulation in this work.

### 4.1 Working Principle of Germanium Detectors

In single atoms, electrons can only be at certain energy levels. It is different for (semi-)conductors, since here the energy levels of a macroscopic crystal are combined into quasi-continuous bands. Two bands are particularly important for semiconductor detectors. On the one hand the so-called *valence band*, which is the band with the highest energy level in which there are still electrons. On the other hand, the so-called *conduction band*, which is the first "empty" one. In order for an electron to move in the solid, it has to pass from the valence into the conduction band. In germanium and other semiconductors, the band gap is of the order of 1 eV, while it is above 5 eV in insulators.

Thermal excitation is enough to move electrons in germanium into the conduction band and thus to generate a so-called *leakage current*. Germanium detectors are usually operated at cryogenic temperatures of 77 – 100 K to minimise the influence of thermal excitation and, thus, the noise introduced by the leakage current. In cryogenic operation, the leakage current from non-thermal processes is usually of the order pA and does hardly influence the measurement.

The basic principle in semiconductor detectors is a p-n junction which refers to the region where a positive (p) doping changes to a negative (n) doping<sup>1</sup>. Here, the controlled inserting of impurities before or during the crystal pulling process is also known as *doping*. The free electrons and holes in the n-type and p-type regions diffuse into the other material. As result, an area in which there are no free charge carriers is formed at this junction. This area is then referred to as the *depletion zone* and represents the active volume of the detector. This zone is usually very small, but can be expanded by applying reverse bias voltage. Here, the p-type (n-type) region is connected to the negative (positive) terminal of the voltage supply. The voltage at which the complete detector crystal is depleted is called the *depletion voltage* and is different for each detector. Normally the depletion voltage of kg scale germanium detectors is of the order a few kV. The applied bias voltage cannot be arbitrarily high, since the higher the voltage, the higher the leakage current.

Germanium detectors can be made *n* or *p*-type, referring to the type of the bulk volume. An n-type bulk volume has more donor impurities while there are more acceptor impurities in the p-type<sup>2</sup>. The p<sup>+</sup>-contact of a germanium detector is formed by adding a p-type layer to one or more surfaces which often consists of boron (acceptor impurity). This layer usually has a thickness of 50 – 100  $\mu\text{m}$  and is conductive due to high impurity concentration. For the n<sup>+</sup> contact, an n-type layer must accordingly be created, which usually consists of lithium (donor impurity). While boron can be applied as a very thin layer by ion implantation, lithium must be evaporated onto the surface. This makes the layer of the n<sup>+</sup>-contact about 0.5 – 1 mm thick.

A particle that enters the active volume of a semiconductor detector can deposit energy by creating electron-hole pairs. The generated charge  $q$  in the

---

<sup>1</sup>Negative (positive) doping refers to an area in the material with free electrons (holes).

<sup>2</sup>Impurities that increases conductivity by donating (accepting) charge are known as donor (acceptor) impurities.

conduction band is proportional to the deposited energy  $E$  and is given by

$$q = \frac{E \cdot e}{\eta} \quad (4.1)$$

where  $e = 1.6 \cdot 10^{-19}$  C is the elementary charge and  $\eta = 2.96$  eV is the average energy needed to create an electron-hole pair in germanium.

## 4.2 Signal Generation

The free charge carriers created due to an energy deposition in the active volume of the detector induce mirror charges at the contacts. The induced charge  $q_i$  in contact  $i$  depends on the positions  $\vec{r}_e$  and  $\vec{r}_h$  of the electron and hole, respectively. The net induced charge can be described by the *Shockley-Ramo theorem* [55, 56]:

$$q_i(\vec{r}_e(t), \vec{r}_h(t)) = q_0 [W_i(\vec{r}_h(t)) - W_i(\vec{r}_e(t))] \quad (4.2)$$

where  $q_0 = |q_e| = q_h$  is the absolute charge of the charge carriers and  $W_i$  is the weighting potential of the contact  $i$ . At  $t = 0$ , electron and hole are still at the same position and according to Equation 4.2 the induced charge at the contacts is zero. Due to the electric field inside the crystal induced by the applied reverse bias voltage and impurities, the charge carriers start drifting towards their respective contacts for  $t > 0$ . The fraction of the charge  $q_0$  that is induced as a mirror charge to the contact  $i$  at a given position  $\vec{r}$  is given by the weighting potential  $W_i$ .  $W$  ranges from 0 to 1 and can be calculated like the electric potential  $\Phi(\vec{r})$  using the first Maxwell equation (Gauss's law):

$$\nabla \cdot \vec{D}(\vec{r}) = \rho(\vec{r}). \quad (4.3)$$

Here,  $\rho$  is the charge density distribution and  $\vec{D}$  the electric displacement field. With  $\vec{D}(\vec{r}) = \epsilon_0 \epsilon_r(\vec{r}) \vec{E}(\vec{r})$  and  $\vec{E}(\vec{r}) = -\nabla \Phi(\vec{r})$  it follows

$$\nabla \cdot (\epsilon_r(\vec{r}) \cdot \nabla \Phi(\vec{r})) = -\frac{\rho(\vec{r})}{\epsilon_0} \quad (4.4)$$

where  $\epsilon_0$ ,  $\epsilon_r$  and  $\vec{E}$  are the dielectric constant, the relative permittivity distribution and the electric field, respectively. Using this to calculate the weighting potential needs specific boundary conditions:  $\rho(\vec{r}) = 0$ ,  $W_i = 1$  at the

contact itself and  $W_i = 0$  at any other contact. From these conditions Equation 4.4 can be written as

$$\nabla \cdot (\epsilon_r(\vec{r}) \cdot \nabla W_i(\vec{r})) = 0 \quad (4.5)$$

where  $\epsilon_r^{\text{Ge}}(\vec{r}) = 16 = \text{constant}$  can be assumed for HPGe detectors due to their low impurity level of the order of  $10^{-13}$  atoms per germanium atom.

### 4.3 Pulse-Shape Simulation using *SolidStateDetectors.jl*

The pulse shape of an event measured with a semiconductor detector is determined by the drift of the charge carriers in the detector volume. The software package *SolidStateDetectors.jl* (SSD) [54] was specially developed for this purpose at the Max Planck Institute for Physics in Munich, Germany. With this open-source package, arbitrary detector geometries and the influence of the surrounding environment can be simulated in 3D using the high-performance programming language *Julia* [57].



In the first step of the simulation with SSD, the electric potential  $\Phi(\vec{r})$  is determined by solving Equation 4.4 for the given geometry, reverse bias and impurity distribution. A 3D grid is set for the volume to be simulated and the potential for each grid point is calculated. The space between the grid points is adaptive and can be refined in several steps which can be specified by the user. For the resulting grid, the calculations are repeated with different boundary conditions to obtain the weighting potential  $W_i(\vec{r})$ . The electric field  $\vec{E}(\vec{r})$  is then being calculated from the electrical potential using  $\vec{E}(\vec{r}) = -\nabla\Phi(\vec{r})$ .

The electric potential for a GERDA germanium detector calculated using SSD is shown in Figure 4.1. In addition, the electric field lines are plotted

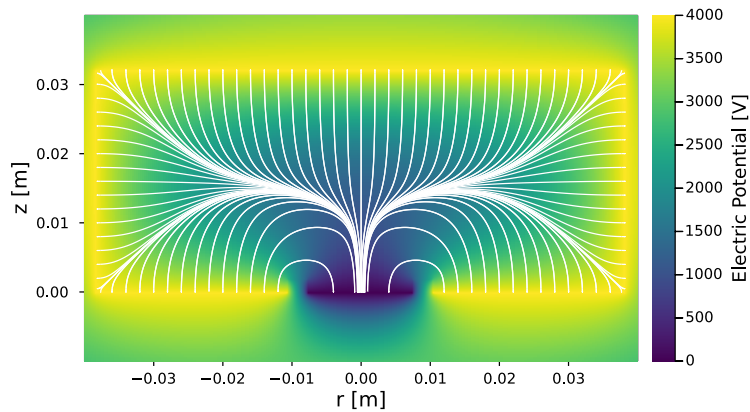


FIGURE 4.1: Electric potential for a GERDA germanium detector calculated using SSD. The electric field lines are plotted as white lines.

in white. The free charge carriers generated as result of an energy deposition, do not exactly follow the shown field lines due to crystal effects and self repulsion between them. The model used in SSD for the charge drift in germanium was originally introduced by Canali [58] and later expanded by Mihailescu [59] and Bruyneel [60, 61]. A detailed description of the underlying calculations in SSD can be found in [54, 62]. An example event with three energy depositions is shown in Figure 4.2. Here, the drift paths of the created holes  $h^+$  and electrons  $e^-$  are shown in green and red, respectively, until they are collected at the contacts. The resulting charge signal for both contacts is shown in Figure 4.3 in units of the absolute charge  $q$  created by the energy depositions. However, only the  $p^+$  contact was read out in the GERDA experiment. The recorded signal will also depend on the response function of the read out electronics. Effectively, the signal shown in Figure 4.3 needs to be convoluted with this response function in order to obtain a realistic pulse shape. The different germanium detector types used in GERDA and their weighting potentials can be seen in Figure 5.2.

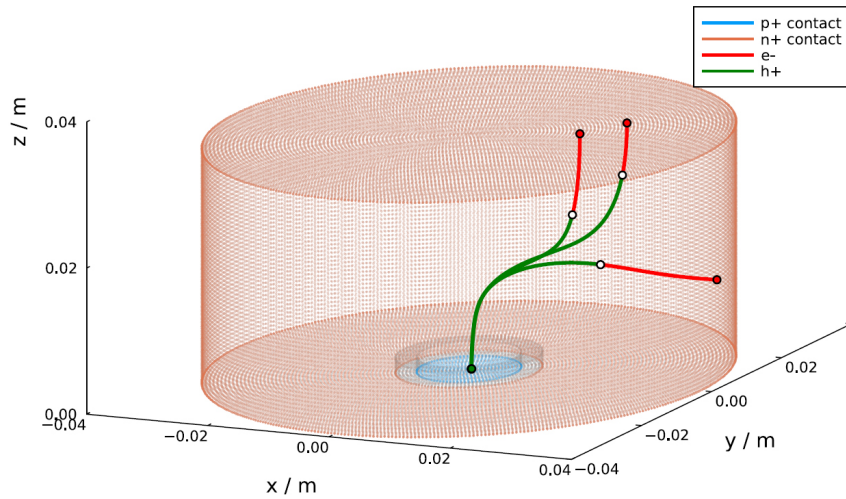


FIGURE 4.2: 3D plot of a GERDA germanium detector. An example event with three energy deposits (white) is shown. The drift paths of the holes  $h^+$  (green) and for the electrons  $e^-$  (red) are shown till they are collected in the contacts.

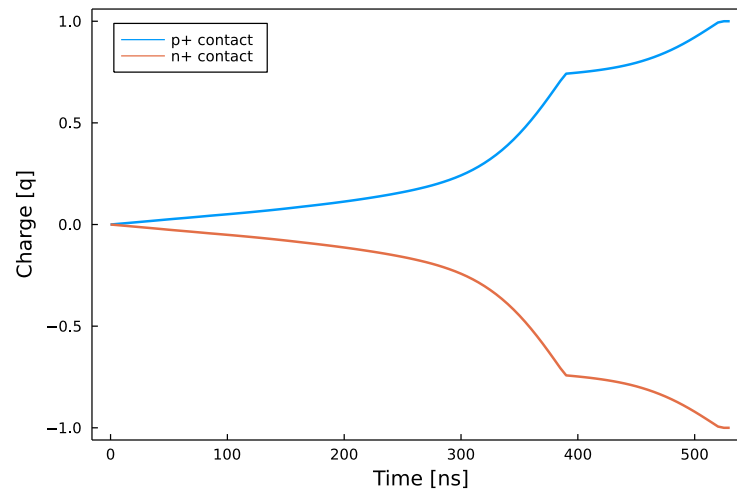


FIGURE 4.3: Charge signal for both contacts of the simulated event shown in Figure 4.2.

## Chapter 5

# Background Sources and their Identification in GERDA

Figure 3.4 clearly shows how significant the effect of the background is on a rare-event search experiment. There are numerous backgrounds that every low-background physics experiment has to contend with. In order to reduce the background as much as it is necessary in LEGEND, all components must be carefully examined and understood. For further improvements, many efficient background identification methods have been developed by the GERDA collaboration. These methods have been proven very successful and will also be used in LEGEND.

In the following, an overview of the main background sources inside an experiment and those coming from the outside is given. Furthermore, how these backgrounds were identified and thus vetoed in GERDA is presented.

### 5.1 Internal Background Sources

All materials of an experiment including the detector itself are a potential source of background. Here, the contamination can be due to the production process of the material or primordial radionuclides [63]. Therefore, the internal radioactivity of the components of an experiment and its effect on the sensitivity have to be understood. This also includes the type, rate and energy of the respective radiation. With this knowledge, it can be evaluated (for example by simulations) whether the radiation is able to reach the detector and, if so, whether the deposited energy is high enough to imitate the signal.

None of the materials normally used for the construction of experiments can be produced completely without radioactive contamination. However, there are a few materials that are particularly suitable for the use in low-background environments. These are often called *low-background materials*

and include: copper, Teflon (PTFE), semiconductor-grade Si, lead and PEN. For each of these materials, manufacturing and cleaning methods exist to get them particularly clean [53, 63, 64].

Primordial radionuclides were already present before Earth was formed (approx.  $4.5 \cdot 10^9$  yr ago). They originate from the matter of the solar system and are expected to be a contamination in all experimental components due to their long half-life. In order to still exist today, the half life of these nuclides must be well above  $50 \cdot 10^6$  yr. In particular,  $^{232}\text{Th}$  and  $^{238}\text{U}$  have to be taken into account for all low-background experiments, because  $^{208}\text{Tl}$  (2614.5 keV  $\gamma$ ),  $^{214}\text{Bi}$  (3270 keV  $\beta$ ) and  $^{222}\text{Rn}$  (5490 keV  $\alpha$ ) are produced in the course of their decay chains [65]. These daughter nuclei produce radiation with sufficiently high energy to be a background near  $Q_{\beta\beta}$  of  $^{76}\text{Ge}$ .

Similar to primordial radionuclides,  $^{40}\text{K}$  is also expected to be in trace quantities in all materials due to its half life of  $1.3 \cdot 10^9$  yr [65]. Its 1461 keV  $\gamma$  radiation does not have enough energy to be a background at  $Q_{\beta\beta}$ , but it forms a background for the  $2\nu\beta\beta$ -decay spectral analysis. This background also leads to performance losses in analysis cuts based on signals with lower energies. [7]

Another source of background at  $Q_{\beta\beta}$  is  $^{42}\text{Ar}$  which is present in natural argon. It is produced by neutron capture  $^{40}\text{Ar}(n, \gamma)^{41}\text{Ar}(n, \gamma)^{42}\text{Ar}$  in neutron-rich surroundings and by cosmic alphas  $^{40}\text{Ar}(\alpha, 2p)^{42}\text{Ar}$  in the atmosphere. A decay product of  $^{42}\text{Ar}$  ( $T_{1/2} = 32.9$  yr) is  $^{42}\text{K}$  which beta decays with a  $Q$  value of 3525 keV ( $T_{1/2} \approx 12$  h).

## 5.2 External Background Sources

While the background introduced by the structural materials can be optimised by their choice and excessive cleaning, the external background from cosmic rays has to be shielded and/or vetoed. The charged particles coming directly from space are referred to as *primary* whereas the radiation that is produced by their interaction with nuclei in the atmosphere is called *secondary* component of cosmic rays. The energy spectrum of the primary radiation goes from  $10^9$  to  $10^{20}$  eV. The interaction with air atoms creates a field of secondary radiation consisting of protons, neutrons, mesons,  $\gamma$  rays and other high-energy particles. The resulting particle showers can cover areas of several square kilometres on the Earth's surface. In order to avoid this cosmic radiation background, many low-background experiments are located deep underground. At LNGS, for example, the muon rate is  $\approx 1.25 \text{ m}^{-2}\text{h}^{-1}$

which relates to a reduction of 6 orders of magnitude compared to the Earth's surface. [66]

Cosmic rays can lead to radioactivity in materials through cosmogenic activation. Here, radionuclides such as  $^{36}\text{Cl}$ ,  $^{39}\text{Ar}$ ,  $^{60}\text{Co}$  and  $^{68}\text{Ge}$  can be produced. In order to suppress this activation process as effectively as possible, the production and storage of low-background materials is also carried out underground [8, 53, 67]. There has also been a study presented in [68] on cosmogenics produced by high energetic muons in germanium detectors and LAr in the GERDA setup using simulations. Here, a contribution of in-situ cosmogenics to the ambient radioactivity of the order of 1 nBq/kg was found, which is three orders of magnitude lower compared to the contribution of natural radioactivity. However, radioactive isotopes like  $^{75}\text{Ga}$  and  $^{77m}\text{Ge}$  produced in the bulk of the detectors have to be considered as their  $\beta$  emission can not be topologically distinguished from double beta decay events.

## 5.3 Background Event Identification in GERDA

Like GERDA and MAJORANA DEMONSTRATOR, the LEGEND experiment is built according to the background-free goal during the lifetime of the experiment. Ideally, all detected background events at  $Q_{\beta\beta}$  are discriminated. In order to achieve the ambitious goal for the corresponding background index of LEGEND, many methods of background identification have already been developed and been in operation.

In this Section, the methods used in GERDA are presented. These include the water-Cherenkov and LAr veto systems, the HPGe detector anti-coincidence cut and HPGe pulse-shape discrimination. A schematic representation of the individual methods can be seen in Figure 5.1. Based on the fact that most of the double beta decay events (yellow) are point-like (within  $1\text{ mm}^3$  [69]), events with energy depositions in other volumes can be discarded as background.

### 5.3.1 Water-Cherenkov Detector

High energetic muons from cosmic rays can deposit energy in all components of the experimental setup. In order to detect  $\mu$ -induced events in the HPGe detectors, a water Cherenkov detector was used to identify through going muons. In addition, three layers of plastic scintillators covering the



coated with TPB. In addition, the nylon mini-shrouds surrounding the detector strings were also coated with TPB. This new method of background identification paved the way for the GERDA experiment towards a background-free  $0\nu\beta\beta$ -decay search. [7, 71]

The threshold for the scintillation light detection was set to 50% of the expected amplitude of a single photo-electron (PE) in one light sensor. Here, the traces from the PMTs and SiPMs were analysed offline. The time window for rejecting a coincident germanium signal was set to  $5\ \mu\text{s}$ . This time window was chosen as it corresponds to the time in which 99% of all photons occurred. The dead time induced by the LAr veto system was  $(2.3 \pm 0.1)\%$ . The  $^{42}\text{K}$  line at 1525 keV was suppressed by a factor of 5 thanks to the LAr veto system [71]. Figure 5.1 shows this principle schematically with a  $\gamma$ -event drawn in dark green.

### 5.3.3 Anti-Coincidence Cut

Due to  $0\nu\beta\beta$ -decay event characteristics, events with energy depositions in multiple germanium detectors can be discarded. This is shown in Figure 5.1 for a  $\gamma$  event in blue. Also, events that succeed each other in a time window of 1 ms were excluded. This was done to exclude events from the decay chains of primordial radionuclides like the radon progenies  $^{214}\text{Bi}$  and  $^{214}\text{Po}$ . [71]

### 5.3.4 Pulse-Shape Discrimination (PSD)

The pulse shape of a germanium detector signal depends on where the energy is deposited. A general distinction is made between *single-site event* (SSE), *multi-site event* (MSE) and *surface event*. SSEs are characterised by an energy deposition within  $\approx 1\ \text{mm}^3$  of the detector volume like in case of the  $2\nu\beta\beta$  and  $0\nu\beta\beta$  decay. In most background events, such as  $\gamma$  rays from natural radioactivity, Compton scattering causes multiple energy depositions. Events close to the  $\text{p}^+$  ( $\text{n}^+$ ) contact show fast (slow) pulse-shape characteristics due to the electric field and are referred to as surface events. Slow pulses also often have incomplete charge collection. The differentiation of MSE and surface events to SSE by the pulse-shapes time-structure is called *pulse-shape discrimination* (PSD).

PSD works especially well for HPGe detectors with point-like contacts, like BEGe or ICPC detectors as used in GERDA or the point-contact detectors used in MAJORANA DEMONSTRATOR. Interactions in BEGe detectors create similar pulse-shapes for a large detector volume due to their small

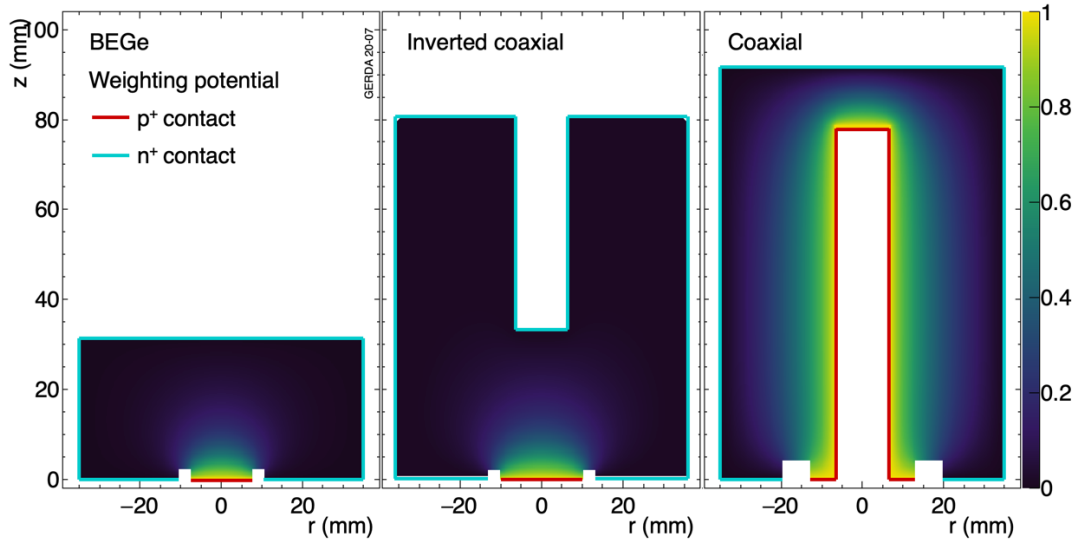


FIGURE 5.2: Weighting potential for different germanium detector types (as labelled) used in GERDA. The contacts are drawn separately. Picture taken from [12].

$p^+$  contacts. For semi-coaxial germanium detectors, the electron and hole drifts have to be taken into account due to the  $p^+$ -contact shape resulting in different pulse-shapes in the whole detector volume. A comparison of the weighting potentials and geometry of the detector types used in GERDA can be seen in Figure 5.2. [12]

Example pulse-shapes recorded with a BEGe detector for SSE, MSE and events near the  $p^+$  and  $n^+$  contacts are shown in Figure 5.3. The normalised charge pulses are drawn in blue with the corresponding current pulses<sup>1</sup> in orange. The amplitude of the charge pulse is proportional to the energy  $E$  of the event (see Equation 4.1). When looking at the current pulses, clear differences in their amplitudes  $A$  can be seen for different event types. By comparing  $A$  and  $E$  using the quotient  $A/E$  a distinction can be made between the event types.

As the  $A/E$  spectrum is continuous and energy dependent, this distinction is not always clear. The so-called  $A/E$  classifier  $\zeta$  was introduced in GERDA for this purpose [12]. It is defined as

$$\zeta = \left( \frac{A/E}{\mu_{A/E}(E)} - 1 \right) / \sigma_{A/E}(E) \quad (5.1)$$

where  $\mu_{A/E}(E)$  and  $\sigma_{A/E}(E)$  are the energy dependent  $A/E$  peak position and width, respectively. The  $A/E$  spectrum used in Equation 5.1 is normalised to 1. These corrections lead to an energy-independent classifier that

<sup>1</sup>The derivative of the charge pulse is the current pulse.

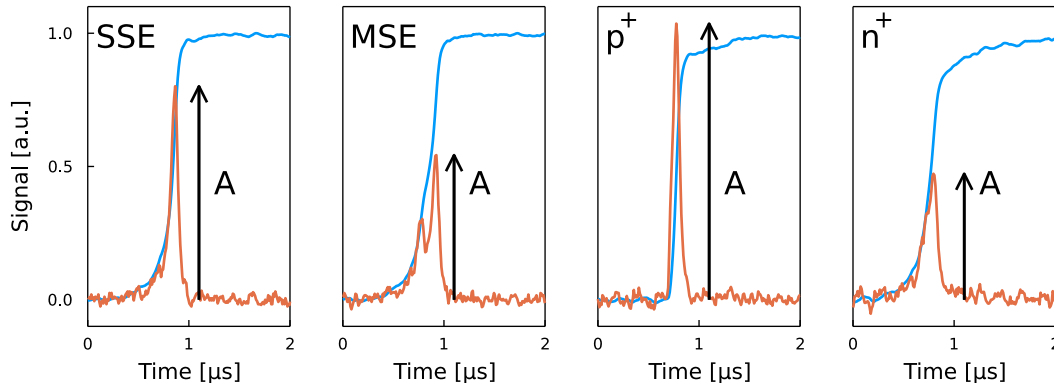


FIGURE 5.3: Normalised charge pulses (blue) of a BEGe detector for different pulse-shape characteristics. The corresponding current pulses (orange) and arrows indicating their amplitude  $A$  are also drawn. Figure adapted from [12].

peaks at 0 and has a standard deviation of 1 for SSEs. A *low cut* value ( $< 0$ ) was defined to distinguish SSE to MSE and  $n^+$  surface events. An additional *high cut* value was set to  $\zeta = 3$  to discriminate  $p^+$  surface events [12]. If not stated different, all  $A/E$  cuts in this thesis are defined by an  $A/E$  classifier  $\zeta$ .

In GERDA, a so-called proxy signal for  $0\nu\beta\beta$  decay with similar properties was used for normalisation of the  $A/E$  classifier spectrum: the double-escape peak (DEP) of  $^{208}\text{Tl}$ . Single and double escape lines are so-called fake spectral lines in which not the entire energy  $E$  of the gamma is deposited in the detector due to the escape of annihilation gammas. If  $E > 1022$  keV pair production can take place in the detector. The resulting positron can be captured in the detector material and thus lead to an emission of two photons with 511 keV each in the annihilation process. If one of them escapes the detector while the other is observed, a line can be measured at  $E - 511$  keV (single-escape peak, SEP). If both escape, the measured energy is at  $E - 1022$  keV (DEP). Consequently, if no photon escapes, the full energy is deposited (full-energy peak, FEP) [72]. In case of double-escape events, the energy deposition by  $e^- + e^+$  shows SSE characteristics.

In GERDA, calibration runs were carried out weekly using a  $^{228}\text{Th}$  source. The energy spectrum contains the DEP, SEP and FEP of  $^{208}\text{Tl}$  [73]. While the DEP shows SSE characteristics, the SEP and FEP can be used as MSE samples to evaluate the discrimination efficiency. The low cut value in GERDA was defined by 90% survival of DEP signals. This value was chosen on the simulation-based expectation that about 10% of  $0\nu\beta\beta$ -decay events show MSE characteristics due to Bremsstrahlung.

The determination of the  $0\nu\beta\beta$ -decay detection efficiency in GERDA was

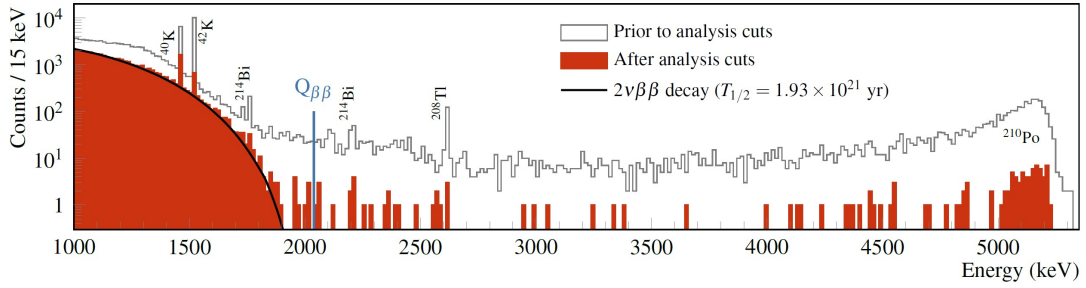


FIGURE 5.4: GERDA Phase II energy spectrum before and after analysis cuts for 103.7 kg·yr exposure. The quasi-background-free ROI around  $Q_{\beta\beta}$  is marked with a blue line. [7]

completely data-based using the DEP. However, the spatial distribution of  $0\nu\beta\beta$  decay and DEP events is not comparable. While  $0\nu\beta\beta$ -decay events are expected to occur homogeneously distributed, the probability for DEP events is higher at the edges of the detectors. In this thesis, a simulation and data-based method is presented in Chapter 8 to determine the  $0\nu\beta\beta$ -decay detection efficiency for GERDA BEGe detectors with reduced systematic uncertainties.

### 5.3.5 Effect of Analysis Cuts in GERDA Phase II

The energy spectrum of GERDA Phase II for 103.7 kg·yr exposure can be seen in grey in Figure 5.4. In addition, the spectrum after all analysis cuts described were applied is shown in red with the fit of the continuous energy spectrum of  $2\nu\beta\beta$  decay drawn in black. In the ROI around  $Q_{\beta\beta}$ , no event could survive the filter which makes this area *quasi background-free*.

## 5.4 Background Considerations in LEGEND

A special feature of the GERDA experiment was the LAr shield, veto and cooling system. Since the same concept is also used in LEGEND-200, prior information on the associated background is available and can be taken into account. LAr can be produced with a high degree of radiopurity, but  $^{42}\text{Ar}$  is very difficult to filter out completely. This background can be located anywhere in the LAr volume and thus also in the vicinity of the germanium detectors. Since the decay product is positively charged, it can drift along the electric field lines and beta decay close to the detector surface [74]. In earlier investigations of the GERDA collaboration in 2012, a specific activity of  $^{42}\text{Ar}$  was measured to be  $(92.8 \pm 6.9) \mu\text{Bq/kg}$  [75]. With the reduction through the

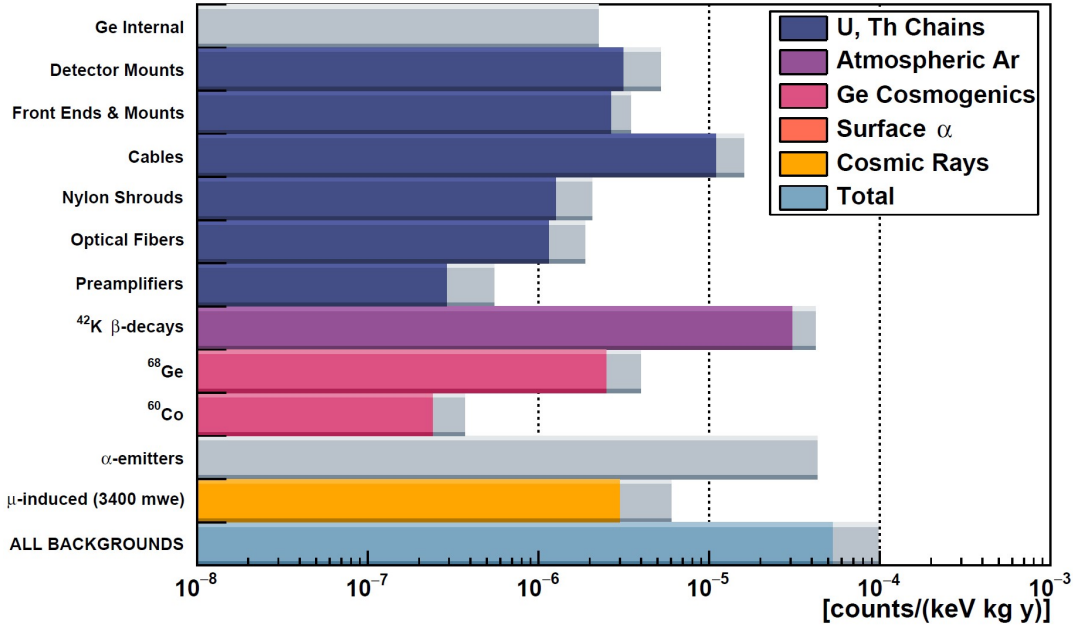


FIGURE 5.5: Expected background contributions of LEGEND-200. The grey bars indicate  $1\sigma$  uncertainties due to screening measurements and Monte Carlo simulations. [70]

use of underground-sourced LAr (UGLAr) in LEGEND-1000, a background contribution for  $^{42}\text{Ar}$  of  $5.1 \cdot 10^{-4}$  cts/(keV·kg·yr) is expected (before analysis cuts). [7, 76]

Another background can be found in the germanium detectors. These are the  $^{60}\text{Co}$  and  $^{68}\text{Ge}$  contaminations in the enriched material introduced by cosmogenic activation.  $^{60}\text{Co}$  impurities in the base material can be effectively removed by zone-refining and crystal-pulling processes during manufacturing. But when the finished detector is exposed to cosmic rays,  $^{60}\text{Co}$  can be generated again. At sea level the production rate is  $(2.55 \pm 1.20)$  atoms/kg·d [77]. The beta decay of  $^{60}\text{Co}$  has  $T_{1/2} = 5.3$  yr and a  $Q$  value of 2824 keV with the coincident emission of two  $\gamma$  rays with 1173 keV and 1333 keV. The two  $\gamma$  rays can form a combined background for  $Q_{\beta\beta}$ . [7]

The  $^{68}\text{Ge}$  isotope is generated under the influence of cosmic rays at sea level at a rate of  $(2.12 \pm 0.39)$  atoms/kg·d [77].  $^{68}\text{Ge}$  can only be removed by the enrichment process. Its short-lived progeny  $^{68}\text{Ga}$  can undergo a  $\beta^+$  decay with a  $Q$  value of 2921 keV. The background contribution of  $^{60}\text{Co}$  and  $^{68}\text{Ge}$  in GERDA was kept at a minimum by only shielded transportation and storage of the detector crystals underground during manufacturing process and whenever not needed above ground. The time of the detectors above ground was tracked in order to estimate the amount of cosmogenic activation. [7]

The surface of the germanium detectors can also be contaminated with,

for example,  $^{210}\text{Po}$  ( $T_{1/2} = 138$  d) and  $^{210}\text{Pb}$  ( $T_{1/2} = 22$  yr). These contaminations can be introduced during fabrication, storage and assembly due to dust or deposition of ionised progeny of  $^{222}\text{Rn}$  decays.  $^{210}\text{Po}$  and  $^{210}\text{Pb}$  emit high-energy  $\alpha$  particles with 5300 keV and 3720 keV [65], respectively, which can deposit part of their energy in the active volume of the detectors. Handling the germanium detectors only in clean environments can limit the surface contamination. In addition, PSD has been shown to be highly effective in identifying  $\alpha$ -induced background events in point-contact germanium detectors. [7]

The expected distribution of backgrounds for LEGEND-200 (after analysis cuts) is shown in Figure 5.5. This results in an estimated total background of  $1 \cdot 10^{-4}$  cts/(keV·kg·yr). A background index after analysis cuts of about  $9 \cdot 10^{-6}$  cts/(keV·kg·yr) is expected for LEGEND-1000. [7]

## Chapter 6

# Polyethylene Naphthalate as Optically Active Structural Material

*Poly(ethylene 2,6-naphthalate)* (PEN) is a commercially-available industrial polymer which is handled as an excellent candidate for an optically active structural material in low-background experiments. It provides scintillation and WLS properties, good mechanical strength, acceptable transparency and a very good intrinsic radiopurity. In addition, PEN is a so-called *unitary* scintillator as it does not need any dopants to emit scintillation light. For use in low-background experiments, this means that fewer substances have to be cleaned to keep the final product clean.

In LEGEND-200, PEN is now used for the first time as an optically active structural material in an ultra-low background experiment. For this purpose, the holders of the germanium detectors were made of PEN. Compared to the Si used in GERDA, scintillation light from LAr in close vicinity or in between the HPGe detectors can be better guided to the fibres due to the WLS properties of PEN. In addition, PEN serves as additional veto system, whose scintillation light can also be absorbed by the fibres. In the past, background events between detectors were not detected in most cases as the scintillation light was absorbed by opaque passive materials.

In this chapter, all parameters of manufacturing and characterisation of the PEN samples are introduced which are relevant for the use in LEGEND-200 presented in Chapter 7. Previously obtained results for custom-made PEN samples from an earlier production are also presented [10]. In addition, the requirements for PEN in LEGEND-200 are discussed. In this thesis, the production series are distinguished between the production for LEGEND-200 and all test production series before.

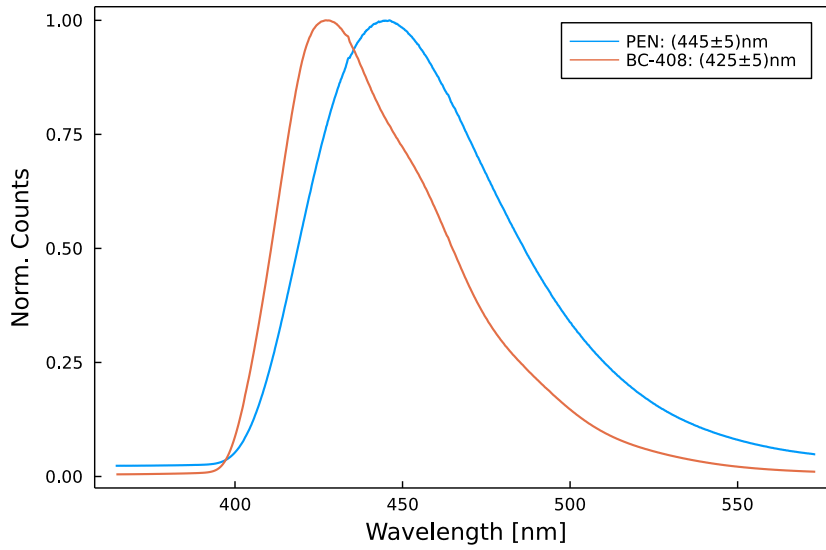


FIGURE 6.1: Emission spectra of PEN and BC-408 scintillator samples excited using a  $(382 \pm 2)$  nm UV lamp. Spectra taken from [10].

## 6.1 Optical Properties

The PEN samples used for the LEGEND-200 germanium detector holders were investigated for their optical properties which are introduced in this section. Since a different manufacturing technique was used for this production, slight deviations from previous results [10] are possible.

### 6.1.1 Emission Spectrum

PEN first got attention among experimental physicists when its scintillation properties were published in 2011 [9]. A few years later the scintillation property could be reproduced by the LEGEND collaboration with custom-made PEN scintillator samples [10]. The emission spectrum was found in the deep blue region with peak wavelength  $\lambda_{\text{peak}} = (445 \pm 5)$  nm. This wavelength region fits well to the peak quantum-efficiency of many standard light-sensors (PMTs, SiPMs) and is visible for the human eye. A comparison of the emission spectra of PEN and a commonly used plastic scintillator BC-408 [78] can be seen in Figure 6.1. The two samples had the same dimensions of  $(30 \times 30 \times 3)$  mm<sup>3</sup> and were excited with a  $(382 \pm 2)$  nm ultra-violet (UV) lamp. The emission spectra were recorded using an *Andor Shamrock 193i* spectrometer.

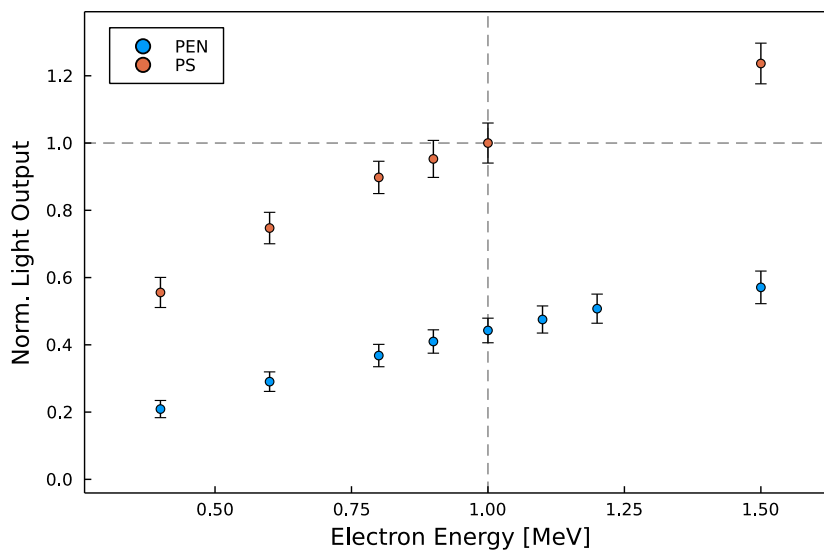


FIGURE 6.2: Comparison of the light output of PEN and PS as function of the electron energy from a  $^{90}\text{Sr}$  source. An electromagnet was used to create distinct energy levels. Data taken from [10].

### 6.1.2 Light Yield & Light Output

With the wavelength of the generated scintillation light in PEN known, the next question concerns the light yield of the custom-made PEN scintillators which refers to the number of photons generated for a given amount of deposited energy in the bulk material. Here, the number of photons actually measured in an experiment is denoted as light output. In an earlier work, a comparison was made with the well-known plastic scintillator polystyrene (PS)<sup>1</sup> in order to estimate the light yield. For this purpose, electrons from a  $^{90}\text{Sr}$  source were used for excitation. In order to obtain mono-energetic electrons, an electromagnet was used as speed selector. The scintillation light generated in the samples by the incoming electrons was then measured with a PMT. The comparison of the signal strength for PEN and PS for electron energies from 0.4 MeV to 1.5 MeV is plotted in Figure 6.2. The values are normalised to the signal strength of PS at 1.0 MeV. It was found that the used PEN tile emitted about 2.5 times less light than the PS tile. This corresponds to about 4000 photons produced in PEN per 1.0 MeV energy deposition [10]. However, this measurement is based on light output and did not consider attenuation effects in PEN, hence can be taken as a lower limit for the light yield.

<sup>1</sup>PS is doped with para-terphenyl (pTP) and 1,4-bis(5-phenyloxazol-2-yl) benzene (POPOP) fluors to produce the scintillation light.

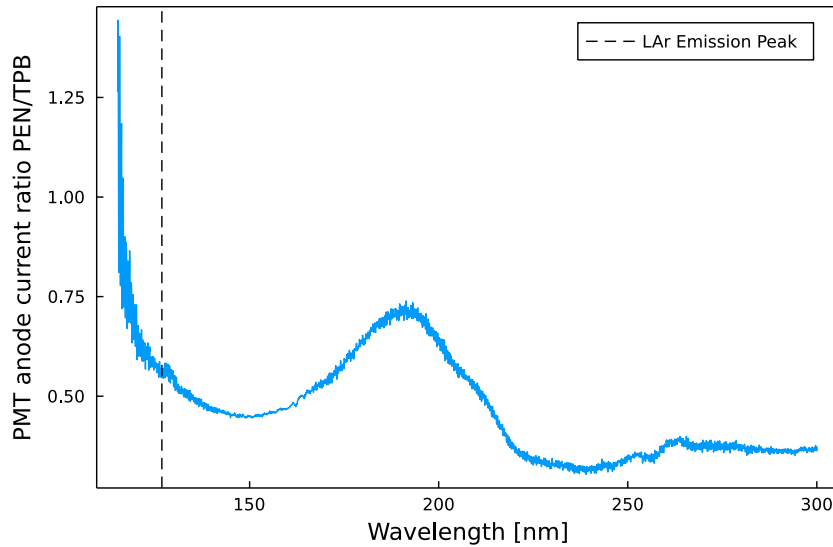


FIGURE 6.3: Comparison of the WLS properties as function of absorption wavelength of a PEN sample to a TPB-coated acrylic sample. The ratio of the anode currents is taken as measure. The peak emission wavelength of LAr scintillation light at 128 nm is marked by the dashed black line. Spectrum taken from [10].

### 6.1.3 Wavelength-Shifting Properties

In addition to its scintillation properties, PEN can improve the LAr veto efficiency in LEGEND due to its WLS properties. The peak emission wavelength of LAr is 128 nm which is in the vacuum-UV (VUV) range [79]. Unfortunately, this light can only be measured by a few special light sensors and even with these, the efficiency is usually below 20%. This is because commercially available SiPMs and PMTs have borosilicate glass windows to protect the sensor. These have a cutoff at  $\approx 300$  nm and, thus, prevent detection of VUV photons. In order to still be able to measure this light, the transparent components in the GERDA experiment were coated with TPB. The VUV scintillation light from LAr is shifted by TPB to the blue wavelength region.

PEN has similar WLS properties as TPB, which was confirmed by comparing a PEN sample to a TPB-coated acrylic sample ( $200 \mu\text{g}/\text{cm}^2$ ). A tunable monochromator was used as light source. The incident wavelength range was scanned from 116 nm to 300 nm. The wavelength-shifted light was then measured using a PMT. For the comparison shown in Figure 6.3, the ratio of the anode currents of the PMT of the two test pieces was formed. At peak emission wavelength of LAr (black dashed line) the ratio of PEN to TPB is approximately 55%. Although PEN has a lower efficiency than TPB, it will still improve the overall efficiency of the LAr veto in LEGEND by replacing

the optically inactive materials.

#### 6.1.4 Attenuation and Bulk Absorption Length

In order to determine how many photons reach the light sensor from the excitation point, the attenuation length has to be included in the simulations. Here, two properties can be measured: the light attenuation length  $\lambda_{\text{att}}$  and the bulk absorption length  $\lambda_{\text{abs}}$ . Both are defined as the distance after which the probability that it was not absorbed has fallen to  $\frac{1}{e}$ .  $\lambda_{\text{att}}$  refers to the length of the material, hence includes reflections in the sample which makes it geometry dependent.  $\lambda_{\text{abs}}$  refers to the distance travelled by the photons.

For PEN scintillators of the previous production series,  $\lambda_{\text{abs}}$  has not been measured. Also, it was not possible to manufacture large-enough scintillator-grade PEN plates to reliably determine  $\lambda_{\text{att}}$ . However, it was already derived that the attenuation length is below 5 cm. This is rather short compared to other plastic scintillators which usually have attenuation lengths of the order of metres. Hence, a short attenuation length limits the size of optically active PEN structures. In LEGEND, the detector holders made of PEN will be less than 10 cm wide and the light will be collected from all sides. This makes the effect of the attenuation length acceptable.

#### 6.1.5 Surface Properties

In order to create an accurate simulation of the scintillation light propagation in PEN using GEANT4 [80], it is important to know the quality of the surface as it influences the scattering angles of photons off the surface. As a measure, the micro facets of the surface can be used, which are described schematically in Figure 6.4 (right). The standard deviation  $\sigma_h$  of the height distribution of the micro facets compared to the average surface can be used to classify which type of reflection (see Figure 6.4, left) will be used in the simulation. For the classification of perfect, specular spike and specular lobe reflection, the ratio  $\sigma_h/\lambda_{\text{peak}}$  is used. For  $\sigma_h/\lambda_{\text{peak}} < 0.025$ , the reflections can be considered perfect, while specular spike is assumed for ratios up to 1.5. Above that, specular lobe reflections are used in the simulation [81, 82].

In addition to the classification of the used reflection type, another parameter is needed as input for the simulation: the standard deviation  $\sigma_\alpha$  of the angular distribution of the micro facets. Here, the angle  $\alpha$  is defined as the angle between the normal of the average surface and the normal of the micro facet as can be seen in Figure 6.4 (right). On a plane surface  $\langle \alpha \rangle = 0$ .

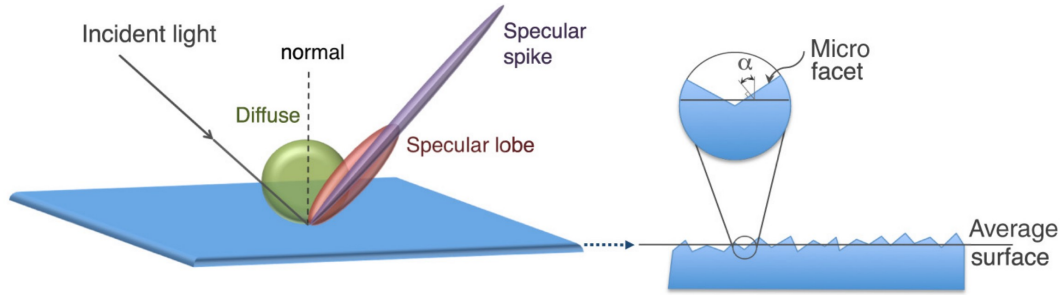


FIGURE 6.4: **Left:** Types of reflections included in GEANT4 for reflective surfaces. **Right:** Cross-section of a surface to illustrate the micro facets. The height is defined as the distance of the micro facet to the average surface (black line). The angle  $\alpha$  is formed by the normal of the micro facet to the normal of the average surface. Picture taken from [82].

For highly polished surfaces with  $\sigma_h/\lambda_{\text{peak}} < 0.025$ ,  $\sigma_\alpha$  is set to zero in the simulation.

### 6.1.6 Detection Efficiency & Energy Threshold

To estimate how the new PEN germanium detector holders can improve the background veto-efficiency of LEGEND-200, it is important to understand the light output after a position-dependent energy deposition in the PEN sample (holder). This can be used to get predictions for detection efficiency via the LAr veto system and to determine the energy threshold which refers to the minimum deposited energy in a PEN holder that will result in a measurable signal.

## 6.2 Requirements for PEN in LEGEND-200

In order to introduce PEN as new structural material in the ultra-low background environment of LEGEND-200, three basic conditions must be met:

1. It must have a high radiopurity
2. It must withstand the loads also under cryogenic conditions
3. It must not increase the leakage current in the germanium detectors

### 6.2.1 Radiopurity

The first condition is related to the stringent background goal of LEGEND-200 (see Chapter 3.3). To reach the goal, the radio impurity per detector holder

( $\approx 6.2$  g) must be less than  $1 \mu\text{Bq}$  [70]. In this requirement, however, the self-vetoing capabilities of PEN are not taken into account. A measurement of the impurities of the raw commercially obtained and unprocessed PEN granulate has shown that this condition is not yet fulfilled. A high  $^{40}\text{K}$  contamination of  $(1.6 \pm 0.4)$  mBq/g was particularly noticeable here. Since this was assumed (and later verified) to be a surface impurity, a cleaning procedure was developed and tested in the course of this work. This is described in Section 7.1.1. The radiopurity achieved after applying this cleaning cycle is presented in Section 7.1.5 and published in [83].

## 6.2.2 Mechanical Properties

In order to evaluate whether PEN fulfils the second condition, a three-point bending flexural test according to *DIN EN ISO 178:2013-09* [85] was carried out at room temperature and in liquid nitrogen (77 K) with custom-made scintillator-grade PEN samples from a previous production batch. By this measurement, the Young's modulus and yield strength were obtained. The test pieces had the dimension  $(15 \times 30 \times 3)$  mm<sup>3</sup> and the measurements were performed at room temperature and with the sample submerged in liquid nitrogen. The results of this series of measurements can be found in Table 6.1. For comparison, the literature values for copper at room temperature are given. It has been shown that the yield strength of PEN compares well to copper at room temperature. The lower Young's modulus compared to copper shows that PEN has a higher elasticity. The deformation in the elastic regime is considered to be acceptable for many components making it suitable as a structural material in LEGEND. At cryogenic conditions, the Young's modulus and the yield strength almost double and, thus, making it even stronger.

	PEN at 296 K	PEN at 77 K	Copper at 296 K
Yield strength [MPa]	$108.6 \pm 2.6$	$209.4 \pm 2.8$	100
Young's modulus [GPa]	$1.86 \pm 0.01$	$3.71 \pm 0.08$	128

TABLE 6.1: Young's modulus and yield strength of PEN samples ( $15 \times 30 \times 3$  mm<sup>3</sup>) at room temperature (296 K) and submerged in liquid nitrogen (77 K) [10]. The values for copper at room temperature are given for comparison [84].

### 6.2.3 Leakage Current

The last condition refers to early experiences of the GERDA collaboration. In the search for suitable materials for the detector strings, it was noticed that some of them led to an increased leakage current (see Section 4.1) in the germanium detectors in certain configurations. Additionally, non-perfect detector contacts can deteriorate the energy resolution due to increase capacitance and resistance. Here, the higher flexibility of PEN as detector holder could lead to a deterioration of the wire-bonds from the electronics to the detector and, thus, lead to bad contacts.

In order to investigate the leakage current of a germanium detector, the mean value of the baseline can be monitored as its change is roughly proportional to the change in leakage current. Therefore, the change in leakage current  $\Delta I_{LC}$  can be calculated by

$$\Delta I_{LC} = \frac{\Delta U_{Bl}}{R_f} \quad (6.1)$$

with the feedback resistance  $R_f$  of the readout electronics and the change in the mean baseline  $\Delta U_{Bl}$ . In order to exclude external factors, a comparison can be made between comparable detectors with different holder materials (e.g. Si & PEN). If the mean baseline values behave comparably over time, there is no observable effect on the leakage current introduced during the given time by PEN.

In the course of this work, two long time measurements were carried out with PEN germanium detector holders produced for the LEGEND-200 experiment. These are described in Section 7.2.

## Chapter 7

# PEN as Optically Active Structural Material in LEGEND-200

It has been shown earlier, that PEN meets the mechanical requirements for an active structural material (see Section 6 and [10]). In order for PEN to be used in an ultra-low background environment like LEGEND-200, it must still be shown that conditions one and three listed in Section 6.2 are also fulfilled for the final components.

Through the first production runs and characterisations of scintillating components made of PEN, a lot of experience was gained which was applied to the production of the LEGEND-200 germanium detector holders. On the one hand, a meticulous cleaning cycle of the raw PEN granulate was carried out before the actual processing to remove surface contamination. On the other hand, a slightly different process was used for production which happened in clean room surrounding. These changes significantly improved the radiopurity and the optical transparency.

The path from commercially available PEN granulate to scintillating ultra-low background components for the LEGEND-200 experiment is described in this section. So far, there were only a few studies on the optical properties of PEN as a scintillator [9, 10]. Therefore, it was not well characterised how the manufacturing process influences its optical properties. Therefore, the characterisation of the finished material in terms of emission spectrum, surface quality, attenuation length and its light yield is presented. An estimation of the energy-dependent photon detection-efficiency and threshold of the PEN holders with the setup described in Section 7.3.3 is also discussed. In addition, two integration tests are presented which show that the custom-made PEN germanium detector holders are ready for use in the next generation  $0\nu\beta\beta$ -decay search experiment LEGEND-200.

In the following, the LEGEND-200 germanium detector holders made of PEN are referred to as *PEN holders*.

## 7.1 From PEN Granulate to Optically Active Ultra-Low Background Components

For the LEGEND-200 production series, PEN with the product designation TN-8065 SC from Teijin-DuPont [86] was used. This raw material came in the form of white granulate in plastic bags. These bags were air-tightly sealed, but consisted only of a thin layer of plastic whose radiopurity was unknown. The untreated material was screened for radio impurities using an HPGe detector. Here, a high  $^{40}\text{K}$  contamination in the Bq/kg range was found (more details in Section 7.1.5). This was attributed to be a surface contamination. Therefore, the granulate was thoroughly cleaned before processing it to scintillator-grade PEN holders. The cleaning procedure and subsequent processing are described in this section. In addition, the results of the radiopurity screening at different stages of the process are presented. The procedure and results are also described in [83].

### 7.1.1 Cleaning Procedures

Two cleaning processes were set up for this work. One for all parts that (might) come into contact with PEN and one for the PEN granulate and moulded PEN structures themselves. The former includes, for example, containers, sieves and tools. These were all newly purchased, rinsed with deionised (DI) water<sup>1</sup>, then washed with 2-propanol<sup>2</sup> and class 100 clean room cloths. The parts were then etched in a nitric acid solution<sup>3</sup> for at least 24h and then rinsed again with DI water. Finally, they were cleaned for 15 minutes in an ultrasonic bath filled with DI water. The clean bench used for this can be seen in Figure 7.1 (left). The three basins on the left are ultrasonic baths, each of which can be filled with up to 50 l of DI water via a direct feed. The fourth basin can be heated by air and was used for drying. All basins are situated inside a laminar flow box. The setup is located in a clean room in the Max Planck Institute for Physics in Munich.

---

<sup>1</sup>Deionised water with 18 M $\Omega$  resistance. The water supply automatically stopped when the resistance started to fall.

<sup>2</sup>The 2-propanol used in all steps was of VLSI grade: Metal ion concentration per impurity element  $\approx 10 - 50$  ppb.

<sup>3</sup>2% HNO<sub>3</sub> (optima grade) [87] and 98% DI water was used in all steps presented.



FIGURE 7.1: **Left:** Clean bench used for the PEN granulate cleaning. The three basins on the left were used for ultrasound cleaning while the one on the right was used for the cleaned granulate to dry. **Right:** Vacuum tank filled with cleaned and wet PEN granulate in a custom-made stainless-steel sieve. The white cables are used to connect temperature sensors.

The exact cleaning procedure of the PEN granulate and moulded structures like PEN holders is described by the following steps:

1. Fill PEN granulate/structures into stainless-steel sieve
2. Rinse with  $\approx 2$  l of DI water inside the laminar flow box
3. Place the sieve inside a PTFE container filled with 2.5 l 2-propanol
4. Place PTFE container in the first ultrasonic bath filled with DI water for 15 minutes
5. Rinse PEN granulate/structures for about one minute with DI water
6. Repeat steps 3.-5. with the second ultrasonic bath
7. Repeat steps 3.-5. with the third ultrasonic bath and a PTFE container filled with DI water instead of 2-propanol

PEN structures such as the LEGEND-200 holders were then dried with pressurised nitrogen gas. The granulate was collected in a larger custom-made sieve and then pre-dried in portions of about 10 kg in a vacuum tank. Here, an oil-free roughing pump was used. To accelerate the evaporation process of the water, the tank was heated to  $60^\circ\text{C}$  from the outside by attached heating bands. The vacuum tank with the custom-made sieve filled with PEN granulate can be seen in Figure 7.1 (right). Temperature sensors connected with white cables were placed in the centre of the granulate and at the sieve

to monitor the temperature while heating. This process took 8 h/batch and the pre-dried granulate was then sealed in two layers of class 100 plastic bags for transportation.

### 7.1.2 Moulding Process of PEN Discs

To achieve good transparency and an overall good surface quality of the PEN holders, injection compression moulding was used for the LEGEND-200 production series. The moulding machine was an *Arburg Allrounder 370S*<sup>4</sup> located at the *Lehrstuhl für Kunststofftechnik* (LKT) at TU Dortmund, Germany. In contrast to normal injection moulding, the cavity volume of the mould changes during the process. This ensures a stable and homogeneous flow of the molten PEN into the cavity, which is important to achieve accurate shapes [88]. The mould used consisted of two new stainless-steel plates (type 316) with a mirror-like surface finishing (roughness  $< 1\mu\text{m}$ ) which is referred to as 1P/2P or No.8 (ASTM A480/A480M) in order to assure good PEN surfaces. With this open mould, discs with variable thickness can be produced. In addition, the diameter of the discs can be adjusted by changing the input PEN volume. The optimisation of the flow and temperature settings was done empirically for optimal transparency and shape.

Before the production started, all containers and removable parts of the moulding machine that would come into contact with PEN and fit into the ultrasonic bath have been cleaned as described in Section 7.1.1. In addition, the barrel and the screw of the machine were replaced with new ones. The open part of the machine including the mould was located inside a class-1000 clean room tent which can be seen in Figure 7.2 (left). The interior of the clean room was cleaned using 2-propanol and class 100 clean room cloths prior to production. The moulding unit was cleaned using Micro-90<sup>®</sup> [89] (machine cleaner) and 2-propanol as it could not be acid etched due to its size. Two laminar flow box units of the clean room were running for three days constantly on maximum before the first PEN disc was produced. On the evening before the production, the storage tank of the machine was filled with the pre-dried PEN pellets. This tank was heated to 80°C to remove the remaining moisture. While heating, the tank was flushed with boil-off nitrogen to create a clean environment and expel radon.

The settings for the moulding process were based on the manufacturer recommendation but were adjusted empirically to achieve high-transparency

<sup>4</sup>ARBURG GmbH, Lossburg, Germany



FIGURE 7.2: **Left:** Injection compression moulding machine used for the LEGEND-200 PEN production series. The class-1000 clean room tent contained all open parts of the machine. **Right:** CNC milling setup in the clean room tent. Picture taken while finished PEN disc was removed.

PEN-structures. A description of the used parameters for the moulding machine can be found in [83]. With these settings, discs with a diameter of up to 35 cm and a thickness of 1.5 mm were produced. After 40 s of cooling time, the finished discs could be removed easily by hand from the moulding plate due to the mirror-like surface of the mould. At the beginning of the production cycle (first 10 – 20 discs), optical defects like local crystallisation and air inclusion occurred in almost every disc. This was accounted to the warm-up phase of the machine, during which there may still be air in the spindle. Discs with severe optical defects were only used for impurity measurements.

The produced PEN discs still had a sprue<sup>5</sup> from the injection process. Touching only the sprue with gloves, the plate was moved to and locked into a CNC (Computerised Numerical Control) milling machine also located in the clean room. This setup can be seen in Figure 7.2 (right). The chamber of this machine was illuminated with UV light to reduce the static charge of the flakes produced during the milling. The support surface of the CNC machine was made of PET (Polyethylene Terephthalate) which was cleaned as described in Section 7.1.1. To reduce the contact points, the plate was held down using a vacuum pump. Here, the sprue was removed and the shape was adjusted in order to match the chambers of the radiopurity screening setups.

The finished PEN discs were individually sealed in class 100 plastic bags and collected in large plastic boxes. These boxes were sealed for storage and transportation with a radon-impermeable film. When stored for more than a week, these boxes were constantly flushed with nitrogen gas.

<sup>5</sup>The sprue refers to the hardened PEN portion that still protruded into the nozzle.

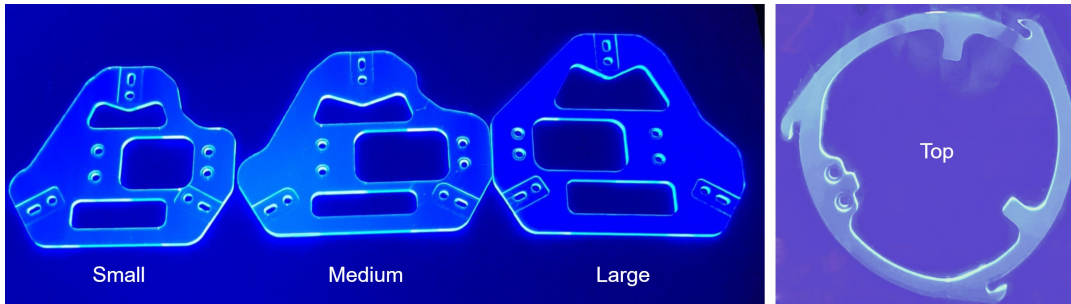


FIGURE 7.3: Final LEGEND-200 PEN holders illuminated with UV light. The four different types are labelled, respectively. The picture on the right was taken by L. Manzanillas with the holder inside a plastic bag.

### 7.1.3 LEGEND-200 Germanium Detector Holder Designs

In LEGEND-200, the formerly used HPGe detectors of GERDA and MAJORANA DEMONSTRATOR in addition to newly produced detectors will be deployed. This gives a wide variety of detector geometries which all have to fit in the detector string (see Section 3.4). It was found, that all detector types could be accommodated with three different sizes of detector holders and one additional top holder for ICPC detectors. The three base holder types are shown in Figure 7.3 (left) and will be referred to as *small*, *medium* and *large holder*, respectively. In the remainder of this work, only the three base holders types will be dealt with.

The shape of the LEGEND-200 PEN holders was based on the previously used Si holders and optimised<sup>6</sup>. In this optimisation process, the goal was to reduce the mass of the holders by removing parts while keeping its mechanical stability. The result of a finite element stress simulation of the detector string combined with a topological optimisation using the software *Abaqus 2017* revealed the areas in the design that have minimal stress values and thus could be removed. The mass of the three holder types could be reduced by 28% on average resulting in 5.3 g, 6.3 g and 7.1 g corresponding to the small, medium and large holder, respectively.

### 7.1.4 Machining of LEGEND-200 Detector Holders

The final machining was organised and carried out at TU Dresden (Germany)<sup>7</sup> and is summarised here for completeness.

A CNC milling machine was used, which was set up in a laminar flow box. All surfaces of the machine were cleaned using 2-propanol. In addition,

<sup>6</sup>By R. Rouhana, LKT of TU Dortmund, Germany

<sup>7</sup>By L. Manzanillas and a technician

the operators wore clean room clothing and no other machine was running. The latter to avoid polluting the air with dust and flakes. To guarantee a minimum risk of introducing radio impurities during the milling process, cleaned diamond milling cutters<sup>8</sup> were used. Due to the hardness of these MKD/mono-crystalline tools, no residues could be rubbed off on the holders.

The support plate of the CNC machine was made of poly-carbonate (new and cleaned). For holding the disc in place, double-sided tape was used on parts that would be cut away and hence not ending up in the final holder. Boil-off nitrogen gas was used to blow away dust and flakes produced by milling. 8 small, 4 medium or 4 large holders could be produced per moulded PEN disc. The burr was removed using another cleaned piece of PEN to avoid contamination.

### 7.1.5 Measurement of Radiopurity

The radio impurity of one PEN detector holder is limited to a maximum of  $1\mu\text{Bq}$  [70]. Three independent radiopurity measurements were carried out on the cleaned and processed PEN material: HPGe screening, *inductively coupled plasma mass spectrometry* (ICP-MS) and radon emanation measurements. How these measurements were performed is described in [83].

The results of the HPGe screening are shown in Table 7.1. Measurements were carried out at LNGS with the GeMPI3 and GeMPI4 screening stations [90] and at the *Modane underground laboratory* (LSM, France) with the OBELIX screening station [91]. In the earlier measurements of the raw and uncleaned PEN granulate, a high level of  $^{40}\text{K}$  contamination was found. By cleaning it, this contamination was drastically reduced in the final product. This confirms the assumption that this was due to a surface contamination. Furthermore, it was shown that the radiopurity for the average LEGEND-200 PEN holder mass of 6.2 g is  $(1.2 \pm 0.2) \mu\text{Bq}$ .

At the *Pacific Northwest National Laboratory* (PNNL), the  $^{232}\text{Th}$  and  $^{238}\text{U}$  radio impurities of the PEN discs were measured using the ICP-MS method. The results were  $(0.0045 \pm 0.0015)$  ppt and  $(0.007 \pm 0.002)$  ppt for  $^{232}\text{Th}$  and  $^{238}\text{U}$ , respectively. With the activity of the isotopes related to mass<sup>9</sup> of 4.1 kBq/g ( $^{232}\text{Th}$ ) and 12.4 kBq/g ( $^{238}\text{U}$ ), the impurities for the average PEN holder

<sup>8</sup>Made for high-gloss mirror finish from *Karnasch professional tools*. Cleaned according to the cleaning procedure used for PEN structures described in Section 7.1.1.

<sup>9</sup>Calculated using  $T_{1/2} = 1.4 \cdot 10^{10}$  yr and  $T_{1/2} = 4.5 \cdot 10^9$  yr for  $^{232}\text{Th}$  and  $^{238}\text{U}$ , respectively. [65]

	Raw TN-8065S GeMPI4	Discs GeMPI4	Discs OBELIX	L200 holders GeMPI3
Mass	-	14.315 kg	5.231 kg	1.07 kg
Time	-	68 days	79 days	68 days
Unit	mBq/kg	$\mu\text{Bq/kg}$	$\mu\text{Bq/kg}$	$\mu\text{Bq/kg}$
$^{228}\text{Ra}$	< 0.15	$92 \pm 25$	$107 \pm 38$	< 460
$^{228}\text{Th}$	$0.23 \pm 0.05$	$32 \pm 16$	$67 \pm 18$	< 480
$^{226}\text{Ra}$	$0.25 \pm 0.05$	$60 \pm 15$	$76 \pm 22$	< 360
$^{234}\text{Th}$	< 11	< 1900	-	< 5800
$^{234}\text{Pa}$	< 3.4	< 1700	-	< 7000
$^{235}\text{U}$	< 0.066	< 56	-	< 2200
$^{40}\text{K}$	$1600 \pm 400$	< 240	< 567	< 4100
$^{137}\text{Cs}$	< 0.057	< 0.15	-	< 91

TABLE 7.1: Radiopurity results from HPGe screening for moulded PEN discs and LEGEND-200 (L200) germanium detector holders. Two sets of moulded PEN discs were measured at LNGS (GeMPI3/4) and LSM (OBELIX) underground laboratories. A previous measurement of untreated PEN granulate [10] is listed, too. With the OBELIX setup, not all listed radionuclides were analysed. Limits are given with 90% confidence level. Results published in [83].

mass results in  $(0.11 \pm 0.04)$  nBq/holder and  $(0.54 \pm 0.15)$  nBq/holder, respectively. These results combined with the HPGe screening confirm an excellent radiopurity of the produced LEGEND-200 samples. Furthermore, the results from the ICP-MS measurement suggest that the remaining surface impurities can be removed by acid etching with  $\text{HNO}_3$  [83]. Thus, the impurity per PEN holder determined by HPGe screening can be understood as an upper limit.

Finally, a radon emanation measurement was carried out at the Institute of Physics of the *Jagiellonian University* in Krakow. However, due to the low sample mass of five LEGEND-200 holders, only limits could be set. The limits obtained here were  $< 12 \mu\text{Bq}$  and  $< 16 \mu\text{Bq}$  per holder for  $^{222}\text{Rn}$  and  $^{220}\text{Rn}$ , respectively.

## 7.2 PEN Integration Tests

With the measurements of mechanical strength [10] and radiopurity (see Section 7.1.5), two of the three requirements for PEN as structural material in LEGEND-200 have already been met. In order to fulfil the third requirement from Section 6.2, it must be proven that PEN as a material does not lead to

an increase in leakage current in the HPGe detectors (see Section 6.2.3). In addition, the mounting process and the stability of the holders under close to final operation conditions had to be tested. In the following, two integration tests are described and the results presented.

### 7.2.1 Baseline Measurement at TUM

The first proof of concept test was conducted in the beginning of 2020 at the physics department of the *Technische Universität München* (TUM)<sup>10</sup>. The GERDA-like setup is located in an underground laboratory which provides a soil overburden of 10 m water equivalent and houses several low-background and cryogenic test stands of the technical university. This setup is used to test new structures and electronics before they are implemented in LEGEND. It is located in a clean tent and has a 600 l LAr cryostat with a GERDA-like lock system. The LAr is actively cooled using liquid nitrogen which is refilled once a week. The LAr level inside the cryostat is about 1.5 m which allows to submerge test structures of up to 1 m in height. More information on the experimental hall and setup can be found in [48].

The setup of the first integration test can be seen in Figure 7.4. Here, a GERDA-like detector string with aluminium rods was used with two germanium detectors mounted on PEN

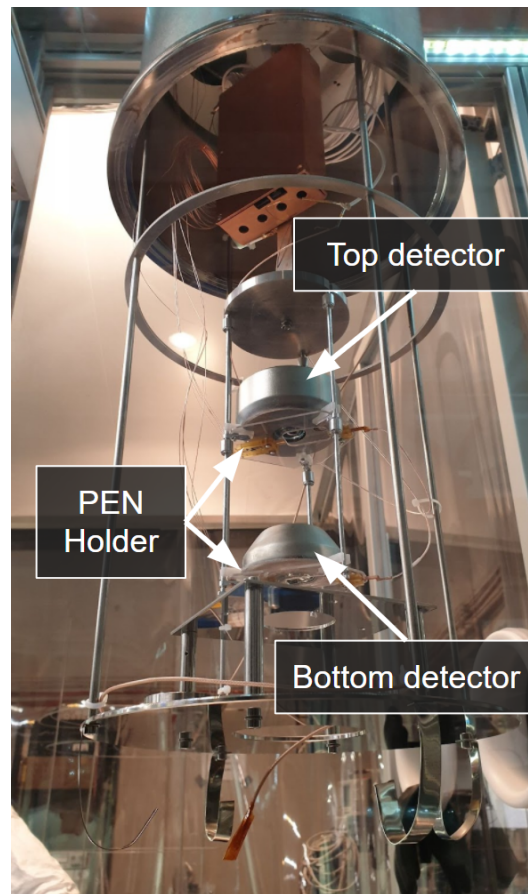


FIGURE 7.4: Experimental setup in the underground laboratory of TUM. Two germanium detectors are mounted on an early version of the PEN holder in a GERDA-like detector string.

holders made of LEGEND-200 material. The used design for the holders corresponds to the original Si holder design. No problems arose during the wire-bonding process, after the machine parameters were adapted to account for the higher flexibility of PEN with respect to Si. The two germanium detectors

<sup>10</sup>In close cooperation with the E15 chair.

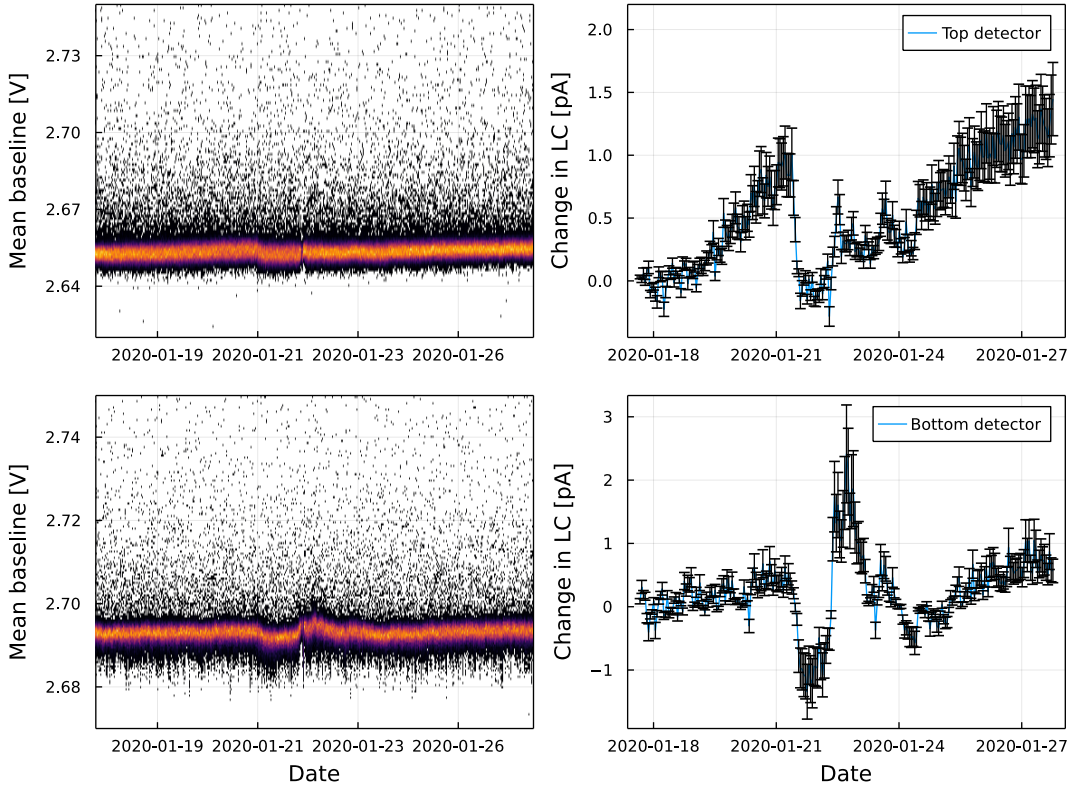


FIGURE 7.5: Results of the baseline measurement taken in the GERDA-like infrastructure at TUM using two germanium detectors mounted on PEN holders. The plots correspond to the top and bottom detector of the detector string, respectively. **Left:** Mean baseline over time. **Right:** Change in the leakage current (LC) over time. The given uncertainties correspond to one standard deviation for an 1 h interval.

used for this measurement are referred to as the top and bottom detector as labelled on the photograph. The setup shown was vacuum sealed in the lock tube that can be seen on the top of the picture. The lock volume was pumped and the structure was then slowly submerged into the LAr.

During the measurement, a pulse-form generator was used to test the read-out electronics. The detector baselines were monitored over 10 days by recording their mean values every 2 s. The mean values of the baselines over time can be seen in Figure 7.5 (left) for both detectors. The liquid nitrogen tank was refilled on the 22<sup>nd</sup> of January during the measurement. Baseline fluctuations can be seen in both detectors around that day. In general, both baselines increased slightly during this period<sup>11</sup>. The corresponding change in the leakage current can be seen in Figure 7.5 (right) for 1 h intervals. The given uncertainties correspond to  $\pm 1$  standard deviation of the mean baselines in the 1 h interval. A maximum variation of approximately 1.25 pA was

<sup>11</sup>Feedback resistance for top and bottom detectors were  $(1.6 \pm 0.32) \text{ G}\Omega$  and  $(1.0 \pm 0.2) \text{ G}\Omega$ , respectively.

determined. This change is attributed to a small but gradual increase in temperature of the detector string.

### 7.2.2 First Data Taking During PGT-Phase of LEGEND-200

During the *post-GERDA test* (PGT) phase of LEGEND-200 in 2020, PEN holders were tested for the first time in the GERDA environment. Four detector strings with a total of 17 HPGe detectors were deployed in the PGTs. The arrangement of the deployed detector strings can be seen in Figure 7.6. These include four PPC, five BEGe and eight ICPC germanium detectors from GERDA, MAJORANA and LEGEND. Seven of the deployed detectors were mounted on PEN holders while Si was used for the other ten. By this, a direct comparison of HPGe detectors mounted on PEN and Si detector holders could be made. Here, the colour of the sketched holding plate is indicating if PEN (red) or Si (grey) was used. Pictures of the PGT detector strings can be seen in Figure 7.7. The bottom view of two HPGe detectors mounted with the low-mass front-end (LMFE) electronics can be seen on the left where the

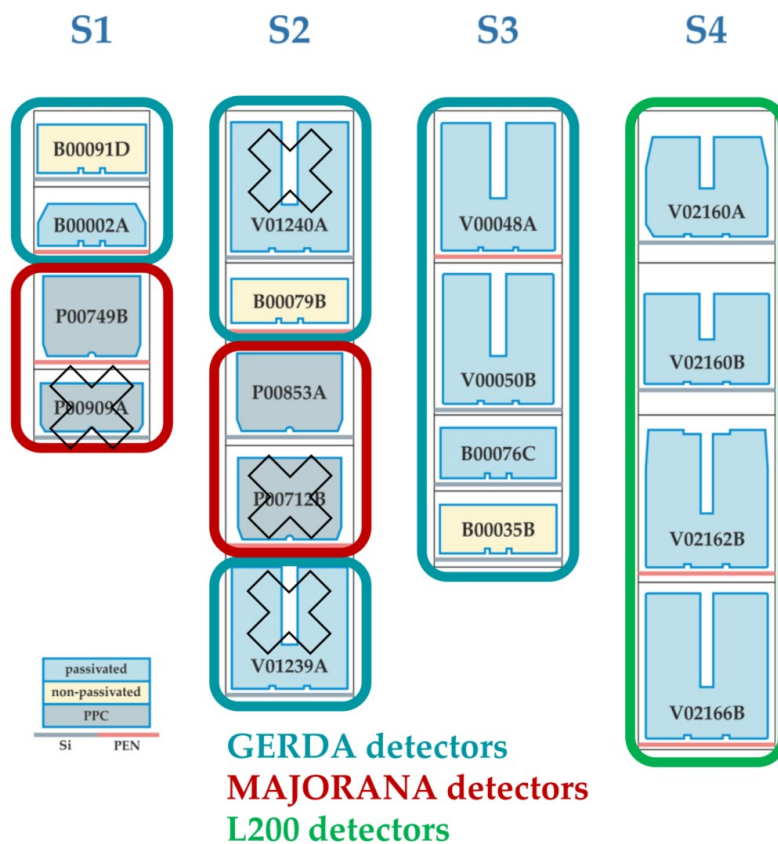


FIGURE 7.6: Arrangement of the four detector strings during PGT-phase of LEGEND. Not connected and not working detectors are marked by a cross. Sketch created by K. Gusev.

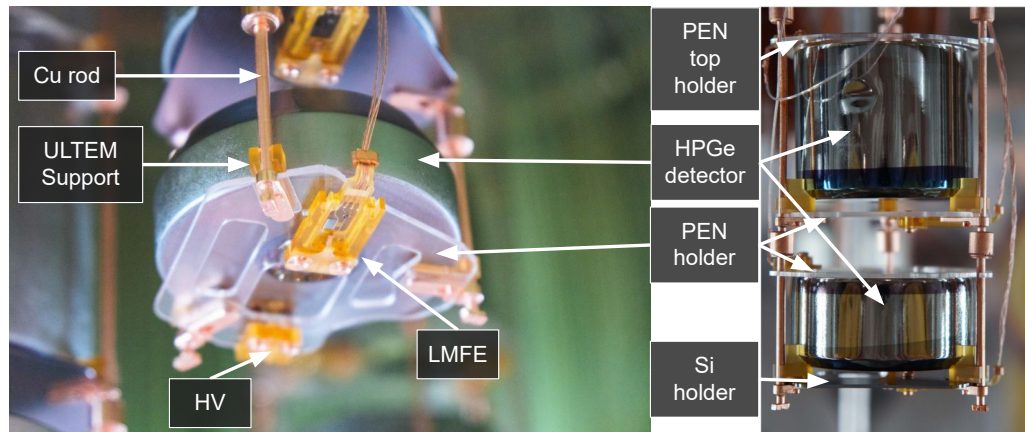


FIGURE 7.7: **Left:** Bottom view of an HPGe detector mounted on a PEN holder during the PGT. **Right:** Side view of a germanium detector string in the GERDA environment. Here, two detectors are mounted using additional PEN top holders. Pictures adapted from [10].

lower one is mounted on a PEN holder. Again, no problems occurred during the wire-bonding process of detectors with PEN holders. A lateral view of a string using also additional top holders made of PEN can be seen on the right of Figure 7.7. The detectors were not directly placed on the PEN/Si holders, but on small ULTEM<sup>®</sup> [92] supports.

The longest continuous measurement during the PGT was from July to August 2020. Over 600 h of data were recorded and an additional calibration measurement of 17 h was carried out. Information on the energy resolution of the HPGe detectors were taken from the calibration data. Three strings with <sup>228</sup>Th sources were used for the calibration. Two of the strings were each equipped with a  $\approx 18$  kBq source. The third string with three  $\approx 4$  kBq <sup>228</sup>Th sources<sup>12</sup>. The calibration <sup>228</sup>Th spectrum of an ICPC germanium detector mounted on a PEN holder can be seen in Figure 7.8.

The targeted average energy resolution at  $Q_{\beta\beta}$  for LEGEND-200 is 2.5 keV (FWHM). The energy resolution at 2039 keV is obtained by interpolation of the FWHM of the gamma lines in the <sup>228</sup>Th spectrum used for calibration. Nine detectors performed particularly well during the PGT with an excellent average energy resolution at  $Q_{\beta\beta}$  of  $\approx 2.2$  keV [7, 93]. Five of the seven detectors mounted on PEN holders are among the nine well-performing detectors. The energy resolution at  $Q_{\beta\beta}$  and at the 2.6 MeV peak of <sup>228</sup>Th for all nine well-performing HPGe detectors are listed in Table 7.2. The holder material and the type of detector are also listed.

For the investigation of possible influences of the holder material on the

<sup>12</sup>Private communication with F. Edzards.

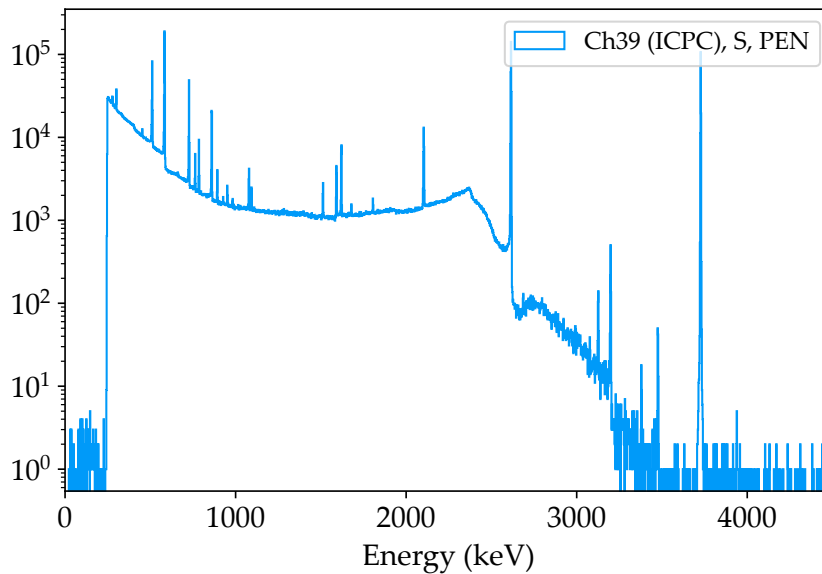


FIGURE 7.8:  $^{228}\text{Th}$  calibration spectrum of an ICPC germanium detector mounted on a PEN holder during PGT. Plot taken from [93].

energy resolution and the leakage current, the detectors V02160A (Si holder) and V02162B (PEN holder) were chosen. The achieved resolution in FWHM of the characteristic  $^{208}\text{Tl}$  line at 2614.5 keV was 2.43 keV and 2.61 keV for the detector mounted on Si and PEN, respectively. The energy resolution at  $Q_{\beta\beta}$  yields 2.17 keV and 2.33 keV, respectively. These deviations are in line with expectations and are not contributed to the type of holder used. [7, 93]

In the long data run, the waveforms of all detectors were recorded when one detector was triggered. Here, a total duration of  $54.464\ \mu\text{s}$  around the rising edge of the trigger signal was recorded with a 62.5 MHz sampling rate [93]. The mean value of the baseline was formed by the average of the first 1000 samples ( $16\ \mu\text{s}$ ) of the waveform in order to monitor changes in the leakage current. This can be seen for the nine well-performing detectors in Figure 7.9 for the whole time span of the measurement. Here, the waveforms of the long measurement have been used<sup>13</sup>. The detectors B00091D (Si holder) and B00002A (PEN holder) were mounted on the same detector string (S1) and show a decrease in the mean baseline corresponding to a decrease in the leakage current or change in gain. For V00048A (PEN holder) and V00050B (Si holder) a correlated discontinuity can be seen at about 280 h. These detectors are also mounted on the same detector string (S3). B00079B and V02166B

<sup>13</sup>The raw data was converted from ADC units to Volt by using the 16-bit resolution of the readout and the dynamic voltage range of 1 V. The readout settings were obtained from private communication with F. Edzards and T. Kihm.

Detector	Type	Holder material	Channel	$\Delta E$ [keV]	
				$Q_{\beta\beta}$	2.6 MeV
B00091D	BEGe	Si	24	2.17	2.43
B00002A	BEGe	PEN	25	2.08	2.36
B00079B	BEGe	PEN	28	2.21	2.50
V00048A	ICPC	PEN	32	2.16	2.46
V00050B	ICPC	Si	33	2.31	2.52
V02160A	ICPC	Si	37	2.17	2.43
V02160B	ICPC	Si	38	2.21	2.45
V02162B	ICPC	PEN	39	2.33	2.61
V02166B	ICPC	PEN	40	2.20	2.50

TABLE 7.2: Energy resolution  $\Delta E$  (FWHM) at  $Q_{\beta\beta}$  of  $^{76}\text{Ge}$  and at the 2.6 MeV peak of the  $^{228}\text{Th}$  calibration spectrum for nine well-performing HPGe detectors during PGT. Results taken from [93].

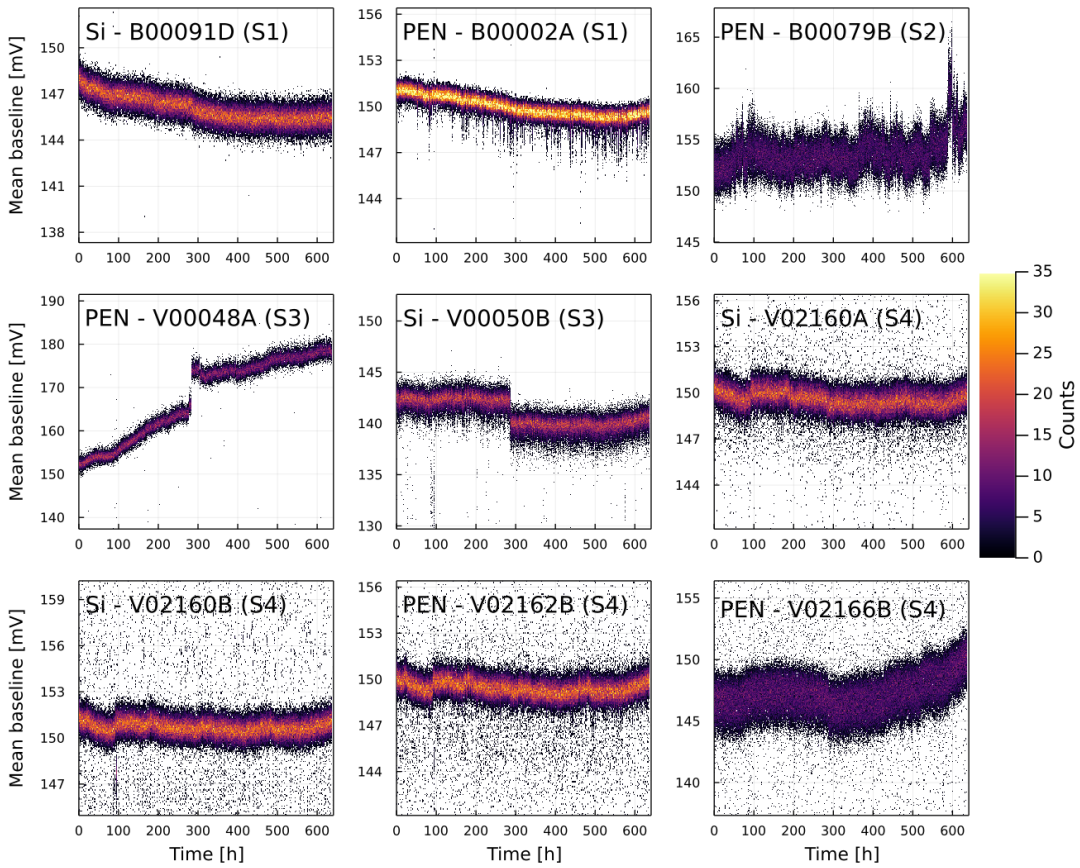


FIGURE 7.9: Mean baseline values over time recorded during the PGT for nine detectors. The names and detector strings of the individual detectors and the holder material (PEN/Si) are written on the plots.

are both mounted on PEN holders but on different strings. These two detectors show an increase in the mean baseline towards the end of the measurement time. The remaining three detectors are all mounted on string S4 and show a very similar behaviour over time. This shows that changes in the

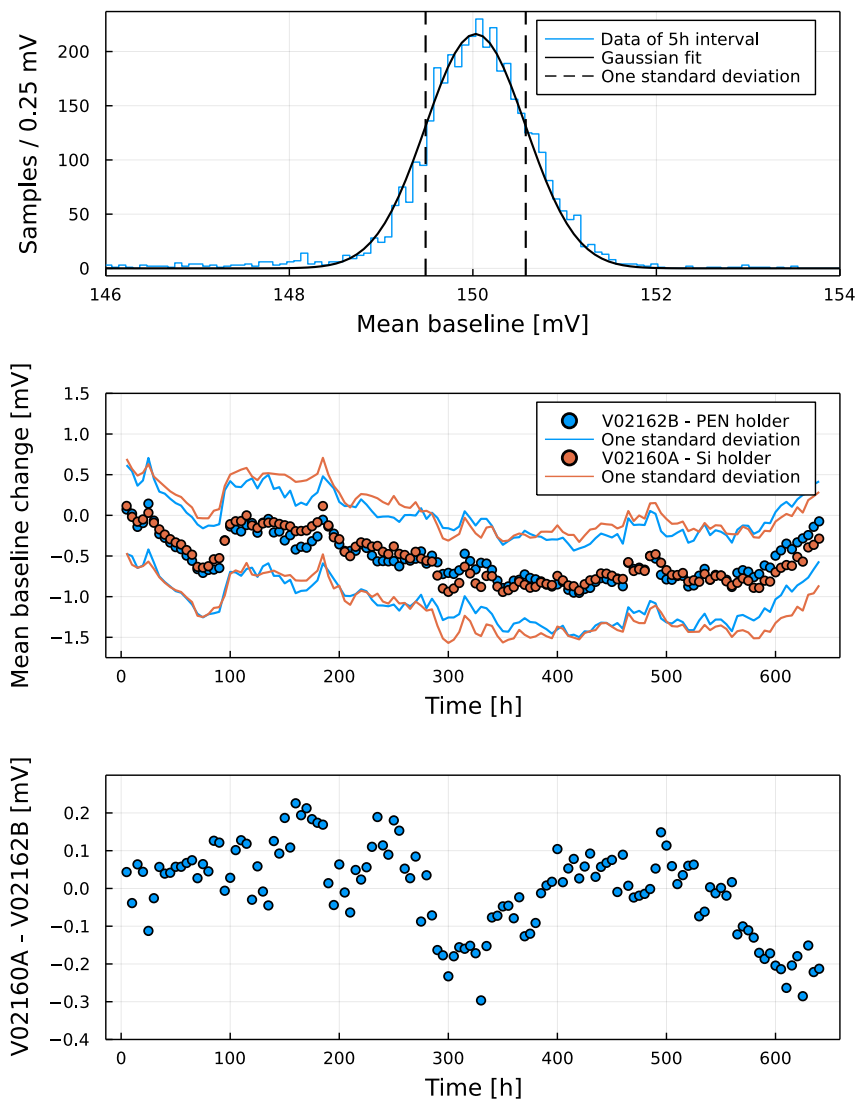


FIGURE 7.10: **Top:** Distribution of the mean baseline values of V02166B in a 5 h interval. The Gaussian fit is drawn in black with  $\pm 1$  standard deviation marked by dashed black lines. **Middle:** Mean baseline over time in 5h intervals for V02162B (PEN holder, blue) and V02160A (Si holder, orange). One standard deviation is marked by lines in the corresponding colour. The mean value of the first 25 h was subtracted as offset. **Bottom:** Residuals of the mean baselines over time for V02162B and V02160A.

leakage current are mostly related to the environment and not the individual holder type.

To compare the change in the leakage current during the measurement time, V02160A (Si holder) and V02162B (PEN holder) were chosen. For this, the mean baselines were determined in 5 h intervals by forming histograms and fitting the distribution. An example distribution of mean baselines for

one 5 h interval of V02162B can be seen in Figure 7.10 (top). The mean baselines are Gaussian distributed and the fit is drawn in black with  $\pm 1$  standard deviation around the peak position marked by dashed lines. The change of the peak position over time is shown in Figure 7.10 (middle) for both detectors. The mean value of the baselines in the first 25 h was subtracted as offset for each detector individually. The lines are indicating  $\pm 1$  standard deviation with the colour corresponding to the detector. The difference between the mean baselines of both detectors is for all time intervals in this measurement less than one standard deviation. The residuals of the mean baseline values of the 5 h intervals of the two detectors can be seen in Figure 7.10 (bottom). All residuals are  $< 0.3$  mV and no trend can be identified that indicates a different behaviour for the detector mounted on PEN.

From the change in the mean baseline over time the change in the leakage current can be estimated. For this, the resistance of the feedback resistor used in the LMFES can be used. It consists of a sputtered thin film of amorphous germanium (aGe). The resistance of the aGe resistors is temperature dependent and was taken as  $\approx 1$  G $\Omega$  at LAr temperature ( $\approx 87$  K) [93]. An increase of the mean baseline of 1 mV relates to an increase of the leakage current of  $\approx 1$  pA. During the measurement, the mean values of the baselines of the detectors V02160A and V02162B have not increased, indicating no increase in the leakage current. B00091D (Si holder) and B00002A (PEN holder) show a decrease of the mean baseline of about 2.2 mV ( $\hat{=}$  2.2 pA) and 1.5 mV ( $\hat{=}$  1.5 pA), respectively. For B00079B and V02166B an increase of 3.8 mV ( $\hat{=}$  3.8 pA) and 3.2 mV ( $\hat{=}$  3.2 pA) was observed, respectively.

In summary, the behaviour of the mean baselines in Figure 7.9 for the nine well-performing HPGe detectors during the PGT shows, that no evidence for an influence of PEN as holder material on the leakage current on the order of pA could be observed, qualifying the holders for long term usage in the vicinity of HPGe detectors.

### 7.3 Setups for Optical Characterisation

For the reproducible determination of the most important optical properties of PEN scintillators, three experimental setups were designed and built at the Max Planck Institute for Physics in Munich. The spectrometer setup was used to determine the emission spectrum and, thus, the peak emission wavelength  $\lambda_{\text{peak}}$ . In the second setup, a digital microscope was used to quantify the surface quality by determining  $\sigma_{\text{h}}$  and  $\sigma_{\alpha}$ . The last setup is based

on single-photon counting using PMTs and was used to determine the light yield, attenuation length  $\lambda_{\text{att.}}$ , detection efficiency of photons and detection energy threshold.

### 7.3.1 Spectrometer Setup

The emission spectrum and the associated peak emission wavelength  $\lambda_{\text{peak}}$  is the key in determining the subsequent parameters. It is also necessary for the choice of light sensor. With the spectrometer setup at the Max Planck Institute for Physics, the emission spectrum can be recorded for PEN and other scintillators. Details of the setup are described elsewhere [10, 94]. For the work described in this thesis, the setup has received a new dark box and excitation source. As all key properties have remained the same, only the most important ones are summarised here.

The heart of the spectrometer setup is the *Shamrock-SR-303I-A* spectrometer [95] with an attached *iDus DV420A* CCD (charge-coupled device) camera [96]. This spectrometer has 1024 channels with a 0.14 nm wavelength resolution and has an in-built cooling system for the sensor to ensure temperature stability. In contrast to previously performed measurements with this setup, here a UV light emitting diode (LED) from Thorlabs (LED341W) with an emission wavelength of  $(340 \pm 10)$  nm was used as excitation source. The LED was mounted on a rail to have the possibility to control the distance between the excitation point and the sensor of the spectrometer. By coupling a light collimator to the LED, a millimetre resolution in the distance was achieved.

In the previous configuration, the spectrometer, excitation source and sample were together in the dark box. Due to the heat generated by the spectrometer, failures and instabilities occurred in rare cases. Therefore, a new and smaller dark box was built with a light-tight coupling to the sensor of the spectrometer. This allowed sufficient cooling of the spectrometer, hence a better temperature stability.

### 7.3.2 Surface Characterisation Setup

To obtain  $\sigma_{\text{h}}$  and  $\sigma_{\alpha}$  for the produced LEGEND-200 PEN samples, a Keyence *VHX-6000* digital microscope [97] was used<sup>14</sup>. Although the PEN samples are transparent, the surface can be focused with this microscope using a

---

<sup>14</sup>In cooperation with Miriam Modjesch from the electronics department of the Max Planck Institute for Physics, Munich, Germany

built-in light focus. The result is an opaque image that is not affected by the background or bulk material. A lens with  $500\times$  magnification was chosen for detailed shots and 3D scans. At an even higher magnification, no more structures could be recognised on the surface.

### 3D Surface Scan

For a small surface area of up to  $\approx 15 \text{ mm}^2$ , a 3D height map can be created using the VHX-6000. The 3D height map was exported by storing it as heat map to an uncompressed image file (format .tif). The individual pixels then contain the height information in their colour while the scale is provided separately. Minimum and maximum correspond to the colours black and white, respectively. Using the programming language Julia [57], this image file can be imported and converted into actual height values. Thus, a complete 3D height map can be created and analysed. However, there is a problem with the actual resolution in  $x$  and  $y$  here. The image file is exported uncompressed, but not with full resolution. Thus, the resolution is dependent on the size of the scanned area. The quoted resolution of the microscope in  $x$  and  $y$  direction is  $0.44 \mu\text{m}$ , while it is  $0.01 \mu\text{m}$  in  $z$ , which can be related to a surface area of up to  $\approx 0.3 \text{ mm}^2$ . For larger areas, the number of pixels remains the same, which reduces the resolution linearly with area scanned. For the smallest surface area, the uncertainty on the resolution is  $0.005 \mu\text{m}$  which corresponds to half of the last digit provided by the microscope and is half the resolution quoted in the manual of the microscope. Unfortunately, even upon request, no further information concerning uncertainties of the resolution was provided by the manufacturer. An example height map obtained

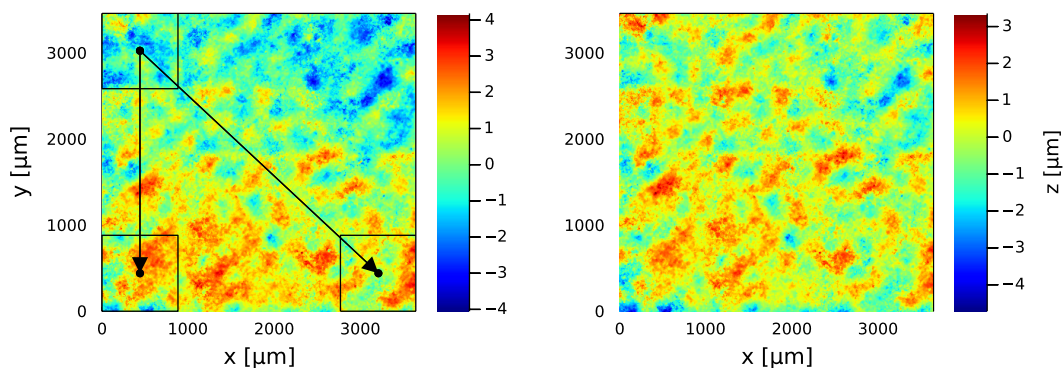


FIGURE 7.11: **Left:** Example height map obtained from the surface of a PEN holder. The image was taken using a VHX-6000 microscope with the maximum size for a 3D scan. **Right:** Same measurement as shown on the left after correcting for the uneven ground.

from one of the PEN holders with  $\approx 13 \text{ mm}^2$  and a resolution in  $x$  and  $y$  of  $\approx 2 \mu\text{m}$  can be seen in Figure 7.11 (left). The area shown was recorded with maximum size.

In order to correct for the uneven ground, three points were defined near the corners of the scanned area. These are shown in black in Figure 7.11 (left). Their  $x$  and  $y$  values correspond to the respective centres of the squares drawn in. Their  $z$  values correspond to the mean value of the  $z$  values of the data points in the respective squares. With the two drawn vectors created from the three points, a plane was calculated which was used for the height correction due to the tilt. The slope-corrected version of the example height map is shown in Figure 7.11 (right). The corrected slope usually corresponds to a maximum of  $0.5 \mu\text{m}$  per  $1 \text{ mm}$ .

### 7.3.3 PMT setup

For the determination of the optical properties of the PEN samples produced for LEGEND-200, another setup was constructed<sup>15</sup>.

The setup is based on PMTs and can be used to investigate different shapes of scintillator samples. For this purpose, a 3D printed support structure was designed for each sample shape with an estimated printing accuracy of  $0.1 \text{ mm}$ . Up to 6 PMTs were used for the light detection which were also mounted on the same support structure to guarantee reproducible measurements. Usually, the PMTs were aligned around the sample to detect the scintillation light leaving at the sides. Additionally, one of the PMTs could be placed below the sample.

The used PMTs for this setup are from *HAMAMATSU photonics* (type H11934-300) and were chosen for their large squared sensitive area of  $23 \times 23 \text{ mm}^2$  and their good quantum efficiency of 39% at  $420 \text{ nm}$  which is very close to  $\lambda_{\text{peak}}$  of PEN. The quantum efficiency of the PMTs as function of wavelength can be seen in Figure A.4 in the Appendix. To improve the light collection, the PMTs were coupled to the scintillator sample using optical grease (type EJ-550 [98]). A two-dimensional motorised stage from *STANDA* (type 8MTF-102LS05) was mounted next to the support structure. This stage can be used to move a mounted object like the source  $10 \text{ cm}$  in  $x$  and  $y$  direction above the scintillator sample with a precision of  $2.5 \mu\text{m}$  given by the manufacturer. In addition, an LED with an emission wavelength of  $450 \text{ nm}$

<sup>15</sup>In close cooperation with L. Manzanillas and M. Guitart Corominas. All simulations of this setup were carried out by L. Manzanillas and more technical details will be published soon.

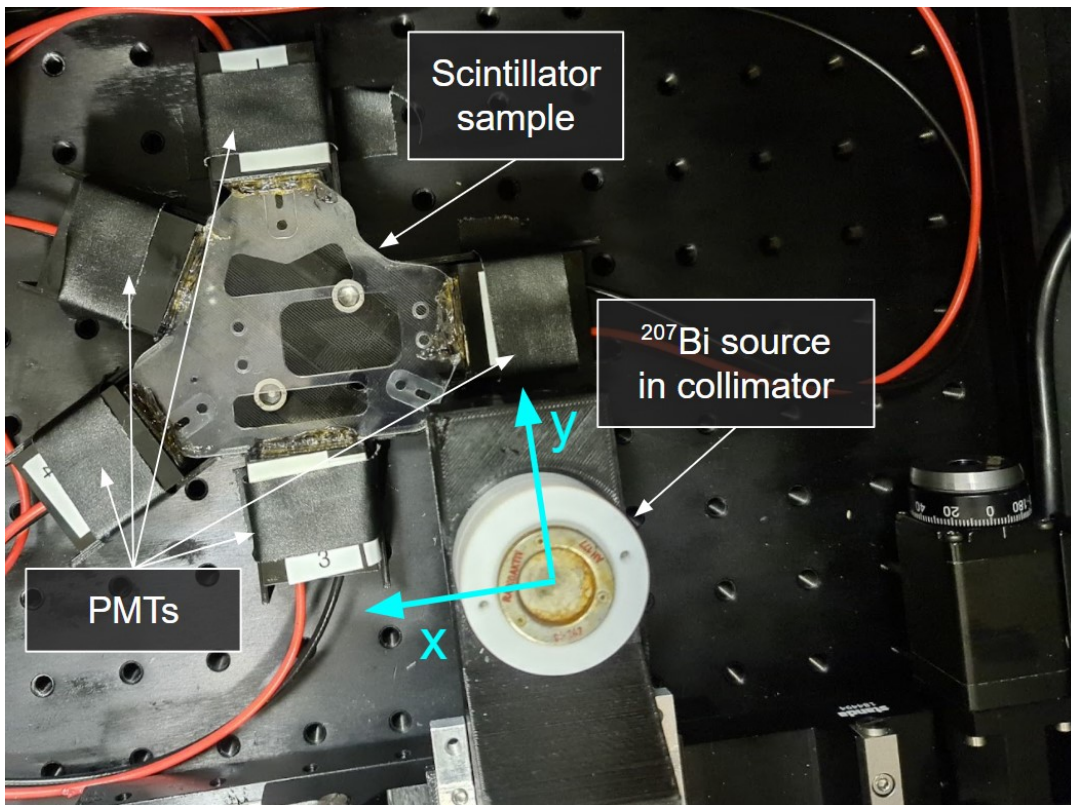


FIGURE 7.12: Photograph of the PMT setup. Five PMTs are coupled with optical grease to the scintillator sample. In this case, a small PEN holder was used. The  $^{207}\text{Bi}$  source in its collimator can be seen on the bottom mounted on the two-dimensional motorised stage with the movable directions indicated by blue arrows.

was attached to a rod above the setup for the calibration of the PMTs. The complete setup was placed in a dark box. The setting for one of the PEN holders can be seen in Figure 7.12 with labels for each component. Here, the source holder is mounted on the motorised stage and the movable directions are indicated by blue arrows.

### Source & Trigger System

The majority of the backgrounds in the LEGEND experiment have energies in the MeV range (see Section 5.4). So in order to match the characterisation of the optical properties of PEN as well as possible,  $^{207}\text{Bi}$  was chosen as source for these measurements due to its conversion electrons with about 1 MeV [65, 99].  $^{207}\text{Bi}$  has a half-life of 32.9 yr and the used source had an activity of  $\approx 170$  kBq. The emitted electrons were collimated using a PTFE collimator with an inner diameter of 2 mm. More information about the decay of  $^{207}\text{Bi}$  can be found in Section A.1.1 in the Appendix.

The source in its collimator was mounted on a 3D printed structure which was connected to the motorised stage. The structure contained the trigger

system which was designed based on [100]<sup>16</sup>. Inside the 3D printed structure, a 90  $\mu\text{m}$  thick EJ-212 plastic scintillator from Eljen Technology [101] was placed directly underneath the collimator. The EJ-212 plastic scintillator provides a fast response to energy deposition with a decay time of 2.5 ns and a reported light yield of  $10000 \pm 200$  photons per MeV energy deposition with a peak emission wavelength at 423 nm. Electrons from the source traversing through this thin scintillator will deposit on average 25 keV according to GEANT4 simulations [80]. The simulated deposited energy in the trigger scintillator can be seen in Figure A.5 in the Appendix. In order to detect the produced photons, the trigger scintillator was coupled to a PMMA light guide which was then coupled to a PMT (type H11934-300). Optical grease (type EJ-550) was used to improve the optical coupling between the PMT, the light guide and the scintillator. To reduce the loss of scintillation light produced in the trigger scintillator to the surrounding, all components of the trigger system were enclosed by the 3D printed holding structure except the beam path. A thin opaque foil was used underneath the scintillator so that its photons would not influence the measurement.

### Beam Spot & Expected Energy Spectrum

The path of the electrons from the  $^{207}\text{Bi}$  source is influenced by the collimator and the interaction with the trigger system. A GEANT4 simulation of the setup was used to determine the resulting beam spot on the scintillator sample. The resulting beam spot can be seen in Figure 7.13 (left). The interactions in the scintillator sample take place within a radius of  $\approx 20$  mm (one standard deviation) which is marked by the white dashed circle. To estimate the effect of this not point-like beam spot on the measurement, the beam spot is folded with the shape of the scintillator sample. The result can be seen in Figure 7.13 (right) for a large PEN holder, with the unaltered shape drawn over it in white.

The size of the beam spot also affects how many of the source's electrons actually hit the scintillator sample. This reduces the number of events in which actually energy is deposited in the scintillator sample in relation to the triggered ones. This is illustrated in Figure 7.14 (left) where the hit distribution is folded with the shape of a large PEN holder. The hit probability for a given position of the source can be calculated by integrating the normalised hit distribution over the shape of the scintillator sample. The hit probability of the  $^{207}\text{Bi}$  conversion electrons as function of position was determined for

---

<sup>16</sup>By L. Manzanillas

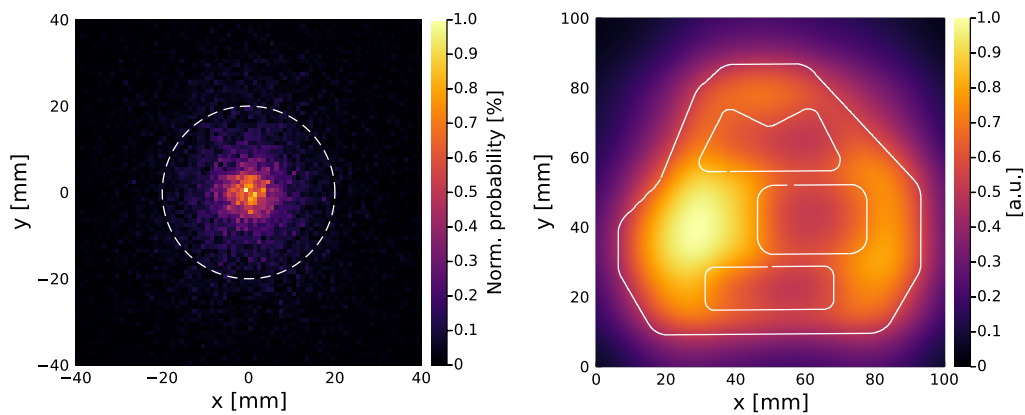


FIGURE 7.13: **Left:** Simulated beam spot of the collimated  $^{207}\text{Bi}$  source on the scintillator sample in the PMT setup. The white circle marks the area where 68% of all interactions take place. **Right:** Effect of the beam spot on the resolution of the PMT setup for a large PEN holder. This was calculated by folding the beam spot with the shape of the holder.

each sample type, which can be seen in Figure 7.14 (right) for the large PEN holder.

In addition to the hit probability of the electrons on the scintillator sample, the quantum efficiency and spatial coverage of the PMTs has to be considered for the overall efficiency of the PMT setup. The peak quantum efficiency of the used PMTs is 39% at 420 nm. For the peak emission wavelength of PEN at  $\approx (440 - 445)$  nm [10], the quantum efficiency reduces to  $\approx 35\%$ <sup>17</sup>. The active areas of the PMTs cover about 48% (46%, 42%) of the outer edges of the large (small, medium) PEN holder. For the large holder this means that only  $\approx 17\%$  of the emitted photons can be measured by the PMTs, without taking attenuation effects into account.

Furthermore, the energy deposition spectrum from the  $^{207}\text{Bi}$  source in the scintillator sample was simulated. Here, the energy loss in the trigger scintillator was taken into account. The spectra for one PEN sample (1.70 mm thickness) and two samples stacked above each other (3.40 mm thickness) can be seen in Figure 7.15 where perfect energy resolution is assumed. For comparison, a measurement of two stacked PEN samples (1.70 mm each) is shown. With the a non-perfect energy resolution, two clear peaks can be seen. These have an average energy of 420 keV and 930 keV corresponding to two of the three major transition energies of  $^{207}\text{Bi}$  (see Section A.1.1). It can be seen, that the amount of 930 keV electrons depositing their full energy

<sup>17</sup>This value was obtained by interpolating the quantum efficiency as function of wavelength given by the manufacturer. See Section A.1.4.

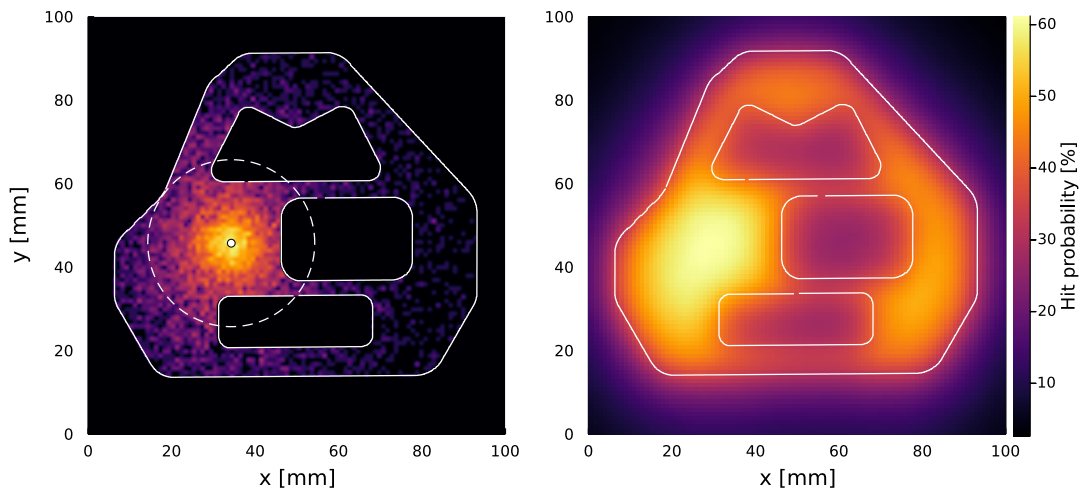


FIGURE 7.14: **Left:** Hit distribution of the beam spot folded with the shape of the large PEN holder type. The outlines of the holder are drawn in white and the colour scale of the distribution is logarithmic and only for illustration. **Right:** Hit probability as function of the position for the large PEN holder type in the PMT setup.

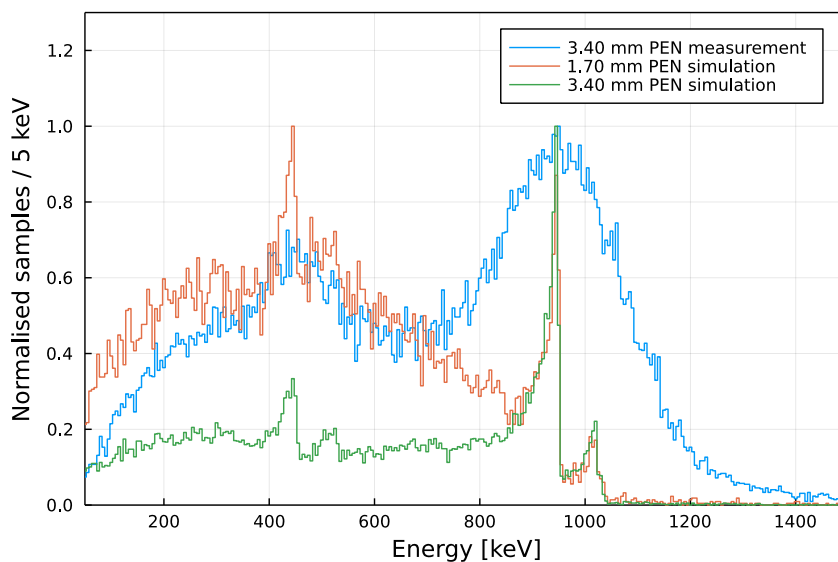


FIGURE 7.15: Energy spectra in the scintillator sample from simulation and data. Here, the  $^{207}\text{Bi}$  source was used. In the simulation, a perfect energy resolution is assumed and the target thickness was corresponding to one (1.70 mm) and two PEN samples (3.40 mm). The data was taken using two stacked 1.70 mm PEN samples.

is lower for only one PEN sample in the setup. This is due to electrons not depositing their full energy in the sample and passing through.

### Data Acquisition

A Struck SIS3316-250-14 digitiser [102] was used to read out the PMT waveforms. This fast analogue to digital converter (ADC) has 16 channels with 250 MHz sampling rate and 14-bit resolution each. The recorded PMT waveforms were set to a length of 128 samples corresponding to a length of the waveform of 512 ns and were stored in ADC units.

The data taking was controlled using a Julia [57] script and could be set to either *calibration* or *physics mode*. When calibration mode was set, a trigger threshold of less than half of the expected 1 PE amplitude was set to each PMT channel while the calibration LED was turned on. Therefore, each PMT channel was triggered individually and the triggered channel waveform was then recorded. The PMT connected to the trigger scintillator was not able to measure the LED light. Here, the scintillation light of the trigger scintillator induced by  $^{207}\text{Bi}$  electrons was used for calibration. These led to signals up to 3 PE. In physics data mode, only the threshold of the trigger system channel was set to the amplitude corresponding to about 1 PE. So if an electron deposited energy in the trigger scintillator and the trigger threshold was exceeded as a result, the waveforms of all PMTs were recorded and stored together as an event. The values for the trigger thresholds were determined in a first calibration study.

Another difference between the two data taking modes was how the motors of the stage were controlled. In calibration mode, the trigger system was moved as far away as possible from all PMTs (usually  $(x, y) = (0, 0)$  mm) so that it would not intercept the light from the calibration LED. In physics mode, a predefined grid was scanned automatically covering the whole surface of the scintillator sample. At each position in this grid, data was recorded for a fixed period of time. This resulted in a file for each measured position.

### Calibration of the PMTs

At the beginning of each measurement, a short calibration of all PMTs including the trigger PMT was carried out to check their stability. For this purpose, the LED above the PMTs was operated using a pulse generator with a frequency of 1 kHz. A square-wave voltage of 2200 mV was applied providing

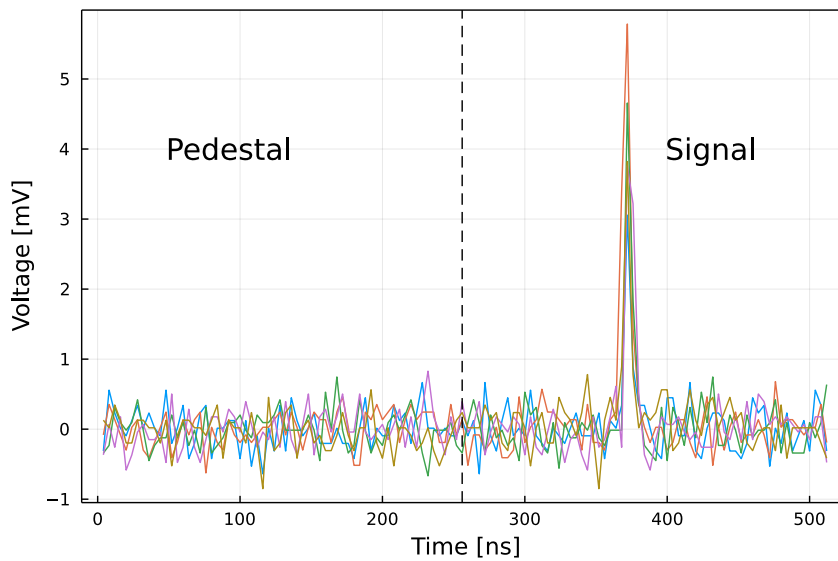


FIGURE 7.16: Example for typical SPE waveforms recorded during PMT calibration. The parts of the waveform that have been integrated for the pedestal and the signal for the SPE distribution are labelled and separated by a dashed black line.

just enough light to see a signal in all PMTs. The recorded waveforms consisted of two parts: the pre-trigger window and the signal. Example SPE waveforms are shown in Figure 7.16. The first part made up 90 of the 128 samples and corresponds to the baseline. Its mean value was subtracted from the whole waveform. By integrating the first half of the waveform (64 samples, 256 ns), the pedestal of the single photo-electron (SPE) distribution was formed. The second part contains the photon signal. By integrating the second half, the charge of the event was determined. These two parts are labelled in Figure 7.16. The resulting integrals are in units of ADC integrated over time which is proportional to the charge.

Due to the low threshold in calibration mode, the complete SPE distribution could be recorded. Out of this, about 90% of the events recorded were dark count events. These could easily be filtered by setting an analysis threshold of about 0.5 PE in amplitude to the signal region of the waveform.

For this fast calibration, the focus was placed only on the SPE peak. It was confirmed in earlier measurements, that this peak really corresponds to the 1 PE peak by measuring also the 2 and 3 PE peaks (see Figure A.2 in the Appendix). In addition, the linearity of the calibration constant up to a few hundred PE was confirmed by comparing a measured energy spectrum of  $^{207}\text{Bi}$  with a simulated one (see Section A.1.3). For events with more than 500 PE a non-linearity is expected which is not relevant for the measurements presented in this work.

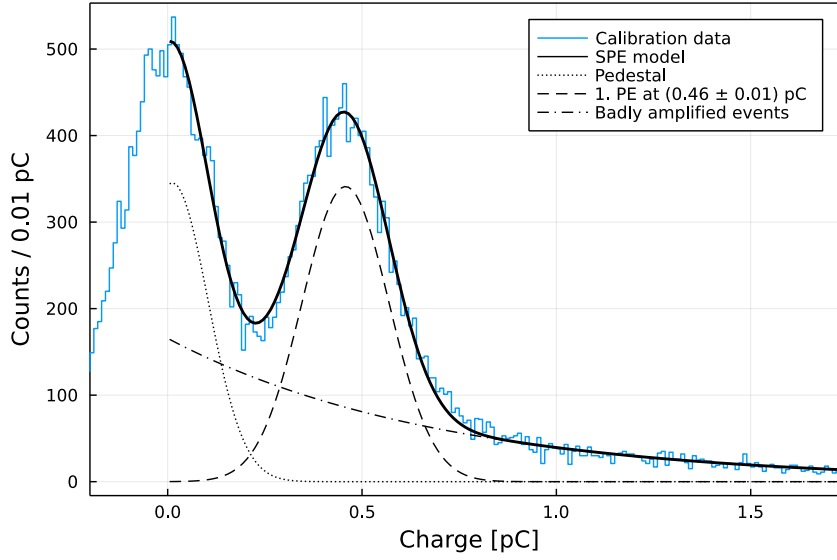


FIGURE 7.17: Example for a typical SPE distribution recorded during calibration of the PMT setup. The parts of the SPE model are drawn separately.

An example calibration SPE distribution is shown in Figure 7.17. The number of 2 PE events recorded during the short measurement time of usually 2 minutes was too low to create a visible peak. The SPE distribution can be described using the model adapted from [103]

$$\begin{aligned}
 f(x) = & \underbrace{\frac{N_{\text{Ped}}}{\sigma_{\text{Ped}} \sqrt{2\pi}} \exp\left(-\frac{(x - \mu_{\text{Ped}})^2}{2\sigma_{\text{Ped}}^2}\right)}_{\text{pedestal}} + \underbrace{\frac{N_{\text{Exp}}}{\tau} \exp\left(-\frac{x}{\tau}\right)}_{\text{badly amplified events}} \\
 & + \underbrace{\frac{N_{1\text{PE}}}{\sigma_{1\text{PE}} \sqrt{2\pi}} \exp\left(-\frac{(x - \mu_{1\text{PE}})^2}{2\sigma_{1\text{PE}}^2}\right)}_{\text{first PE}} \\
 & + \underbrace{\sum_{i=2}^n \frac{N_{i\text{PE}}}{\sigma_{i\text{PE}} \sqrt{2\pi}} \exp\left(-\frac{(x - i(\mu_{1\text{PE}} - \mu_{\text{Ped}}) + \mu_{\text{Ped}})^2}{2\sigma_{i\text{PE}}^2}\right)}_{i\text{th PE}}
 \end{aligned} \tag{7.1}$$

where  $N$ ,  $\sigma$  and  $\mu$  correspond to the number of events, the width and the position of the individual peaks, respectively. In a PMT, electrons released from the photo cathode may follow a non-ideal trajectory which can lead to not reaching the next amplification stage. Events where this happens are referred to as *badly amplified* events and were taken into account by an exponential with the decay constant  $\tau$ . This model applies for  $x \geq 0$  and the peak

position of the  $i$ th PE peak can be calculated by using  $\mu_{1PE}$ . The SPE calibration factor for the signal charge is given by  $g_{SPE,j} = \mu_{1PE,j} - \mu_{PED,j}$  for PMT  $j$ . The uncertainties on  $g_{SPE,j}$  were on average 2% and were taken from the fit. The individual parts of the SPE model are drawn separately in Figure 7.17.

### Data Analysis & Background Filter

An event recorded in physics mode contains the waveforms of all PMTs. Using the calibration constants  $g_{SPE,j}$ , the respective number of PEs was determined. For the total number of detected PEs of the event, the sum of all PEs of the PMTs coupled to the scintillator sample was formed.

In order to identify background events like dark counts and uncorrelated energy depositions in data recorded in physics mode, several filters were applied in the analysis. First of all, an analysis threshold of usually 3 PE on the trigger PMT was set. In addition, a threshold of 0.6 PE was set for each individual PMT. If the collected charge was below that threshold, it was set to zero for this PMT. An overall threshold on the total number of photons collected in all PMTs coupled to the scintillator sample was set to 2 PE. For the PMTs coupled to the scintillator sample, a time-coincidence filter was set with a time window of 120 ns (30 samples) starting at the rising edge of the trigger signal. Charges collected outside of this time window were marked as uncorrelated and discarded from the analysis.

Measurements without a scintillator sample showed, that a maximum of 1.8% of the events could still be background after these filters were applied. These are due to interactions of the electrons with the setup, like scattering on the active area of the PMTs. The survival fraction of events after the background filters for a scan of the whole setup without a sample is shown in Figure 7.18. In this background measurement, 5 PMTs were connected and mounted on a support structure for the small type of LEGEND-200 holders. For measurements with sample, the background contribution surviving the

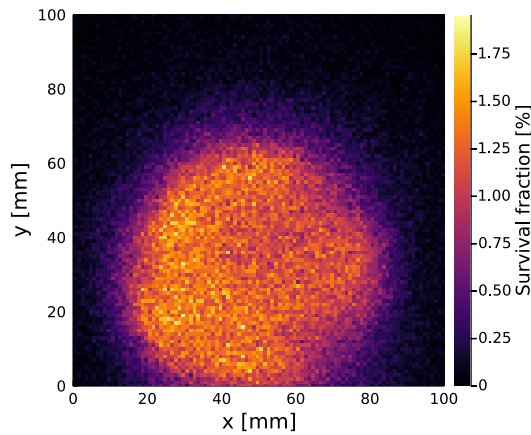


FIGURE 7.18: Dark count measurement of the PMT setup with 5 connected PMTs. The colour is indicating how many of the triggered events survived the background filters.

filters is expected to be significantly lower as less electrons can reach the support structure and also scattered electrons can be absorbed by the sample.

## 7.4 Optical Characterisation of the LEGEND-200 PEN Scintillator

In preparation for the simulations of LEGEND-200, the newly produced LEGEND-200 PEN scintillators were characterised for their optical properties. In the process, all three LEGEND-200 germanium detector holder designs were evaluated using the experimental setups described in Section 7.3. The results presented here are also available in [83] and will be published separately soon.

### 7.4.1 Emission Spectrum

From previous results [10], an attenuation length below 5 cm was already assumed for the scintillation light in PEN. Since this also affects the emission spectrum, it was recorded for different distances of the LED excitation point to the light sensor of the spectrometer. The result<sup>18</sup> can be seen in Figure 7.19 for distances from 3 mm to 25 mm between the excitation point and the CCD camera of the spectrometer. Here, a  $74 \times 20 \times 1.7 \text{ mm}^3$  PEN sample of the LEGEND-200 production run was used. The peak emission wavelength  $\lambda_{\text{peak}}$  was found to be  $(440 \pm 3) \text{ nm}$  for the closest position while the whole spectrum shifts to higher wavelengths with increasing distance. The resulting peak emission wavelength is in accordance with previous production series and an influence of the changed production process can thus be excluded.

The peak emission wavelength as function of the distance to the CCD camera of the spectrometer can be used with the simulation of the path length in the material and the surface quality to derive the attenuation length.

### 7.4.2 Surface Quality

Two areas on a large LEGEND-200 PEN holder were evaluated for the characterisation of the surface. One of them was chosen because it is representative for the surface of this production series. The other has clear defects and is

---

<sup>18</sup>The data presented was taken by L. Manzanillas. The setup and the data taking software was created by the author of this work and C. Hayward.

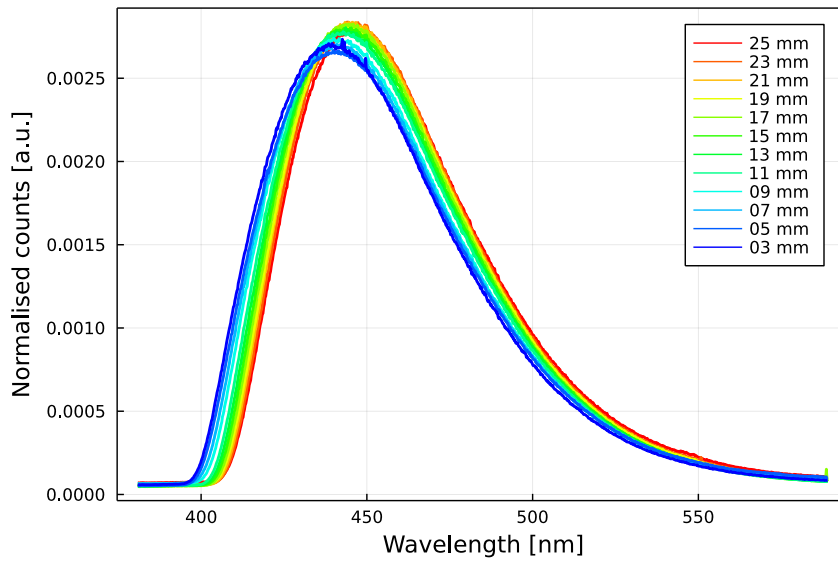


FIGURE 7.19: Emission spectrum of a LEGEND-200 PEN sample for different distances between the excitation point and the CCD camera of the spectrometer.

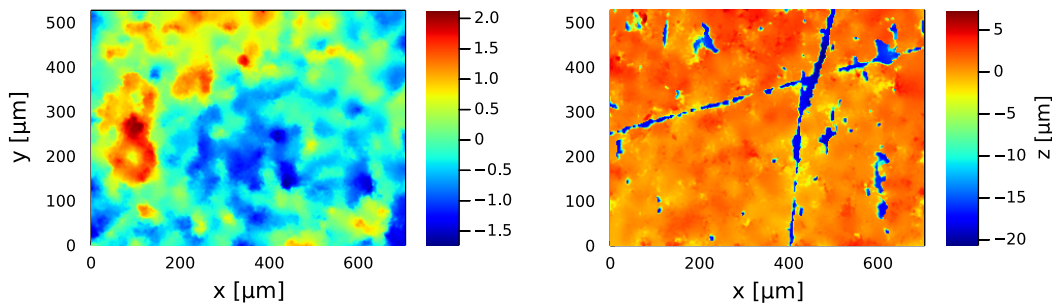


FIGURE 7.20: 3D surface scans of a representative (left) and a worst case (right) area on a large LEGEND-200 PEN holder.

considered the worst case. The 3D scans of the two areas are shown in Figure 7.20. While in the representative scan no unevenness  $> \pm 2 \mu\text{m}$  can be seen, there are two deep scratches in the other sample.

For an even surface without major irregular features, the distribution of the height values follows a Gaussian distribution with standard deviation  $\sigma_h$ . To also obtain the angular distribution, the average angle for each position in the height map was determined. To do this, the eight surrounding bins were determined for each data point in the height map with a bin width of 440 nm corresponding to the resolution in  $x$  and  $y$ . The angles were then calculated from the normal of the average surface to the normal of the vectors from the central point to its surrounding ones. As the unevenness of the average

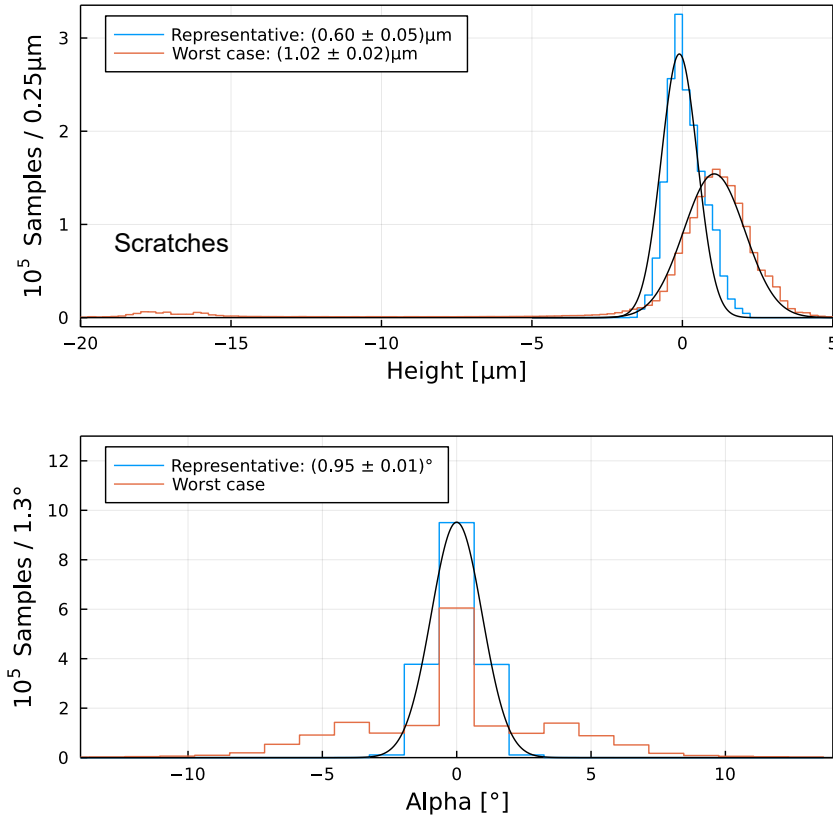


FIGURE 7.21: Height (top) and angular (bottom) distributions of the representative and worst case measurements of the LEGEND-200 PEN holder. The bin size for the angular distribution corresponds to the angular resolution of the measurement. The given uncertainties of the standard deviations were obtained from the fit.

surface was corrected (see Section 7.3.2), the angles could be determined by calculating the slope between the points using a differentiation. The average of these eight angles was then used for the distribution. The resulting distribution follows a Gaussian distribution with the standard deviation  $\sigma_\alpha$ .

For both surface scans from Figure 7.20, the height and angular distributions were evaluated with the results shown in Figure 7.21. This resulted in a standard deviation of  $\sigma_{h,\text{rep.}} = (0.60 \pm 0.05) \mu\text{m}$  for the representative area and  $\sigma_{h,\text{worst}} = (1.02 \pm 0.02) \mu\text{m}$  for the worst case. The height distributions including fits can be seen in Figure 7.21 (top). For the worst case area, two contributions to the height distribution are expected: the normal surface and the scratches. The scratches found in the worst case area are not included in the Gaussian fit formed to obtain  $\sigma_{h,\text{worst}}$ . The contribution of the scratches can be seen on the far left side of the height distribution of the worst case sample.

The type of reflections used in the simulation was obtained for the two

evaluated surface areas by forming the ratio  $\sigma_h/\lambda_{\text{peak}}$ . Here, the peak emission wavelength obtained in Section 7.4.1 was used. For the representative surface area, the ratio was found to be below 1.5, which means that specular spike can be assumed. For the scratched area, the ratio was found to be above 1.5 resulting in specular lobe reflections for the worst case.

The angular distribution for both surface areas can be seen in Figure 7.21 (bottom). Here,  $\sigma_\alpha = (0.95 \pm 0.01)^\circ$  was determined for the representative area including the uncertainty given by the fit. For the worst case area, the angular distribution did not follow a Gaussian distribution. Here, a pattern with three peaks was identified. Two of which can be attributed to the scratches and the one in the middle to the overall surface. In order to obtain an estimation on an overall  $\sigma_\alpha$  for this area, the standard deviation was calculated without fit resulting in  $\sigma_\alpha \approx 4.5^\circ$  for the worst case area.

Both results shown in Figure 7.21 (top) are in agreement with expectations relying on the used mould surface roughness of  $< 1 \mu\text{m}$ . Putting the scratches aside, the surface quality is to be classified as polished. For values of  $\sigma_\alpha$  between  $0^\circ$  (highly polished) and  $5^\circ$  (close to polished) only a minor effect on the light propagation in PEN was found in simulations [104]. Nevertheless, as the condition  $\sigma_h/\lambda_{\text{peak}} < 0.025$  is not fulfilled, the surface quality of the PEN holders cannot be neglected in the simulation.

The uncertainties on  $\sigma_h$  and  $\sigma_\alpha$  were dominated by the resolution of the microscope. As  $\sigma_h$  was only used for a first estimation of the scattering type, its uncertainty was not evaluated in this work. However, the systematic uncertainty was estimated to be below 2% as the resolution in  $z$  and its uncertainty were very small compared to the measured values which are of the order of  $\mu\text{m}$ . The angular resolution is decisive for the determination of  $\sigma_\alpha$  and, thus, for its uncertainty. The angular resolution is  $(1.30 \pm 0.65)^\circ$  given by the resolution in  $x$  (or  $y$ ) and  $z$  direction<sup>19</sup>. The influence of the angular uncertainty on the determination of  $\sigma_\alpha$  can be obtained by assuming the best and worst resolution given by  $(1.30 - 0.65)^\circ$  and  $(1.30 + 0.65)^\circ$ , respectively. Using these as bin size of the distribution and determining the Gaussian fit, the largest deviation to  $1.30^\circ$  as bin size was assumed to be the systematic uncertainty. For  $\sigma_\alpha$  of the representative area, a systematic uncertainty of  $0.11^\circ$  was determined resulting in  $\sigma_\alpha = (0.95 \pm 0.11)^\circ$ . Here, the sum of squares was used to calculate the total uncertainty.

<sup>19</sup>Here, the angular resolution was calculated following the minimum possible angle:  $\tan(\alpha_{\text{min}}) = (10 \pm 5) \text{ nm} / (440 \pm 5) \text{ nm}$ .

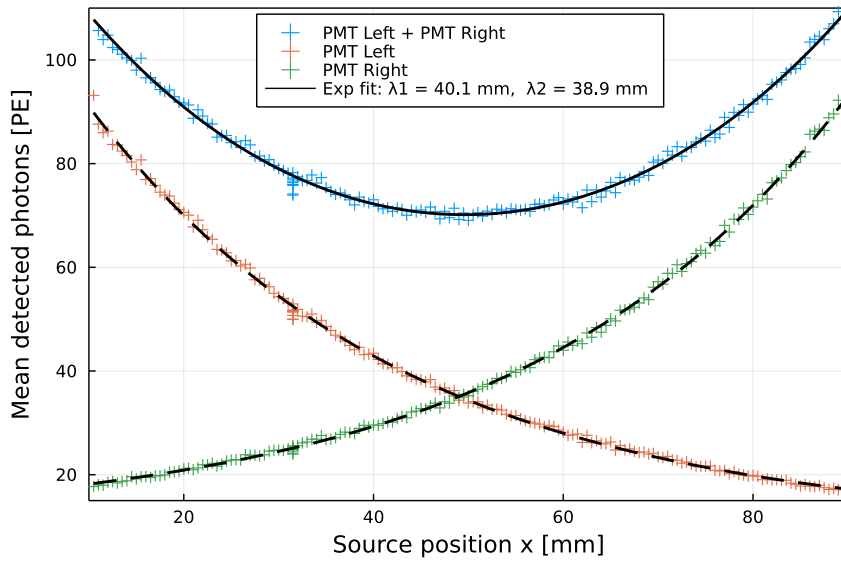


FIGURE 7.22: Average number of detected photons as function of the position on a LEGEND-200 PEN tile ( $100 \times 20 \times 1.7 \text{ mm}^3$ ). Here, two PMTs were used. Results are drawn for PMTs separately and combined including the corresponding fits.

### 7.4.3 Attenuation Length

Using the PMT setup described in Section 7.3.3, the attenuation length of a LEGEND-200 PEN sample was measured<sup>20</sup>. Here, a  $100 \times 20 \times 1.7 \text{ mm}^3$  tile was cut from one of the produced PEN discs (see Section 7.1). One PMT was placed on each of the two short sides of the sample coupled using optical grease (type EJ-550). A scan using the  $^{207}\text{Bi}$  source for excitation was performed, measuring for 60 s at each position in steps of 0.5 mm along the sample from one PMT to the other. The result can be seen in Figure 7.22 where the average number of detected photons per triggered event are plotted as function of the source position on the sample. Results for both PMTs are drawn separately (orange & green) and combined (blue). The individual results of the PMTs have been fitted using an exponential decay to obtain the corresponding attenuation lengths  $\lambda_1$  and  $\lambda_2$ . From this measurement, an attenuation length of the LEGEND-200 PEN sample of  $\lambda_{\text{att.}} = (39.5 \pm 1.5) \text{ mm}$  was found when combining the results of both fits.

The geometry-independent bulk absorption length  $\lambda_{\text{abs.}}$  was determined<sup>21</sup> using a *UV-VIS Lambda 850* spectrophotometer from Perkin Elmer [105]. With this instrument, the transmission and reflection of a sample can be measured using an integrating sphere. By measuring the absorption and reflection for

<sup>20</sup>This measurement was performed and analysed by L. Manzanillas. The code to perform the scan, take data and convert the data was developed by the author of this work.

<sup>21</sup>In cooperation with A. Leonhardt, Technische Universität München, Germany

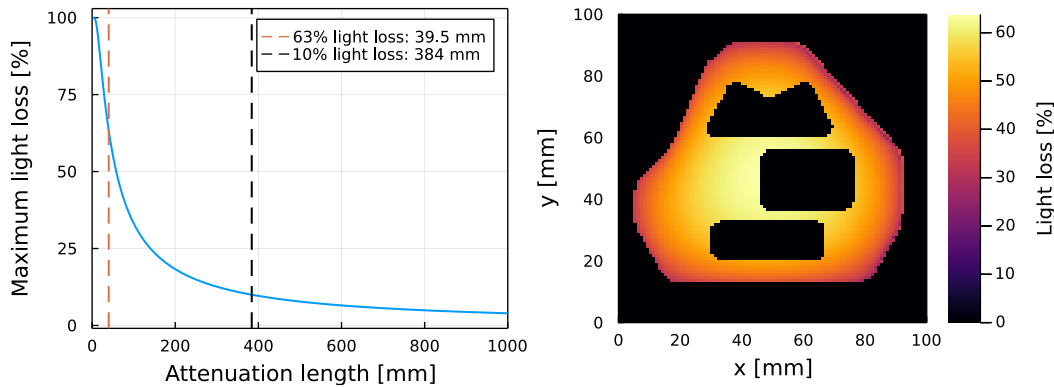


FIGURE 7.23: **Left:** Maximum light loss in the large LEGEND-200 holder design as function of the attenuation length. The value for PEN is marked by dashed orange lines, while the value for a maximum light loss of 10% is marked by dashed black lines. **Right:** Light loss due to attenuation in the large PEN holder as function of the position on the holder.

a given wavelength, the absorption length can be determined. Here, the operational range of the built-in monochromator goes from 175 nm to 900 nm. Using a  $30 \times 30 \times 1.7 \text{ mm}^3$  PEN scintillator,  $\lambda_{\text{abs.}} = (60 \pm 3) \text{ mm}$  was measured for an incident wavelength of 450 nm.

The attenuation and bulk absorption lengths are far below conventional plastic scintillators ( $> 1 \text{ m}$ ). This has an influence on the measured light output of the used sample. This effect was already observed when measuring the emission spectrum (see Section 7.4.1). An approximation of how the generated scintillation light is attenuated in a large PEN holder is shown in Figure 7.23 (right). Here, the PEN scintillation light loss according to the attenuation length  $\lambda_{\text{att.}}$  in the sample was calculated for each position in steps of  $1 \times 1 \text{ mm}^2$ . By using the attenuation length, the reflections inside the sample are taken into account. For this approximation, only photons travelling from the excitation point to the outer edges of the holder were taken into account and the holes in the holder were neglected. A maximum light loss of  $\approx 63\%$  was determined for PEN. As a comparison, the same calculations were performed for the EJ-200 scintillator with  $\lambda_{\text{att.}} = 3800 \text{ mm}$  [101] resulting in a maximum light loss of  $\approx 1\%$ . Following this approximation, the maximum light loss as function of the attenuation length can be determined. This can be seen in Figure 7.23 (left) for the large holder design. To lose a maximum of 10% of the light,  $\lambda_{\text{att.}} > 380 \text{ mm}$  (dashed black line) was found. The result obtained for PEN is marked by a dashed orange line.

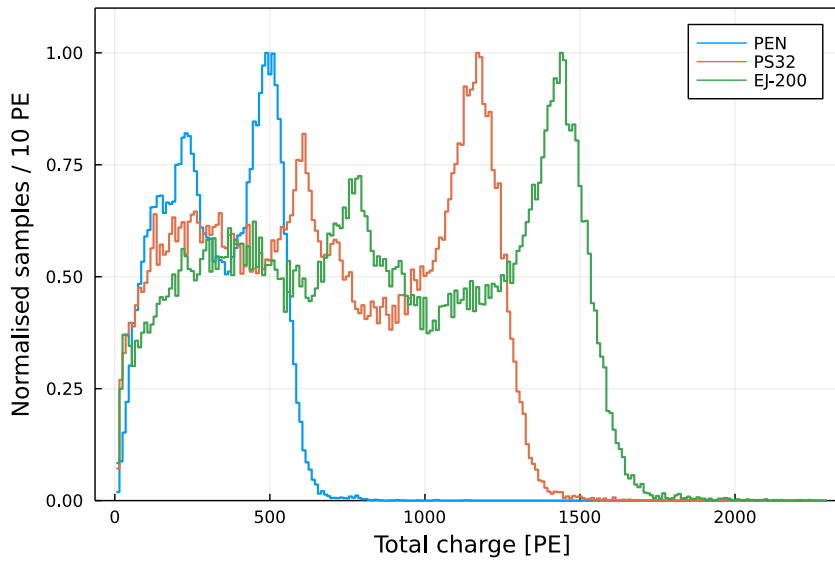


FIGURE 7.24: Light output in terms of PE measured for PEN, PS32 and EJ-200. The number of samples are normalised for comparison.

#### 7.4.4 Light Yield

To determine the light yield of the LEGEND-200 PEN scintillator, all of the properties that have been found so far were necessary. Here, a two-step procedure was used<sup>22</sup>. First, the light output was measured with the PMT setup and then a correction for the optical effects was determined via simulation. For the first part, two stacked samples of PEN with the dimensions  $30 \times 30 \times 1.7 \text{ mm}^3$  were used to obtain full energy deposition of the 930 keV electrons. The samples were optically coupled using optical grease (type EJ-550) to five PMTs: four surrounding the samples and one below them. For excitation of the samples, the  $^{207}\text{Bi}$  source was placed centrally above them. For comparison, the same measurement was also performed with the well-known scintillators EJ-200 and PS32 with reported absolute light yields of  $10000 \pm 200$ <sup>23</sup> and  $\approx 8750$  photons per MeV energy deposition, respectively.

The results of the light output measurement for PEN, PS32 and EJ-200 can be seen in Figure 7.24. By simply comparing the number of photons at the peak position, a light yield of about 3000 photons per MeV energy deposition can be obtained for PEN. However, this does not include the optical properties of the scintillators. In order to take these into account, a simulation of the setup for PEN and the well-known EJ-200 [101] including the surface and attenuation properties was performed. For EJ-200,  $\sigma_\alpha < 10^\circ$  was

<sup>22</sup>This measurement was performed, analysed and simulated by L. Manzanillas. The code to perform the measurement was developed by the author of this work.

<sup>23</sup>Uncertainty from direct communication of L. Manzanillas with Eljen technology.

determined using the setup described in Section 7.3.2. The light attenuation in EJ-200 ( $\lambda_{\text{att.}} = 380 \text{ cm}$ ) can be neglected for the used sample size. The light detection efficiency of the setup was determined by comparing the 930 keV peak position in the simulated to the data energy spectrum of EJ-200. This resulted in an efficiency of  $(62 \pm 2)\%$ . Here, the uncertainty was determined by repeating the simulation with different  $\sigma_\alpha$  values going from  $0^\circ$  to  $10^\circ$ .

Knowing the detection efficiency of the setup, the simulation was repeated with PEN. The light detection efficiency of the setup was determined again for different simulated light yields of PEN<sup>24</sup>. Calibrating this to 62% led to a light yield of  $5437 \pm 218$  photons per MeV energy deposition. Here, the uncertainty contains the effect of the uncertainties of  $\sigma_\alpha$  on the simulation for PEN (1%) and EJ-200 (2%), the uncertainty on the light yield of EJ-200 (2%), the attenuation in PEN (1%) and the reproducibility (1%) of the measurement. A more detailed discussion on the uncertainties will soon be published separately.

### 7.4.5 Detection Efficiency

The detection efficiency of the PEN holders in the PMT setup was determined by comparing the number of triggered events to the number of detected events from the sample.

A rough estimation of the efficiency can be obtained by estimating the ratio of scintillation light collected by the PMTs. Here, the attenuation length of the sample, the spatial coverage of the PMTs, the fraction of scintillation light lost due to total reflections and the efficiency of the PMTs ( $\approx 35\%$  at 440 nm) have to be taken into account. Considering a centrally located point on the sample like  $(x, y) = (40, 40)$  mm, the number of scintillation photons generated in the sample will be reduced by  $\approx 62\%$  due to attenuation until they reach the outer edges of the holder. The spatial coverage is  $\approx 48\%$  for 6 PMTs coupled to the large PEN holder (perimeter  $\approx 286$  mm). In order to reduce total reflections of the scintillation photons, optical grease (type EJ-550) is used in the PMT setup to optically couple the PEN holder to the PMTs. The refractive index of the optical grease is  $n_{\text{EJ-550}} = 1.46$  while  $n_{\text{PEN}} = 1.60$  is assumed for PEN<sup>25</sup>. Assuming randomly distributed incident angles of the scintillation photons, about 27% of them will undergo total reflections and, thus, are

<sup>24</sup>The relation between the detection efficiency of the setup and the light yield of PEN is not linear for lower light yields due to attenuation effects of PEN.

<sup>25</sup>The refractive index of PEN produced for LEGEND-200 has not been measured, yet. It is assumed to be comparable to PET at 440 nm [106].

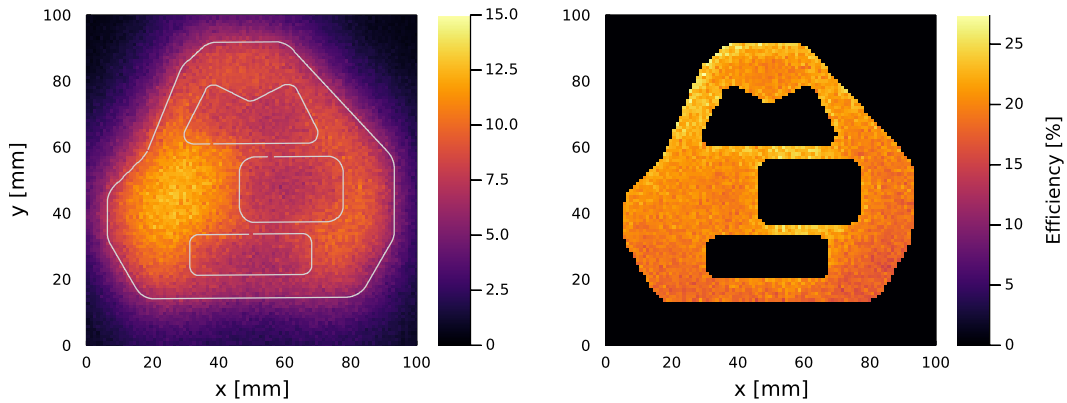


FIGURE 7.25: Measured ratio of number of detected to triggered events for the large PEN holder. **Left:** Measured results for each position on the grid. **Right:** Measured results for each position on the holders surface corrected for the hit probability of the electrons of the  $^{207}\text{Bi}$  source.

considered not be detected by the PMTs. This assumption is based on the critical angle  $\theta_C$  of Snell's law. For the PMT setup, the transition of the light from PEN to the optical grease corresponds to  $\theta_C = \arcsin(n_{\text{EJ-550}}/n_{\text{PEN}}) \approx 66^\circ$ . This leads to a  $\approx 27\%$ <sup>26</sup> probability of total reflection. The window of the PMTs is made of borosilicate glass [107] which provides a refractive index of  $n_{\text{B.Glass}} > 1.5$  [108]. Therefore, no total reflections are expected for the transition from EJ-550 to the sensor of the PMT.

Taking all the effects mentioned into account, about 5% of the produced scintillation-photons that would leave the sample at the edges will be detected by the PMTs. For comparison, about 12% will be collected for the same position using EJ-200. In addition, the probability of the electrons from  $^{207}\text{Bi}$  to hit the sample for that position is 54%. Also, the number of photons measured must be above 2 PE in order not to be lost in the background.

For the large PEN holder<sup>27</sup>, the measured setup-dependent detection efficiency of the PMT setup can be seen in Figure 7.25 (left). The efficiency distribution fits the expected hit distribution shown in Figure 7.14 (right) very well. A maximum of about 15% of all triggered events have also been recorded by the PMTs coupled to the PEN holder. Correcting for the probability of the electrons coming from the  $^{207}\text{Bi}$  source to hit the sample increases this efficiency to an average of about 20%. The distribution of the corrected

<sup>26</sup> $66^\circ/90^\circ \approx 73\%$  which will not undergo total reflections.

<sup>27</sup>All scans of the PEN holders were performed by the author of this work in co-work with A. Capogrosso.

efficiency can be seen on the right hand-side of Figure 7.25. The thresholds for this analysis were set to 3 PE for the trigger and 2 PE for the sum of the PMTs coupled to the sample.

The same measurement and analysis was performed for the small and medium type of the PEN holders and the results can be found in Figure A.6 in the Appendix.

#### 7.4.6 Energy Threshold

A limit on the minimum deposited energy needed in the PEN holder at a given position to detect a certain number of photons in the PMTs was determined. For simplicity, this is referred to as the *energy threshold* of the sample.

For this, an energy calibration for the number of measured photons had to be carried out for individual positions first. This calibration is different for each position of the source above the PEN holder, because the distances from the excitation point to the PMTs are different. For the energy calibration, the 930 keV peak of the  $^{207}\text{Bi}$  source was used (see Figure 7.15). The peak position is marked by an orange dashed line in the uncalibrated spectrum in Figure 7.26 (left), taken at one position on the large PEN holder. Due to the short exposure time of 30 s, the events recorded at the surrounding eight positions were added to the distribution to improve the peak resolution. To find the peak position, a fit function consisting of an exponential function and a Gaussian for the peak was used. Using the peak position, the number of detected photons per event was calibrated to energy for each scanned position.

Due to the short exposure, for some positions with relatively bad detection efficiency the 930 keV peak was not visible even after summing up the neighbouring bins. For about 15 to 20 positions, depending on the holder type, and their neighbouring bins a clear peak was visible. These points were searched for manually and were mainly located in areas with a high detection efficiency (see Figure 7.25, left). A linear dependency between the average number of detected photons per event collected with all PMTs and the 930 keV peak position was found. This can be seen in Figure 7.26 (right). Using this dependency, the energy calibration can be done for all positions. For the next step, the 930 keV peak position in terms of average number of detected photons is needed. This can be obtained using the determined linear dependency.

The 930 keV peak is Poisson distributed around its position. Therefore, by integrating the Poisson probability distribution from 0 PE to a certain

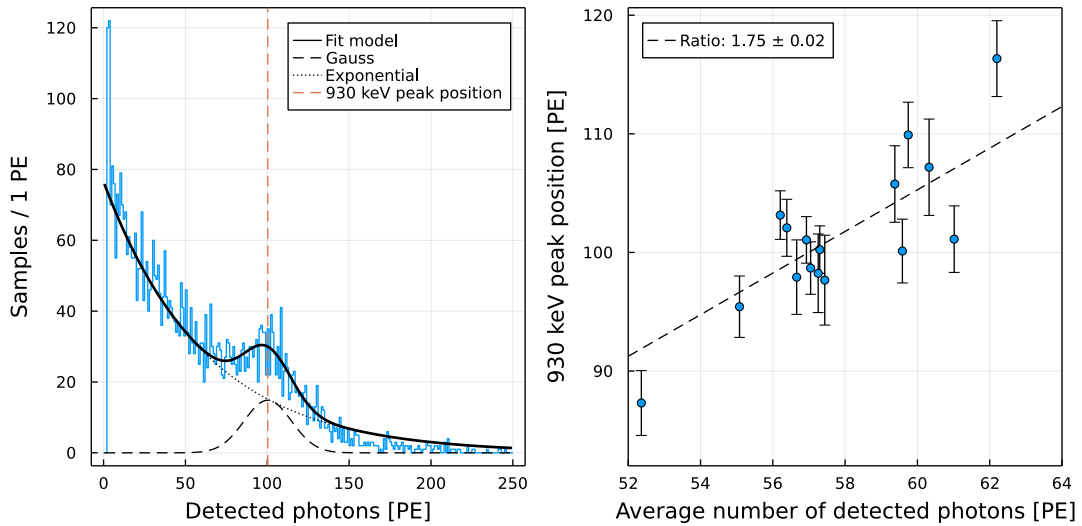


FIGURE 7.26: **Left:** Distribution of number of detected photons per event collected with all PMTs coupled to the large PEN holder in the PMT setup. The used events were recorded at one position and its eight surrounding positions. The parts of the fit model are drawn separately. The 930 keV peak position is marked by a dashed orange line. **Right:** 930 keV peak position as function of the average number of detected photons per event for the large PEN holder. The uncertainties given were obtained by the fit.

amount, the probability of detecting at least that amount of PE for a 930 keV energy deposition can be calculated. Assuming a linear energy dependency, this can also be calculated for arbitrary energy depositions. Furthermore, by fixing the amount of photons that have to be detected, the minimum needed energy deposition to detect that amount can be calculated. This refers to the energy threshold of the scintillator sample at one position.

The energy threshold to detect at least 2 PE was determined for every measured position on the large PEN holder. The result is shown in Figure 7.27. Here, a 99.7% ( $3\sigma$ ) detection probability for 2 PE was assumed on

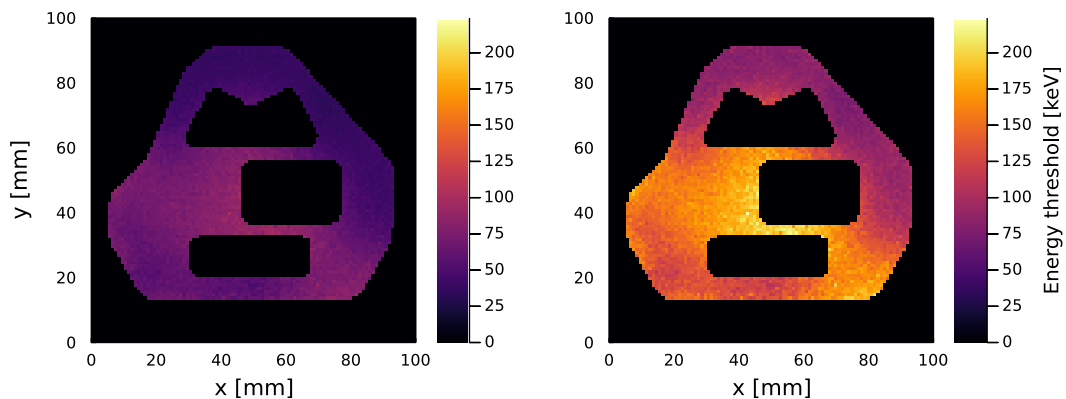


FIGURE 7.27: Energy threshold as function of the position on the large PEN holder with an 99.7% (left) and 99.99994% (right) detection probability of 2 PE.

the left and 99.99994% ( $5\sigma$ ) on the right plot. As expected, the energy threshold is lower close to a PMT and higher in the middle of the sample. The maximum value of 102 keV (224 keV) can be interpreted as the minimum energy deposition in the sample needed for a  $3\sigma$  ( $5\sigma$ ) detection of 2 PE in the PMT setup.

The same measurement and analysis was also done for the other two PEN holder types. The determined energy thresholds for the small and medium size were 97 keV (213 keV) and 112 keV (247 keV) for a  $3\sigma$  ( $5\sigma$ ) detection probability of 2 PE, respectively. The energy threshold as function of the position for these two geometries can be found in Figure A.7 in the Appendix.

### 7.4.7 Estimation of the Veto Energy Threshold of PEN in LEGEND-200

In the following, it is estimated how much energy has to be deposited in one of the PEN holders in LEGEND-200 to have a 95% probability of detecting at least one photon of the scintillation light with the SiPMs of the LAr veto.

**Scintillation light leaving the PEN holder in LAr:** The measured number of photons in the PMT setup corresponds to  $\approx 12.8\%$  of the total number of photons reaching the outer edges of the PEN holder<sup>28</sup>. By using the results from Section 7.4.6, a relation between this number and the needed energy deposition can be drawn.

In LEGEND-200, the PEN holders will be submerged in LAr with a refractive index of  $\approx 1.2$  [109], leading to total reflections of the PEN scintillation photons which are considered as lost in this approximation. This results in a loss of  $\approx 46\%$  of the photons leaving the outer edges of the PEN holder due to total reflections.

**Light propagation in LAr and through the nylon mini-shroud:** On the way from the PEN holder to the WLS fibres of the LAr veto system, the photons will be attenuated by the LAr. The attenuation length of LAr for visible light is not well known, but is assumed (in simulations) to be about 1000 m for wavelengths above 200 nm [110]. For an estimated distance from the HPGe detectors to the WLS fibres of  $\approx 10$  cm, an attenuation length above

<sup>28</sup>Here, the coverage ( $\approx 50\%$ ), quantum efficiency ( $\approx 35\%$  at 440 nm) of the PMTs and the total reflections in the transition from PEN to the optical grease ( $\approx 27\%$  loss, see Section 7.4.5) were taken into account.

10 m is negligible as the light attenuation would be below 1%. Therefore, the light attenuation in LAr can be neglected.

The scintillation photons of PEN have to go through the TPB-coated nylon mini-shroud before reaching the WLS fibres. These have a thickness of  $125\ \mu\text{m}$  and the absorption length of visible light is assumed (in simulations) to be about 100 m [111]. Again, for an absorption length above 10 cm the effect is negligible as it would be below 1% for the thin nylon sheet. The light attenuation due to absorption in the nylon mini-shrouds can also be neglected.

**Light collection in the WLS fibre:** The scintillation light has to be absorbed by the WLS fibres (type BCF-91A) in order to be guided to the SiPM readout. These have an absorption length of  $(0.700 \pm 0.001)$  mm for blue light [48]. The overlap of the absorption spectrum of the fibres with the emission spectrum of PEN is estimated to be 60% (see Section A.2.1) resulting in a loss of the incoming scintillation light of 40%. Due to the squared shape of the WLS fibres with a cross section of  $1 \times 1\ \text{mm}^2$ , there are no significant scintillation light losses due to insufficient depth of the fibre expected. The coverage of the WLS fibres around the HPGe detectors can be approximated with 50%, as two sides of the HPGe detector strings are covered in LEGEND-200. Following this, 70% of the photons emitted by PEN are not collected by the WLS fibres.

**Light propagation in the WLS fibre:** The absorbed scintillation light is diffusely re-emitted in the WLS fibre with a peak emission wavelength of 494 nm (green) [112]. The index of refraction of the fibres core is  $n_{\text{core}} = 1.6$ . The fibres have two cladding layers made of PMMA with decreasing indices of refraction of  $n_{c1} = 1.49$  and  $n_{c2} = 1.42$  from inside to outside, respectively [48, 113]. This significantly improves the trapping efficiency by increasing the number of total reflections inside the fibre. To estimate how much of the diffuse emitted light is lost, three transitions have to be considered. First, from the fibre core to the first cladding layer. About 77% of the emitted light can pass through this transition while the rest is guided towards a SiPM. The second transition is from the first into the second cladding layer. Here, about 80% of the light can escape. The last transition is to the LAr, where only 64% of the light can make the transition. In total, about 61% of the emitted scintillation light of the WLS fibre is trapped and guided to the SiPMs.

The WLS fibres have a total length of about 2 m with an attenuation length of 3.5 m [48]. The fibres are bent in the middle by 180° and SiPMs are connected to both ends. Half of the scintillation light emitted by the fibre is guided towards each of the two SiPMs. Considering the different distances of the emission point to the SiPMs, a maximum light loss of 25% due to attenuation can be calculated<sup>29</sup>.

A total loss of  $\approx 55\%$  is thus assumed for the propagation of the light in the WLS fibre.

**Light detection with SiPMs:** The used SiPMs (PM33100, Ketek GmbH) have an active sensor area of  $3 \times 3 \text{ mm}^2$  with 3600 pixels ( $50 \times 50 \mu\text{m}^2$  each). The geometrical efficiency is about 70% and the peak quantum efficiency is about 40 to 50% between 410 and 440 nm provided by the manufacturer<sup>30</sup>. From actual measurements, an overall detection efficiency of the SiPMs of  $\approx 25\%$  can be assumed for the wavelength-shifted photons of the fibres<sup>31</sup>.

**Summary:** For a Poisson distributed signal in the SiPMs of the LAr veto system, three photons have to be detected on average in order to achieve a 95% probability of detecting at least one photon originating from a PEN holder in LEGEND-200. Following the approximation described in this section, this corresponds to a total of about 183 photons reaching the outer edges of the PEN holder<sup>32</sup>. Accordingly, background events that deposit energy in an HPGe detector and at least 365 keV in one of the PEN holders can be identified with 95% probability as background.

<sup>29</sup>The minimum of the intensity  $I(x) = 0.5 \cdot I_0 \exp(-x/\lambda_{\text{att.}}) + 0.5 \cdot I_0 \exp(-(l-x)/\lambda_{\text{att.}})$  was found to be  $\approx 75\%$  with  $l = 2 \text{ m}$  and  $\lambda_{\text{att.}} = 3.5 \text{ m}$  being the length and the attenuation length of the fibre, respectively, and  $x \in [0, 2] \text{ m}$ .

<sup>30</sup>Ketek GmbH has sold its SiPM assets to Broadcom and there are no official documents available anymore for this type of SiPM. The given information are from documents that are not publicly available.

<sup>31</sup>Private communication with P. Krause.

<sup>32</sup>A 90% probability is assumed in the relation between the number of photons reaching the outer edges of the PEN holder and the energy deposition in the PEN holder. Accordingly, an additional 10% loss of photons is used to compensate for this. Thus, in order to detect on average three photons with the SiPMs  $3/(0.9 \cdot 0.54 \cdot 0.3 \cdot 0.45 \cdot 0.25) \approx 183$  photons have to reach the outer edge of the holder.

## 7.5 Summary

The whole production process of the PEN scintillators for LEGEND-200 was carried out in the means of a low-background experiment. The commercially procured raw PEN granulate was excessively cleaned before producing discs using injection compression moulding. The specially designed low-mass LEGEND-200 germanium detector holders were then manufactured from the discs under cleanroom conditions using a CNC milling machine. The uncleaned granulate, the discs and the finished holders were screened for radio impurities using two independent HPGe detector based screening stations, ICP-MS and radon emanation. Compared to measurements of the untreated granulate, the results show that most of the impurities were on the surface of the granulate. Here, a radiopurity limit of  $< 1.2 \mu\text{Bq}$  per LEGEND-200 holder was set [83].

The produced PEN scintillator was examined in terms of its optical properties in order to find all necessary parameters for future LEGEND simulations. Here, the emission spectrum was recorded using a spectrometer resulting in a peak emission wavelength of  $(440 \pm 3) \text{ nm}$  which is favourable for most light sensors. The surface quality was examined using a digital microscope. This was done to obtain the standard deviations  $\sigma_h$  and  $\sigma_\alpha$  of the height and angular distributions of the micro facets on the surface, respectively, which are important to model the light propagation. For a representative area of the LEGEND-200 PEN holders,  $\sigma_h = (0.60 \pm 0.05) \mu\text{m}$  and  $\sigma_\alpha = (0.95 \pm 0.11)^\circ$  were determined, indicating an excellent surface quality which is in-line with expectations due to the surface quality of the mould. In addition, the bulk absorption length at 450 nm was determined to be  $(60 \pm 3) \text{ mm}$  using a spectrophotometer. With a PMT-based setup, the attenuation length, scintillation light yield and an estimation on the detection efficiency and energy threshold of the PEN detector holders were determined. The light yield was found to be  $5463 \pm 220$  photons per MeV energy deposition. The setup-dependent detection efficiency of the three LEGEND-200 holder designs was determined to be  $\approx 20\%$ . Also, an energy threshold of 112 keV (247 keV) for a  $3\sigma$  ( $5\sigma$ ) detection of at least 2 photo electrons was estimated. Following this estimation, background events in LEGEND-200 with energy depositions in an HPGe detector and additional energy depositions of at least 365 keV in one of the PEN holders can be identified as background with 95% probability.

The production run of the LEGEND-200 germanium detector holders made

---

of PEN was a complete success and all parameters necessary for simulating background expectations could be determined. Enough PEN holders were produced during the course of this work to equip all HPGe detectors in LEGEND-200. With the new PEN holders, the until now difficult detection and identification of background events close and between the HPGe detectors will be improved. And with the newly acquired knowledge of the optical properties of the custom-made PEN holders, realistic simulations can be created for LEGEND in order to obtain the veto efficiency.



## Chapter 8

# $0\nu\beta\beta$ -Decay Detection Efficiency for GERDA Phase II

PSD was used in the GERDA analysis to discriminate signal from background events where an event is defined by energy depositions in the HPGe detectors. Some signal events have background-like pulse-shape characteristics and are therefore also discarded. Thus, the signal recognition efficiency of a PSD cut says what fraction of signal-like events is kept. In the GERDA analysis, the cuts and how they affect background and signal-like events were evaluated based on calibration data [12]. This data-based analysis entails uncertainties arising from the differences between DEP and  $0\nu\beta\beta$ -decay events. Such differences are different spatial distributions of energy depositions in the HPGe detectors and effects due to Bremsstrahlung. In order to mitigate these uncertainties, simulations of the detectors and their signals are necessary.

In this chapter, a simulation-based analysis chain is presented to determine the detection efficiency for  $0\nu\beta\beta$ -decay events in BEGe detectors used in GERDA Phase II. Using GEANT4, the underlying physics leading to the energy depositions of an event in the detector were simulated. From the spatial distribution of energy deposits, the pulses of the events were simulated using the charge drift in the detector due to the electric field. In order to obtain realistic simulated pulses, an electronics model was applied and noise from GERDA data was added to the simulated pulses.  $A/E$  analysis (see Section 5.3.4) was then used as the main analysis method for PSD, whereby the individual pulse shapes were analysed for their time structure by comparing the amplitude  $A$  of the current pulse to the total energy deposition  $E$  of the simulated event. The same method was then applied to several real events from calibration data of GERDA Phase II and to simulated data. After the analysis chain has been validated by comparing cut survival fractions of data and simulation, it was used to determine the  $0\nu\beta\beta$ -decay detection

efficiency.

In the following, the individual GERDA detectors are named with their internal abbreviations and/or the respective channel. An allocation can be found in Table B.1 in the Appendix.

## 8.1 Data Sets & Event Selection

In the course of GERDA Phase II,  $^{228}\text{Th}$  calibration runs were carried out every 7-10 days. The collected data were used in this work for the calibration and validation of the analysis chain. During a calibration run, the array was exposed to three custom-made low-neutron emission  $^{228}\text{Th}$  sources ( $\approx 10$  kBq) which were lowered from the lock system to the detector strings. The sources were moved to three different heights with respect to the detector array (see Figure 3.1) during the measurement. Data was recorded for 30 minutes at each position resulting in  $\approx (1 - 3) \times 10^3$  events from  $^{208}\text{Tl}$  at the prominent 2614.5 keV FEP  $\gamma$ -line per BEGe detector [73]. Additional strong lines in the calibration energy spectrum are the  $^{208}\text{Tl}$  DEP at 1592.5 keV,  $^{212}\text{Bi}$  FEP at 1620.7 keV and the  $^{208}\text{Tl}$  SEP at 2103.5 keV, which were used for the energy calibration of the HPGe detectors and for validation of PSD. The main signal libraries of the  $^{228}\text{Th}$  calibration spectrum are listed in Table 8.1. The average number of events per detector used for the presented analysis are also given for GERDA data and simulation.

The calibration process was simulated with MaGe [114, 115] which is not part of this work. In the simulation, the array geometry and the position of the sources were taken into account. However, the simulation of the decay of the  $^{228}\text{Th}$  source was reduced to the decay of the daughter isotopes  $^{212}\text{Bi}$  and  $^{208}\text{Tl}$  which provide all necessary  $\gamma$ -lines of the spectrum. Only a few parameters of interest were extracted for each event: energy deposits, position of the depositions within the detector and the channel numbers of detectors involved in the event.

Source	Name	$E$ [keV]	$N_{\text{Data}} [\times 10^3]$	$N_{\text{Sim.}} [\times 10^3]$
$^{208}\text{Tl}$	DEP	1592.5	6	35
$^{212}\text{Bi}$	FEP	1620.7	4	33
$^{208}\text{Tl}$	SEP	2103.5	7	55
$^{208}\text{Tl}$	FEP	2614.5	50	500

TABLE 8.1: Main signal libraries of the  $^{228}\text{Th}$  calibration spectrum and their corresponding peak energy  $E$ . The average number of events per detector used for this analysis is given for GERDA data ( $N_{\text{Data}}$ ) and simulation ( $N_{\text{Sim.}}$ ) for each peak.

The GERDA data taken between June 2017 and April 2018 was evaluated which contains about 12.6 kg·yr of exposure. However, four detectors were not considered in this work (GD89B, GD02D, GD91C and GD32A corresponding to channel numbers 05, 06, 07 and 13, respectively). They were excluded from the analysis as they did not contribute valid exposure<sup>1</sup> in the selected runs. For the purpose of this work, only BEGe detectors were evaluated due to their favourable PSD properties. Two additional simulated datasets with  $2\nu\beta\beta$  and  $0\nu\beta\beta$  decays in the detectors were used for the evaluation of the  $A/E$  cut survival fractions.

**Event selection criteria & simulation settings:** The GERDA Phase II data and the simulated data were treated in the same way as far as possible in order to validate the analysis chain. However, some filters have to be applied to both data sets at the beginning in order to obtain a uniform set of events. Due to the different kind of data format and provided information, filters between data and simulation vary.

For data and simulation, events that have energy depositions in more than one detector were discarded ( $multiplicity = 1$ ). The energy threshold for the events was set to 350 keV as events below that energy were not relevant for the presented analysis. In addition, events in GERDA Phase II data which were flagged invalid by the standard GERDA analysis [73] were excluded.

For GERDA Phase II data, pulses with a length of 10  $\mu\text{s}$  and a sampling time of 10 ns were used. The simulated pulses were calculated using the positions and energies of individual energy deposits in the detector and the following settings: Sampling time = 1 ns, hit clustering radius = 0.2 mm and extended pulse length = 10  $\mu\text{s}$  (baseline & tail as constants). The clustering radius describes the spatial distance between energy deposits within which they can be merged to a single deposition (position resolution of PSD analysis). The simulated charge pulses were folded with a response function describing the electronics model mentioned before. Afterwards, the pulses were time aligned to their half maximum and cut to a length of 8  $\mu\text{s}$ . In order to match the data, the sampling time of all simulated pulses was reduced to 10 ns. Finally, realistic noise baselines from GERDA data was added to all simulated pulses as explained in Section 8.2.3.

From here on, the GERDA Phase II data are referred to as *data* and the simulated data as *simulation*.

---

<sup>1</sup>These detectors were either not in operation or had too high a noise level to provide usable data.

## 8.2 Detector Simulation

The newly developed open-source software package *SolidStateDetectors.jl* [54] (see Section 4.3) was used to determine the pulses for each event simulated with GEANT4. Here, for each detector the geometry needs to be determined as well as the operational voltage and impurity profile. From previous simulation work [115, 116], all needed parameters already exist and most of them could directly be used. The detector specifications for this were available in SigGen [117] configuration files. In order to check the depletion of a simulated detector and later calculate pulses, a few things had to be calculated for each detector including the electric potential, electric field and the weighting potential as described in Section 4.2 and Section 4.3. Afterwards the corresponding charge drift model was applied (see Section 4.3). Additionally, a suitable electronics model (see Section 8.2.2) and realistic noise (see Section 8.2.3) was added to the generated pulses, in order to compare with real data.

### 8.2.1 Verification of Detector Depletion

Not all available SigGen configurations could be used directly, because some of the detectors showed undepleted regions in simulation with these parameters. In GERDA, all detectors have been characterised [116] and their operational voltage was chosen 500 V above the measured depletion voltage. A deviation of the measured depletion voltage in the simulation leads to a poor agreement between the pulse shapes of data and simulation. For the verification of the simulation parameters in this work, a lower limit for the electric field strength within the detector was chosen at  $50 \frac{\text{V}}{\text{m}}$ . For electric fields below this limit, the charge drifts are still simulated but can lead to slow pulses which are not expected for this volume of the detectors. Three detectors (GD35C, GD00D, GD35A) show incomplete depletion with their default parameters. Figure 8.1 shows a cross-section of GD35A, in which the depleted (green) and non-depleted (yellow) areas are drawn. The impurities of a detector were described by a starting value and a gradient in  $z$  direction. In order to reach a depleted state of the whole detector volume, the starting value of the impurity level was decreased in steps of  $1 \cdot 10^{12} \frac{\text{e}}{\text{cm}^3}$  while the gradient was not changed. This was done as often as needed until a completely depleted state was reached. Table B.1 in the Appendix contains all impurity and HV levels used for the simulations in this work.

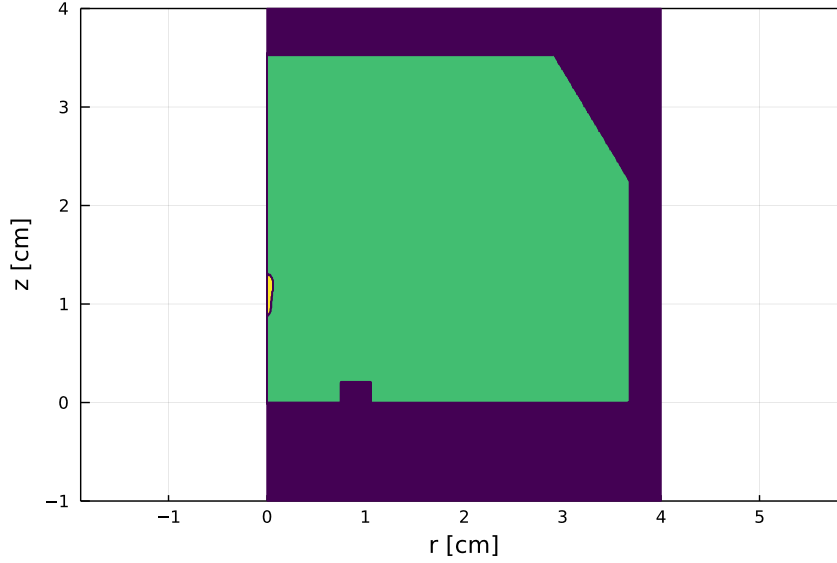


FIGURE 8.1: Cross section of GD35A showing the state of depletion. The green area is depleted, whereas the electrical field strength in the yellow area is below  $50 \frac{\text{V}}{\text{m}}$  and thus undepleted. The surrounding LAr that is taken into account in the simulation is shown in dark purple.

### 8.2.2 Optimisation of Electronics Model Parameters

Pulse shapes are calculated directly from the simulated energy depositions for individual events using *SolidStateDetectors.jl* [54]. Here, an event is defined by the sum of the simulated hits in the detector volume. A pulse shape is generated for each of these hits individually and the sum weighted by the energies of these then describes the pulse shape of the event. The electronics model is applied to the simulated pulses by convoluting them with the response function  $h(t)$  of the charge-sensitive preamplifier. The analytical model of the circuit shown in Figure 8.2 is used for  $h(t)$ . Its derivation is described in [118] and is summarised briefly in the following.

The electronics model function is defined as a transfer function  $T(s)$  of the complex continuous frequency  $s$ . The impulse response can be obtained by calculating the inverse Laplace transformation

$$h(t) = \mathcal{L}^{-1}\{T(s)\}. \quad (8.1)$$

The transfer function is defined as

$$T(s) = \frac{v_{\text{out}}(s)}{i_{\text{in}}(s)} = \frac{1}{C_f s + \frac{1}{C_f R_f} + \frac{1}{H_{\text{pre}}(s)} \left( \frac{C_f + C_d}{C_f} \right) \left( s + \frac{1}{R_f(C_d + C_f)} \right)} \quad (8.2)$$

with the voltage gain  $H_{\text{pre}}(s) = \frac{GBP}{s + \omega_{\text{pre}}} = -\frac{v_{\text{out}}}{v_{\text{d}}}$  and the gain-bandwidth product  $GBP$ , also known as  $GBWP$ . All parameters of  $T(s)$  are labelled

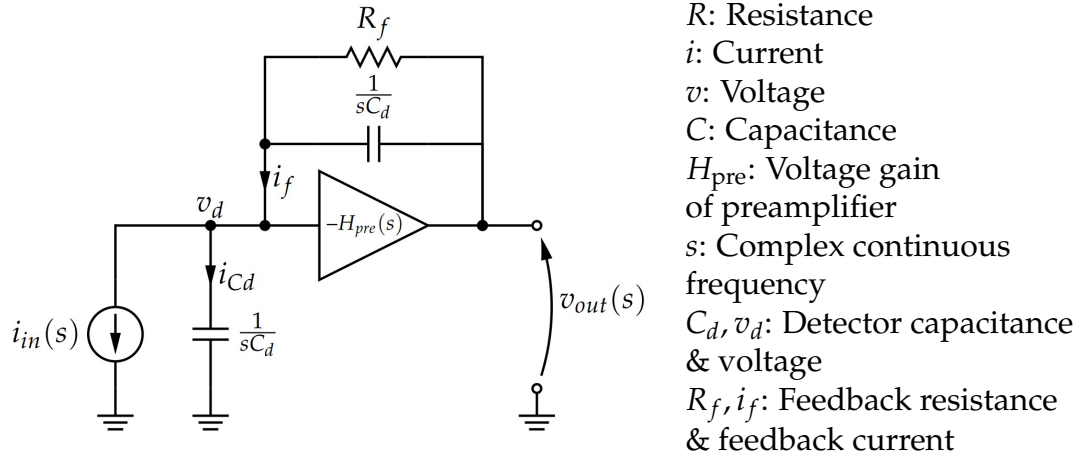


FIGURE 8.2: Configuration of the simplest version of a charge-sensitive preamplifier. Picture taken from [118].

in Figure 8.2. This transformation function describes the effect of a charge-sensitive preamplifier as used in GERDA. The Julia implementation of the electronics model is provided in the Appendix B.1.

In previous simulations, parameters for the electronics model were already determined for the individual GERDA detectors. However, since the configurations, as described in Section 8.2.1, were changed for some detectors, they had to be refined. Furthermore, the existing parameters were slightly optimised in this work. In order to do so, all events from the DEP of  $^{208}\text{Tl}$  were selected from a single calibration run and from one simulated calibration. DEP type of events are used to optimise the electronics model parameters because they contain mostly SSEs. Both, simulation and data were filtered according to the criteria explained in Section 8.1. The energy range was limited to  $(E_{\text{DEP}} \pm 2.5)$  keV and a simple PSD cut based on  $A/E$  was applied to reduce the proportion of MSEs. The amplitude  $A$  of the current pulse was determined by simply taking the maximum value. The energy is taken from the GEANT4 simulation for the simulated events and from official GERDA analysis for real data. The  $A/E$  distribution of all DEP events follows a Gaussian curve and only the events with an  $A/E$  value within 2 standard deviations were used to exclude MSEs.

For the assessment of the quality of the electronics model parameters, superpulses were constructed by the superposition of all DEP event charge pulses<sup>2</sup>. Here, all pulses were time alignment to their half maximum and no noise was added to the simulation. The superpulse for the simulation was determined for various electronics-model parameter-sets. In order to

<sup>2</sup>The superpulses were created by adding the samples of all pulses and dividing them by the number of pulses.

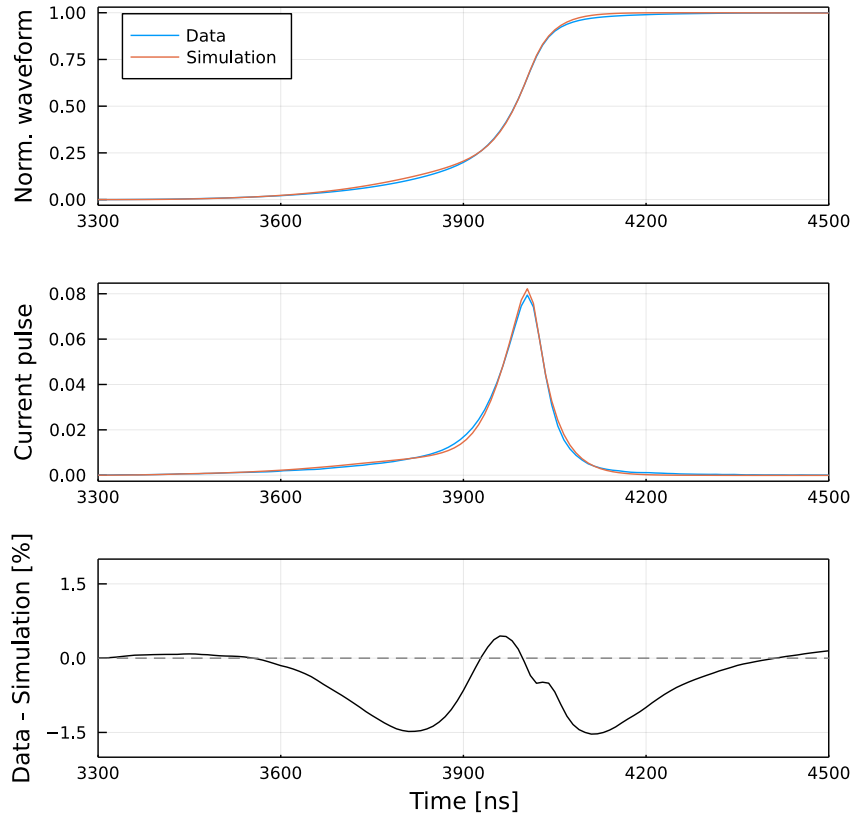


FIGURE 8.3: Comparison of DEP charge superpulses (top) for data and simulation of GD35B. The comparison of the current superpulses and the difference between the charge superpulses of data and simulation are shown in the middle and bottom, respectively.

obtain the best configuration, the superpulses of the DEP events for data and simulation were compared.

Figure 8.3 (top) shows the normalised DEP charge superpulses for data and simulation of GD35B. The associated current pulses can be seen in the middle plot and the difference between the charge superpulses of data and simulation in the bottom plot. In order to find the best possible parameter set, the sum of squared differences  $\chi^2$  was calculated and minimised by changing the parameters  $GBP$  and  $\tau$  of Equation 8.2. The parameters found in this way are listed in Table B.1 with the associated  $\chi^2$  values for all detectors. Of all available parameters for the electronics model ( $GBP$ ,  $\tau$ ,  $C_d$ ,  $C_f$ ,  $R_f$ ) only  $GBP$  and  $\tau$  have been adjusted where  $\tau$  describes the average decay constant of the pulse tail. The only exception is GD35A, in which  $C_d$  and  $C_f$  were also newly determined as no fitting parameter set could be obtained without changing them. These two parameters and  $R_f$  were constant for all other BEGe detectors with  $C_d = 50.0$  pF,  $C_f = 0.35$  pF and  $R_f = 500$  M $\Omega$ . The maximum difference between the measured and simulated DEP superpulses for 20 detectors are better than 3%. For GD91B the highest difference was

found with 5.3%.

### 8.2.3 Realistic Noise Contribution

For realistic simulated pulses, real noise was added to the pulses after folding with the optimised electronics model. Noise was taken from GERDA data, which includes baselines taken by random triggers. These baseline pulses had to comply with the following criteria:

1. The baselines must be calibrated to energy (adjust signal to noise ratio)
2. The baselines must not contain any bias like slopes or ringing
3. Every noise baseline must be unique

A collection of noise baselines was created for each detector using the random trigger baselines of the used GERDA Phase II data set (see Section 8.1). Each baseline is  $10\ \mu\text{s}$  long. So if there were more simulated events than baselines for a detector, these could be used multiple times. For example, the ranges  $0\ \mu\text{s}$  to  $8\ \mu\text{s}$  and  $2\ \mu\text{s}$  to  $10\ \mu\text{s}$  were used. The distribution of the baselines to the simulated pulses of a given detector is done at random, whereby no  $8\ \mu\text{s}$  long baseline was used twice.

The samples and therefore also the *root mean square* (RMS) of the collected baselines were not calibrated to energy. For each simulated event, the energy is known and thus the charge pulse could be normalised to the corresponding energy. For the RMS calibration of the baselines, a simplified calibration

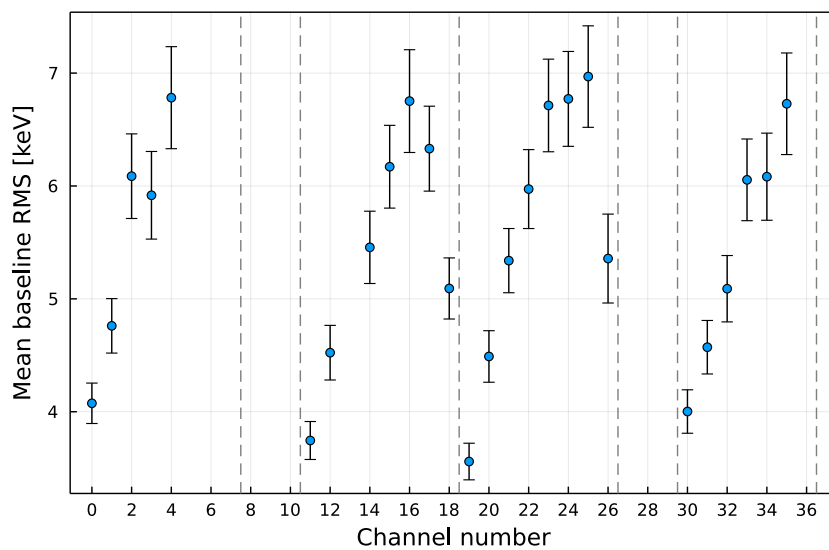


FIGURE 8.4: Mean baseline RMS for all GERDA BEGe detectors for the used data set. The error bars represent one standard deviation. The dashed grey lines mark the detector strings.

has been performed using the FEP of  $^{208}\text{Tl}$ . The amplitudes of the charge pulses in the energy range  $(2614.5 \pm 1)$  keV were determined. The amplitude distribution of FEP pulses has been fitted with a Gaussian to determine its mean value. The ratio of the mean value and the known FEP energy has been applied as a calibration factor to the baselines.

In order to test for a possible bias in the energy-calibrated baselines, the distribution of the baseline RMS values were fitted with a Gaussian for each detector. Channels 30 – 35 show a shift in the baseline that affects a small part of the dataset, which has been excluded from the analysis. Only baselines within three standard deviations around the RMS mean were used. The RMS mean values calibrated to energy of the individual detectors are plotted in Figure 8.4. The error bars given here represent one standard deviation. The mean RMS values show a clear pattern, which can be attributed to the position of the detector in the string. Detectors further down in a string show higher noise attributed to their cable paths.

## 8.3 Energy Calibration

Up to this point in the analysis, the used energy values for individual events were either given by the simulation or by previous analysis of the GERDA collaboration. The methods used to determine these values are different, however. Therefore, a uniform procedure for energy calibration is used in the following. The procedure is presented in this section. In order for the calibration to be carried out, the parameters  $A$  and  $E$  were determined. A comparison of data and simulation is also shown.

### 8.3.1 A & E Determination

The energy  $E$  and the amplitude  $A$  of each event were determined using the same technique. First, the charge pulse was filtered several times by applying a *moving window average* (MWA) in order to reduce the noise. The current pulse was then calculated using a derivative<sup>3</sup> and the maximum of the current pulse was determined from this. The only difference for the  $A$  and  $E$  determination was in the parameters for the MWA filter. For the current amplitude  $A$  this was applied three times with a window size of 50 ns

---

<sup>3</sup>By calculating the slope between neighbouring bins.

(5 samples) prior to differentiation. To determine the uncalibrated energy estimator  $E_{\text{uncal.}}$ , it was applied 13 times with a 2010 ns (201 samples) window. The energy estimator  $E_{\text{uncal.}}$  is proportional to  $E$ .

This process differs from the  $E_{\text{uncal.}}$  determination done in the official analysis of GERDA [73]. Here, an improved energy resolution was achieved by applying a *Zero Area Cusp* (ZAC) filter to each pulse [119]. The ZAC filter was not applied in this work as the energy resolution is not essential in the presented analysis. A comparison of the energy resolution achieved in this work compared to the results of the official GERDA analysis can be found in Section B.3 in the Appendix.

### 8.3.2 Energy Calibration Process

The high statistics peaks mentioned in Section 8.1 and three additional  $\gamma$ -lines at 583.2 keV and 860.6 keV from  $^{208}\text{Tl}$  and 727.3 keV from  $^{212}\text{Bi}$  were used for the energy calibration. In order to calibrate the energy estimator  $E_{\text{uncal.}}$ , a linear calibration with offset was carried out as done in GERDA. For this purpose, the position of all seven peaks were precisely determined and a linear dependence was then calculated. The model for the fit of each peak was used as described in [73]. Two examples of the peak model can be seen in Figure 8.5 for the DEP (top) and the FEP ( $^{208}\text{Tl}$ , bottom) of GD35B (data). The basis of this model is a Gaussian distribution

$$g(E) = \frac{N}{\sqrt{2\pi}\sigma} \exp\left[-\frac{(E - \mu)^2}{2\sigma^2}\right] \quad (8.3)$$

where the parameters  $N$ ,  $\mu$  and  $\sigma$  are the scaling factor, position and width of the peak, respectively. For the flat background, due to multiple Compton scatters, a step function is used

$$f_{\text{step}}(E) = \frac{d}{2} \operatorname{erfc}\left(\frac{E - \mu}{\sqrt{2}\sigma}\right) \quad (8.4)$$

with  $d$  corresponding to the step functions height (given by the flat background contribution at  $E > E_{\text{peak}}$ ) and  $\operatorname{erfc}$  to the complementary error function. Finally, the residual presence of pile-up events and incomplete charge collection is modelled using a low-energy tail defined as:

$$h(E) = \frac{c}{2\beta} \exp\left(\frac{E - \mu}{\beta} + \frac{\sigma^2}{2\beta^2}\right) \operatorname{erfc}\left(\frac{E - \mu}{\sqrt{2}\sigma} + \frac{\sigma}{\sqrt{2}\beta}\right) \quad (8.5)$$

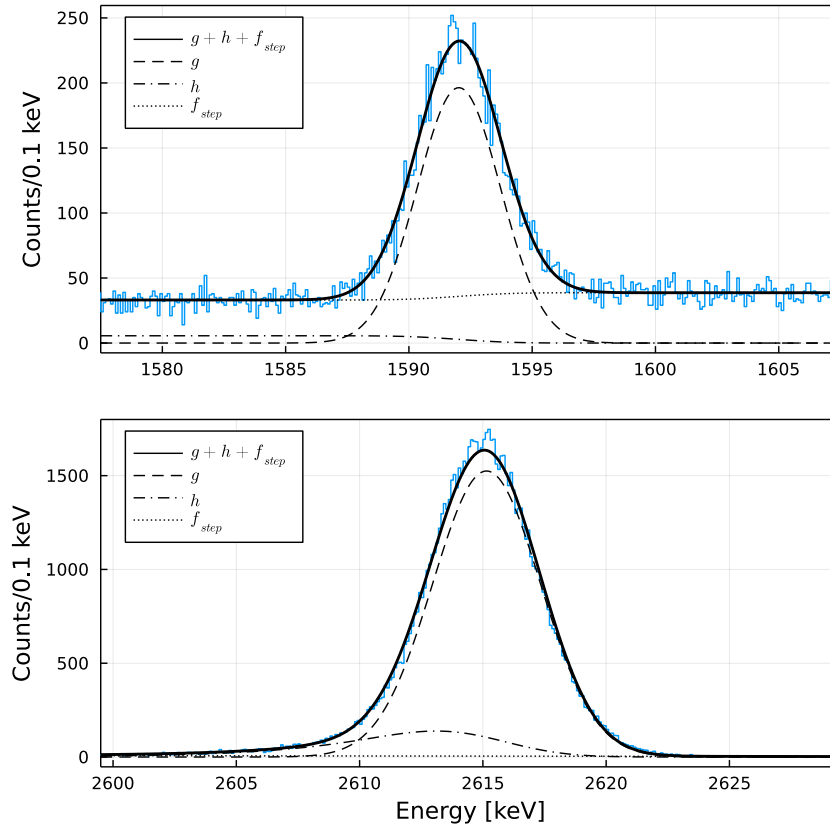


FIGURE 8.5: Fit of the DEP (top) and the FEP (bottom) of  $^{208}\text{Tl}$  in the energy spectrum of GD35B (data) with the components of the fit drawn separately.

where  $\beta$  and  $c$  are the height and slope of the tail, respectively. All three components  $g(E)$ ,  $f_{\text{step}}(E)$  and  $h(E)$  are shown separately in Figure 8.5.

After all peak positions had been determined, the energy calibration was done using a linear fit with energy offset. The resulting energy spectrum for GD35B can be seen in Figure 8.6. The seven peaks used for the calibration are labelled with their respective energy.

In order to model the energy resolution of the simulation to the real data as well as possible the simulated energy values had to be smeared. A Gaussian distribution located at 0 with the width

$$\sigma = \sqrt{a + b \cdot E + c \cdot E^2} \quad (8.6)$$

was used for this. Here,  $E$  is the raw but calibrated energy of the simulated event and  $a$ ,  $b$  and  $c$  are parameters optimised in a former analysis performed by the GERDA collaboration. For the smearing, a random value was determined using this normal distribution, which was then added to the original value. Subsequently, the seven peaks were fitted again to confirm the energy calibration has not changed due to the smearing which could be confirmed

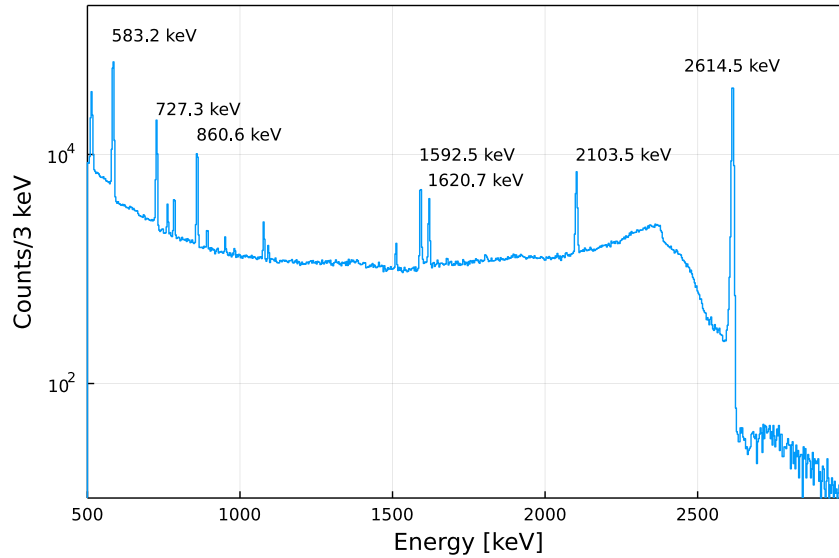


FIGURE 8.6: Energy spectrum for  $^{228}\text{Th}$  calibration data taken with GD35B. The seven high statistics peaks used for the energy calibration are labelled with their corresponding energy.

for all detectors.

### 8.3.3 Comparison GERDA Phase II & Simulation Data: Energy Calibration

Since the DEP plays a fundamental role in this analysis, it is also used for comparing the energy resolution of data and simulation. Figure 8.7 (top) shows the FWHM for all GERDA Phase II BEGe detectors for data and simulation. A clear dependence on the physical position in the detector string as already shown for the noise can be seen in both cases.

Fitting the resolution as a linear function of energy, the resolution at  $Q_{\beta\beta}$  can be interpolated. This is shown for GD35B in Figure 8.8 for data and simulation. For data and simulation, different slopes for the FWHM as function of the energy can be observed. For the derivation of the FWHM at  $Q_{\beta\beta}$ , however, the resulting deviations are within uncertainties. The values derived for all detectors can be seen in Figure 8.7 (bottom). In addition, this plot contains the resolution obtained by fitting of simulated  $0\nu\beta\beta$ -decay peaks with energy smearing applied. The comparisons as shown in Figure 8.8 for all detectors can be seen in the Appendix in Figure B.3. The uncertainties for the interpolated energy resolutions were calculated by using the fit uncertainties. For the  $0\nu\beta\beta$ -decay resolutions obtained by fitting, the uncertainty of the fit is used.

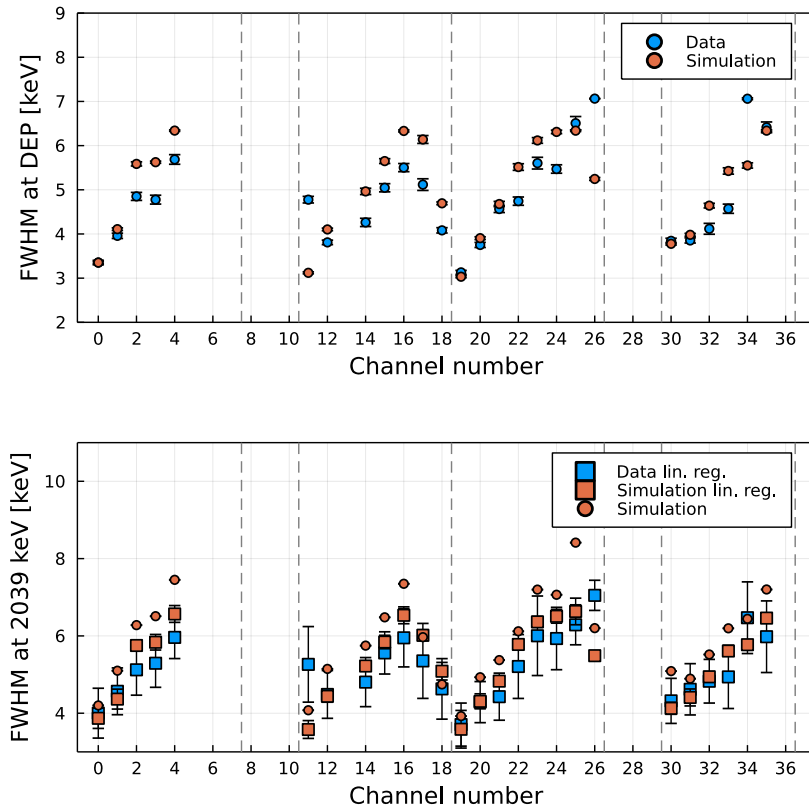


FIGURE 8.7: **Top:** FWHM of the DEP for all GERDA Phase II BEGe detectors from data and simulation. **Bottom:** FWHM at  $Q_{\beta\beta}$  derived using linear regression for all GERDA BEGe detectors for data and simulation. The values determined by fitting the simulated  $0\nu\beta\beta$ -peak are also shown marked by circles.

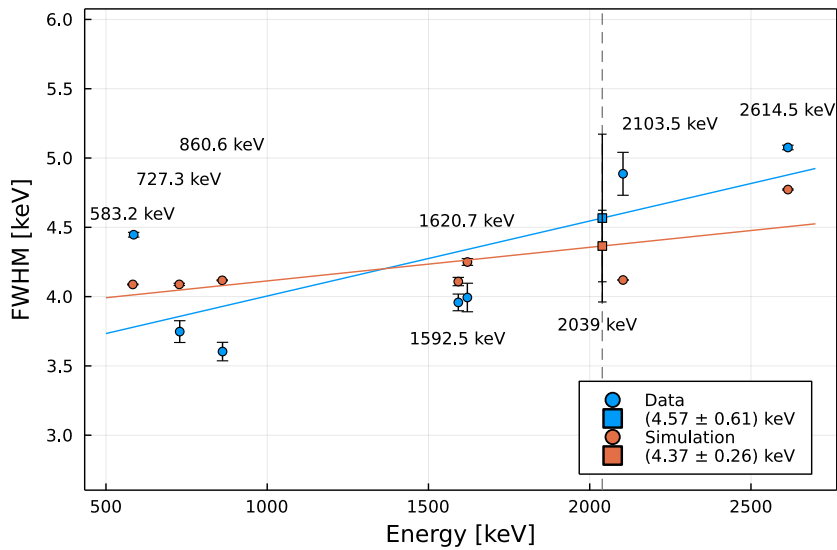


FIGURE 8.8: FWHM as function of energy for data and simulation for GD35B. A linear regression is used to estimate the values at  $Q_{\beta\beta}$  which are marked with squares.

## 8.4 $A/E$ Calibration

Using the parameter  $A/E$ , SSEs can be discriminated from MSEs and surface events as described in Section 5.3.4 with good efficiency. For this, an individual low cut value on the  $A/E$  classifier  $\zeta$  has to be determined for each detector. Before these  $A/E$  cuts are applied in Section 8.5, a comparison between data and simulation is presented.

### 8.4.1 $A/E$ Spectrum & $A/E$ Classifier

In order to calculate the  $A/E$  classifier  $\zeta$ , as defined in Equation 5.1, from the determined amplitudes  $A$  and the calibrated energy  $E$ , the energy dependent peak positions  $\mu_{A/E}(E)$  and widths  $\sigma_{A/E}(E)$  of the  $A/E$  spectrum had to be determined. For this purpose, the  $^{228}\text{Th}$  calibration spectrum was divided into 44 energy ranges of 30 keV each which are referred to as *slices*. The slices

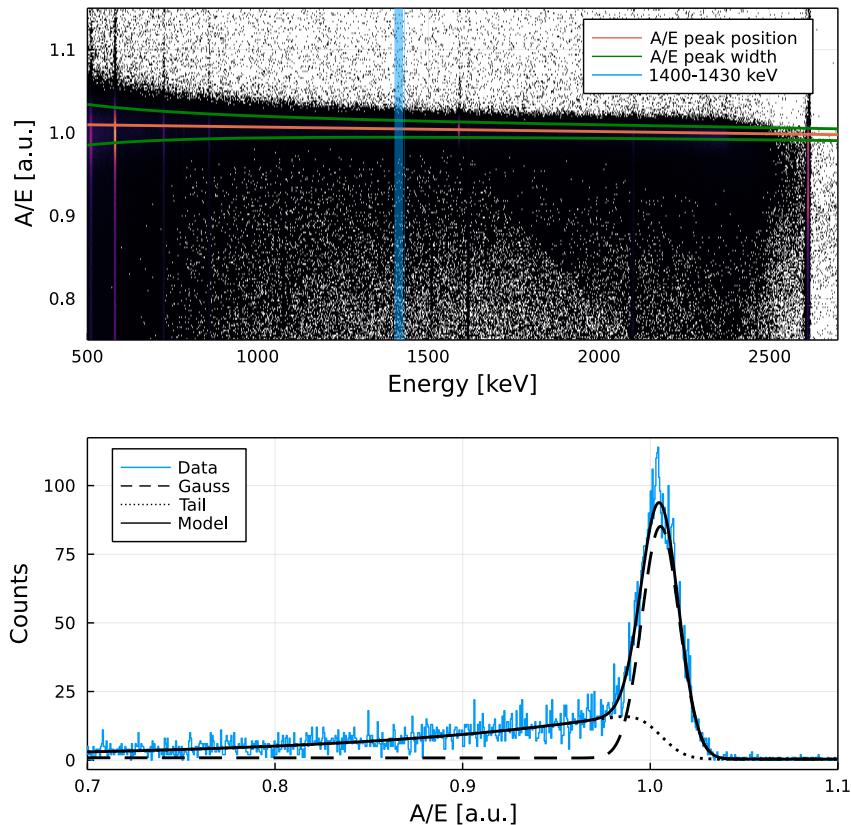


FIGURE 8.9: **Top:** Scatter plot of  $A/E$  values for GD35B (data). The fitted energy dependent  $A/E$  peak position  $\mu_{A/E}(E)$  and width  $\sigma_{A/E}(E)$  are marked in orange and green, respectively. The blue band highlights the energy range 1400 – 1430 keV for which the  $A/E$  distribution is shown in the lower plot. **Bottom:**  $A/E$  distribution for a 30 keV wide energy range and the fitted model for GD35B. Here, the linear and step background contribution of the fit model are not drawn as they are negligible.

were evaluated individually for these parameters. The selected total energy range was from 600 to 2355 keV excluding known peaks. The energy slices can be found in the Appendix B.5.

A scatter plot of the normalised  $A/E$  values of GD35B (data) can be seen in Figure 8.9 (top). Here, a simple normalisation was done using the mean  $A/E$  peak position obtained by fitting a Gaussian to the  $A/E$  distribution of all events. The model with low-energy tail described in Section 8.3.2 was used to fit all  $A/E$  distributions in the following. In this model, the Gaussian describes the SSE distribution while the tail describes the MSE distribution. The energy range 1400 – 1430 keV for an example  $A/E$  slice is shown in Figure 8.9 (bottom), with the parts of the fit drawn separately. The  $A/E$  peak position  $\mu_{A/E}$  and width  $\sigma_{A/E}$  can be obtained from the Gaussian. The results for all slices can be seen in Figure 8.10 for GD35B. A linear energy dependence is assumed for  $\mu_{A/E}(E)$  and a  $\sqrt{a + b/E^2}$  energy dependence for  $\sigma_{A/E}(E)$ . The peak position  $\mu_{A/E}(E)$  is linear only for energies above 1000 keV, which is also the relevant energy range for this analysis. However, the full energy range from 600 to 2355 keV was used for the fitting as

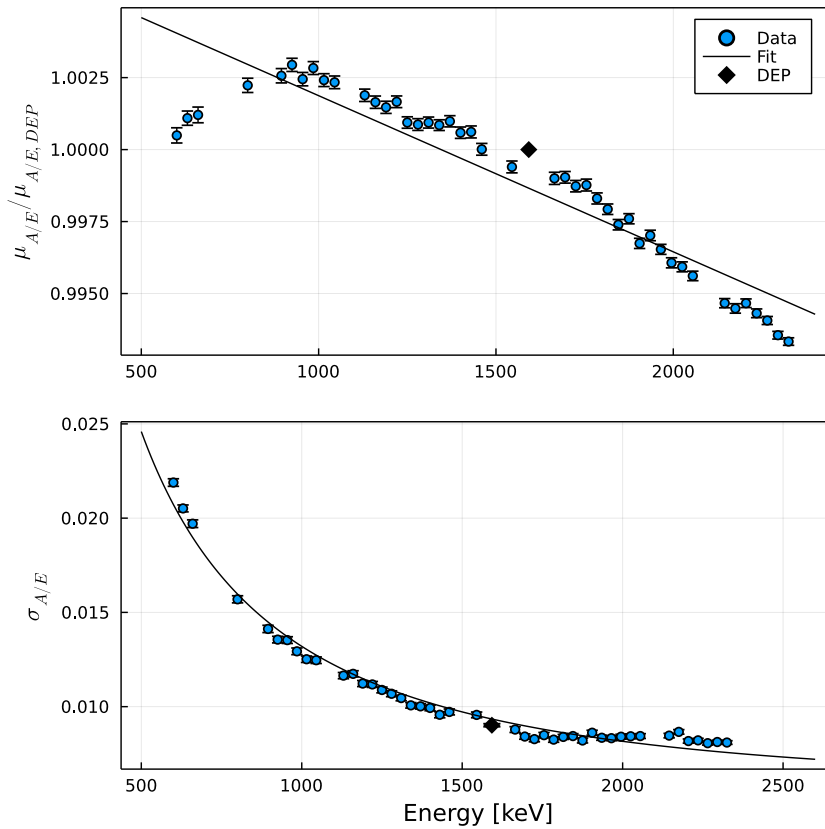


FIGURE 8.10: Energy dependent  $A/E$  peak position  $\mu_{A/E}(E)$  normalised to  $\mu_{A/E,DEP}$  (top) and width  $\sigma_{A/E}(E)$  (bottom) for GD35B (data) including fits. The given uncertainties for each point are given by the fit.

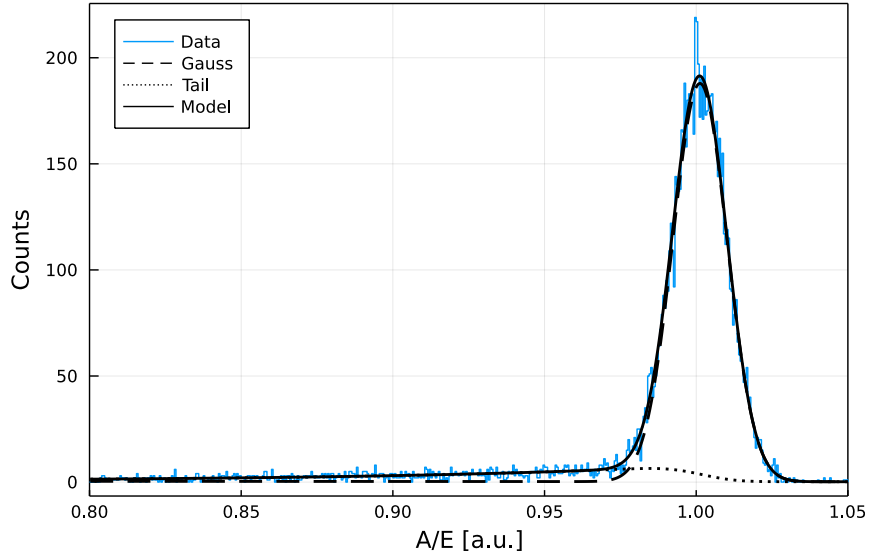


FIGURE 8.11:  $A/E$  distribution of DEP events for GD35B (data). From the almost perfect Gaussian shape of the distribution it can be inferred that there is only a small MSE contribution.

the influence on the  $A/E$  calibration was found to be negligible. The results for  $\mu_{A/E}(E)$  and  $\sigma_{A/E}(E)$  are also plotted as lines in the  $A/E$  spectrum in Figure 8.9 (top). In the same way,  $\mu_{A/E,DEP}$  and  $\sigma_{A/E,DEP}$  were obtained from the  $A/E$  distribution of the DEP shown in Figure 8.11. Here, the energy range  $E_{DEP} \pm 3\sigma_{DEP}$  was used. The  $A/E$  peak position of the DEP  $\mu_{A/E,DEP}$  was used as normalisation for  $\mu_{A/E}(E)$ .

Using the results for  $\mu_{A/E}(E)$  and  $\sigma_{A/E}(E)$ , the  $A/E$  classifier  $\zeta$  can be calculated for each pulse shape which is shown as a scatter plot for GD35B in Figure 8.12. For each energy peak of the  $^{228}\text{Th}$  calibration spectrum a higher

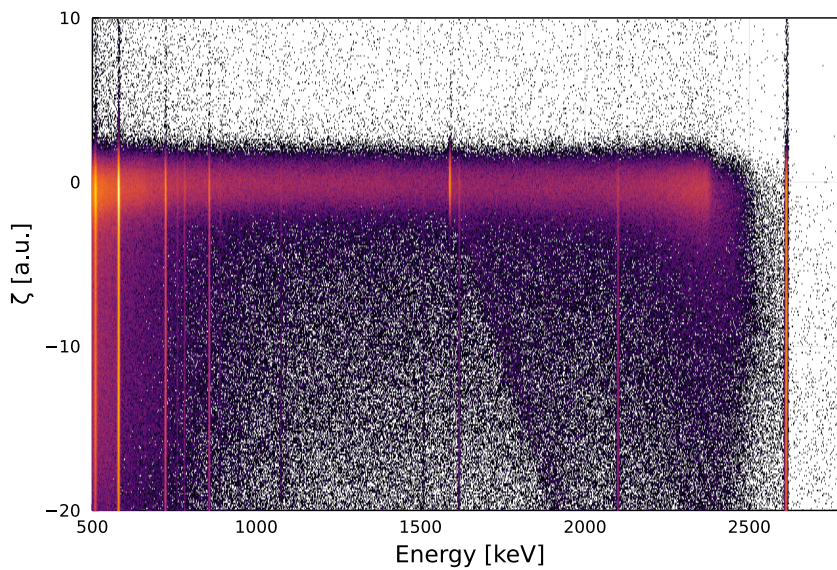


FIGURE 8.12:  $A/E$  classifier  $\zeta$  of GD35B for GERDA Phase II data. The colour scale is logarithmic and only for illustration.

number of MSEs at lower  $\zeta$  values can be seen, except for the DEP.

### 8.4.2 90 % DEP Acceptance Cut Determination

In order to identify MSEs as background with high efficiency while keeping  $0\nu\beta\beta$ -decay detection efficiency high, cut values were defined on the  $A/E$  classifier  $\zeta$ . In the following, all  $A/E$  cut values, such as the low and high  $A/E$  cuts, refer to  $A/E$  classifier values. The high  $A/E$  cut value was set to 4 for all detectors to discriminate surface events near the  $p^+$  contact. This value was chosen as it removes most surface events without decreasing  $0\nu\beta\beta$ -decay detection efficiency. The low  $A/E$  cut value was determined individually to identify MSEs and surface events near the  $n^+$  contact. For this purpose, pulses shapes of DEP events have been chosen due to their SSE characteristics. The low  $A/E$  cut value in GERDA analyses is defined at 90% survival of the DEP events after the low cut has been applied.

Two different methods were used to determine the 90% DEP acceptance cut value. These are referred to as *counting* and *fitting* methods and are independent of one another. In both cases, the high  $A/E$  cut was not applied. The uncertainties in determining the cut value are discussed in Section 8.7.2.

#### Counting Method

The effect of the low  $A/E$  cut on SSEs is examined by subtracting the contribution of MSEs from the DEP energy region using its side bands. For this, three energy ranges are defined by

$$\begin{aligned}
 \text{DEP:} & \quad E_{\text{DEP}} - n_1 \cdot \sigma_{\text{DEP}} < E < E_{\text{DEP}} + n_1 \cdot \sigma_{\text{DEP}} \\
 \text{I:} & \quad E_{\text{DEP}} - (2n_1 + n_2) \cdot \sigma_{\text{DEP}} < E < E_{\text{DEP}} - (n_1 + n_2) \cdot \sigma_{\text{DEP}} \\
 \text{II:} & \quad E_{\text{DEP}} + (n_1 + n_2) \cdot \sigma_{\text{DEP}} < E < E_{\text{DEP}} + (2n_1 + n_2) \cdot \sigma_{\text{DEP}}
 \end{aligned} \tag{8.7}$$

with  $E_{\text{DEP}}$  and  $\sigma_{\text{DEP}}$  as the DEP energy and width. The parameters  $n_1, n_2 \in [1, 4]$  define the width of the ranges and the distance between them, respectively, which is visualised in Figure 8.13 (top). The sum of the widths of the energy ranges I & II (the side bands of the peak, highlighted in orange) is equal to the width of the energy range used for the DEP (highlighted in blue). The energy range of the DEP contains both, DEP and background events like MSEs and surface events. The side bands are chosen to be far enough away from the DEP to consist mainly of background events. For most of the detectors,  $n_1$  and  $n_2$  were set to 3. For detectors with bad energy resolution, the

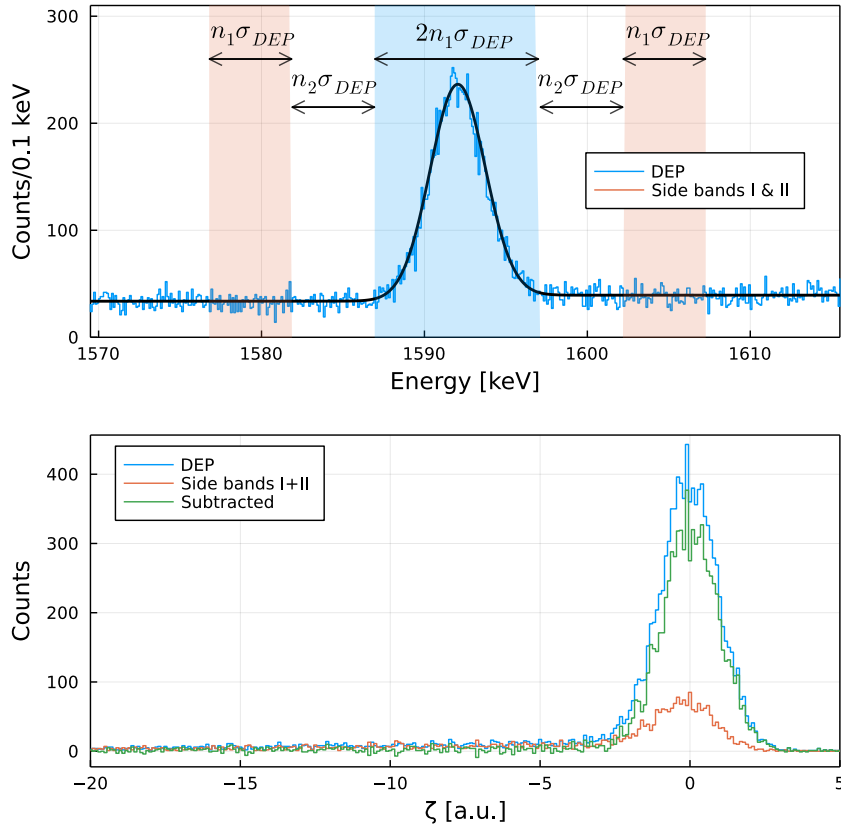


FIGURE 8.13: **Top:** DEP in the energy spectrum of GD35B (data). The DEP energy region is highlighted in blue and the two side bands in orange. The widths of the energy ranges are labelled. **Bottom:**  $A/E$  classifier  $\zeta$  distribution for the DEP (blue) and the two Compton ranges (orange) of GD35B (data). The Compton subtracted histogram is shown in green.

right side band can reach the FEP of  $^{212}\text{Bi}$ . Here, the width of the area and the distance were decreased in steps of 0.5.

After calculating the  $A/E$  classifier values for all events in the three energy ranges, two histograms can be formed which can be seen in Figure 8.13 (bottom). One histogram with the  $A/E$  classifier values of the DEP and background events (blue) and one with background events only (orange). The latter consists of the events in the two side bands. With the assumption that the composition of the background in the DEP energy region is the same as in the side bands, the bins content of the two  $A/E$  classifier histograms can be subtracted. The  $A/E$  classifier distribution created by this (green) is approximately background free. The  $A/E$  low cut value can be determined by integrating the bin content until 90% is reached. This corresponds to the 90% DEP acceptance cut value.

The fraction of events surviving the  $A/E$  low cut value, the *survival fraction*, is plotted for the background-subtracted histogram as function of the  $A/E$  cut value in Figure 8.14 as dashed line (data in blue and simulation

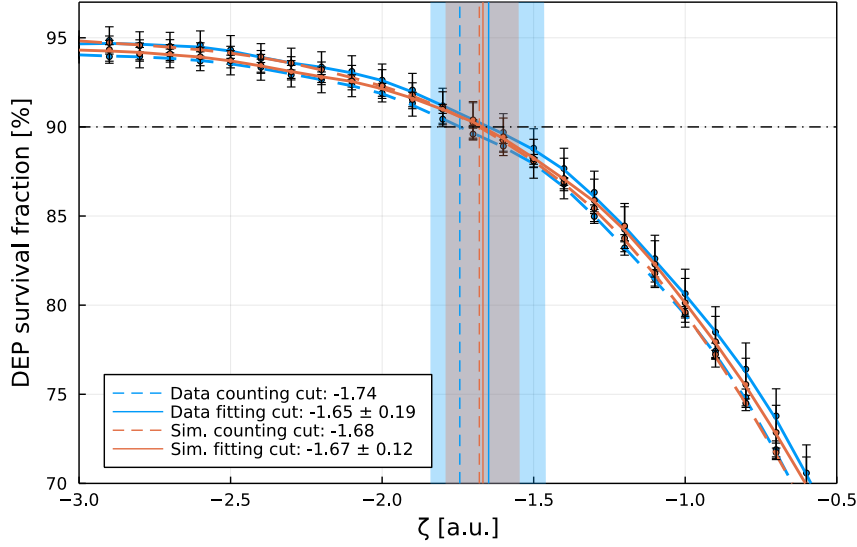


FIGURE 8.14: DEP survival fraction in percent as function of the  $A/E$  low cut value for the counting (dashed line) and fitting (solid line) method applied to data (blue) and simulation (orange) of GD35B. The determined 90% acceptance values are marked by vertical lines with their uncertainties highlighted by bands of the respective colour. The uncertainties of the individual points are statistical.

in orange). To smoothen the curve, a MWA with a fixed window size of  $\Delta\zeta_{\text{cut}} = 0.3$  was applied. The final cut value at 90% survival fraction was then determined by interpolation.

### Fitting method

The number of SSEs in the DEP is determined by fitting the energy spectrum of the DEP using the peak model from Section 8.3.2. The scaling factor  $N$  of the Gaussian distribution (Equation 8.3) in the peak model describes the area under the Gaussian and can therefore be used to determine the number of SSEs in the DEP. After applying an  $A/E$  low cut and fitting the energy peak of the remaining events, the survival fraction can be calculated. The energy spectrum of the DEP of GD35B before and after applying an  $A/E$  low cut is shown in Figure 8.15. This was done in steps of  $\Delta\zeta = 0.1$  to determine the survival fraction as function of the  $A/E$  low cut value which can be seen as solid lines (blue for data and orange for simulation) in Figure 8.14.

As with the counting method, the 90% DEP acceptance cut value was determined by applying a MWA ( $\Delta\zeta = 0.3$ ) to the survival fraction as function of  $\zeta$  followed by interpolation. The relative difference in the two methods can be used as indication for the systematic uncertainty of the cut value determination. The result of both methods are shown in Figure 8.14 for GD35B

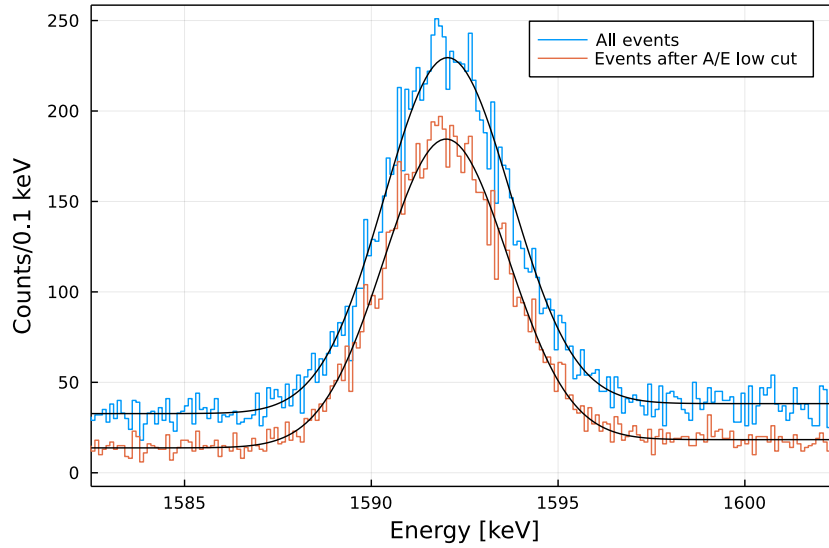


FIGURE 8.15: Fit of the DEP in the energy spectrum of GD35B (data) before and after applying a low  $A/E$  cut at  $\zeta = -1.65$ .

(data in blue and simulation in orange). Here, the survival fraction as function of the  $A/E$  low cut value is shown for both methods. The interpolated 90% DEP acceptance cut values are marked by vertical lines, solid for the fitting and dashed for the counting method. The given uncertainties on the cut value are discussed in Section 8.7.2. The fitting method is defined as the standard in the GERDA analysis.

### 8.4.3 Comparison GERDA Data & Simulation: $A/E$ Calibration & $A/E$ Low Cut

To compare the energy dependence of the  $A/E$  distribution of data and simulation (see Section 8.4.1), GD35B is used as an example. In Figure 8.16 (top) the  $A/E$  peak position  $\mu_{A/E}(E)$  is shown as a function of energy. Both, data (blue) and the simulation (orange) are normalised to their respective DEP  $A/E$  peak position  $\mu_{A/E,DEP}$  (diamond). The energy dependence of the  $A/E$  peak position was significantly weaker for the simulation, as can be seen in the example. On average, the slope of the linear fit was 5 times smaller for the simulation as for the data. For the  $A/E$  peak width  $\sigma_{A/E}(E)$ , shown in Figure 8.16 (bottom), the agreement is much better, although there is a slight discrepancy towards higher energies. Both could be explained by charge cloud diffusion as proposed in [120], which is not taken into account in the simulation. The comparisons for all detectors can be found in the Appendix in Figure B.5. In general, the  $A/E$  peak position shows a similar behaviour as can be seen in Figure 8.16 (top) for all detectors. The agreement between

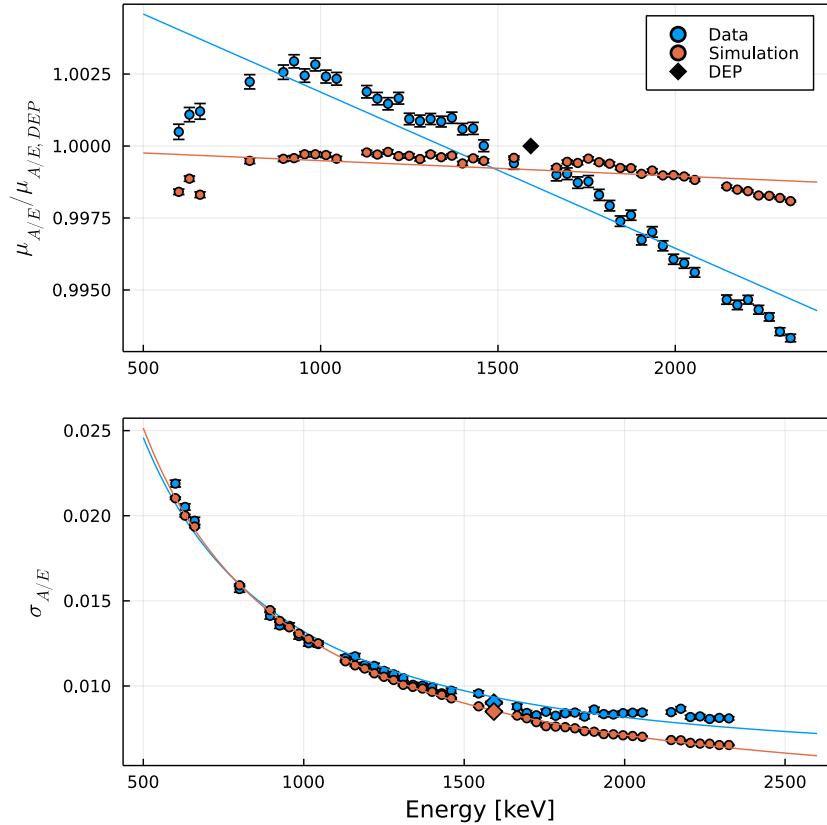


FIGURE 8.16: Energy dependent  $A/E$  peak position  $\mu_{A/E}(E)$  normalised to  $\mu_{A/E,DEP}$  (top) and width  $\sigma_{A/E}(E)$  (bottom) for data and simulation of GD35B including fits.

data and simulation for all detectors is good for the  $A/E$  peak width, but the slight discrepancy towards higher energies appears for almost all detectors. Three detectors (Ch21, Ch33, Ch34) show an overall worse  $A/E$  resolution in the data compared to the simulation.

After correction of the energy dependence of the SSE band, it was found in simulation and data that the peak position  $\mu_{A/E,DEP}$  of the DEP systemically has a slightly higher  $A/E$  value. Figure 8.17 (top) shows the peak position of the DEP  $A/E$  spectrum for all detectors, with the SSE band corresponding to the value 1. This difference between the SSE band and the DEP  $A/E$  peak position has not yet been explained. The average distance of the DEP  $A/E$  peak position to the SSE band for data is  $(0.16 \pm 0.05)\%$  while it is  $(0.07 \pm 0.02)\%$  for the simulation. One possible explanation for the difference of  $\mu_{A/E,DEP}$  to the SSE band might be the composition of MSEs and SSEs at the DEP. The ratio of MSEs in the Compton regions contributing to the Gaussian of the  $A/E$  distribution is higher compared to the DEP leading to a slightly lower peak position. When looking at the  $A/E$  resolution of the DEP, there is a good agreement between data and simulation for most detectors. These are shown, converted to FWHM, in Figure 8.17 (bottom). Here,

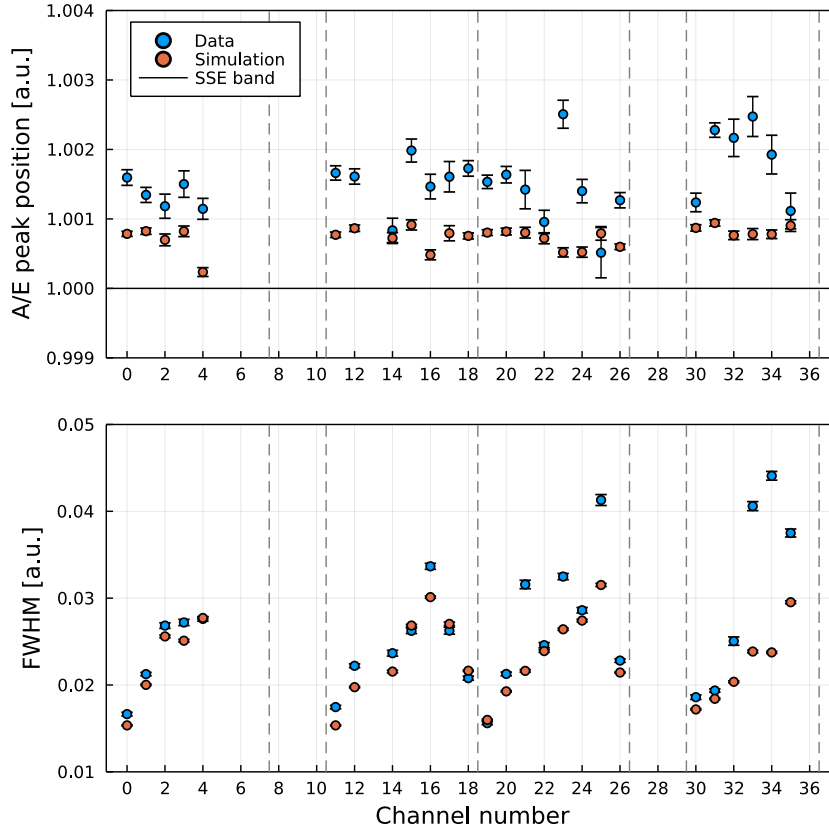


FIGURE 8.17:  $A/E$  peak position  $\mu_{DEP}$  (top) and resolution  $\sigma_{DEP}$  converted to FWHM (bottom) of the DEP for data and simulation.

the pattern due to the string position can be seen again.

The determination of the 90% DEP acceptance cut values for GD35B is shown for data and simulation in Figure 8.14. Here, the DEP survival fraction is plotted as function of the  $A/E$  low cut value. The determined results for the 90% acceptance cut are marked by vertical solid lines with bands illustrating the uncertainties which are discussed in Section 8.7.2. All determined low cut values for all detectors can be found in Figure 8.18 and in Table B.5 in the Appendix. A good match between data and simulation can be found for most detectors. The large deviation for Ch00 is likely due to a different contribution of  $p^+$  surface events in the simulation<sup>4</sup>. The respective plots for determining the cut value for all detectors can be found in the Appendix in Figure B.6.

<sup>4</sup>This was tested for Ch00 by determining the 90% DEP acceptance low cut after applying the  $A/E$  high cut ( $\zeta = 4$ ). By this, surface events were filtered and a good agreement between data and simulation was achieved.

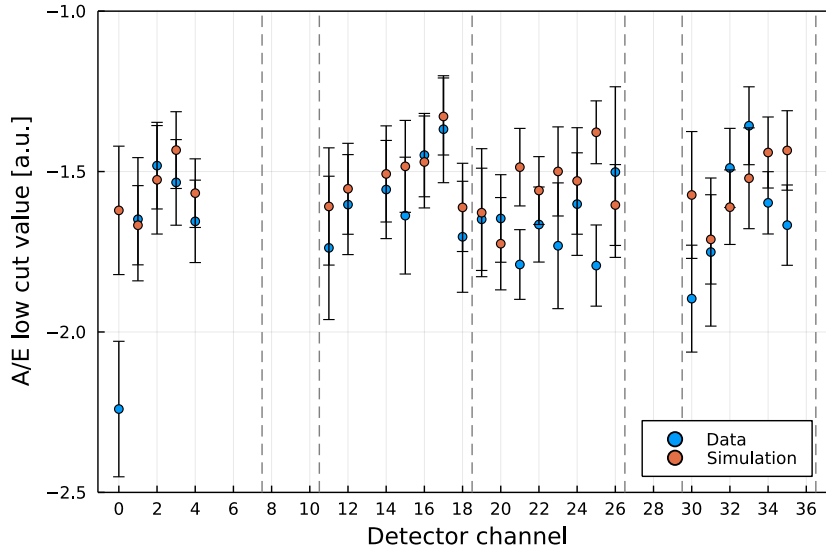


FIGURE 8.18: 90% DEP acceptance cut values for all detectors with data in blue and simulation in orange.

## 8.5 $A/E$ Cut Survival Fractions for Different Energy Regions

In order to validate the use of the simulation for the  $0\nu\beta\beta$ -decay detection efficiency, the simulated survival fractions were compared to data.

### 8.5.1 $A/E$ Survival Fraction Determination

The  $A/E$  survival fraction for different event types were calculated in a similar way as the fitting method described in Section 8.4.2. For the DEP, SEP, FEP ( $^{212}\text{Bi}$ ) and FEP ( $^{208}\text{Tl}$ ) a clear peak in the energy spectrum was visible for all detectors. These were fitted once for all events and once after applying both, the high and low  $A/E$  cuts. For the fits, the peak model with low-energy tail described in Section 8.3.2 was used. The survival fraction is given by the ratio of the areas under the fitted Gaussians after and before applying the  $A/E$  cuts. The effect of the  $A/E$  cuts is demonstrated on the energy spectrum shown in Figure 8.19. The plotted energy range shows the  $^{208}\text{Tl}$  DEP and  $^{212}\text{Bi}$  FEP of GD35B (data). As expected, the  $^{208}\text{Tl}$  DEP is only slightly affected by the  $A/E$  cuts, while the  $^{212}\text{Bi}$  FEP almost vanishes after applying the cuts.

The studied event libraries are listed in Table 8.2 including their type and the used data set. Only simulated events are available for the  $0\nu\beta\beta$  decay. For event types with continuous energy distribution (labelled with "Region" in Table 8.2), the survival fraction has been determined by event counting

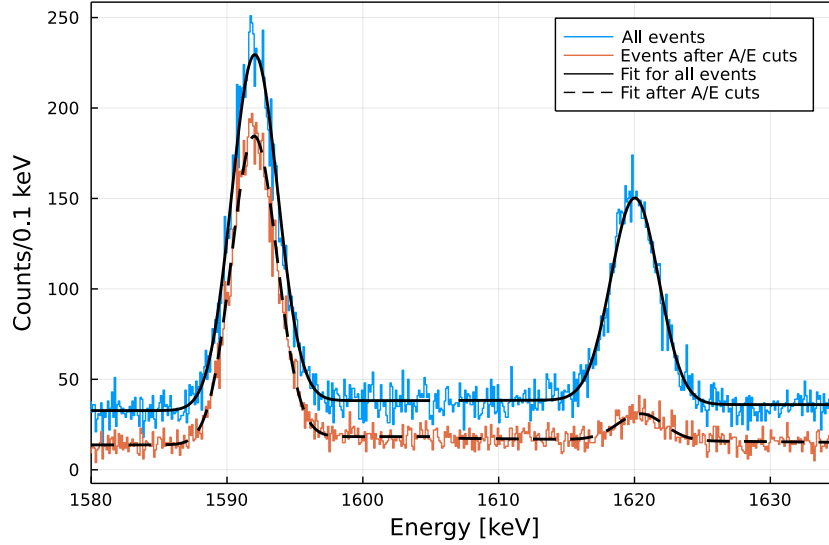


FIGURE 8.19: Energy spectrum of GD35B (data) in the range of the  $^{208}\text{Tl}$  DEP and  $^{212}\text{Bi}$  FEP. The spectrum is shown before (blue) and after applying the high and low  $A/E$  cuts (orange). The corresponding fits are plotted for each peak individually.

Source	Name	$E$ [keV]	Type	Data	Characteristic
$^{208}\text{Tl}$	DEP	1592.5	Peak	Calibration	SSE
$^{212}\text{Bi}$	FEP	1620.7	Peak	Calibration	MSE
$^{208}\text{Tl}$	SEP	2103.5	Peak	Calibration	MSE
$^{208}\text{Tl}$	FEP	2614.5	Peak	Calibration	MSE
-	Compton	1100 – 1400	Region	Calibration	SSE & MSE
-	Compton	1700 – 2000	Region	Calibration	SSE & MSE
$^{76}\text{Ge}$	$2\nu\beta\beta$	700 – 1300	Region	Physics	SSE
$^{76}\text{Ge}$	$0\nu\beta\beta$	2039.1	Peak	Only sim.	SSE

TABLE 8.2: Signal libraries for  $A/E$  cut survival fractions analysis. GERDA Phase II and simulated data is used for the calibration and physics data type.

before and after applying the  $A/E$  cut. One of these is the  $2\nu\beta\beta$  decay between 700 and 1300 keV. Physics data after applying the anti coincidence and LAr veto cuts were used for this. In addition, two Compton continua were examined from the calibration data.

### 8.5.2 Survival Fraction Results

Figure 8.20 shows, from top (a) to bottom (d), the  $A/E$  cut survival fractions for data and simulation for DEP, FEP ( $^{212}\text{Bi}$ ), SEP and FEP ( $^{208}\text{Tl}$ ), respectively. The combined DEP survival fractions for all detectors weighted to their individual exposure contribution (see Table 8.3) in the used data set are  $(87.7 \pm 1.7)\%$  for data and  $(87.8 \pm 1.7)\%$  for simulation showing excellent agreement. Here, the weighted mean uncertainty of all detectors is given.

Also, the trends for the MSE samples for data and simulation are in good agreement, even though channels 21, 25, 33, 34 and 35 show noticeable deviations. For these detectors, deteriorated *A/E* DEP resolutions can be seen in Figure 8.17 (bottom) for the data. The complete list of survival fractions of the DEP, SEP and the FEPs can be found in Table B.2 and B.3 in the Appendix for all detectors individually.

The survival fraction for two Compton continua can be seen in Figure 8.21 (a & b). Here, the simulation shows on average a 5% higher survival fraction compared to data. This is likely due to hits in the transition layer of the detector leading to slow or incomplete charge collection which were not simulated. This only affects event types defined by an energy region. All survival fractions of the Compton continua can be found in Table B.4 in the Appendix.

Figure 8.21 (c) shows the survival fractions for data and simulation for  $2\nu\beta\beta$  decay. The combined survival fractions of  $2\nu\beta\beta$  events for all detectors weighted to their individual exposure contribution (see Table 8.3) in the used data set are  $(85.3 \pm 2.7)\%$  for data and  $(90.4 \pm 1.7)\%$  for simulation. Most of this difference is due to energy depositions in the transition layer, just like the for the Compton continua. In addition, a background-free spectrum was used for the simulation, whereas in the data there were still a few background events that survived the anti coincidence and LAr cuts. For GERDA analysis, another classifier was introduced to discriminate events with incomplete charge collection: the  $\delta E$  classifier [12]. Removing the surface events that have been discriminated by the  $\delta E$  classifier from the data set<sup>5</sup>, leads to a survival fraction of  $(86.6 \pm 2.7)\%$  for the data.

The uncertainties given in Figure 8.20 and 8.21 contain both, statistical and systematic uncertainties and are discussed in Section 8.7.

---

<sup>5</sup>The classification of the official GERDA analysis has been used here.

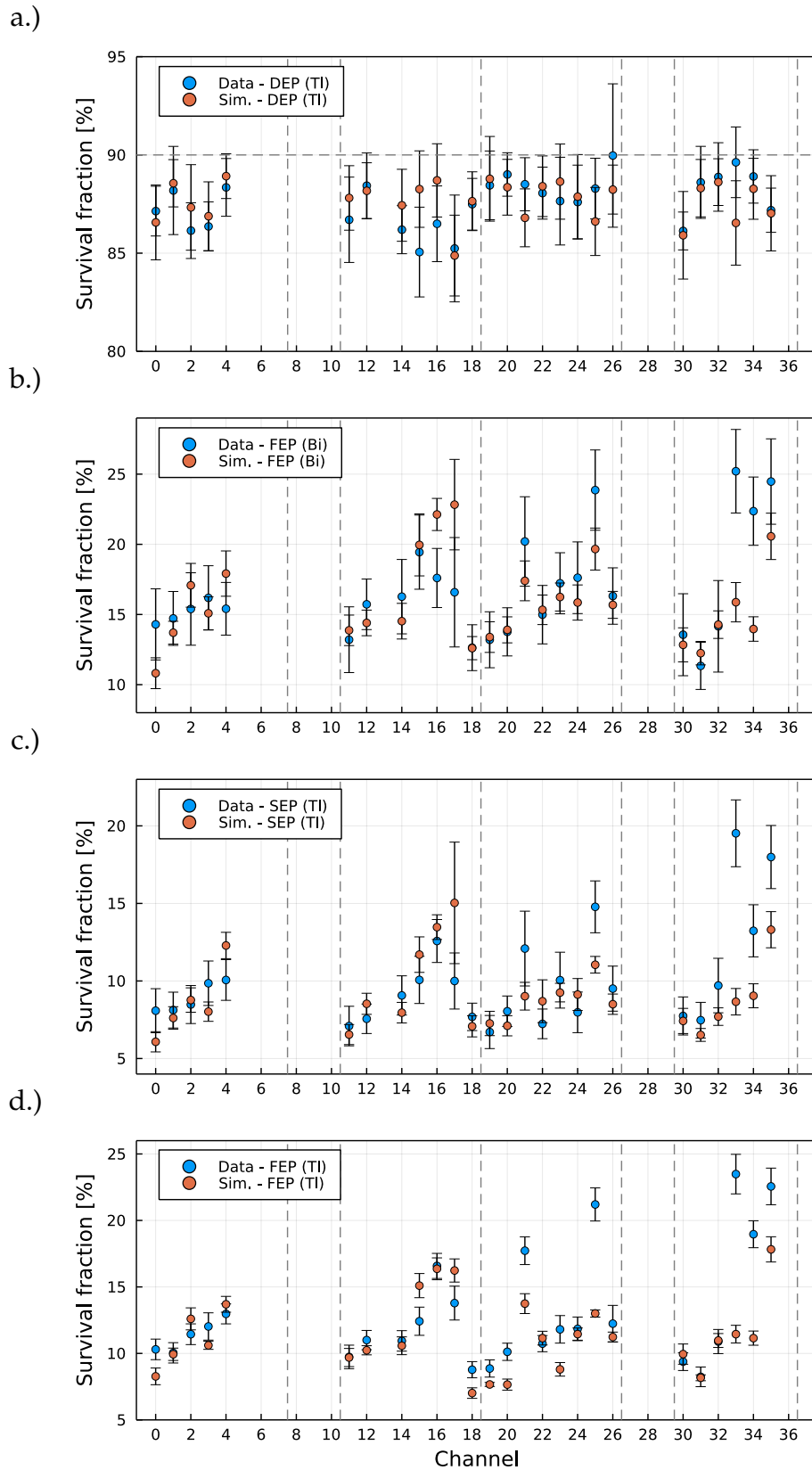


FIGURE 8.20: Comparison of the survival fractions after low and high  $A/E$  cut for the (a) DEP, (c) SEP and (d) FEP of  $^{208}\text{Tl}$  and the (b) FEP of  $^{212}\text{Bi}$  for data and simulation. The values are given with statistical and systematic uncertainties.

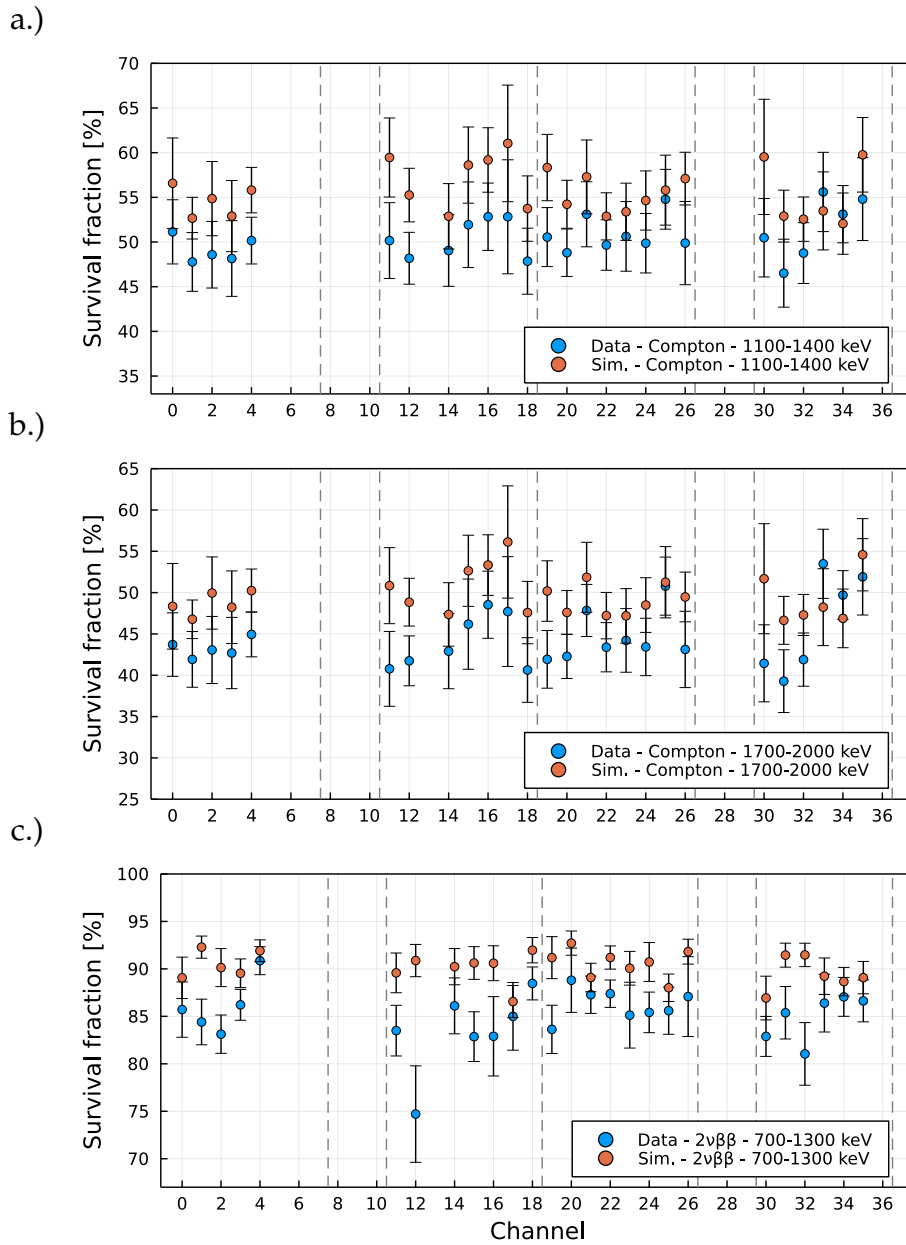


FIGURE 8.21: Comparison of the survival fractions after low and high  $A/E$  cut for two Compton continua (a & b) and  $2\nu\beta\beta$ -decay (c) for data and simulation. The values are given with statistical and systematic uncertainties.

## 8.6 $0\nu\beta\beta$ -Decay Detection Efficiency

After validation of the simulation, the  $0\nu\beta\beta$ -decay detection efficiency was determined. The pulses were created from  $0\nu\beta\beta$  decays simulated with MaGe as described in Section 8.1 and their energy values smeared, just as it was done for every other pulse. The efficiency was determined by fitting<sup>6</sup> the  $0\nu\beta\beta$  peak for all events before and after applying the  $A/E$  high and low cut. The results are shown for all detectors in orange in Figure 8.22. All detectors with their  $0\nu\beta\beta$ -decay detection efficiency and exposure are listed in Table 8.3. The mean weighted by exposure gives an efficiency of  $(85.9 \pm 1.8)\%$  for a total exposure of 12.6 kg·yr.

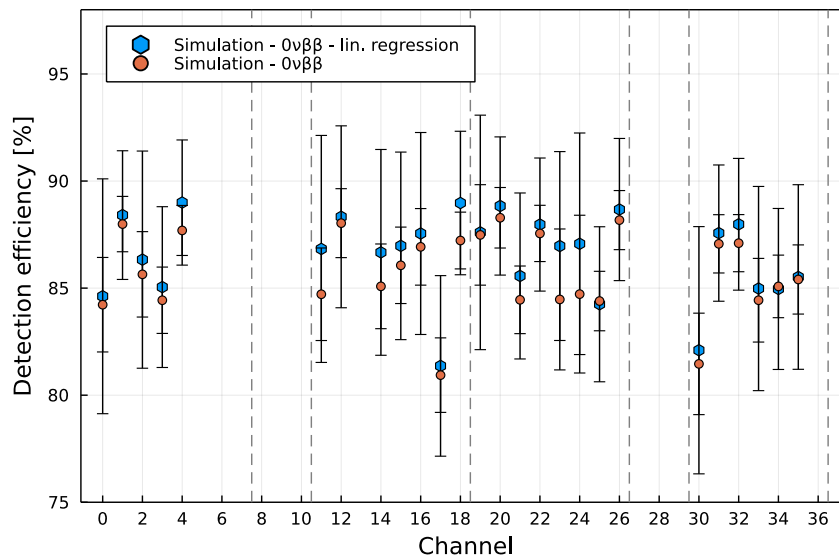


FIGURE 8.22:  $A/E$  cut efficiencies for  $0\nu\beta\beta$  decay for the simulation (orange). In addition, the results from extrapolating the  $2\nu\beta\beta$ -decay survival fractions are given in blue. All values are given with statistical and systematic uncertainties.

A further estimate on the  $0\nu\beta\beta$ -decay detection efficiency was determined by extrapolating the  $2\nu\beta\beta$ -decay survival fraction as function of energy. For this, the  $2\nu\beta\beta$ -decay survival fraction after applying the  $A/E$  cuts was determined from 700 keV to 1300 keV in steps of 100 keV. In simulation, this results in a clear linear trend as can be seen in Figure 8.23 for GD35B. By extrapolating to higher energies, the  $0\nu\beta\beta$ -decay detection efficiency can be determined. The results can be seen in blue in Figure 8.22 and in Table 8.3

<sup>6</sup>The Counting method could also have been used for this, since the simulated data set does not contain any background events. However, the fitting method was used to have a better comparison to the determination of the DEP survival fraction. The results obtained using the counting method deviate by less than 1% from the results obtained using the fitting method.

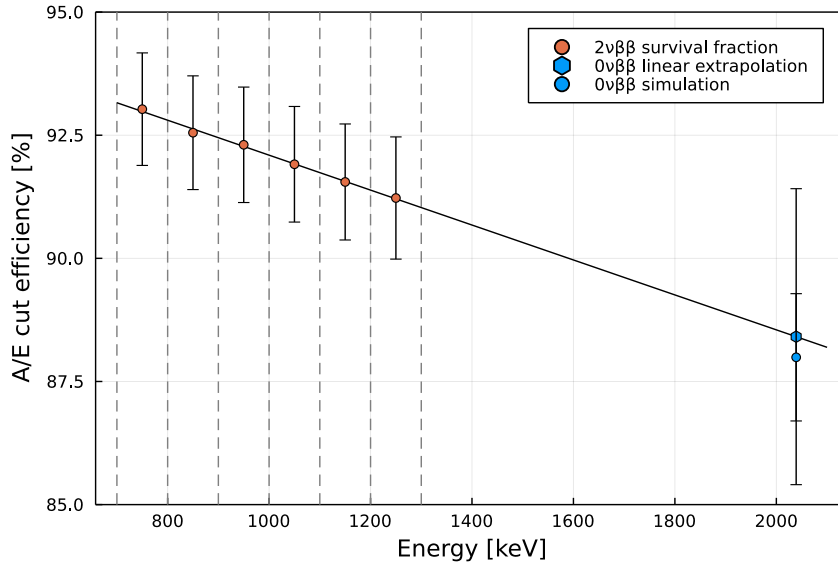


FIGURE 8.23:  $A/E$  survival fraction as function of energy for  $2\nu\beta\beta$  decays for GD35B (simulation). The extrapolated  $0\nu\beta\beta$ -decay detection efficiency is marked by a blue hexagon. The energy ranges for the individual survival fractions are marked by dashed grey lines. In addition, the result from fitting the survival fraction is shown as blue dot.

given by  $\epsilon_{0\nu\beta\beta, \text{Ext}}$  for all detectors. The weighted mean efficiency of all detectors results in  $(86.8 \pm 4.1)\%$ .

The uncertainties for the  $2\nu\beta\beta$ -decay survival fractions used for the estimation were calculated as described in Section 8.7.3. The uncertainties for the extrapolated  $0\nu\beta\beta$ -decay detection efficiencies were then calculated by propagating the uncertainties of the energy dependent  $2\nu\beta\beta$ -decay survival fraction through the process of linear regression. Unfortunately, no comparison could be made to real data because the statistics were not sufficient.

In the data-driven analysis performed by the GERDA collaboration [12], the  $0\nu\beta\beta$ -decay detection efficiency was derived by extrapolating the survival fractions of the DEP ( $^{208}\text{Tl}$ ) and  $2\nu\beta\beta$ -decays using BEGe detector data from July 2018 to November 2019. Here, a result of  $(89.0 \pm 4.1)\%$  was determined for 21.9 kg·yr of exposure which is in agreement with the results of this work.

The survival fraction of the DEP from simulation is 1.9% higher compared to the  $0\nu\beta\beta$ -decay detection efficiency. This difference can partly be attributed to the different spatial distributions of energy deposits for different event types. Figure 8.24 shows the spatial distribution of simulated DEP events for a GERDA simulation run of GD35B. In addition, the event distribution of the SSEs and the events cut by the high and low cut are also shown separately. It is expected, that the events are mainly located at the edge of the

Ch.	Exposure in kg·yr	$\epsilon_{2\nu\beta\beta}$ , Data in %	$\epsilon_{2\nu\beta\beta}$ , Sim. in %	$\epsilon_{0\nu\beta\beta}$ , Ext. in %	$\epsilon_{0\nu\beta\beta}$ in %
00	0.46	85.71 ± 2.91	89.06 ± 2.18	84.62 ± 5.48	84.23 ± 2.21
01	0.62	84.41 ± 2.40	92.29 ± 1.17	88.41 ± 3.00	87.99 ± 1.29
02	0.48	83.12 ± 2.02	90.14 ± 2.00	86.33 ± 5.07	85.64 ± 1.99
03	0.48	86.21 ± 1.63	89.54 ± 1.51	85.05 ± 3.75	84.43 ± 1.55
04	0.56	90.86 ± 1.47	91.91 ± 1.15	89.00 ± 2.92	87.69 ± 1.17
11	0.40	83.50 ± 2.67	89.58 ± 2.09	86.83 ± 5.30	84.71 ± 2.16
12	0.53	74.71 ± 5.08	90.88 ± 1.70	88.33 ± 4.25	88.03 ± 1.61
14	0.55	86.11 ± 2.94	90.23 ± 1.91	86.67 ± 4.81	85.08 ± 1.98
15	0.39	82.86 ± 2.62	90.62 ± 1.72	86.97 ± 4.38	86.06 ± 1.79
16	0.47	82.90 ± 4.18	90.60 ± 1.84	87.55 ± 4.72	86.93 ± 1.79
17	0.27	85.00 ± 3.57	86.55 ± 1.69	81.37 ± 4.22	80.94 ± 1.74
18	0.60	88.47 ± 1.74	91.97 ± 1.34	88.97 ± 3.35	87.22 ± 1.33
19	0.48	83.63 ± 2.54	91.18 ± 2.22	87.60 ± 5.48	87.48 ± 2.35
20	0.52	88.80 ± 3.39	92.71 ± 1.28	88.84 ± 3.23	88.29 ± 1.41
21	0.38	87.28 ± 1.97	89.09 ± 1.50	85.57 ± 3.88	84.45 ± 1.58
22	0.62	87.38 ± 1.44	91.20 ± 1.22	87.97 ± 3.11	87.55 ± 1.31
23	0.62	85.13 ± 3.47	90.07 ± 1.78	86.97 ± 4.41	84.47 ± 3.29
24	0.59	85.42 ± 2.14	90.73 ± 2.05	87.07 ± 5.17	84.72 ± 3.68
25	0.40	85.60 ± 2.49	88.01 ± 1.45	84.25 ± 3.62	84.40 ± 1.39
26	0.57	87.08 ± 4.21	91.82 ± 1.31	88.67 ± 3.32	88.18 ± 1.38
30	0.38	82.89 ± 2.11	86.93 ± 2.30	82.10 ± 5.77	81.46 ± 2.37
31	0.60	85.38 ± 2.76	91.45 ± 1.26	87.57 ± 3.18	87.07 ± 1.36
32	0.22	81.04 ± 3.30	91.47 ± 1.23	87.98 ± 3.08	87.10 ± 1.33
33	0.45	86.39 ± 3.04	89.23 ± 1.92	84.98 ± 4.77	84.43 ± 1.95
34	0.55	87.05 ± 2.05	88.66 ± 1.50	84.96 ± 3.76	85.08 ± 1.46
35	0.40	86.63 ± 2.21	89.08 ± 1.71	85.52 ± 4.31	85.40 ± 1.62
	12.6	85.3 ± 2.7	90.4 ± 1.7	86.8 ± 4.1	85.9 ± 1.8

TABLE 8.3: Exposure,  $2\nu\beta\beta$  and  $0\nu\beta\beta$  detection efficiency for all detectors in the used data set.

detector and are strongly aligned to the position of the source. Figure 8.25 shows the event distributions for simulated  $0\nu\beta\beta$ -decay events. As expected, these events are evenly distributed throughout the entire detector volume. In a data-driven analysis, the different event distributions have to be taken into account by assumptions. Hence, the uncertainty on the  $0\nu\beta\beta$ -decay detection efficiency is higher compared to the presented simulation-driven analysis.

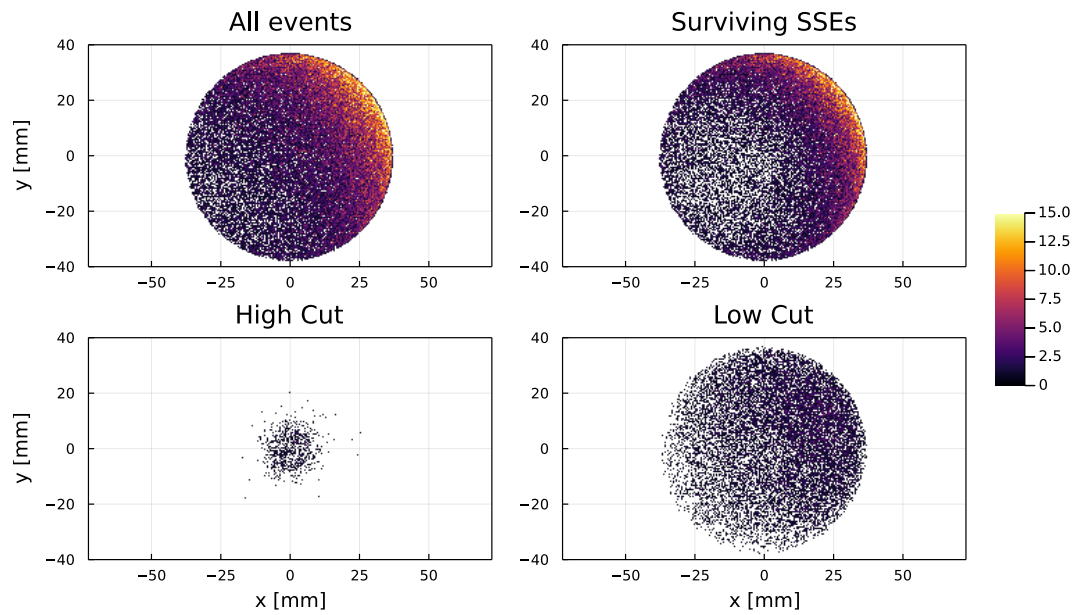


FIGURE 8.24: Spatial distribution of all DEP events of the simulation of GD35B. All events in the energy range  $1592.5 \text{ keV} \pm 3\sigma$  are shown at the top left. On the top right, all events that survived the  $A/E$  cuts. The effect of the high and low cuts can be seen in the two lower plots, respectively.

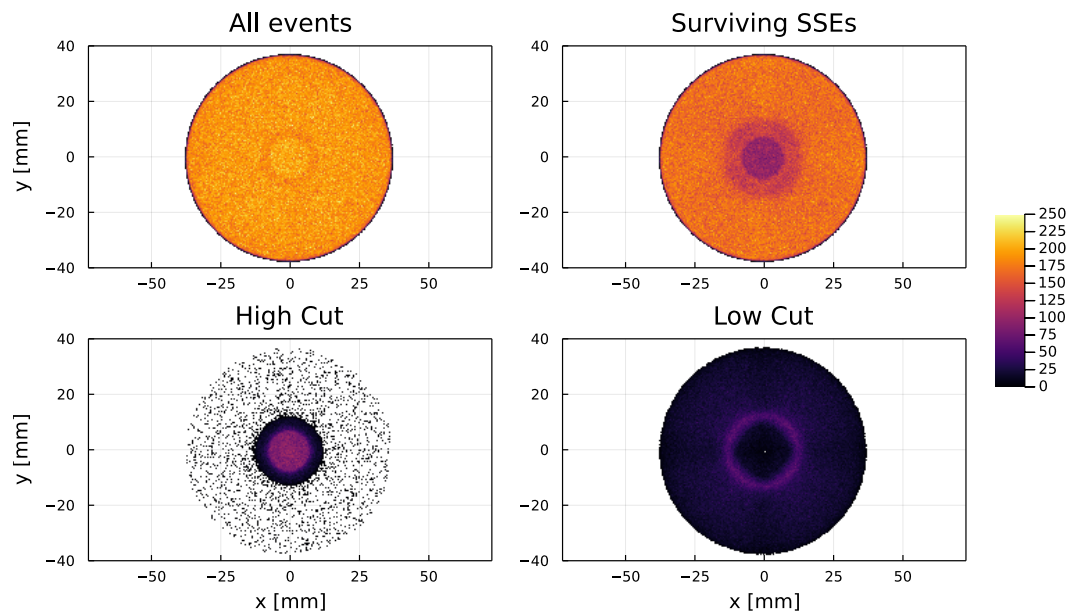


FIGURE 8.25: Spatial distribution of all  $0\nu\beta\beta$  events of the simulation of GD35B. All events are shown at the top left. On the top right, all events that survived the  $A/E$  cuts. The effect of the high and low cuts can be seen in the two lower plots, respectively.

## 8.7 Uncertainty Evaluation

When determining the uncertainties of the  $A/E$  cut survival fractions and the  $0\nu\beta\beta$ -decay detection efficiency, a few points must be considered. First of all, the individual components of the  $A/E$  classifier  $\zeta$  from Equation 5.1 need to be evaluated. These represent the basis for all further uncertainties as the individual cut values were determined from the classifier values and the efficiencies were determined by applying these.

### 8.7.1 $A/E$ Classifier

When calculating the  $A/E$  classifier  $\zeta$  using Equation 5.1, the following parameters are used:  $A$ ,  $E$ ,  $\mu(E)$ ,  $\sigma(E)$ . Each parameter has its own uncertainties, which arise either through the determination of the value and/or through calibration.

**$A$  &  $E_{\text{uncal.}}$  determination:** Here, the reproducibility of the method was investigated by using simulated pulses. The events close to the DEP are particularly important for this analysis and the determination of the cut value, which is why simulated DEP events were used here. For all DEP pulses of one detector after applying the electronics model and adding realistic noise,  $A$  and  $E_{\text{uncal.}}$  were determined. Since these are simulated events, the influence of background events can be excluded.

The distributions of the determined  $A$  and  $E_{\text{uncal.}}$  values are shown in Figure 8.26 for GD35B as an example. As expected, they are very well described by a Gaussian distribution due to the normally distributed noise component. In the example shown, the standard deviations were  $\sigma_A = 0.8\%$  and  $\sigma_{E_{\text{uncal.}}} = 0.1\%$  which can be taken as the systematic uncertainties for  $A$  and  $E_{\text{uncal.}}$ , respectively. Both deviations were very small, whereby that of  $E_{\text{uncal.}}$  is negligible as it will be absorbed by the uncertainties of the energy calibration. The method of determining  $A$  therefore is dominated by  $\sigma_A$  and results in a systematic uncertainty of  $\Delta A = 0.8\%$  for  $\zeta$  of GD35B. In general,  $\Delta E_{\text{uncal.}}$  is about a factor of 10 smaller than  $\Delta A$  for all detectors. The uncertainties  $\Delta A$  and  $\Delta E_{\text{uncal.}}$  for all detectors are listed in Table B.5 in the Appendix.

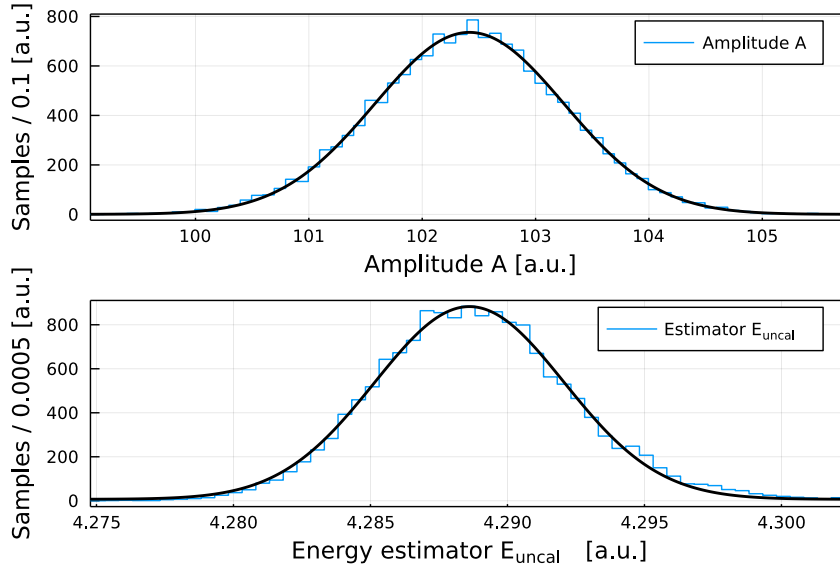


FIGURE 8.26: Distribution of the determined amplitudes  $A$  (top) and energy estimators  $E_{\text{uncal}}$ . (bottom) for simulated DEP pulses of GD35B

**Energy calibration:** The systematic uncertainty on the  $E_{\text{uncal}}$ . determination is negligible, but not for the energy calibration. A linear dependence between  $E_{\text{uncal}}$ . and the energy  $E$  was assumed in Section 8.3.2. This is described by

$$E(E_{\text{uncal}}) = m_E \cdot E_{\text{uncal}} + t_E \quad (8.8)$$

where  $m_E$  and  $t_E$  are parameters of the linear fit with uncertainties  $\Delta m_E$  and  $\Delta t_E$  given by the fit, respectively. Following the rule of error propagation, the uncertainty  $\Delta E$  is given by

$$\Delta E = \sqrt{\left(\frac{\partial E}{\partial m_E} \cdot \Delta m_E\right)^2 + \left(\frac{\partial E}{\partial t_E} \cdot \Delta t_E\right)^2} = \sqrt{(E_{\text{uncal}} \cdot \Delta m_E)^2 + \Delta t_E^2}. \quad (8.9)$$

For GD35B this results in an uncertainty for a DEP event of  $(1592.5 \pm 0.8)$  keV.

**$A/E$  energy dependence:** Only the corrections for the energy dependent peak position  $\mu(E)$  and width  $\sigma(E)$  are relevant for the final determination of the classifier uncertainty. Again, a linear dependence was assumed for  $\mu(E)$ , whereby the uncertainty can be calculated according to Equation 8.9 resulting in

$$\Delta \mu = \sqrt{(E \cdot \Delta m_\mu)^2 + \Delta t_\mu^2} \quad (8.10)$$

where  $\Delta m_\mu$  and  $\Delta t_\mu$  are the uncertainties of the linear fit parameters. However,  $\sigma(E)$  was described by  $\sqrt{a + b/E^2}$ . The associated uncertainty  $\Delta \sigma$  can

be calculated by

$$\begin{aligned}\Delta\sigma &= \sqrt{\left(\frac{\partial\sigma}{\partial a} \cdot \Delta a\right)^2 + \left(\frac{\partial\sigma}{\partial b} \cdot \Delta b\right)^2 + \left(\frac{\partial\sigma}{\partial E} \cdot \Delta E\right)^2} \\ &= \frac{1}{2\sqrt{a + b/E^2}} \sqrt{\Delta a^2 + \frac{\Delta b^2}{E^4} + \frac{b^2 \cdot \Delta E^2}{E^6}}\end{aligned}\quad (8.11)$$

taking the fit uncertainties  $\Delta a$  and  $\Delta b$  as well as the energy calibration uncertainty  $\Delta E$  from Equation 8.9 into account.

**$A/E$  Classifier  $\zeta$ :** The uncertainties for the classifier  $\Delta\zeta$  were calculated according to the rules of error propagation. The energy calibration, the peak position  $\mu(E)$  and width  $\sigma(E)$  have to be taken into account. The calculation was then carried out via

$$\begin{aligned}\Delta\zeta' &= \sqrt{\left(\frac{\partial\zeta}{\partial E} \cdot \Delta E\right)^2 + \left(\frac{\partial\zeta}{\partial\mu} \cdot \Delta\mu\right)^2 + \left(\frac{\partial\zeta}{\partial\sigma} \cdot \Delta\sigma\right)^2} \\ &= \sqrt{\left(\frac{\partial\zeta}{\partial E} \cdot \Delta E\right)^2 + \left(\frac{-A/E}{\mu^2\sigma} \cdot \Delta\mu\right)^2 + \left(\left(1 - \frac{A/E}{\mu}\right) \cdot \frac{\Delta\sigma}{\sigma^2}\right)^2}\end{aligned}\quad (8.12)$$

with

$$\frac{\partial\zeta}{\partial E} = -\frac{\left(bm_\mu^2 + 2Aam_\mu\right) E^2 + (2bm_\mu + Aa) t_\mu E + bt_\mu^2 + Abm_\mu}{\left(\frac{b}{E^2} + a\right)^{\frac{3}{2}} E^3 (m_\mu E + t_\mu)^2}$$

which takes the energy dependence of  $\mu(E)$  and  $\sigma(E)$  into account. Furthermore, the systematic uncertainty of the determination of the amplitude  $\Delta\zeta_A = \zeta \cdot \sigma_A$  must now be considered. The final uncertainty for the  $A/E$  classifier  $\Delta\zeta$  results from:

$$\Delta\zeta = \sqrt{\Delta\zeta'^2 + \Delta\zeta_A^2}.\quad (8.13)$$

### 8.7.2 $A/E$ Cut Value

The  $A/E$  low cut value is in principle an  $A/E$  classifier value, but the uncertainty cannot be calculated using Equation 8.13. This is because it is not based on a pulse shape but was determined from a distribution of  $\zeta$  values of events in the DEP region. To estimate the uncertainty, all events in the range

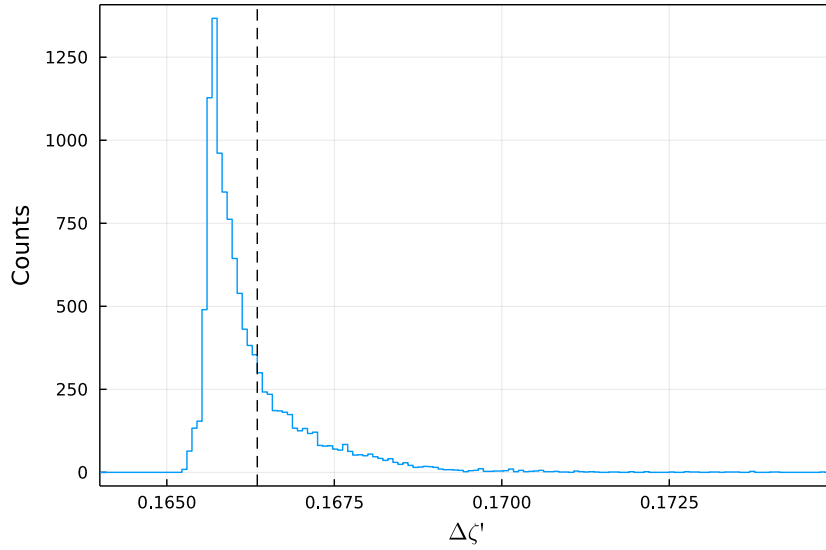


FIGURE 8.27: Distribution of  $A/E$  classifier uncertainties for the events in the region of the DEP of GD35B (data). When summing up the number of events starting from the left, the vertical dashed line marks the point where 68% of all events are reached.

$\pm 10$  keV around the DEP were therefore looked at. All classifiers  $\zeta$  and the associated uncertainties were calculated and plotted in a histogram. Figure 8.27 shows a histogram of all obtained uncertainties for GD35B (data). The total number of events was now determined and the bins of the histogram were added up from the left until one standard deviation (68%) was reached. This point is marked in the histogram by the dashed vertical line. This value was then used for the uncertainty  $\Delta\zeta'_{\text{cut}}$  of the  $A/E$  low cut value for the given detector.

For those calculations,  $\Delta\zeta'$  was considered for the individual uncertainties.  $\Delta\zeta_{A,\text{cut}}$  was taken into account for the cut value itself by using  $\Delta\zeta_{A,\text{cut}} = \zeta_{\text{cut}} \cdot \sigma_A$ . In addition, the difference between the counting and fitting methods  $\Delta\zeta_{\text{method}}$  (see Section 8.4.2) was considered. The final uncertainty  $\Delta\zeta_{\text{cut}}$  is defined by

$$\Delta\zeta_{\text{cut}} = \sqrt{\Delta\zeta'_{\text{cut}}{}^2 + \Delta\zeta_{A,\text{cut}}{}^2 + \Delta\zeta_{\text{method}}{}^2}. \quad (8.14)$$

The cut values and their uncertainties can be found in Table B.5 in the Appendix, also including all components.

### 8.7.3 $A/E$ Cut Efficiency & Survival Fraction

When determining the  $A/E$  efficiencies and survival fractions, two uncertainties must be taken into account: the systematic uncertainty of the low cut

value  $\Delta\zeta_{\text{cut}}$  and the statistical uncertainty  $\Delta\epsilon_{\text{stat}}$  when determining the efficiency. The former was defined by Equation 8.14. In order to understand the effect of this uncertainty, the survival fraction was calculated three times using  $\zeta_{\text{cut}}$ ,  $\zeta_{\text{cut}} + \Delta\zeta_{\text{cut}}$  and  $\zeta_{\text{cut}} - \Delta\zeta_{\text{cut}}$  as cut values. The differences in survival fractions represent the systematic uncertainties  $\Delta\epsilon_{\text{sys}}$ .

The statistical uncertainty in determining a survival fraction cannot be determined by a simple error propagation. Such a calculation would inevitably lead to uncertainties including values above 100% or below 0% in some cases. The correct calculation is derived in [121] and corresponds to a binomial error. The standard deviation  $\sigma_k$  of the distribution of the events passing the cut can be described by

$$\sigma_k = \sqrt{\text{var}(k)} = \sqrt{\epsilon_{\text{true}}(1 - \epsilon_{\text{true}})N}. \quad (8.15)$$

Here,  $\epsilon_{\text{true}}$  stands for the true cut efficiency,  $N$  for the sample size and  $\langle k \rangle = \epsilon_{\text{true}}N$  for the events that survive the cut. As the true cut efficiency is not known, the estimated cut efficiency  $\epsilon = k/N$  can be used resulting in

$$\Delta\epsilon_{\text{stat}} = \sigma_k = \frac{1}{N} \sqrt{k(1 - k/N)}. \quad (8.16)$$

This uncertainty strongly depends on the sample size. For GD35B (data) it is  $\Delta\epsilon_{\text{stat, DEP}} = 0.39\%$ . The systematic uncertainties are dominating for all detectors (data & simulation). Combining statistical and systematic uncertainties for this example using the sum of squares, results in

$$\epsilon_{\text{DEP}} = 84.17^{+3.05}_{-3.36}\%. \quad (8.17)$$

The asymmetrical uncertainties were relatively similar for most  $A/E$  cut efficiencies and were therefore equated in the results. The higher uncertainty was used here, resulting in  $\epsilon_{\text{DEP}} = (84.17 \pm 3.36)\%$  for GD35B (data).

The procedure is the same for the determination of the uncertainties of the  $0\nu\beta\beta$ -decay detection efficiency of individual detectors. In order to obtain the uncertainty of the overall efficiency, the mean uncertainty of all detectors weighted by their exposure in the used data set was formed resulting in  $\epsilon_{0\nu\beta\beta} = (85.9 \pm 1.8)\%$  and  $\epsilon_{0\nu\beta\beta, \text{Ext.}} = (86.8 \pm 4.1)\%$  for the two methods described in Section 8.6.

## 8.8 Summary

In the GERDA analysis, *pulse-shape discrimination* (PSD) was used to discriminate signal from background by analysing the time structure of pulses. In order to estimate the effect of PSD on the  $0\nu\beta\beta$ -signal detection, a so-called *signal proxy* has been used. The *double-escape peak* (DEP) of  $^{208}\text{Tl}$  was chosen as it shows similar characteristics as expected for  $0\nu\beta\beta$  signals. However, this entails uncertainties as the spatial distributions of DEP and  $0\nu\beta\beta$ -decay events are not comparable. In addition, stronger effects due to Bremsstrahlung are expected for  $0\nu\beta\beta$ -decay events.

In this work, an analysis chain was developed to obtain  $0\nu\beta\beta$ -decay detection efficiency via simulated data. Each step was validated using calibration and physics data from GERDA Phase II with 12.6 kg·yr valid exposure from 26 BEGe detectors. In preparation for the analysis, the simulations of the individual electric fields and electronics-model parameters for all detectors have been optimised. The new simulation package *SolidStateDetectors.jl* [54] written in Julia [57] was used for pulse-shape simulation. The effect of the read-out electronics in the experimental setup on the pulse was taken into account by an electronics model developed in GERDA [118]. In addition, unique noise baselines from physics data were used to obtain realistic pulses.

For PSD,  $A/E$  analysis was used with which the time structure of pulses can be exploited by relating the amplitude  $A$  of the current pulse and the energy  $E$  of the event. This works especially well for BEGe detectors. Due to their small  $p^+$  contacts, interactions in a large volume of the detector lead to similar pulses. Here, *single-site events* (SSEs) like  $0\nu\beta\beta$  decays are distinguished from *multi-site events* (MSEs) and surface events. Two  $A/E$  cut values were determined for each detector individually. While the *high* cut to discriminate surface events close to the  $p^+$  contact was set constant, the *low* cut was determined using the DEP to discriminate MSEs and surface events close to the  $n^+$  contact. As  $\approx 90\%$  of  $0\nu\beta\beta$ -decay events are expected to show SSE characteristics, the low cut was set to 90% survival of DEP events.

The  $A/E$  cut survival fractions for data and simulation was determined for multiple MSE samples, two Compton areas and  $2\nu\beta\beta$ -decay events. A good agreement between data and simulation was achieved for all MSE samples. For the Compton areas and  $2\nu\beta\beta$ -decay events a difference of about 5% was found. The obtained  $0\nu\beta\beta$ -decay detection efficiency for all BEGe detectors weighted by their contribution to the exposure was  $(85.9 \pm 1.8)\%$ .

This was additionally validated by determining the energy-dependent  $2\nu\beta\beta$ -decay  $A/E$  cut survival fraction from simulation and extrapolating it to  $0\nu\beta\beta$ -decay. Here, a weighted  $0\nu\beta\beta$ -decay detection efficiency of  $(86.8 \pm 4.1)\%$  was obtained. Both results are in agreement with the previously performed analysis of the GERDA collaboration [12]. In comparison to the fully data-driven analysis, the uncertainty on the  $0\nu\beta\beta$ -decay detection efficiency was reduced by about a factor of two by including pulse-shape simulations. In addition, effects due to the different spatial distributions of the energy depositions of DEP and  $0\nu\beta\beta$ -decay events can be accounted for.

## Chapter 9

# Conclusions & Outlook

One of the biggest fundamental questions in modern physics are the properties of the neutrino. The most promising approach to assess this question is the neutrinoless double beta ( $0\nu\beta\beta$ ) decay search. If the half-life  $T_{1/2}^{0\nu}$  of  $0\nu\beta\beta$  decay is  $< 10^{28}$  yr, it will be detected by the *Large Enriched Germanium Experiment for Neutrinoless  $\beta\beta$  Decay* (LEGEND). In the course of the year 2022, LEGEND will start its search for  $0\nu\beta\beta$  decay of  $^{76}\text{Ge}$ . In its first phase, LEGEND-200, about 200 kg of high-purity germanium (HPGe) detectors made of  $^{76}\text{Ge}$ -enriched material will be deployed in the infrastructure of the *GERmanium Detector Array* (GERDA) experiment at the *Laboratori Nazionali del Gran Sasso* (LNGS). The main challenge in the  $0\nu\beta\beta$ -decay search is the reduction and identification of background events. To achieve the targeted sensitivity on the  $0\nu\beta\beta$ -decay half-life of  $T_{1/2}^{0\nu} > 10^{28}$  yr in the final phase of the experiment within ten years of data taking, the background level must be reduced by a factor of 50 compared to GERDA corresponding to  $< 10^{-5}$  cts/(keV·kg·yr).

Two aspects of background suppression are elaborated in this thesis work. In the first, the background identification capability of LEGEND was improved by replacing the optically opaque detector holders with an optically transparent, scintillating and wavelength-shifting (WLS) new structural material. In the second, an analysis chain for determining the  $0\nu\beta\beta$ -decay detection efficiency for broad-energy germanium (BEGe) detectors based on GERDA data and simulation was developed and validated in order to reduce the systematic uncertainties introduced by purely data-driven analyses.

As part of the LEGEND collaboration and the international PEN working group, a major part of this thesis work was dedicated to the production, characterisation and deployment of a new active structural material for ultra-low background environments. *Poly(ethylene 2,6-naphthalate)* (PEN) is a commercially-available plastic which can be procured with relatively high intrinsic radiopurity. Importantly, PEN can be used to create almost arbitrarily-shaped scintillating structures with good mechanical strength and

WLS properties. In the course of this thesis work, it was investigated whether the opaque detector holders used in GERDA could be replaced by PEN holders that are radio pure enough to be used in close vicinity of HPGe detectors. For this, a radio clean production process was developed and finally a batch of PEN plates was produced for LEGEND-200. In the whole production process, special attention was paid to achieve the highest possible radiopurity. Also, thanks to a new cleaning procedure of the raw PEN granulate and the radio clean moulding process, a radiopurity limit of  $< 1.2 \mu\text{Bq}$  per holder was achieved.

The germanium detector holders for LEGEND-200 were successfully produced and all parameters necessary for simulating background expectations could be determined. Due to the scintillation properties of PEN, some background contribution can now be identified with higher efficiency compared to GERDA. In addition, the veto efficiency of the liquid argon veto system will be increased due to the WLS properties of PEN.

The possibilities of PEN as structural material in low-background experiments are far from exhausted. As part of the LEGEND collaboration, researchers from *Oak Ridge National Laboratory* are currently investigating contactless 3D-printing of structures with high radiopurity in-house synthesised PEN. This would allow the entire manufacturing process to take place in the underground laboratory reducing the exposure to cosmic radiation. Furthermore, research is planned on production of PEN sheets for enshrouding of germanium detectors in the tonne-scale phase of LEGEND.

Thanks to the success of the R&D, all HPGe detectors in LEGEND-200 will be mounted on the newly developed PEN holders. This is the first application of PEN as optically active structural material in an ultra-low background experiment.

As part of the GERDA collaboration, an analysis of the  $0\nu\beta\beta$ -decay detection efficiency of BEGe detectors in GERDA based on pulse-shape simulations was performed. *Pulse-shape discrimination* (PSD) was used in the GERDA analysis to discriminate signal from background events. Like this, together with ultra-low background and additional veto techniques a (in the region of interest) quasi-background free measurement could be achieved. For BEGe detectors, the so-called *A/E* method is used in which the time structure of the pulse shape is exploited by comparing the amplitude *A* of the current pulse and the energy *E* of the event. In doing so, *single-site events* (SSEs) like  $0\nu\beta\beta$  decays can be distinguished from *multi-site events* (MSEs) as well

as from surface events. To estimate the effect of PSD on the  $0\nu\beta\beta$ -decay detection efficiency, a so-called *signal proxy* is being used. However, this entails systematic uncertainties as the spatial distributions of the proxy differs from  $0\nu\beta\beta$  decay.

In this work, an analysis chain was developed to validate the  $0\nu\beta\beta$ -decay detection efficiency using pulse-shape simulations. Each step of the analysis was validated using a data set from GERDA Phase II from 26 BEGe detectors with 12.6 kg·yr valid exposure. Here, the newly developed simulation code *SolidStateDetectors.jl* [54] was used for pulse-shape simulation. The PSD efficiencies for data and simulation were compared using multiple complementary MSE and SSE samples. The obtained  $0\nu\beta\beta$ -detection efficiency for all BEGe detectors weighted by their contribution to the exposure is  $(85.9 \pm 1.8)\%$  including statistical and systematic uncertainties. In addition, the energy-dependent  $2\nu\beta\beta$ -decay detection efficiency was determined from simulation and extrapolated to  $0\nu\beta\beta$ -decay. From this, a weighted  $0\nu\beta\beta$ -decay detection efficiency of  $(86.8 \pm 4.1)\%$  is obtained. Both results are in agreement with previously performed analyses of the GERDA collaboration [12]. Importantly, the total uncertainty could be reduced which has a direct impact on setting new limits on  $T_{1/2}^{0\nu}$ .

In the LEGEND analysis, PSD will be used to discriminate signal from background events. Up to 400 new ICPC germanium detectors will be deployed in the tonne-scale phase of LEGEND [7]. The simulation-supported analysis chain presented in this thesis can be used in LEGEND to determine the  $0\nu\beta\beta$ -decay detection efficiency for each of the new detectors individually to obtain the overall efficiency of the experiment with lower uncertainties as provided by completely data-driven analyses.



## Appendix A

# Appendix - Part I

## A.1 PMT Setup

### A.1.1 The $^{207}\text{Bi}$ Radioactive Source

A  $^{207}\text{Bi}$  source was used for the PMT setup. This decays by electron capture (99.9%) into excited states of  $^{207}\text{Pb}$  [65, 99, 122]. The decay scheme can be seen in Figure A.1. There are three major  $\gamma$  lines for  $^{207}\text{Pb}$  going to its ground state: 570, 1064 and 1770 keV. The  $\gamma$  rays of  $^{207}\text{Pb}$  going from its excited states to the

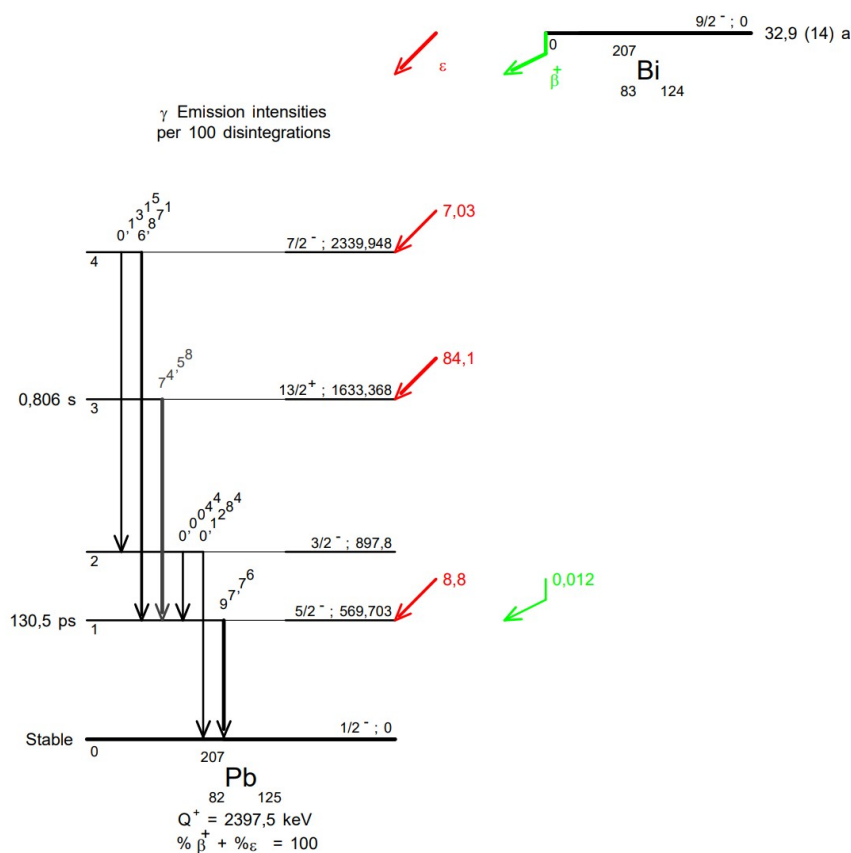


FIGURE A.1: Decay scheme of  $^{207}\text{Bi}$ . Taken from [122].

Transition [keV]	Shell	Energy [keV]	Probability [%]
569.7	K	482	1.55
	L	555	0.43
	M	566	0.11
1063.7	K	976	7.11
	L	1049	1.84
	M	1060	0.44
	N	1063	0.12
1770.2	K	1682	0.02

TABLE A.1: Conversion electrons of  $^{207}\text{Bi}$  for its main transitions. Taken from [99, 122].

ground state can be replaced by atomic K, L or M shell conversion electrons as listed in Table A.1. Mono-energetic electrons between 976 and 1063 keV are emitted with a probability of about 9.5%. These can be absorbed by a few millimetres of, for example, PEN leading to a well defined energy deposition.

## A.1.2 PMT Calibration

The calibration of the PMTs were carried out before every measurement to find the SPE calibration factor. In order to prove that this is not a superposition of signals, multiple measurements with increasing amplitude trigger levels were carried out to measure the individual photo-electron peaks. Using different trigger levels leads to a non-continuous exponential in each peak due to badly amplified events. Therefore, the SPE model described in Equation 7.1 can not be used to describe this spectrum.

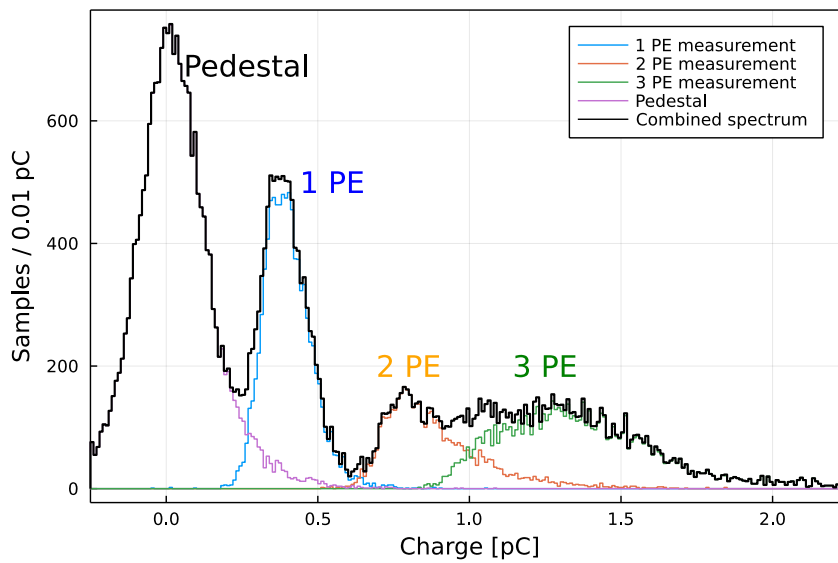


FIGURE A.2: Calibration spectrum of one PMT in the PMT setup. The spectrum is a composition of three measurements with different trigger levels. The combined spectrum is shown in black.

### A.1.3 PMT SPE Stability

The stability of the SPE calibration up to at least 500 PE was confirmed by comparing a simulated to a measured energy spectrum of  $^{207}\text{Bi}$ . The result for two squared PEN samples ( $1.7 \times 30 \times 30 \text{ m}^3$  each) can be seen in Figure A.3. The simulation (orange spectrum) is smeared using a 7.5% energy resolution, which was found manually in order to match the data. The simulated distribution was scaled linearly from keV to PE by using the PMT response of the 930 keV peak in terms of mean detected photons per event from data (blue spectrum). Both, the 420 keV and 930 keV peaks of data and simulation overlap, which is only possible if the gain behaves linearly over the given range.

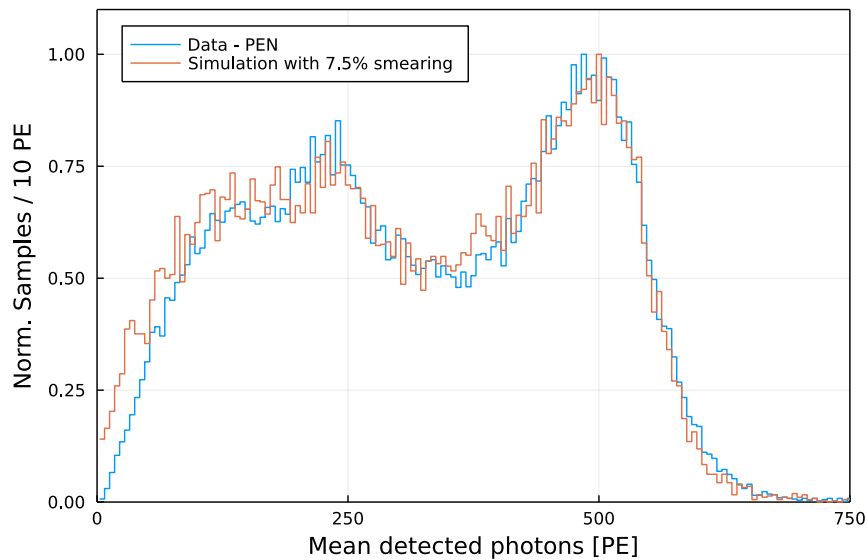


FIGURE A.3: Measured and simulated energy spectrum of  $^{207}\text{Bi}$  measured with five PMTs attached to two squared PEN samples ( $1.7 \times 30 \times 30 \text{ m}^3$ ). Four PMTs optically coupled to the sides and one below the samples. The simulated spectrum is smeared using a 7.5% energy resolution.

### A.1.4 PMT Quantum Efficiency

The quantum efficiency of the PMT is given by the manufacture as function of wavelength. It is shown in Figure A.4 and gives a quantum efficiency for the peak emission wavelength of PEN at 440 nm of  $\approx 35\%$ .

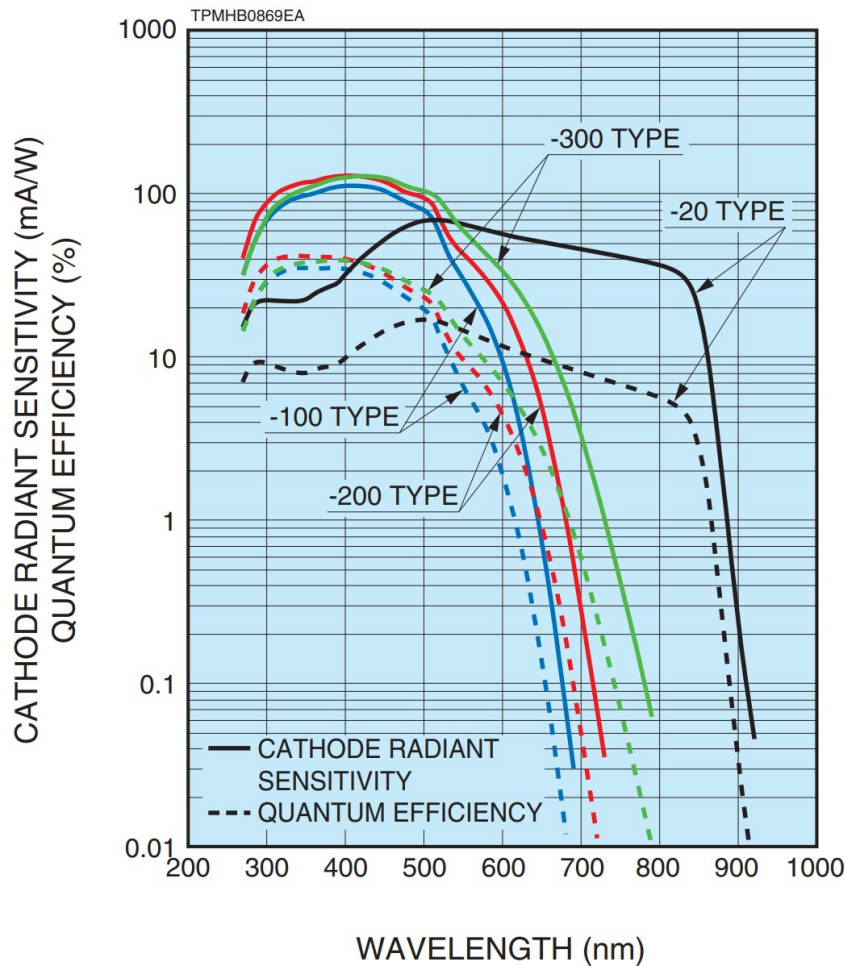


FIGURE A.4: Quantum efficiency of the HAMAMATSU photonics PMT of type H11934-300 as function of wavelength. Taken from the manual [107].

### A.1.5 PMT Setup Simulation

The PMT setup described in Section 7.3.3 was simulated in different configurations by Luis Manzanillas. A detailed description will be published soon separately. The deposited energy by the  $^{207}\text{Bi}$  source was found to have a peak value at 25 keV. The energy spectrum of the depositions can be seen in Figure A.5.

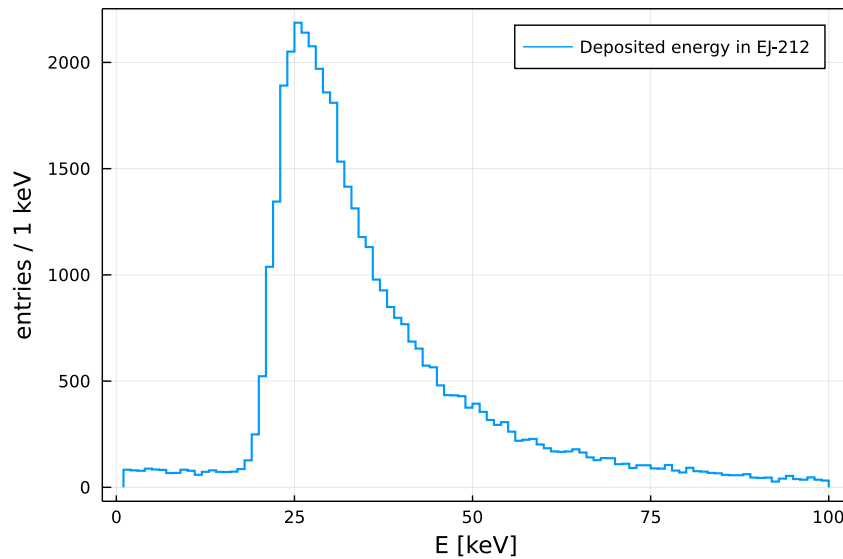


FIGURE A.5: Simulated energy deposition spectrum in the  $90\ \mu\text{m}$  thick EJ-212 scintillator by the  $^{207}\text{Bi}$  source used in the PMT setup. Spectrum will be published soon separately.

## A.2 Detection Efficiency & Energy Threshold of the Small and Medium Type Holder

The detection efficiency and energy threshold for all three types of LEGEND-200 PEN Ge detector holders were determined. The resulting efficiencies and energy deposition thresholds as function of the position on the holder can be seen in Figure A.6 and Figure A.7, respectively, for the small (top) and medium (bottom) type. A power failure happened in the laboratory during the measurement of the small holder. Afterwards, the measurement was restarted but the air conditioning was not working anymore. Therefore, the room was about 10°C warmer than during the first part of the measurement. This already influenced the PMT gain as can be seen in the results. A second calibration was performed before the measurement was restarted.

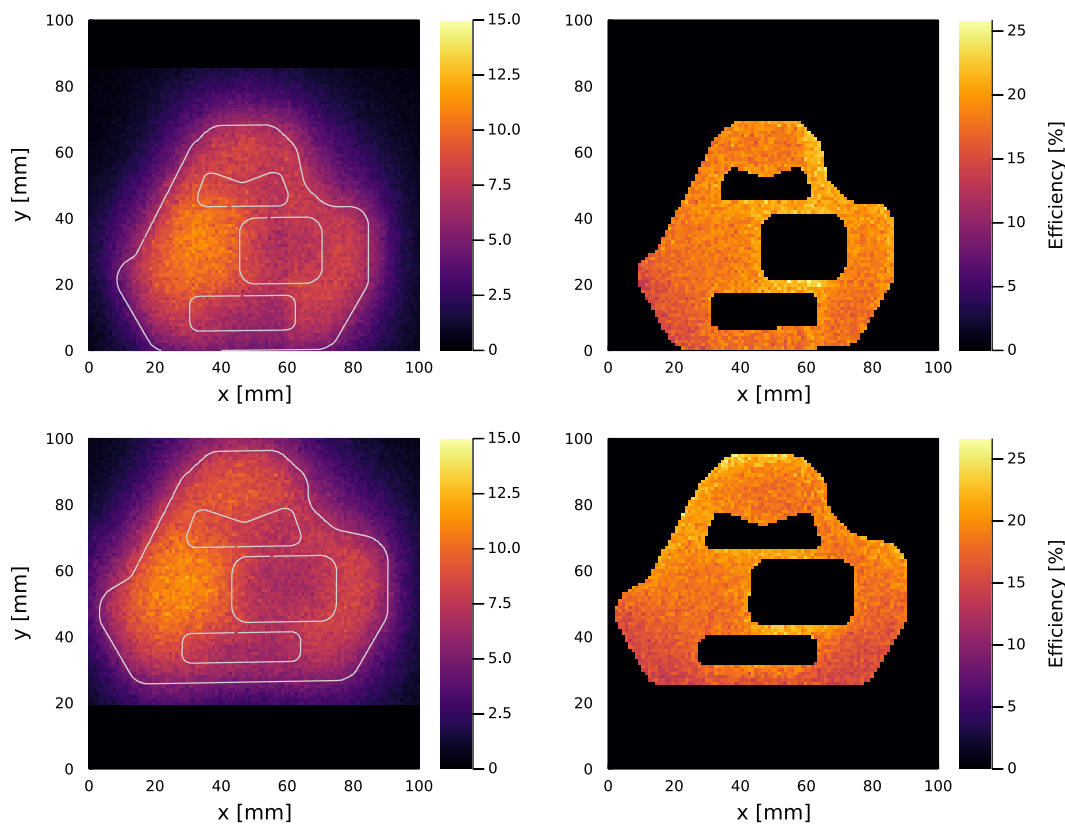


FIGURE A.6: Measured ratio of number of detected to triggered events for the small (top) and medium (bottom) PEN holders. **Left:** Measured results for each position on the grid. **Right:** Measured results for each position on the holders surface corrected for the hit probability.

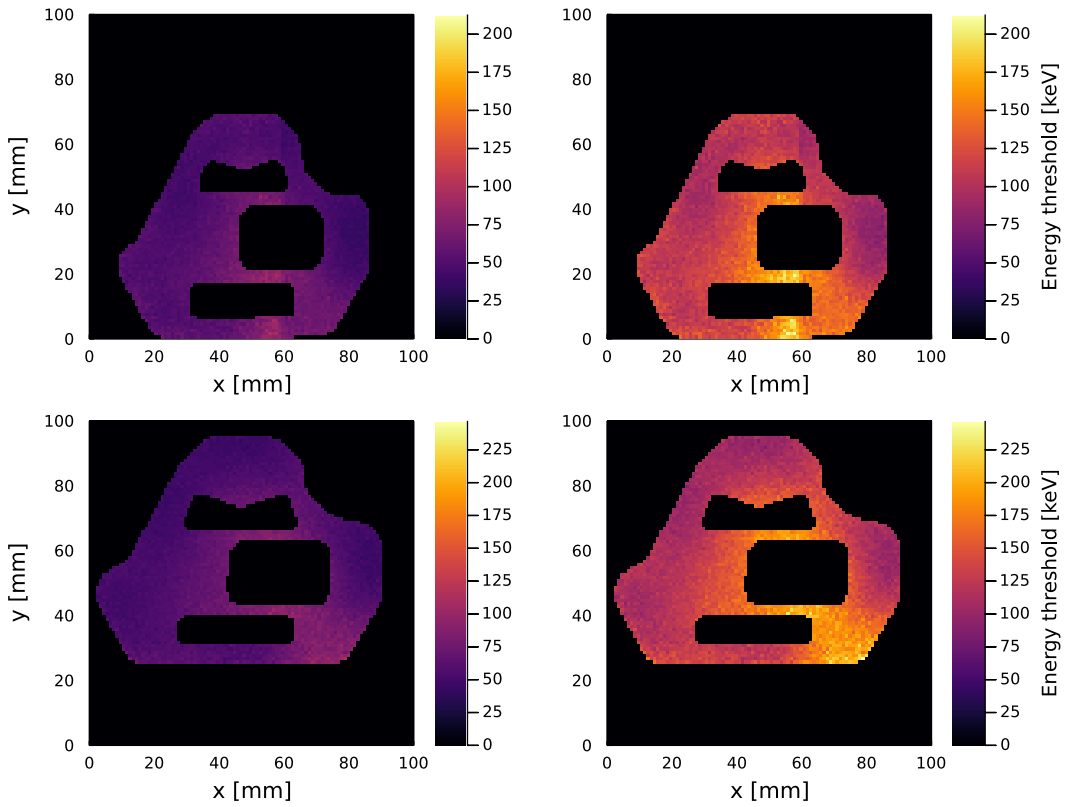


FIGURE A.7: Energy threshold as function of the position on the small (top) and medium (bottom) PEN holders with an 99.7% (left) and 99.99994% (right) detection probability of 2 PE.

### A.2.1 Emission Spectra of PEN & TPB

For the estimation of the absorption of PEN scintillation light in the WLS fibres of LEGEND-200, a comparison of the emission spectra of PEN and TPB was made as can be seen in Figure A.8. For TPB, it is assumed that about 60% of the wavelength-shifted light can be absorbed by the fibres [110]. The overlap of the absorption spectrum of the fibres with the emission spectra of TPB and PEN was determined and in both cases a match of 60 – 70% was found. Therefore, a 40% loss due to the absorption in the WLS fibres of PEN scintillation photons was assumed in the estimation of the veto energy threshold of the PEN holders in LEGEND-200 (see Section 7.4.7).

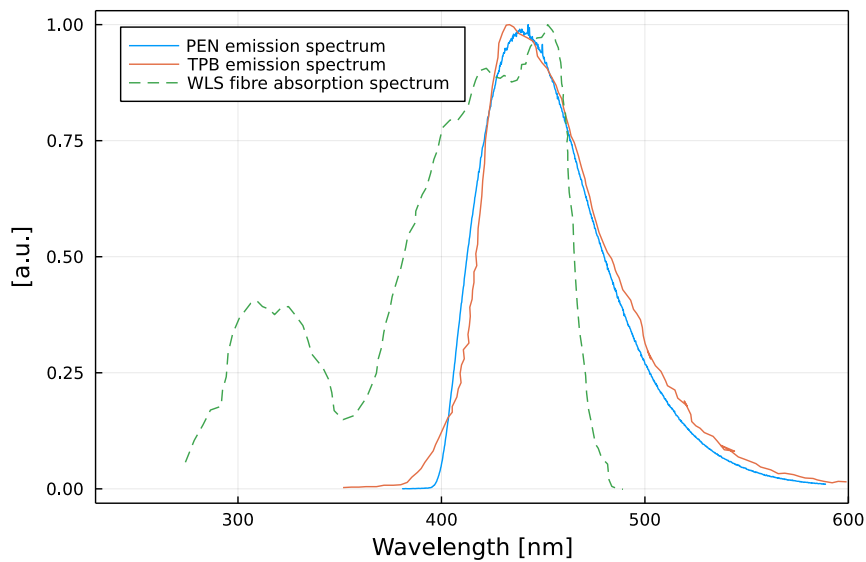


FIGURE A.8: Emission spectra of PEN (blue) and TPB (orange) compared to the absorption spectrum of the WLS fibres (green). All spectra are normalised to their individual maximum to show the overlap. TPB emission spectrum and WLS fibre absorption spectrum taken from [48].



## Appendix B

# Appendix - Part II

## B.1 Julia Implementation of the Electronics Response Function

The electronics model described in Section 8.2.2 can be used in Julia by the following function:

```
function applyElectronics(pulse; Ts = 10e-9, GBP = 2750e6,
    tau = 180e-6, Kv = 150e3, Cd = 50e-12,
    Cf = 0.35e-12, Rf = 500e6)

    wop = GBP / (2 * pi * Kv) # Kv = constant = 150e3
    Cmod = Cf + Cd
    wmod = 1.0 / (Rf * Cmod)
    alfa = Cmod / (Cf * GBP)

    b0 = 1.0 / alfa
    a2 = 1.0
    a1 = 1.0 / alfa + wop + wmod
    a0 = 1.0 / (tau * alfa) + wmod*wop

    # then the transfer function in the *Laplace* s-domain
    # looks like this:
    #
    #                               b0
    #   T(s) = -----
    #                a2 * s^2 + a1 * s + a0
    # PolynomialRatio needs z-transform paramters: s- and
    # z-domains can be connected by
    # the bilinear transform:
    #           z - 1
```

```

# s = K ----- , K = 2/Ts , Ts - sampling period
#       z + 1
# we can then convert T(s) to T(z):
#       bz2 * z^2 + bz1 * z + bz0
# T(z) = -----
#       az2 * z^2 + az1 * z + az0

K = 2/Ts

az2 = 1.0 # normalised
az1 = (2*a0 - 2*K^2)/(K^2 + a1*K + a0)
az0 = (K^2 - a1*K + a0)/(K^2 + a1*K + a0)

bz2 = b0/(K^2 + a1*K + a0)
bz1 = 2*b0/(K^2 + a1*K + a0)
bz0 = b0/(K^2 + a1*K + a0)

myfilter = PolynomialRatio([bz2, bz1, bz0], [az2, az1, az0])
filtered = filt(myfilter, vcat([0], diff(pulse)))
end

```

The effect of the *applyElectronics()* function applied to a simulated waveform is shown in Figure B.1.

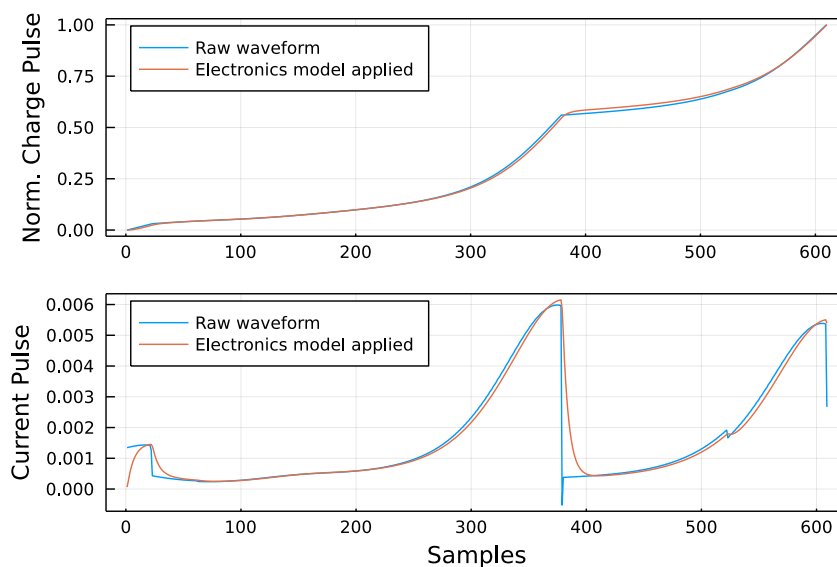


FIGURE B.1: Electronics model applied to a simulated charge pulse (top). The corresponding current pulses are shown in the bottom.

## B.2 Detector Parameters for Simulation and Electronics Model

Channel	Detector	Impurity in $10^{12} \frac{e}{\text{cm}^3}$	HV in V	GBP MHz	$\tau$ $\mu\text{s}$	$\chi^2$
00	GD91A	-1.2	3500	7285	110	0.127
01	GD35B	-1.9	4000	4290	115	0.031
02	GD02B	-1.4	3000	3104	121	0.040
03	GD00B	-1.2	3200	2476	103	0.025
04	GD61A	-2.2	4400	2739	112	0.222
11	GD02A	-1.4	2500	5172	115	0.042
12	GD32B	-1.7	3200	3200	105	0.130
14	GD32C	-1.8	4000	3228	103	0.032
15	GD89C	-2.7	4000	3268	126	0.033
16	GD61C	-2.44	3700	2337	109	0.021
17	GD76B	-2.06	3500	3147	144	0.036
18	GD00C	-1.3	3500	4730	113	0.008
19	GD35C	-2.4	3500	7475	87	0.067
20	GD76C	-1.6	3500	3496	110	0.072
21	GD89D	-2.8	4000	4507	127	0.174
22	GD00D	-1.75	3500	3149	101	0.052
23	GD79C	-1.5	3500	3073	135	0.042
24	GD35A	-1.5	3800	1818	120	0.018
25	GD91B	-1.3	3000	1910	131	0.362
26	GD61B	-2.3	4000	2760	124	0.016
30	GD00A	-1.0	2500	5076	116	0.064
31	GD02C	-1.3	3500	4739	112	0.023
32	GD79B	-2.0	3500	4312	99	0.272
33	GD91D	-1.51	4500	3177	129	0.126
34	GD32D	-1.5	4000	3048	106	0.187
35	GD89A	-2.4	4000	2339	112	0.119

TABLE B.1: Levels of impurity at  $z = 0$  and high voltage (HV) used for the SSD detector simulation. Used values for the gain-bandwidth product  $GBP$  and the decay time  $\tau$  for the electronics model for all GERDA BEGe detectors. The other parameters are constant:  $C_d = 50.0$  pF,  $C_f = 0.35$  pF and  $R_f = 500$  M $\Omega$ . For GD35A  $C_d = 52.0$  pF,  $C_f = 0.52$  pF was used as only exception. For the comparison of data and simulation with the given parameters, the  $\chi^2$  value is also given.

### B.3 Achieved Energy Resolution Compared to GERDA

The energy resolution achieved in this work is worse compared to the official results of GERDA. This is due to missing corrections as applying the ZAC filter to the waveforms before determining  $A$  and  $E$ . The aim of this work was not to achieve the best possible energy resolution, so the ZAC parameters were not determined in an optimisation procedure for the simulated detectors. The ratio of the energy resolution (FWHM) determined in this work and the results of GERDA are shown in Figure B.2 for the DEP and FEP of  $^{208}\text{Tl}$ . For the determination of the GERDA results, the FWHM was determined using the calibrated energy values evaluated by the collaboration analysis team.

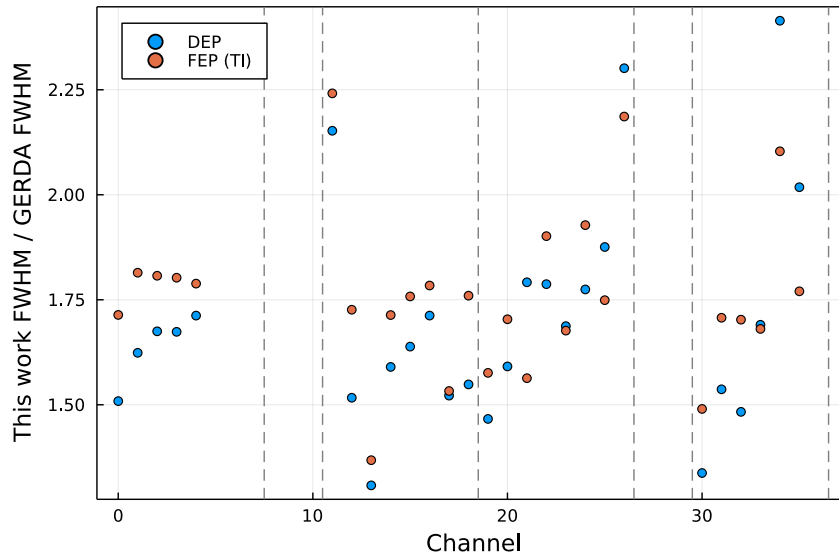
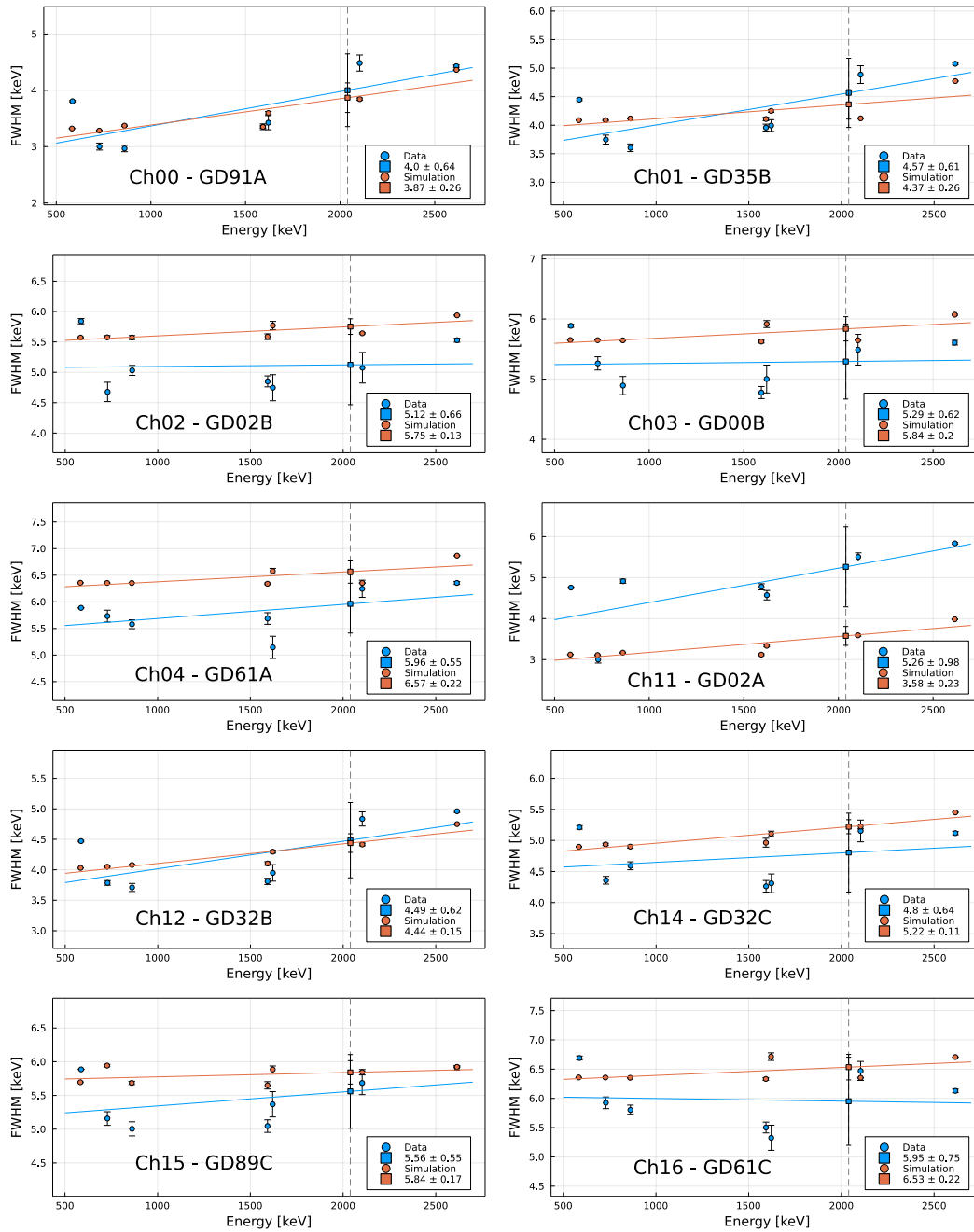
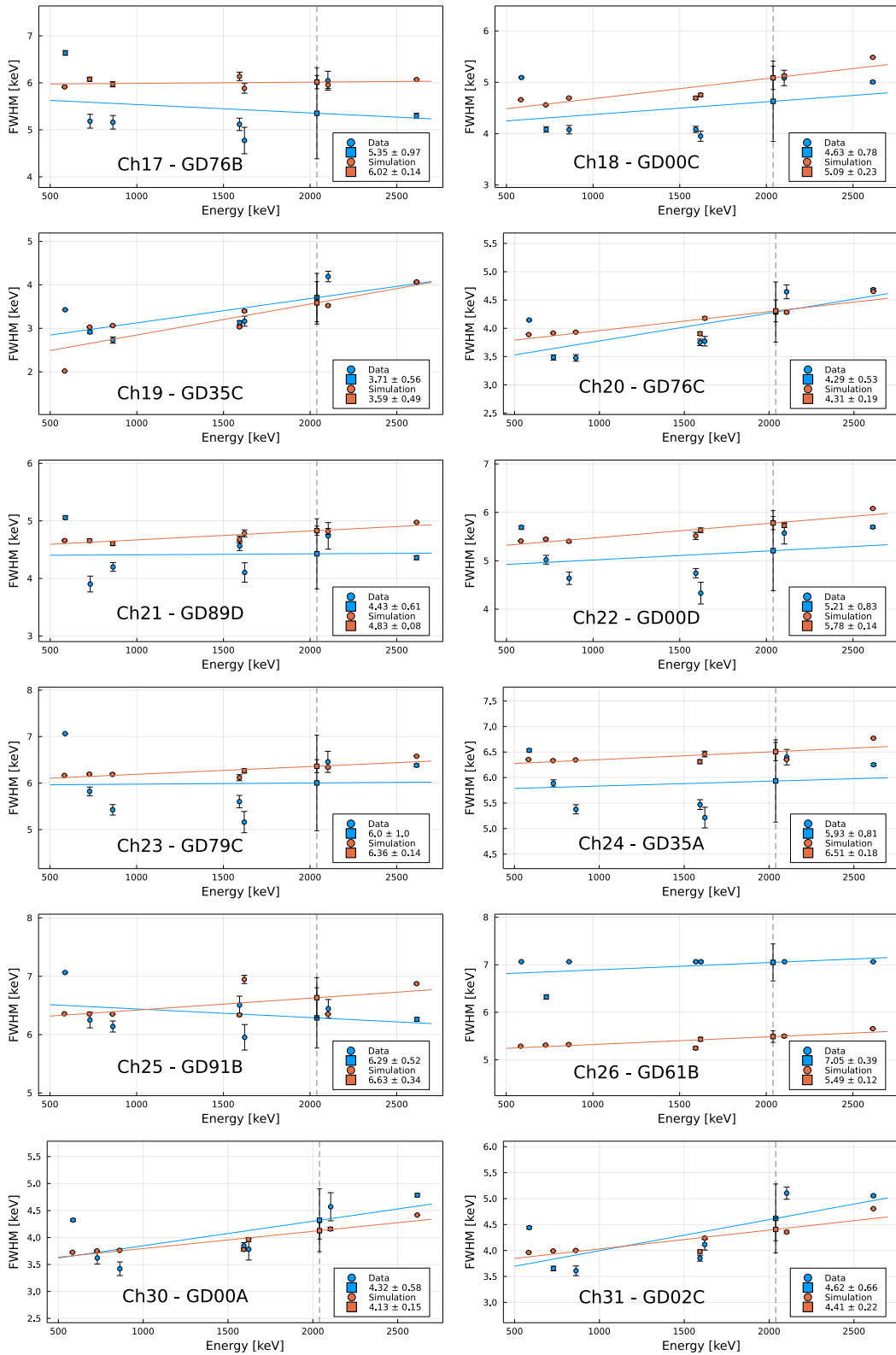


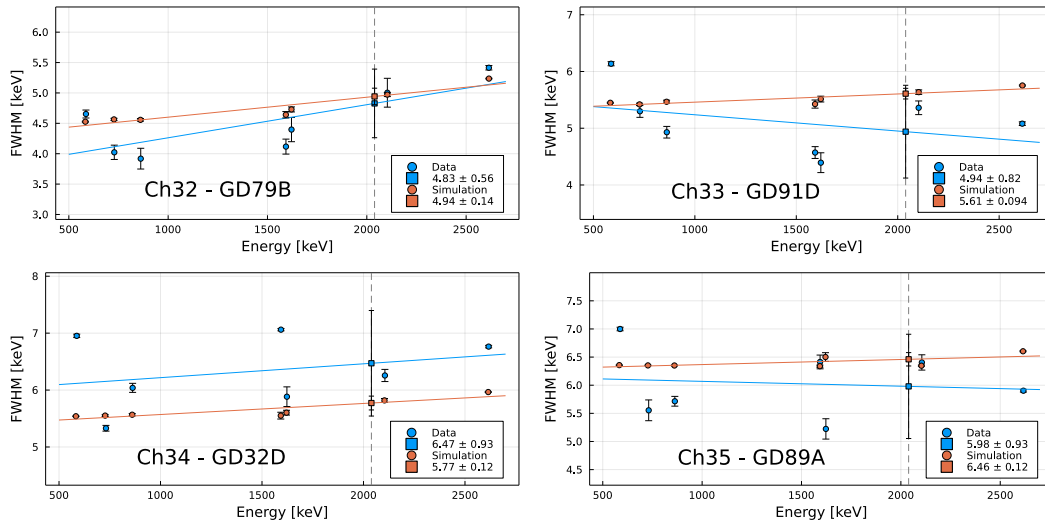
FIGURE B.2: Ratio of the energy resolution achieved in this work and the results of GERDA. Plotted are the ratios for each detector for the DEP (blue) and the FEP of  $^{208}\text{Tl}$  (orange).

## B.4 FWHM Comparison of Data and Simulation

FIGURE B.3: FWHM as function of energy for data and simulation. A linear regression is used to estimate the values at  $Q_{\beta\beta}$ .







## B.5 Energy Ranges for $A/E$ Energy Dependence Determination

The energy dependency of  $\mu_{A/E}(E)$  and  $\sigma_{A/E}(E)$  was determined in energy ranges of 30 keV (slices). To increase the comparability, a fixed set of slices was used. The complete used range is highlighted in Figure B.4 in blue. The energy ranges are: (600 – 690) keV, (800 – 830) keV, (895 – 1075) keV, (1130 – 1490) keV, (1545 – 1575) keV, (1665 – 2085) keV and (2145 – 2355) keV.

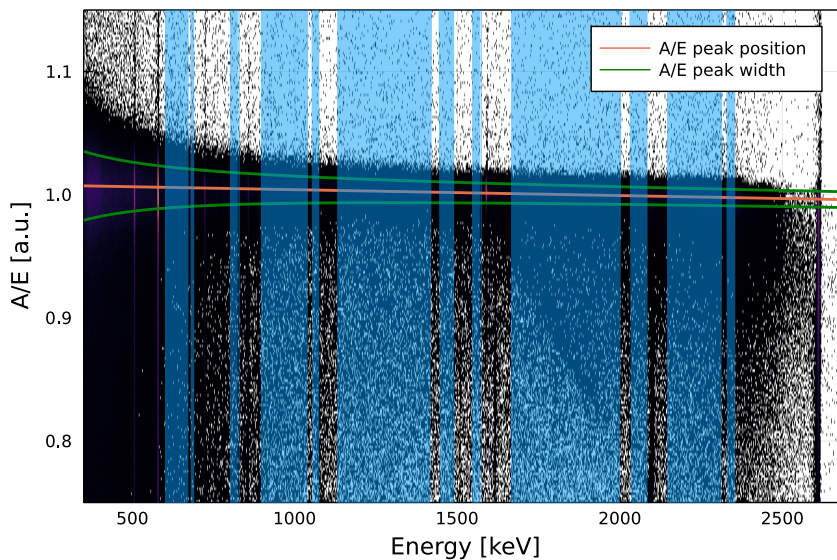
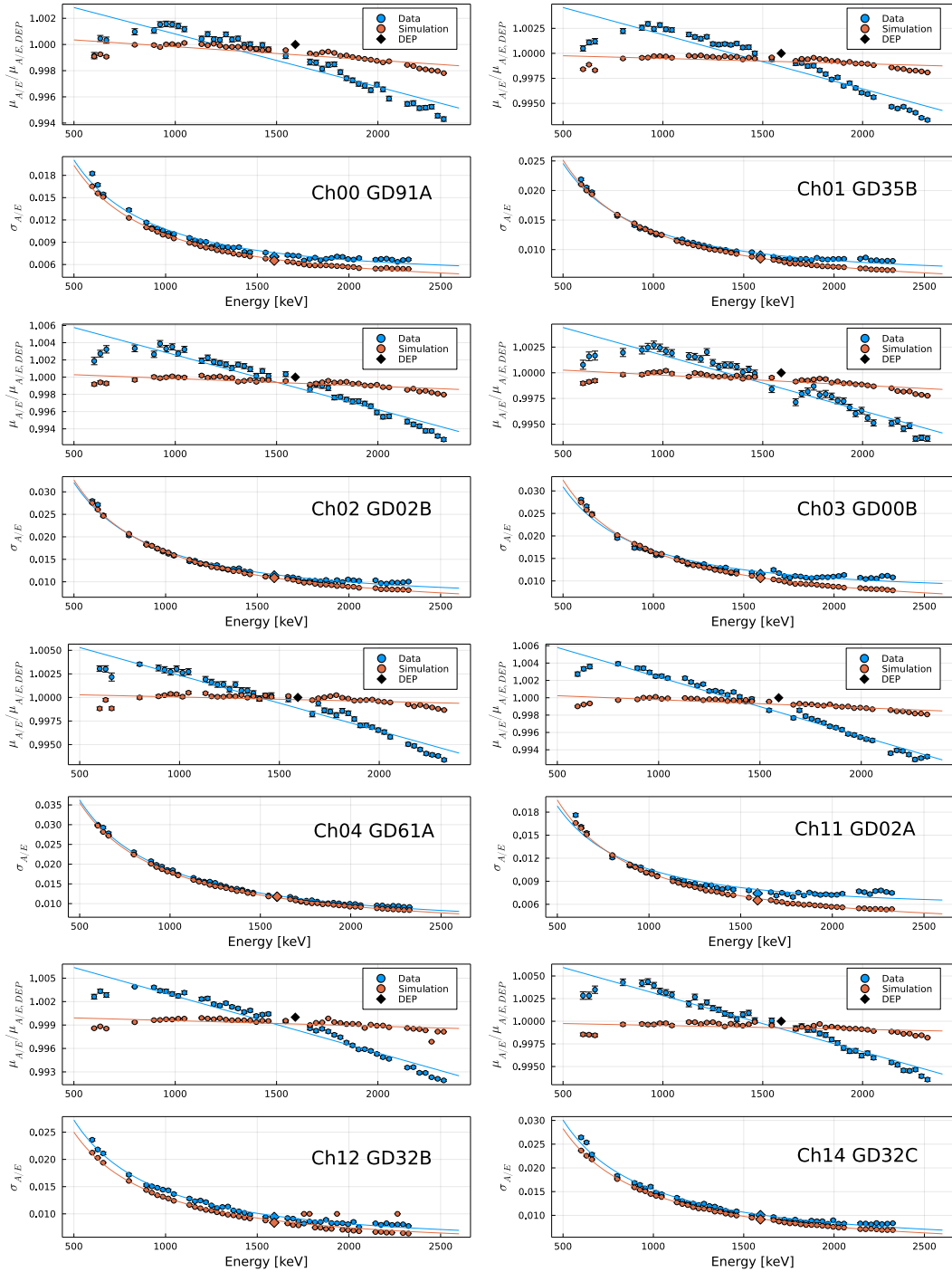
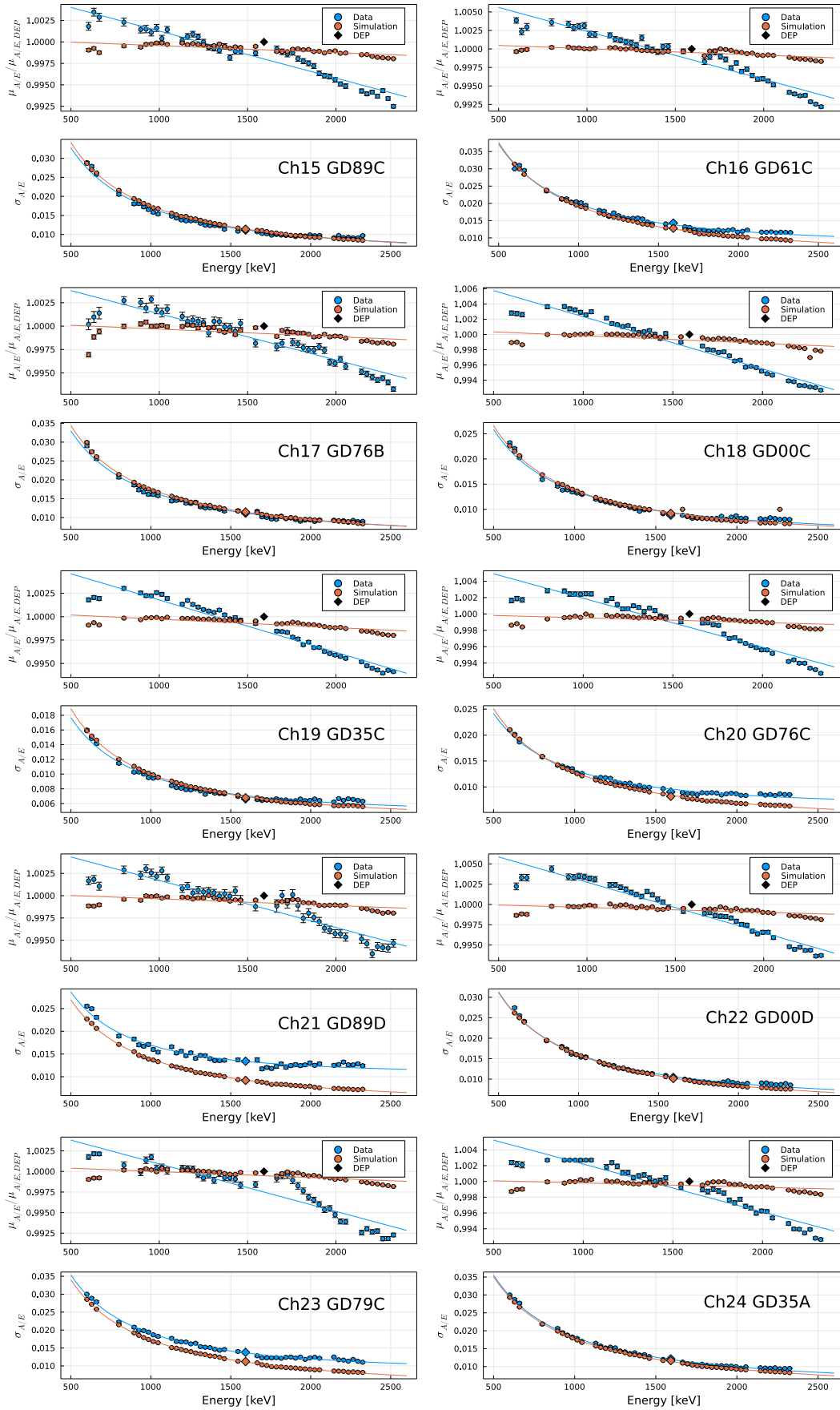


FIGURE B.4: Scatter plot of  $A/E$  values for GD35B (data). The energy range used for the calibration of  $\mu_{A/E}(E)$  and  $\sigma_{A/E}(E)$  are highlighted in blue.

FIGURE B.5: Energy dependent  $A/E$  peak position  $\mu_{A/E}(E)$  normalised to  $\mu_{A/E,DEP}$  (top) and width  $\sigma_{A/E}(E)$  (bottom) for data and simulation including fits.





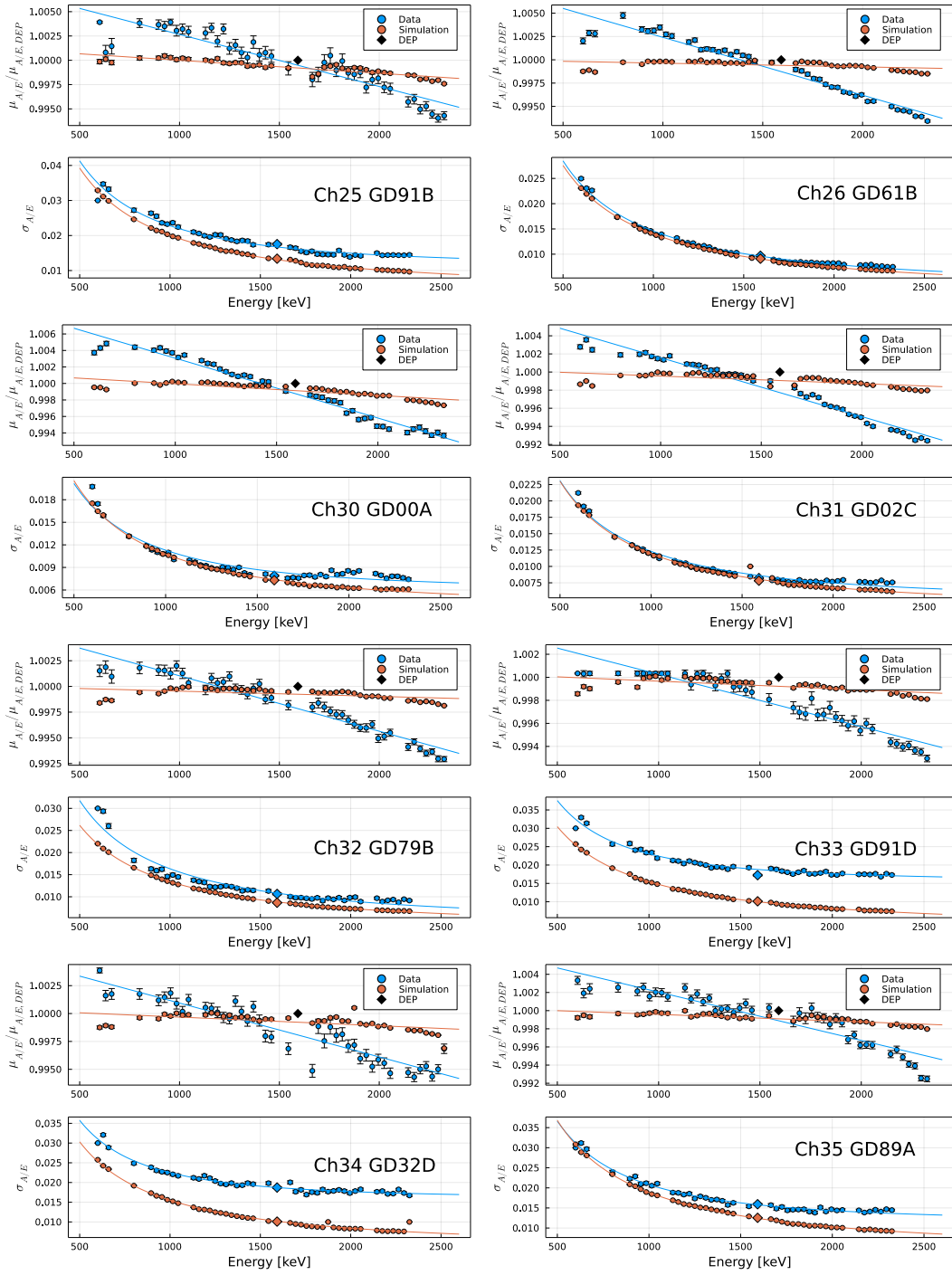
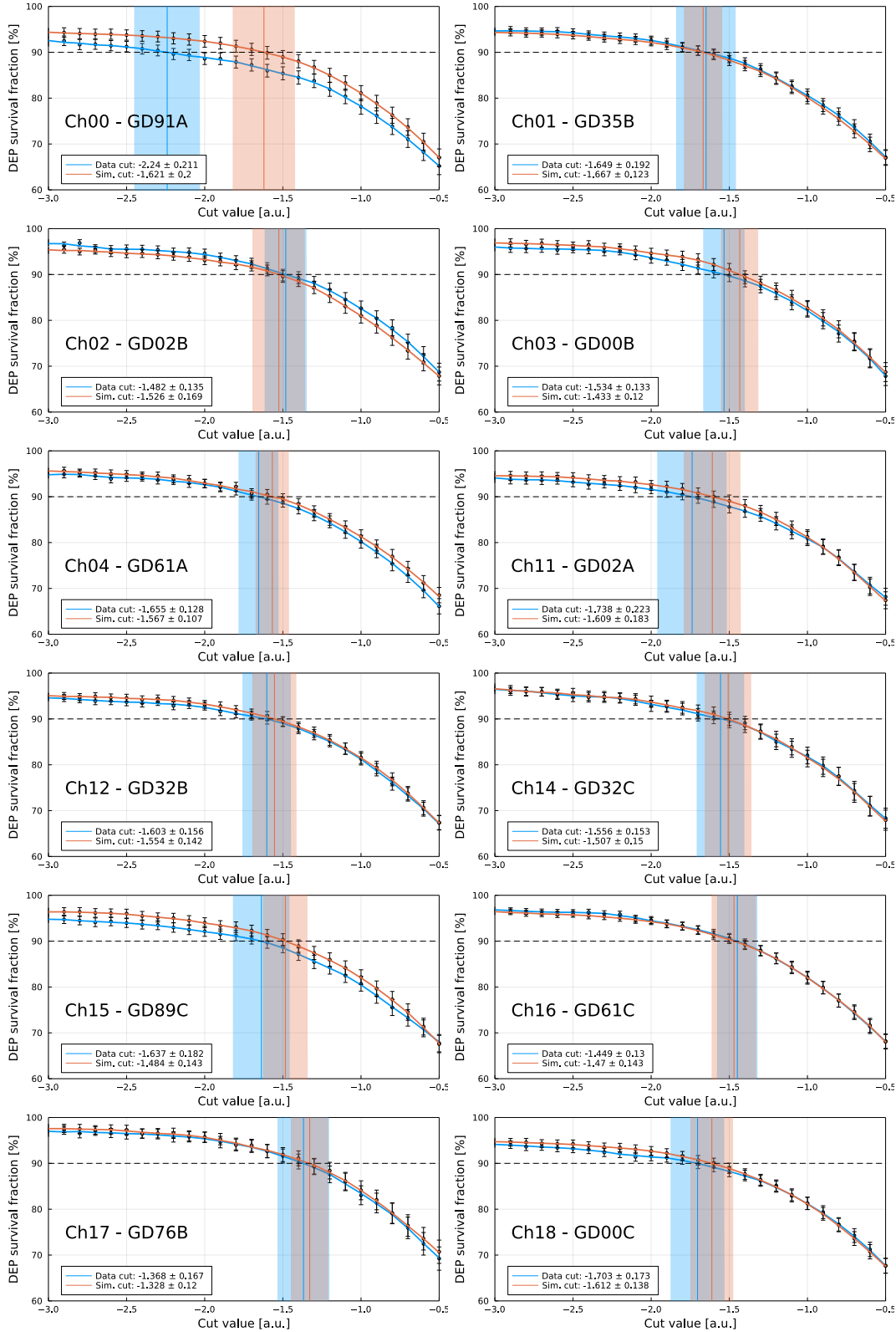
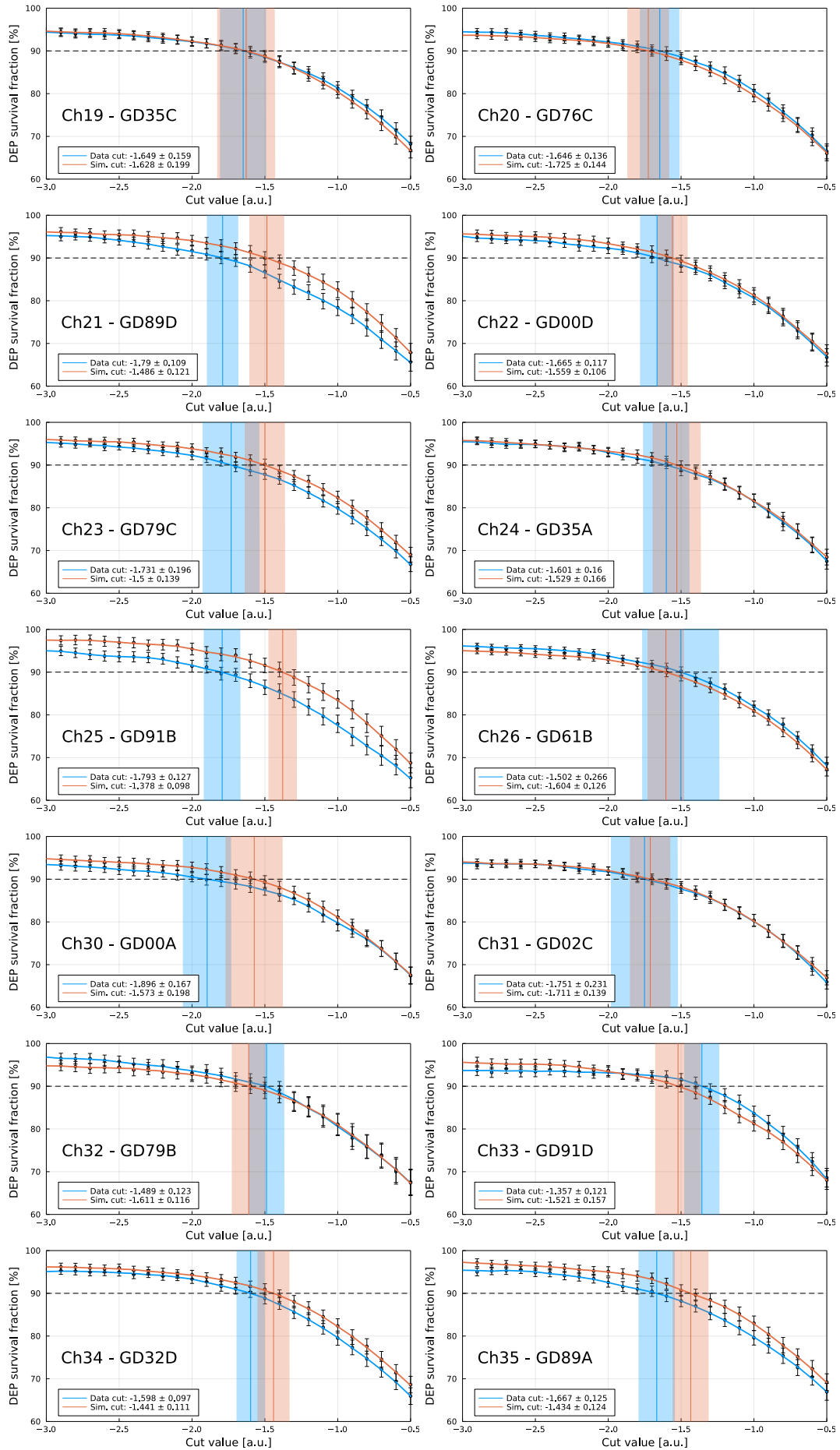


FIGURE B.6: DEP survival fraction as function of the A/E cut value for data and simulation. The given uncertainties of the survival fractions were calculated using Equation 8.16 while the uncertainty of the determined cut value at 90% is defined in Equation 8.14.





## B.6 *A/E Cut Survival Fractions*

Channel	$\epsilon_{\text{DEP, data}}$ in %	$\epsilon_{\text{DEP, sim.}}$ in %	$\epsilon_{\text{FEP Bi, data}}$ in %	$\epsilon_{\text{FEP Bi, sim.}}$ in %
00	87.14 ± 1.27	86.56 ± 1.90	14.29 ± 2.53	10.81 ± 1.10
01	88.19 ± 2.24	88.56 ± 1.20	14.72 ± 1.92	13.70 ± 0.81
02	86.15 ± 1.42	87.33 ± 2.18	15.39 ± 2.58	17.08 ± 1.56
03	86.36 ± 1.25	86.88 ± 1.75	16.18 ± 2.29	15.08 ± 1.18
04	88.35 ± 1.47	88.92 ± 1.14	15.41 ± 1.88	17.91 ± 1.61
11	86.70 ± 2.17	87.81 ± 1.64	13.20 ± 2.34	13.87 ± 1.09
12	88.43 ± 1.67	88.17 ± 1.43	15.72 ± 1.80	14.40 ± 0.91
14	86.19 ± 1.22	87.44 ± 1.83	16.27 ± 2.65	14.52 ± 1.27
15	85.06 ± 2.28	88.26 ± 1.95	19.44 ± 2.64	19.96 ± 2.21
16	86.50 ± 1.93	88.70 ± 1.86	17.60 ± 2.11	22.13 ± 1.14
17	85.24 ± 2.72	84.88 ± 2.06	16.58 ± 3.90	22.83 ± 3.22
18	87.49 ± 1.32	87.64 ± 1.50	12.63 ± 1.63	12.60 ± 0.83
19	88.45 ± 1.75	88.78 ± 2.16	13.20 ± 1.99	13.39 ± 1.09
20	89.00 ± 1.11	88.36 ± 1.42	13.76 ± 1.72	13.90 ± 0.93
21	88.51 ± 1.35	86.80 ± 1.47	20.20 ± 3.19	17.40 ± 1.42
22	88.06 ± 1.32	88.41 ± 1.54	14.99 ± 2.08	15.33 ± 1.05
23	87.65 ± 2.23	88.64 ± 1.91	17.22 ± 2.18	16.24 ± 1.00
24	87.60 ± 1.88	87.88 ± 2.14	17.62 ± 2.55	15.85 ± 1.25
25	88.29 ± 1.55	86.61 ± 1.73	23.86 ± 2.86	19.66 ± 1.50
26	89.97 ± 3.65	88.24 ± 1.25	16.31 ± 2.01	15.68 ± 0.96
30	86.13 ± 0.96	85.91 ± 2.23	13.56 ± 2.92	12.84 ± 1.21
31	88.60 ± 1.83	88.31 ± 1.46	11.34 ± 1.68	12.24 ± 0.84
32	88.88 ± 1.74	88.62 ± 1.19	14.16 ± 3.26	14.28 ± 0.98
33	89.63 ± 1.80	86.54 ± 2.15	25.21 ± 2.98	15.87 ± 1.40
34	88.90 ± 1.36	88.28 ± 1.55	22.36 ± 2.43	13.96 ± 0.87
35	87.19 ± 1.12	87.03 ± 1.91	24.47 ± 3.04	20.57 ± 1.65

TABLE B.2: *A/E* cut survival fractions  $\epsilon$  for the DEP of  $^{208}\text{Tl}$  and FEP of  $^{212}\text{Bi}$  from data and simulation. Statistical and systematic uncertainties are combined.

Channel	$\epsilon_{\text{SEP, data}}$ in %	$\epsilon_{\text{SEP, sim.}}$ in %	$\epsilon_{\text{FEP Tl, data}}$ in %	$\epsilon_{\text{FEP Tl, sim.}}$ in %
00	$8.08 \pm 1.42$	$6.08 \pm 0.65$	$10.30 \pm 0.77$	$8.27 \pm 0.63$
01	$8.12 \pm 1.16$	$7.61 \pm 0.73$	$10.04 \pm 0.76$	$9.93 \pm 0.46$
02	$8.48 \pm 1.23$	$8.77 \pm 0.79$	$11.44 \pm 0.78$	$12.60 \pm 0.83$
03	$9.85 \pm 1.43$	$8.02 \pm 0.62$	$12.03 \pm 1.03$	$10.61 \pm 0.30$
04	$10.06 \pm 1.31$	$12.29 \pm 0.85$	$12.97 \pm 0.75$	$13.69 \pm 0.60$
11	$7.09 \pm 1.27$	$6.54 \pm 0.65$	$9.74 \pm 0.89$	$9.69 \pm 0.68$
12	$7.56 \pm 0.95$	$8.53 \pm 0.68$	$11.00 \pm 0.72$	$10.24 \pm 0.34$
14	$9.07 \pm 1.26$	$7.96 \pm 0.66$	$10.94 \pm 0.77$	$10.58 \pm 0.67$
15	$10.07 \pm 1.52$	$11.70 \pm 1.14$	$12.42 \pm 1.06$	$15.10 \pm 0.91$
16	$12.58 \pm 1.38$	$13.47 \pm 0.80$	$16.58 \pm 0.94$	$16.36 \pm 0.82$
17	$10.00 \pm 1.81$	$15.03 \pm 3.92$	$13.78 \pm 1.27$	$16.24 \pm 0.87$
18	$7.69 \pm 0.88$	$7.08 \pm 0.68$	$8.77 \pm 0.61$	$7.02 \pm 0.40$
19	$6.71 \pm 1.07$	$7.26 \pm 0.78$	$8.86 \pm 0.65$	$7.67 \pm 0.15$
20	$8.05 \pm 0.99$	$7.11 \pm 0.65$	$10.12 \pm 0.65$	$7.65 \pm 0.42$
21	$12.09 \pm 2.41$	$9.02 \pm 0.89$	$17.72 \pm 1.04$	$13.74 \pm 0.75$
22	$7.23 \pm 0.96$	$8.69 \pm 1.38$	$10.74 \pm 0.61$	$11.15 \pm 0.52$
23	$10.05 \pm 1.80$	$9.25 \pm 0.60$	$11.81 \pm 1.04$	$8.80 \pm 0.51$
24	$7.98 \pm 1.31$	$9.13 \pm 1.03$	$11.85 \pm 0.89$	$11.45 \pm 0.46$
25	$14.78 \pm 1.67$	$11.05 \pm 0.54$	$21.20 \pm 1.24$	$13.00 \pm 0.27$
26	$9.51 \pm 1.45$	$8.50 \pm 0.66$	$12.24 \pm 1.37$	$11.23 \pm 0.37$
30	$7.74 \pm 1.23$	$7.42 \pm 0.81$	$9.38 \pm 0.67$	$9.95 \pm 0.76$
31	$7.47 \pm 1.15$	$6.52 \pm 0.41$	$8.24 \pm 0.74$	$8.17 \pm 0.22$
32	$9.71 \pm 1.76$	$7.70 \pm 0.56$	$10.89 \pm 0.91$	$10.97 \pm 0.52$
33	$19.52 \pm 2.15$	$8.66 \pm 0.85$	$23.48 \pm 1.49$	$11.45 \pm 0.67$
34	$13.23 \pm 1.68$	$9.04 \pm 0.77$	$18.96 \pm 1.01$	$11.15 \pm 0.53$
35	$17.99 \pm 2.04$	$13.31 \pm 1.17$	$22.56 \pm 1.38$	$17.82 \pm 0.95$

TABLE B.3:  $A/E$  cut survival fractions  $\epsilon$  for the SEP and FEP of  $^{208}\text{Tl}$  from data and simulation. Statistical and systematic uncertainties are combined.

Channel	$\epsilon_{\text{Compton 1, data}}$ in %	$\epsilon_{\text{Compton 1, sim.}}$ in %	$\epsilon_{\text{Compton 2, data}}$ in %	$\epsilon_{\text{Compton 2, sim.}}$ in %
00	51.14 ± 3.59	56.57 ± 5.07	43.71 ± 3.84	48.35 ± 5.18
01	47.77 ± 3.29	52.67 ± 2.34	41.92 ± 3.37	46.77 ± 2.33
02	48.58 ± 3.73	54.86 ± 4.15	43.06 ± 4.06	49.95 ± 4.37
03	48.15 ± 4.24	52.90 ± 3.98	42.69 ± 4.31	48.23 ± 4.39
04	50.16 ± 2.62	55.81 ± 2.54	44.94 ± 2.71	50.25 ± 2.61
11	50.16 ± 4.24	59.46 ± 4.42	40.77 ± 4.53	50.84 ± 4.60
12	48.18 ± 2.90	55.26 ± 3.00	41.74 ± 3.02	48.84 ± 2.89
14	49.05 ± 4.00	52.88 ± 3.66	42.91 ± 4.54	47.36 ± 3.84
15	51.93 ± 4.79	58.61 ± 4.26	46.18 ± 5.46	52.64 ± 4.30
16	52.83 ± 3.77	59.18 ± 3.61	48.53 ± 4.06	53.33 ± 3.67
17	52.82 ± 6.38	61.04 ± 6.52	47.70 ± 6.65	56.12 ± 6.79
18	47.85 ± 3.69	53.74 ± 3.66	40.64 ± 3.91	47.59 ± 3.77
19	50.55 ± 3.30	58.34 ± 3.71	41.93 ± 3.49	50.19 ± 3.66
20	48.80 ± 2.66	54.23 ± 2.69	42.28 ± 2.67	47.60 ± 2.65
21	53.10 ± 3.64	57.29 ± 4.13	47.84 ± 3.15	51.85 ± 4.24
22	49.66 ± 2.83	52.87 ± 2.64	43.39 ± 2.98	47.22 ± 2.81
23	50.63 ± 3.90	53.39 ± 3.20	44.21 ± 3.85	47.19 ± 3.30
24	49.87 ± 3.33	54.65 ± 3.31	43.43 ± 3.47	48.49 ± 3.31
25	54.78 ± 3.35	55.81 ± 3.92	50.78 ± 3.51	51.26 ± 4.31
26	49.88 ± 4.66	57.10 ± 2.95	43.13 ± 4.62	49.47 ± 3.01
30	50.48 ± 4.39	59.53 ± 6.45	41.44 ± 4.66	51.68 ± 6.66
31	46.51 ± 3.80	52.90 ± 2.90	39.29 ± 3.80	46.65 ± 2.90
32	48.76 ± 3.40	52.56 ± 2.48	41.89 ± 3.22	47.30 ± 2.48
33	55.60 ± 4.44	53.48 ± 4.37	53.49 ± 4.19	48.24 ± 4.65
34	53.12 ± 3.20	52.06 ± 3.43	49.70 ± 2.96	46.88 ± 3.55
35	54.80 ± 4.63	59.76 ± 4.17	51.91 ± 4.62	54.58 ± 4.37

TABLE B.4: *A/E* cut survival fractions  $\epsilon$  for two Compton continua from data and simulation. *Compton 1* is defined as the energy range 1100 – 1400 keV while *Compton 2* defined by 1700 – 2000 keV. Statistical and systematic uncertainties are combined.

Ch.	$\zeta_{\text{cut,data}}$	$\Delta\zeta'_{\text{cut}}$	$\Delta\zeta_{\text{met.}}$	$\zeta_{\text{cut,sim}}$	$\Delta\zeta'_{\text{cut}}$	$\Delta\zeta_{\text{met.}}$	$\Delta A$ in %	$\Delta E_{\text{uncal.}}$ in %
00	$-2.24 \pm 0.21$	0.19	0.09	$-1.62 \pm 0.20$	0.16	0.12	0.06	0.09
01	$-1.65 \pm 0.19$	0.17	0.10	$-1.67 \pm 0.12$	0.12	0.01	0.82	0.11
02	$-1.48 \pm 0.14$	0.13	0.03	$-1.53 \pm 0.17$	0.09	0.14	1.04	0.15
03	$-1.53 \pm 0.13$	0.13	0.04	$-1.43 \pm 0.12$	0.09	0.08	0.98	0.15
04	$-1.66 \pm 0.13$	0.12	0.03	$-1.57 \pm 0.11$	0.09	0.06	1.09	0.17
11	$-1.74 \pm 0.22$	0.22	0.02	$-1.61 \pm 0.18$	0.16	0.09	0.61	0.08
12	$-1.60 \pm 0.16$	0.15	0.03	$-1.55 \pm 0.14$	0.13	0.07	0.80	0.11
13	$-1.37 \pm 0.12$	0.12	0.02	$-1.35 \pm 0.12$	0.09	0.08	0.96	0.13
14	$-1.56 \pm 0.15$	0.15	0.02	$-1.51 \pm 0.15$	0.11	0.10	0.87	0.13
15	$-1.64 \pm 0.18$	0.18	0.05	$-1.48 \pm 0.14$	0.08	0.12	1.09	0.15
16	$-1.45 \pm 0.13$	0.12	0.05	$-1.47 \pm 0.14$	0.07	0.12	1.19	0.18
17	$-1.37 \pm 0.17$	0.16	0.03	$-1.33 \pm 0.12$	0.09	0.08	1.05	0.16
18	$-1.70 \pm 0.17$	0.16	0.06	$-1.61 \pm 0.14$	0.12	0.07	0.87	0.12
19	$-1.65 \pm 0.16$	0.14	0.08	$-1.63 \pm 0.20$	0.15	0.13	0.66	0.08
20	$-1.65 \pm 0.14$	0.13	0.02	$-1.72 \pm 0.14$	0.13	0.06	0.79	0.10
21	$-1.79 \pm 0.11$	0.10	0.03	$-1.49 \pm 0.12$	0.10	0.07	0.87	0.13
22	$-1.67 \pm 0.12$	0.11	0.05	$-1.56 \pm 0.11$	0.10	0.02	0.96	0.15
23	$-1.73 \pm 0.20$	0.18	0.08	$-1.50 \pm 0.14$	0.09	0.10	1.04	0.16
24	$-1.60 \pm 0.16$	0.15	0.06	$-1.53 \pm 0.17$	0.09	0.14	1.10	0.17
25	$-1.79 \pm 0.13$	0.11	0.05	$-1.38 \pm 0.10$	0.07	0.06	1.25	0.18
26	$-1.50 \pm 0.27$	0.20	0.17	$-1.60 \pm 0.13$	0.12	0.05	0.85	0.14
30	$-1.90 \pm 0.17$	0.16	0.03	$-1.57 \pm 0.20$	0.14	0.14	0.69	0.10
31	$-1.75 \pm 0.23$	0.19	0.14	$-1.71 \pm 0.14$	0.14	0.02	0.75	0.11
32	$-1.49 \pm 0.12$	0.12	0.01	$-1.61 \pm 0.12$	0.12	0.01	0.84	0.12
33	$-1.36 \pm 0.12$	0.09	0.07	$-1.52 \pm 0.16$	0.10	0.12	0.92	0.15
34	$-1.60 \pm 0.10$	0.10	0.003	$-1.44 \pm 0.11$	0.10	0.03	0.94	0.15
35	$-1.67 \pm 0.13$	0.12	0.001	$-1.43 \pm 0.12$	0.08	0.09	1.15	0.17

TABLE B.5:  $A/E$  low cut values  $\zeta_{\text{cut}}$  and uncertainties for data and simulation.  $\Delta\zeta_{\text{cut}}$  is defined in Equation 8.14 taking the uncertainties of  $A/E$   $\Delta\zeta'_{\text{cut}}$ , the amplitude determination method  $\Delta A$  and the cut determination method  $\Delta\zeta_{\text{met.}}$  into account. The uncertainty on determining the energy estimator  $\Delta E_{\text{uncal.}}$  was considered to be negligible.

# Bibliography

- [1] D. Adams. *The Hitchhiker's Guide to the Galaxy*. Hitchhiker series volume 1. New York : Harmony Books, 1979.
- [2] "GALLEX solar neutrino observations: results for GALLEX IV". In: *Physics Letters B* 447.1 (1999), pp. 127–133. ISSN: 0370-2693. DOI: [https://doi.org/10.1016/S0370-2693\(98\)01579-2](https://doi.org/10.1016/S0370-2693(98)01579-2).
- [3] T. Araki et al. "Measurement of neutrino oscillation with KamLAND: Evidence of spectral distortion". In: *Phys. Rev. Lett.* 94 (2005), p. 081801. DOI: [10.1103/PhysRevLett.94.081801](https://doi.org/10.1103/PhysRevLett.94.081801). arXiv: [hep-ex/0406035](https://arxiv.org/abs/hep-ex/0406035).
- [4] M. H. et al. Ahn. "Measurement of neutrino oscillation by the K2K experiment". In: *Phys. Rev. D* 74 (7 2006), p. 072003. DOI: [10.1103/PhysRevD.74.072003](https://doi.org/10.1103/PhysRevD.74.072003).
- [5] Evgeny Akhmedov. "Majorana neutrinos and other Majorana particles: Theory and experiment". In: Dec. 2014. arXiv: [1412.3320](https://arxiv.org/abs/1412.3320) [[hep-ph](https://arxiv.org/abs/1412.3320)].
- [6] GERDA collaboration. "Final Results of GERDA on the Search for Neutrinoless Double- $\beta$  Decay". In: *Phys. Rev. Lett.* 125 (25 2020), p. 252502. DOI: [10.1103/PhysRevLett.125.252502](https://doi.org/10.1103/PhysRevLett.125.252502).
- [7] LEGEND collaboration. "The Large Enriched Germanium Experiment for Neutrinoless  $\beta\beta$  Decay: LEGEND-1000 Preconceptual Design Report". In: (July 2021). arXiv: [2107.11462](https://arxiv.org/abs/2107.11462) [[physics.ins-det](https://arxiv.org/abs/2107.11462)].
- [8] LEGEND. <https://legend-exp.org/>. Accessed: 2021-11-11.
- [9] H. Nakamura et al. "Evidence of deep-blue photon emission at high efficiency by common plastic". English. In: *EPL* 95.2 (2011). URL: [www.scopus.com](http://www.scopus.com).
- [10] Y. Efremenko et al. "Use of poly(ethylene naphthalate) as a self-vetoing structural material". In: *JINST* 14.07 (2019), P07006. DOI: [10.1088/1748-0221/14/07/P07006](https://doi.org/10.1088/1748-0221/14/07/P07006). arXiv: [1901.03579](https://arxiv.org/abs/1901.03579) [[physics.ins-det](https://arxiv.org/abs/1901.03579)].
- [11] GERDA collaboration. "Pulse shape discrimination for GERDA Phase I data". In: *Eur. Phys. J. C* 73.10 (2013), p. 2583. DOI: [10.1140/epjc/s10052-013-2583-7](https://doi.org/10.1140/epjc/s10052-013-2583-7). arXiv: [1307.2610](https://arxiv.org/abs/1307.2610) [[physics.ins-det](https://arxiv.org/abs/1307.2610)].

- [12] GERDA collaboration. “Pulse shape analysis in GERDA Phase II”. In: *Eur. Phys. J. C* 82.4 (2022), p. 284. DOI: [10.1140/epjc/s10052-022-10163-w](https://doi.org/10.1140/epjc/s10052-022-10163-w). arXiv: [2202.13355](https://arxiv.org/abs/2202.13355) [physics.ins-det].
- [13] C. L. Cowan et al. “Detection of the Free Neutrino: a Confirmation”. In: *Science* 124.3212 (1956), pp. 103–104. DOI: [10.1126/science.124.3212.103](https://doi.org/10.1126/science.124.3212.103).
- [14] David Griffiths. *Introduction to Elementary Particles*. 2nd. Wiley-VCH, 2008. ISBN: 3527406018,9783527406012.
- [15] P. A. Zyla et al. “Review of Particle Physics”. In: *PTEP* 2020.8 (2020), p. 083C01. DOI: [10.1093/ptep/ptaa104](https://doi.org/10.1093/ptep/ptaa104).
- [16] “Complete results for five years of GNO solar neutrino observations”. In: *Physics Letters B* 616.3 (2005), pp. 174–190. ISSN: 0370-2693. DOI: <https://doi.org/10.1016/j.physletb.2005.04.068>.
- [17] “Determination of solar neutrino oscillation parameters using 1496 days of Super-Kamiokande-I data”. In: *Physics Letters B* 539.3 (2002), pp. 179–187. ISSN: 0370-2693. DOI: [https://doi.org/10.1016/S0370-2693\(02\)02090-7](https://doi.org/10.1016/S0370-2693(02)02090-7).
- [18] Y. Ashie et al. “Evidence for an oscillatory signature in atmospheric neutrino oscillation”. In: *Phys. Rev. Lett.* 93 (2004), p. 101801. DOI: [10.1103/PhysRevLett.93.101801](https://doi.org/10.1103/PhysRevLett.93.101801). arXiv: [hep-ex/0404034](https://arxiv.org/abs/hep-ex/0404034).
- [19] Y. Abe et al. “Reactor electron antineutrino disappearance in the Double Chooz experiment”. In: *Phys. Rev. D* 86 (2012), p. 052008. DOI: [10.1103/PhysRevD.86.052008](https://doi.org/10.1103/PhysRevD.86.052008). arXiv: [1207.6632](https://arxiv.org/abs/1207.6632) [hep-ex].
- [20] J. H. et al. Choi. “Observation of Energy and Baseline Dependent Reactor Antineutrino Disappearance in the RENO Experiment”. In: *Phys. Rev. Lett.* 116 (21 2016), p. 211801. DOI: [10.1103/PhysRevLett.116.211801](https://doi.org/10.1103/PhysRevLett.116.211801).
- [21] P. F. de Salas et al. “2020 global reassessment of the neutrino oscillation picture”. In: *JHEP* 02 (2021), p. 071. DOI: [10.1007/JHEP02\(2021\)071](https://doi.org/10.1007/JHEP02(2021)071). arXiv: [2006.11237](https://arxiv.org/abs/2006.11237) [hep-ph].
- [22] “Neutrino mass hierarchy”. In: *Progress in Particle and Nuclear Physics* 83 (2015), pp. 1–30. ISSN: 0146-6410. DOI: <https://doi.org/10.1016/j.pnpnp.2015.05.002>.

- [23] Paul Adrien Maurice Dirac and Ralph Howard Fowler. “The quantum theory of the electron”. In: *Proceedings of the Royal Society of London. Series A, Containing Papers of a Mathematical and Physical Character* 117.778 (1928), pp. 610–624. DOI: [10.1098/rspa.1928.0023](https://doi.org/10.1098/rspa.1928.0023).
- [24] Paul Adrien Maurice Dirac and Ralph Howard Fowler. “The quantum theory of the Electron. Part II”. In: *Proceedings of the Royal Society of London. Series A, Containing Papers of a Mathematical and Physical Character* 118.779 (1928), pp. 351–361. DOI: [10.1098/rspa.1928.0056](https://doi.org/10.1098/rspa.1928.0056).
- [25] C. F. v. Weizsäcker. “Zur Theorie der Kernmassen”. In: *Zeitschrift für Physik* (1935). DOI: [10.1007/BF01337700](https://doi.org/10.1007/BF01337700).
- [26] “Average and recommended half-life values for two-neutrino double beta decay”. In: *Nuclear Physics A* 935 (2015), pp. 52–64. ISSN: 0375-9474. DOI: <https://doi.org/10.1016/j.nuclphysa.2015.01.001>.
- [27] Benjamin J. P. Jones. “The Physics of Neutrinoless Double Beta Decay: A Primer”. In: *Theoretical Advanced Study Institute in Elementary Particle Physics: The Obscure Universe: Neutrinos and Other Dark Matters*. Aug. 2021. arXiv: [2108.09364 \[nucl-ex\]](https://arxiv.org/abs/2108.09364).
- [28] Dusan Stefanik et al. “Reexamining the light neutrino exchange mechanism of the  $0\nu\beta\beta$  decay with left- and right-handed leptonic and hadronic currents”. In: *Phys. Rev. C* 92.5 (2015), p. 055502. DOI: [10.1103/PhysRevC.92.055502](https://doi.org/10.1103/PhysRevC.92.055502). arXiv: [1506.07145 \[hep-ph\]](https://arxiv.org/abs/1506.07145).
- [29] Heinrich Päs and Werner Rodejohann. “Neutrinoless Double Beta Decay”. In: *New J. Phys.* 17.11 (2015), p. 115010. DOI: [10.1088/1367-2630/17/11/115010](https://doi.org/10.1088/1367-2630/17/11/115010). arXiv: [1507.00170 \[hep-ph\]](https://arxiv.org/abs/1507.00170).
- [30] V. D’Andrea. “Improvement of Performances and Background Studies in GERDA Phase II”. PhD thesis. Gran Sasso Science Institute, Apr. 2017.
- [31] P Dirac. “The quantum theory of the emission and absorption of radiation”. In: *Proc. R. Soc. Lond. A* 114 (1927), p. 243.
- [32] J. M. Zhang and Y. Liu. “Fermi’s golden rule: its derivation and breakdown by an ideal model”. In: *Eur. J. Phys.* 37.6 (2016), p. 065406. DOI: [10.1088/0143-0807/37/6/065406](https://doi.org/10.1088/0143-0807/37/6/065406). arXiv: [1604.06916 \[quant-ph\]](https://arxiv.org/abs/1604.06916).

- [33] Matteo Agostini, Giovanni Benato, and Jason Detwiler. “Discovery probability of next-generation neutrinoless double- $\beta$  decay experiments”. In: *Phys. Rev. D* 96.5 (2017), p. 053001. DOI: [10.1103/PhysRevD.96.053001](https://doi.org/10.1103/PhysRevD.96.053001). arXiv: [1705.02996 \[hep-ex\]](https://arxiv.org/abs/1705.02996).
- [34] A. et al. Gando. “Search for Majorana Neutrinos Near the Inverted Mass Hierarchy Region with KamLAND-Zen”. In: *Phys. Rev. Lett.* 117 (8 2016), p. 082503. DOI: [10.1103/PhysRevLett.117.082503](https://doi.org/10.1103/PhysRevLett.117.082503).
- [35] M. et al. Aker. “Analysis methods for the first KATRIN neutrino-mass measurement”. In: *Phys. Rev. D* 104 (1 2021), p. 012005. DOI: [10.1103/PhysRevD.104.012005](https://doi.org/10.1103/PhysRevD.104.012005).
- [36] M. Aker et al. “Direct neutrino-mass measurement with sub-electronvolt sensitivity”. In: *Nature Phys.* 18.2 (2022), pp. 160–166. DOI: [10.1038/s41567-021-01463-1](https://doi.org/10.1038/s41567-021-01463-1). arXiv: [2105.08533 \[hep-ex\]](https://arxiv.org/abs/2105.08533).
- [37] P. A. R. Ade et al. “Planck 2015 results. XIII. Cosmological parameters”. In: *Astron. Astrophys.* 594 (2016), A13. DOI: [10.1051/0004-6361/201525830](https://doi.org/10.1051/0004-6361/201525830). arXiv: [1502.01589 \[astro-ph.CO\]](https://arxiv.org/abs/1502.01589).
- [38] Michelle J. Dolinski, Alan W. P. Poon, and Werner Rodejohann. “Neutrinoless Double-Beta Decay: Status and Prospects”. In: *Ann. Rev. Nucl. Part. Sci.* 69 (2019), pp. 219–251. DOI: [10.1146/annurev-nucl-101918-023407](https://doi.org/10.1146/annurev-nucl-101918-023407). arXiv: [1902.04097 \[nucl-ex\]](https://arxiv.org/abs/1902.04097).
- [39] Brianna J. Mount, Matthew Redshaw, and Edmund G. Myers. “Double- $\beta$ -decay  $Q$  values of  $^{74}\text{Se}$  and  $^{76}\text{Ge}$ ”. In: *Phys. Rev. C* 81 (3 2010), p. 032501. DOI: [10.1103/PhysRevC.81.032501](https://doi.org/10.1103/PhysRevC.81.032501).
- [40] Joachim Ebert et al. “Results of a search for neutrinoless double- $\beta$  decay using the COBRA demonstrator”. In: *Phys. Rev. C* 94.2 (2016), p. 024603. DOI: [10.1103/PhysRevC.94.024603](https://doi.org/10.1103/PhysRevC.94.024603). arXiv: [1509.04113 \[nucl-ex\]](https://arxiv.org/abs/1509.04113).
- [41] A. E. Chavarria et al. “A high-resolution CMOS imaging detector for the search of neutrinoless double  $\beta$  decay in  $^{82}\text{Se}$ ”. In: *JINST* 12 (2017), P03022. DOI: [10.1088/1748-0221/12/03/P03022](https://doi.org/10.1088/1748-0221/12/03/P03022). arXiv: [1609.03887 \[physics.ins-det\]](https://arxiv.org/abs/1609.03887).
- [42] GERDA collaboration. “The GERDA experiment for the search of  $0\nu\beta\beta$  decay in  $^{76}\text{Ge}$ ”. In: *Eur. Phys. J. C* 73.3 (2013), p. 2330. DOI: [10.1140/epjc/s10052-013-2330-0](https://doi.org/10.1140/epjc/s10052-013-2330-0). arXiv: [1212.4067 \[physics.ins-det\]](https://arxiv.org/abs/1212.4067).

- [43] GERDA collaboration. “Probing Majorana neutrinos with double- $\beta$  decay”. In: *Science* 365 (2019), p. 1445. DOI: [10.1126/science.aav8613](https://doi.org/10.1126/science.aav8613). arXiv: [1909.02726](https://arxiv.org/abs/1909.02726) [hep-ex].
- [44] GERDA collaboration. “Upgrade for Phase II of the GERDA experiment”. In: *Eur. Phys. J. C* 78.5 (2018), p. 388. DOI: [10.1140/epjc/s10052-018-5812-2](https://doi.org/10.1140/epjc/s10052-018-5812-2). arXiv: [1711.01452](https://arxiv.org/abs/1711.01452) [physics.ins-det].
- [45] GERDA Home Page. <https://www.mpi-hd.mpg.de/gerda/home.html>. Accessed: 2021-11-09.
- [46] *GeDet plots*. <https://github.com/gipert/gedet-plots>. Accessed: 2021-11-10.
- [47] L. Pertoldi. “Search for new physics with two-neutrino double-beta decay in GERDA data”. PhD thesis. Università degli Studi di Padova, 2020.
- [48] J. Janicskó Csáthy et al. “Optical fiber read-out for liquid argon scintillation light”. In: (June 2016). arXiv: [1606.04254](https://arxiv.org/abs/1606.04254) [physics.ins-det].
- [49] V. E. Guiseppe et al. “The Majorana Neutrinoless Double-Beta Decay Experiment”. In: *2008 IEEE Nuclear Science Symposium and Medical Imaging Conference and 16th International Workshop on Room-Temperature Semiconductor X-Ray and Gamma-Ray Detectors*. 2008, pp. 1793–1798. DOI: [10.1109/NSSMIC.2008.4774740](https://doi.org/10.1109/NSSMIC.2008.4774740). arXiv: [0811.2446](https://arxiv.org/abs/0811.2446) [nucl-ex].
- [50] D. G. Phillips II et al. “The Majorana experiment: an ultra-low background search for neutrinoless double-beta decay”. In: *J. Phys. Conf. Ser.* 381 (2012). Ed. by Sean Freeman et al., p. 012044. DOI: [10.1088/1742-6596/381/1/012044](https://doi.org/10.1088/1742-6596/381/1/012044). arXiv: [1111.5578](https://arxiv.org/abs/1111.5578) [nucl-ex].
- [51] S. I. Alvis et al. “A Search for Neutrinoless Double-Beta Decay in  $^{76}\text{Ge}$  with 26 kg-yr of Exposure from the MAJORANA DEMONSTRATOR”. In: *Phys. Rev. C* 100.2 (2019), p. 025501. DOI: [10.1103/PhysRevC.100.025501](https://doi.org/10.1103/PhysRevC.100.025501). arXiv: [1902.02299](https://arxiv.org/abs/1902.02299) [nucl-ex].
- [52] *The MAJORANA Neutrinoless Double-beta Decay Experiment*. <https://www.npl.washington.edu/majorana/>. Accessed: 2021-11-10.
- [53] Glenn F. Knoll. *Radiation Detection and Measurement*. 4th. Wiley, 2010. ISBN: 9780470131480.
- [54] I. Abt et al. “Simulation of semiconductor detectors in 3D with Solid-StateDetectors.jl”. In: *Journal of Instrumentation* 16.08 (Aug. 2021), P08007. DOI: [10.1088/1748-0221/16/08/p08007](https://doi.org/10.1088/1748-0221/16/08/p08007).

- [55] W. Shockley. “Currents to conductors induced by a moving point charge”. In: *J. Appl. Phys.* 9.10 (1938), pp. 635–636. DOI: [10.1063/1.1710367](https://doi.org/10.1063/1.1710367).
- [56] S. Ramo. “Currents Induced by Electron Motion”. In: *Proceedings of the IRE* 27.9 (1939), pp. 584–585. DOI: [10.1109/JRPROC.1939.228757](https://doi.org/10.1109/JRPROC.1939.228757).
- [57] *The Julia Programming Language*. <https://julialang.org/>. Accessed: 2022-01-07.
- [58] C. Canali et al. “Electron and hole drift velocity measurements in silicon and their empirical relation to electric field and temperature”. In: *IEEE Trans. Electron. Dev.* 22.11 (1975), pp. 1045–1047. DOI: [10.1109/t-ed.1975.18267](https://doi.org/10.1109/t-ed.1975.18267).
- [59] L. Mihailescu et al. “The influence of anisotropic electron drift velocity on the signal shapes of closed-end HPGe detectors”. In: *Nucl. Instrum. Meth. A* 447 (2000), pp. 350–360. DOI: [10.1016/S0168-9002\(99\)01286-3](https://doi.org/10.1016/S0168-9002(99)01286-3).
- [60] “Characterization of large volume HPGe detectors. Part I: Electron and hole mobility parameterization”. In: *Nuclear Instruments and Methods in Physics Research Section A: Accelerators, Spectrometers, Detectors and Associated Equipment* 569.3 (2006), pp. 764–773. ISSN: 0168-9002. DOI: <https://doi.org/10.1016/j.nima.2006.08.130>.
- [61] B. Bruyneel, B. Birkenbach, and P. Reiter. “Pulse shape analysis and position determination in segmented HPGe detectors: The AGATA detector library”. In: *Eur. Phys. J. A* 52.3 (2016), p. 70. DOI: [10.1140/epja/i2016-16070-9](https://doi.org/10.1140/epja/i2016-16070-9).
- [62] L. Hauertmann. “Surface Characterization of Segmented Germanium Detectors with Alpha, Beta and Gamma Particles”. PhD thesis. Technische Universität München, 2021.
- [63] P. Theodórsson. *Measurement of Weak Radioactivity*. World Scientific, 1996. ISBN: 978-981-02-2315-1.
- [64] G. Heusser. “Low-Radioactivity Background Techniques”. In: *Annual Review of Nuclear and Particle Science* 45.1 (1995), pp. 543–590. DOI: [10.1146/annurev.ns.45.120195.002551](https://doi.org/10.1146/annurev.ns.45.120195.002551).
- [65] *Table of Isotopes decay data*. <http://nucleardata.nuclear.lu.se>. Accessed: 2021-11-16.
- [66] C. Grupen. *Astroparticle Physics*. Springer, 2005. ISBN: 3-540-25312-2.

- [67] W. Petzold H. Krieger. *Strahlenphysik, Dosimetrie und Strahlenschutz: Band 1 Grundlagen*. Vieweg+Teubner Verlag, 1992. ISBN: 978-3-519-23052-6.
- [68] C. Wiesinger. “No Neutrinos not Found. First exploration of neutrinoless double beta decay half-lives beyond  $10^{26}$  years”. PhD thesis. Technische Universität München, 2020.
- [69] “Background reduction in neutrinoless double beta decay experiments using segmented detectors — A Monte Carlo study for the GERDA setup”. In: *Nuclear Instruments and Methods in Physics Research Section A: Accelerators, Spectrometers, Detectors and Associated Equipment* 570.3 (2007), pp. 479–486. ISSN: 0168-9002. DOI: <https://doi.org/10.1016/j.nima.2006.10.188>.
- [70] F. Edzards. “The Future of Neutrinoless Double Beta Decay Searches with Germanium Detectors”. In: *J. Phys. Conf. Ser.* 1690.1 (2020). Ed. by Petr Teterin, p. 012180. DOI: [10.1088/1742-6596/1690/1/012180](https://doi.org/10.1088/1742-6596/1690/1/012180).
- [71] GERDA collaboration. “Background-free search for neutrinoless double- $\beta$  decay of  $^{76}\text{Ge}$  with GERDA”. In: *Nature* 544 (2017), p. 47. DOI: [10.1038/nature21717](https://doi.org/10.1038/nature21717). arXiv: [1703.00570 \[nucl-ex\]](https://arxiv.org/abs/1703.00570).
- [72] S.S. Kapoor and V.S. Ramamurthy. *Nuclear Radiation Detectors*. B M Udgaonkar. New Age International Publishers, 1986. ISBN: 9780852264966. URL: <https://books.google.de/books?id=RX5Xdo030X0C>.
- [73] GERDA collaboration. “Calibration of the GERDA experiment”. In: *Eur. Phys. J. C* 81.8 (2021), p. 682. DOI: [10.1140/epjc/s10052-021-09403-2](https://doi.org/10.1140/epjc/s10052-021-09403-2). arXiv: [2103.13777 \[physics.ins-det\]](https://arxiv.org/abs/2103.13777).
- [74] K. Pelczar. “Backgrounds in the GERDA and DARKSIDE Experiments. Radioactive Ions in Cryogenic Liquids”. PhD thesis. Jagiellonian University, Krakow, 2016.
- [75] R. Brugnera et al. “Measurement of the  $^{42}\text{Ar}$  contamination in natural argon with GERDA”. In: (2012). GSTR-12-004, internal GERDA report.
- [76] A. S. Barabash, R. R. Saakyan, and V. I. Umatov. “On concentration of  $^{42}\text{Ar}$  in the Earth’s atmosphere”. In: *Nucl. Instrum. Meth. A* 839 (2016), pp. 39–42. DOI: [10.1016/j.nima.2016.09.042](https://doi.org/10.1016/j.nima.2016.09.042). arXiv: [1609.08890 \[nucl-ex\]](https://arxiv.org/abs/1609.08890).

- [77] S. R. Elliott et al. "Fast-Neutron Activation of Long-Lived Isotopes in Enriched Ge". In: *Phys. Rev. C* 82 (2010), p. 054610. DOI: [10.1103/PhysRevC.82.054610](https://doi.org/10.1103/PhysRevC.82.054610). arXiv: [0912.3748](https://arxiv.org/abs/0912.3748) [nucl-ex].
- [78] BC-400, BC-404, BC-408, BC-412, BC-416. <https://www.crystals.saint-gobain.com/products/bc-408-bc-412-bc-416>. Accessed: 2022-01-09.
- [79] GERDA Collaboration. "LArGe – Active background suppression using argon scintillation for the GERDA  $0\nu\beta\beta$ -experiment". In: *arXiv:1501.05762v1* (Jan. 2015).
- [80] S. Agostinelli et al. "GEANT4—a simulation toolkit". In: *Nucl. Instrum. Meth. A* 506 (2003), pp. 250–303. DOI: [10.1016/S0168-9002\(03\)01368-8](https://doi.org/10.1016/S0168-9002(03)01368-8).
- [81] A. Levin and C. Moisan. "A more physical approach to model the surface treatment of scintillation counters and its implementation into DETECT". In: *1996 IEEE Nuclear Science Symposium. Conference Record*. Vol. 2. 1996, 702–706 vol.2. DOI: [10.1109/NSSMIC.1996.591410](https://doi.org/10.1109/NSSMIC.1996.591410).
- [82] Vesna Cuplov et al. "Extension of the GATE Monte-Carlo simulation package to model bioluminescence and fluorescence imaging". In: *Journal of biomedical optics* 19 (Feb. 2014), p. 26004. DOI: [10.1117/1.JBO.19.2.026004](https://doi.org/10.1117/1.JBO.19.2.026004).
- [83] Y. Efremenko et al. "Production and validation of scintillating structural components from low-background Poly(ethylene naphthalate)". In: *JINST* 17.01 (2022), P01010. DOI: [10.1088/1748-0221/17/01/P01010](https://doi.org/10.1088/1748-0221/17/01/P01010). arXiv: [2110.12791](https://arxiv.org/abs/2110.12791) [physics.ins-det].
- [84] *Material: Copper (Cu), bulk*. <https://www.memnet.org/material/coppercubulk/>. Accessed: 2022-01-09.
- [85] "ISO 178:2010 + md.1:2013.Plastics - Determination of flexural properties". In: *International Organization for Standardization* (2013).
- [86] TEIJIN. *Polyethylene naphthalate (pen) resin teonex*. <https://www.teijin.com/products/resin/teonex/index2.html>. Accessed: 2021-08-01.
- [87] *Nitric Acid 67-69%*. <https://www.fishersci.com/shop/products/nitric-acid-67-69-optima-ultra-trace-elemental-analysis-fisher-chemical/A467250>. Accessed: 2022-02-18.

- [88] *Injection compression moulding*. <https://www.arburg.com/en/products-and-services/injection-moulding/processes/injection-compression-moulding/>. Accessed: 2022-01-21.
- [89] *Micro cleaning solution (micro-90)*. <https://www.emsdiasum.com/microscopy/technical/datasheet/71054.aspx>. Accessed: 2022-01-27.
- [90] Matthias Laubenstein. "Screening of materials with high purity germanium detectors at the Laboratori Nazionali del Gran Sasso". In: *Int. J. Mod. Phys. A* 32.30 (2017), p. 1743002. DOI: [10.1142/S0217751X17430023](https://doi.org/10.1142/S0217751X17430023).
- [91] V. B. Brudanin et al. "Development of the ultra-low background HPGe spectrometer OBELIX at Modane underground laboratory". In: *JINST* 12.02 (2017), P02004. DOI: [10.1088/1748-0221/12/02/P02004](https://doi.org/10.1088/1748-0221/12/02/P02004).
- [92] *ULTEM (PEI)*. <https://www.polytron-gmbh.de/ultem-pei.aspx>. Accessed: 2022-02-18.
- [93] F. Edzards. "Characterization of Point Contact Germanium Detectors and Development of Signal Readout Electronics for LEGEND". PhD thesis. Technische Universität München, 2021.
- [94] F. Fischer. "Investigation of PEN as Structural Self Vetoing Material for Cryogenic Low Background Experiments". MA thesis. Technische Universität München, Mar. 2018.
- [95] *Instrument Database: Andor Technology - SHAMROCK - SR-303I-A Spectrograph*. <http://www.speciation.net/Database/Instruments/Andor-Technology/SHAMROCK--SR303IA-Spectrograph-i2094>. Accessed: 2022-01-23.
- [96] *Andor Learning - Sensitivity*. <http://www.andor.com/scientificcameras/idus-spectroscopy-cameras/idus-420-series>. Accessed: 2022-01-23.
- [97] *Digitalmikroskop - Modellreihe VHX-6000*. <https://www.keyence.de/products/microscope/digital-microscope/vhx-6000/models/vhx-6000/>. Accessed: 2022-01-24.
- [98] Eljen Technologies. "Silicone Grease EJ-550, EJ-552". In: (). Accessed: 2022-03-28.
- [99] D. E. Alburger and A. W. Sunyar. "Decay of Bi<sup>207</sup>". In: *Phys. Rev.* 99 (3 1955), pp. 695–702. DOI: [10.1103/PhysRev.99.695](https://doi.org/10.1103/PhysRev.99.695).

- [100] Y. Abreu et al. "Optimisation of the scintillation light collection and uniformity for the SoLid experiment". In: *JINST* 13.09 (2018), P09005. DOI: [10.1088/1748-0221/13/09/P09005](https://doi.org/10.1088/1748-0221/13/09/P09005). arXiv: [1806.02461](https://arxiv.org/abs/1806.02461) [[physics.ins-det](https://arxiv.org/abs/1806.02461)].
- [101] *General Purpose EJ-200, EJ-204, EJ-208, EJ-212*. <https://eljentechnology.com/products/plastic-scintillators/ej-200-ej-204-ej-208-ej-212>. Accessed: 2022-02-18.
- [102] *SIS3316 16 Chanel VME Digitizer Family*. <https://www.struck.de/sis3316.html>. Accessed: 2022-01-24.
- [103] C. Bauer et al. "Qualification Tests of 474 Photomultiplier Tubes for the Inner Detector of the Double Chooz Experiment". In: *JINST* 6 (2011), P06008. DOI: [10.1088/1748-0221/6/06/P06008](https://doi.org/10.1088/1748-0221/6/06/P06008). arXiv: [1104.0758](https://arxiv.org/abs/1104.0758) [[physics.ins-det](https://arxiv.org/abs/1104.0758)].
- [104] C. Weber. *Characterizing optical properties of PEN for the LEGEND-200 simulation framework*. Bachelor thesis. Mar. 2022.
- [105] *LAMBDA 850+ UV/Vis Spectrophotometer*. <https://www.perkinelmer.com/de/product/lambda-850-uv-vis-spectrophotometer-1850>. Accessed: 2022-02-17.
- [106] X. Zhang et al. "Complex refractive indices measurements of polymers in visible and near-infrared bands". In: *Appl. Opt.* 59.8 (2020), pp. 2337–2344.
- [107] *Manual of the H11934 PMT series*. [https://www.hamamatsu.com/content/dam/hamamatsu-photonics/sites/documents/99\\_SALES\\_LIBRARY/etd/R11265U\\_H11934\\_TPMH1336E.pdf](https://www.hamamatsu.com/content/dam/hamamatsu-photonics/sites/documents/99_SALES_LIBRARY/etd/R11265U_H11934_TPMH1336E.pdf). Accessed: 2022-03-18.
- [108] *Optical constants of OHARA - BSL (Borosilicate, low-index)*. <https://refractiveindex.info/?shelf=glass&book=OHARA-BSL&page=BSL1>. Accessed: 2022-04-01.
- [109] Emily Grace and James A. Nikkel. "Index of refraction, Rayleigh scattering length, and Sellmeier coefficients in solid and liquid argon and xenon". In: *Nucl. Instrum. Meth. A* 867 (2017), pp. 204–208. DOI: [10.1016/j.nima.2017.06.031](https://doi.org/10.1016/j.nima.2017.06.031). arXiv: [1502.04213](https://arxiv.org/abs/1502.04213) [[physics.ins-det](https://arxiv.org/abs/1502.04213)].

- [110] A. Wegmann. “Characterization of the liquid argon veto of the GERDA experiment and its application for the measurement of the  $^{76}\text{Ge}$  half-life”. PhD thesis. Combined Faculties of the Natural Sciences and Mathematics of the Ruperto-Carola-University of Heidelberg. Germany, Jan. 2017.
- [111] A. Lubashevskiy et al. “Nylon mini-shroud coated with wavelength shifter for the GERDA Phase II detectors array”. In: (2015). GSTR-15-504, internal GERDA report.
- [112] *Fiber | Scintillating and Light Transmitting*. <https://www.crystals.saint-gobain.com/radiation-detection-scintillators/fibers>. Accessed: 2022-04-01.
- [113] C. Wiesinger and L. Pertoldi. “A LAr veto Monte Carlo model for GERDA Phase II”. In: (2020). GSTR-20-009, internal GERDA report.
- [114] Melissa Boswell et al. “MaGe-a Geant4-based Monte Carlo Application Framework for Low-background Germanium Experiments”. In: *IEEE Trans. Nucl. Sci.* 58 (2011), pp. 1212–1220. DOI: [10.1109/TNS.2011.2144619](https://doi.org/10.1109/TNS.2011.2144619). arXiv: [1011.3827 \[nucl-ex\]](https://arxiv.org/abs/1011.3827).
- [115] M. Agostini et al. “Modeling of GERDA Phase II data”. In: *JHEP* 03 (2020), p. 139. DOI: [10.1007/JHEP03\(2020\)139](https://doi.org/10.1007/JHEP03(2020)139). arXiv: [1909.02522 \[nucl-ex\]](https://arxiv.org/abs/1909.02522).
- [116] GERDA Collaboration. “Characterization of  $^{30}\text{Ge}$  enriched Broad Energy Ge detectors for GERDA Phase II”. In: *Eur. Phys. J. C* 79.11 (2019), p. 978. DOI: [10.1140/epjc/s10052-019-7353-8](https://doi.org/10.1140/epjc/s10052-019-7353-8). arXiv: [1901.06590 \[physics.ins-det\]](https://arxiv.org/abs/1901.06590).
- [117] *ICPC SigGen*. [https://github.com/radforddc/icpc\\_siggen](https://github.com/radforddc/icpc_siggen). Accessed: 2021-11-29.
- [118] K. Panas. “Development of Pulse Shape Discrimination Methods as Tools for Background Suppression in High Purity Germanium Detectors used in the GERDA Experiment”. PhD thesis. Jagiellonian U. (main), 2018.
- [119] M. Agostini et al. “Improvement of the energy resolution via an optimized digital signal processing in GERDA Phase I”. In: *Eur. Phys. J. C* 75.6 (2015), p. 255. DOI: [10.1140/epjc/s10052-015-3409-6](https://doi.org/10.1140/epjc/s10052-015-3409-6). arXiv: [1502.04392 \[physics.ins-det\]](https://arxiv.org/abs/1502.04392).

- 
- [120] B. Schweisshelm. "Influence of the Charge Cloud Size on Germanium Detector Pulse Shapes in the GERDA Experiment". MA thesis. Technische Universität München, Apr. 2018.
- [121] Marc Paterno. "Calculating efficiencies and their uncertainties". In: (Dec. 2004). DOI: [10.2172/15017262](https://doi.org/10.2172/15017262).
- [122] M. Be and V. Chiste. "Table de Radionucléides, Bi-207". In: (2009). Accessed: 2022-03-21, [http://www.nucleide.org/DDEP\\_WG/Nuclides/Bi-207\\_tables.pdf](http://www.nucleide.org/DDEP_WG/Nuclides/Bi-207_tables.pdf).